Synthesis, Morphological, Optical and Photocatalytic Studies of lead sulfide and tin sulfide Nanoparticles

Thandi Bongiwe MBUYAZI

College of Agriculture, Engineering and Science

2022

UNIVERSITY OF KWAZULU-NATAL
INYUVESI YAKWAZULU-NATALI

January 2022

Synthesis, Morphological, Optical and Photocatalytic Studies of lead sulfide and tin sulfide Nanoparticles

By

Thandi Bongiwe MBUYAZI (216006335)

B. Sc., B. Sc. (Honours) Chemistry (UKZN)

Being a dissertation submitted to the College of Agriculture, Engineering, and Science in fulfillment of the requirements for the award of the degree of

Master of Science in Chemistry

of the

University of KwaZulu-Natal

South Africa

Supervisor: Professor P. A. Ajibade

DECLARATION BY CANDIDATE

I declare that this dissertation is my own work carried out in the School of Physics and Chemistry at the University of KwaZulu-Natal and has not been submitted for any degree or examination to any other university. I further declare that all sources I have used or quoted have been indicated and acknowledged by complete references.

18/1/22 [redacted]

Date Thandi Bongiwe Mbuyazi

DECLARATION: PLAGIARISM

I, Thandi Bongiwe Mbuyazi declare that:

(i) The research in this dissertation, except where otherwise indicated, is my original research;

(ii) This dissertation has not been submitted for any degree or examination at other university;

(iii) This dissertation does not contain other persons' data or graphics unless specifically acknowledged as being sourced from them.

(iv) This dissertation does not contain any other persons' writing, unless specifically acknowledged as being sourced from other researchers. Where other written sources have been quoted, then:

(a) Their words have been re-written, but the general information attributed to them has been properly referenced.

(b) In instances where the exact words of other authors have been used, then their writing has been placed inside quotation marks and referenced.

(v) This dissertation does not contain text, graphs, pictures or tables from the internet copied and pasted, unless specifically acknowledged, and the source being detailed in the dissertation and in the references section.

18/1/22 [redacted]

Date Thandi Bongiwe Mbuyazi

CERTIFICATION

This is to certify that this research is a record of original work carried out by Thandi Bongiwe Mbuyazi under my supervision in the Inorganic Materials Research laboratory of the School of Physics and Chemistry, University of Kwa Zulu Natal in fulfilments of the requirements for the award of Master of Science degree in Chemistry.

[redacted]

24/1/22_____ _____

Date **Supervisor**

P. A. Ajibade

Professor of Inorganic Materials Chemistry

B.Sc (Hons), MSc (Ibadan);

PhD (UniZul); MRSC (London)

DEDICATION

This dissertation is dedicated to my mother, Nokuthula Mbuyazi, whose love, support and encouragement have enriched my soul and inspired me to pursue and complete this research.

ACKNOWLEDGEMENTS

I would like to thank the Almighty God for giving me strength throughout this project, for having seen this work to completion; I could have never done this without Him. I extend my utmost gratitude to my supervisor Prof. P. A. Ajibade for his support and guidance towards my project. I would also like to thank the National Research Foundation for the award of master's innovation scholarship. Thank you to all the members of the Inorganic Materials Chemistry Research Laboratory for all the assistance and support. To my family and friends, words cannot describe how grateful I am for all your sacrifices and patience.

Contents

List of Figures

List of Schemes

List of Tables

List of Abbreviations and Symbols

DTC – Dithiocarbamates

Pb – Lead

Sn – Tin

NPs – Nanoparticles

SSP – Single-source precursor

DMSO – Dimethyl sulfoxide

DCM – Dichloromethane

NMR – Nuclear magnetic resonance

FTIR – Fourier Transform Infrared spectroscopy

UV-Vis – Ultraviolet Visible spectroscopy

p-XRD – Powder X-Ray diffraction

SEM – Scanning electron microscopy

TEM – Transmission electron microscopy

EDX – Energy dispersive X-ray

TOP – Trioctylphosphine

HDA – Hexadecylamine

TOPO – Trioctylphosphine oxide

ODA – Octadecylamine

JCPDS – Joint Committee on Powder Diffraction Standards

LMCT – Ligand to Metal Charge Transfer

h – Hour

nm – Nanometer

a.u – Arbitrary unit

eq – Equation

Fig – Figure

et al – Et alia

ν – frequency

δ – Chemical Shift

% – Percentage

Θ – Theta

RhB – Rhodamine B

Research Outputs

1. Ajibade, P. A.; **Mbuyazi, T. B**.; Oluwalana, A. E., Lead sulphide nanoparticles as photocatalyst for the degradation of methylene blue: Effects of pH, time, adsorption kinetics and recyclability studies. *Journal of Inorganic and Organometallic Polymers and Materials*, **2021**, 31 (5), 2197-2208.
2. **Mbuyazi, T. B**.; Ajibade, P. A., bis(4-methylpiperidine-1-carbodithioato)-lead(II) and bis(4-benzylpiperidine-1-carbodithioato)-lead(II) as precursors for lead sulphide nano photocatalysts for the degradation of rhodamine B. *Molecules*, **2021**, 26 (23).

ABSTRACT

Five dithiocarbamate ligands were synthesized from morpholine, thiomorpholine, N-(2-hydroxyethyl)aniline, 4-methylpiperidine, and 4-benzylpiperidine. Five lead(II) dithiocarbamate and five tin(II) dithiocarbamate complexes were synthesized from the dithiocarbamate ligands. The ligands and their respective lead(II) and tin(II) complexes were analyzed by NMR, FTIR, UV-Vis, elemental analysis and mass spectrometry. Two of the lead(II) complexes were characterized by single-crystal X-ray crystallography. The infrared spectra studies confirmed bidentate coordination of the dithiocarbamato anions to the metal(II) ions to form four coordinate complexes. Single crystal X-ray structures of bis(4-methylpiperidine-1-carbodithioato)-lead(II) and bis(4-benzylpiperidine-1-carbodithioato)-lead(II) confirmed four coordinate distorted tetrahedral geometries.

The synthesized lead(II) and tin(II) complexes were used as single-source precursors to prepare fourteen metal sulfide nanoparticles. The optical and morphological properties of nanoparticles were studied using UV-Visible spectroscopy, photoluminescence (PL), powder X-ray diffraction (p-XRD), high-resolution transmission electron microscopy (HRTEM), scanning electron microscopy (SEM), and energy-dispersive X-ray spectroscopy (EDS). Nine lead sulfide nanoparticles were prepared using Pb(II) complexes as single-source precursors. Three lead(II) were thermolyzed at 180°C to investigate the effect of the precursor on the structural and optical properties of the PbS nanoparticles. To study the effect of capping agents on the structural and optical properties of the nanoparticles, the other two lead(II) complexes were each thermolyzed using three different capping agents, hexadecylamine (HDA), octadecylamine(ODA), and trioctylphosphine oxide (TOPO). The p-XRD diffraction patterns for all PbS nanoparticles were

indexed to the face-centered cubic phase of PbS. The shape and particles sizes of the PbS nanoparticles were determined using HRTEM which showed some agglomeration and varying shapes from quasi-spherical to cubic shapes. Five Sn(II) dithiocarbamate complexes were thermolyzed at 180℃ to study the effect of precursor on the morphological and optical properties of the SnS nanoparticles. The p-XRD patterns revealed that the SnS nanoparticles have orthorhombic phase of SnS. SEM images showed varying surface morphology with different precursor and the EDX confirmed the presence of sulfur and metals in the particles. The optical studies revealed that the PbS and SnS nanoparticles are quantum confined as the calculated energy band gaps showed blue shift relative to bulk. The interaction of the capping agents with the nanoparticles was confirmed with FTIR.

The as-prepared PbS and SnS nanoparticles were used as photocatalysts for the decomposition of methylene blue, rhodamine B, phenol and brilliant green. The photodegradation efficiencies of 47-75% for methylene blue, 30 - 45% for rhodamine B, 11-32 % for phenol and 90- 93% for brilliant green were observed. In the assessment of the influence of pH and recyclability studies of the as-prepared nanoparticles, the dyes were found to degrade better in the alkaline medium than in an acidic medium. The PbS nanoparticles were found to be recyclable up to four cycles and SnS were reusable for five cycles of photocatalytic reaction with good stability.

CHAPTER ONE

INTRODUCTION AND LITERATURE REVIEW

1.1 Introduction

1.1.1 Nanomaterials

Nanoparticles have been around since the fourth century AD, when metal nanoparticles were utilized to manufacture coloured glass. Some nanoparticles occur in nature, including organic as well as inorganic compounds[1]. Weathering, volcano eruptions, wildfires, and microbiological activities all contribute to the formation of these naturally occurring nanoparticles[2, 3]. Richard Feynman predicted nanoscience in his address at the American Physical Society annual conference[4], "There's Plenty of Room at the Bottom." The current wave of interest in nanotechnology dates from 1996 to 1998, when major institutes and organizations began sponsoring nanotechnology initiatives. Because of the necessity for solutions in real-world applications, nanotechnology has grown into a significant field that has advanced in modern research. The emergence of this field of study has led to advancements in analytical procedures and equipment, as evidenced by Richard Zsigmondy's Nobel Prize in Chemistry in 1925 for his work on the ultra-microscope and metal colloids[5].

Nanotechnology has made a breakthrough as a multidisciplinary scientific discipline and is rapidly expanding. Nanotechnology could help prevent water quality issues in the long run by utilizing better filtration materials that allow for more water reprocessing and desalination. Other water treatment technologies have achieved significant improvements in recent years by integrating

nanotechnology to address contamination issues and make future advancements. Another area where nanotechnology has shown considerable promise is in the catalytic decomposition of dyes and other harmful organic chemicals in wastewater treatment.

1.1.2 Semiconductor nanomaterials

Semiconductor nanocrystals are small crystalline particles with optical and electrical characteristics that vary with size[6]. When compared to their typical bulk analogues and molecular compounds, semiconductor nanostructures exhibit intriguing chemical and physical properties as well as valuable functionalities. The most appealing aspects of these materials are their narrow and intense emission, strong chemical stability, continuous absorption bands, and surface functions. Amongst the distinctive features of nanomaterials, the electron flow and holes in semiconductor nanoparticles is principally driven by the quantum confinement effect, while the transportation of photons and phonons are highly influenced by the size and shape of the materials[7-10]. As particle size shrinks, there is an increase in bandgap energy and discrete energy levels (Fig. 1.1), causing a drastic alteration in the particle's optical and electrical properties[11]. The surface area and the ratio of surface area to volume increase significantly with decreasing material size[8, 12]. Size and morphology can be manipulated to modify the characteristics of the material for various applications.

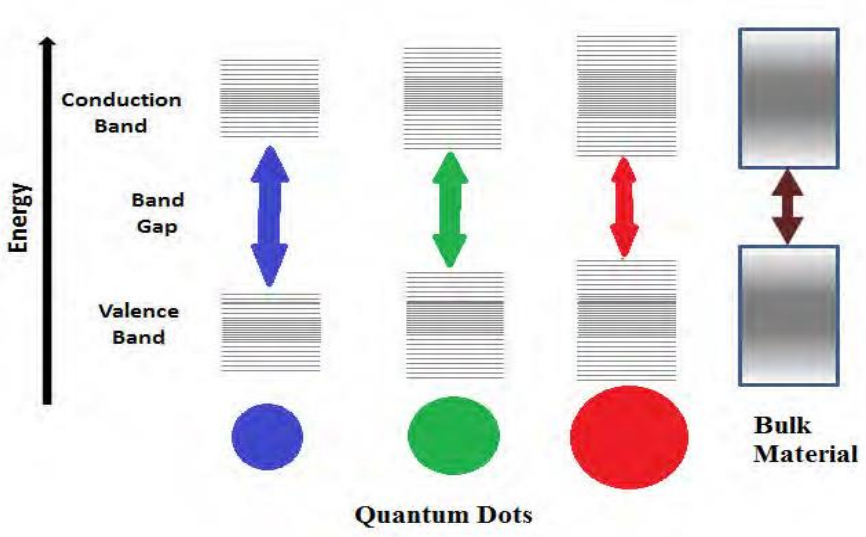

Figure 1.1 Schematic image of the energy bands as a function of particle size[11]

Semiconductors are potential materials for heterogeneous photocatalysis because their unique electronic design enables a spatial separation of excited charge carriers when photons with energies greater than or equal to the semiconductor energy band gap are absorbed[13]. In reduction or oxidation (redox) reactions, the spatially separated charge carriers can react with target species adsorbed to the semiconductor's surface. Heterogeneous photocatalysis occurs when the semiconductor stays unaltered following continuous and exothermic interfacial charge transfer.

1.1.3 Properties of PbS and SnS nanomaterials

Metal sulfides are plentiful and inexpensive because they occur naturally in many different forms[14]. The chemistry of metal sulfides is a vast subject given the diverse range of known forms and their various attributes. Pigments, cathode ray tube luminescent materials, the preparation of

lubricants are all examples of industrial applications for bulk metal sulfide materials. The increased, size-dependent characteristics of metal sulfide nanoparticles lead to new applications[15].

1.1.3.1 Lead Sulfide

Lead sulfide has a rock salt crystal structure and is a diamagnetic semiconductor. The small bandgap (0.41 eV)[16, 17], and large Bohr exciton radius (18 nm)[18] of lead sulfide make it ideal for size-dependent optical properties. The mass of the hole in bulk lead sulfide (PbS) is almost equivalent to the mass of the electron. Furthermore, PbS particles have a high dielectric constant and high carrier mobility[19]. Owing to these attributes, electrons, and holes, and hence the exciton can be effectively confined. As a result, this system is a promising platform for studying exciton in the strong confinement regime.

1.1.3.2 Tin Sulfide

Tin sulfide has attracted much research interest owing to its natural availability, cost-effectiveness, and low toxicity[20, 21]. Tin sulfide comes in three major phases[22], each with a bandgap energy of 1.3 eV (SnS), 2.18 eV (SnS_2), and 0.95 eV (Sn_2S_3). High hole mobility and absorption are attractive properties of SnS phase. Hence it is a suitable candidate for use in a variety of fields such as optoelectronics, solar cells, and photocatalysis. Tin sulfide is a p-type semiconductor that exhibits an indirect bandgap of 1.09 eV and a direct bandgap of 1.3 eV[23].

1.1.4 Applications of nanoparticles

Manipulation of the size, shape, and composition of nanoparticles can be used to influence their properties. The properties of these new compounds will be completely unique from those of their bulk counterparts. As a result, industries can reengineer a wide range of existing items and create new products or processes that perform at historically unprecedented levels. Some nanoparticle applications are discussed below.

1.1.4.1 Solar cells

Solar cells based on semiconductor nanomaterials have the potential to replace silicon-based cells because they are relatively inexpensive, have a configurable band gap, can generate multiple electron-hole pairs, and exhibit a quantum size effect. Some metal chalcogenides such as PbSe[24], PbS[25], CdSe[26], and Ag_2S[27] have been employed in solar cells.

1.1.4.2 Anticancer

The use of metal-based treatments in cancer chemotherapy is becoming more difficult due to decompositional behaviour that occur during carriage within the cell membrane, resulting in non-selectivity of drug activity[28]. Non-traditional nanomaterials used in the functionalization of metallodrugs, on the other hand, offer distinct mechanistic forms of damaging cell DNA and causing malignant cell destruction. Therefore, occupy a pioneering role in drug development and design. Owing to their non-toxicity and magnetic composition, biostability, and cost-effectiveness, iron oxide nanoparticles are among the most significant semiconductor nanoparticles with versatile features, notably for cancer diagnosis and treatment[29-31].

1.1.4.3 Electronics

The possibility for cheaper costs than traditional silicon printed technologies has piqued interest in the advancement of printed electronics in the past few years. Electronics printed with various inks are projected to emerge speedily. These inks could also comprise carbon nanotubes, ceramic and organic nanoparticles[32]. One-dimensional semiconductors and metals have unique structural, electrical[33], and optical features[34] that make them ideal building blocks for photonic, electronic, and sensor development[35]. Novel semiconducting materials are being explored at a rapid pace in the electrical field currently. Nonetheless, as an alternative to vacuum tubes, diodes, and transistors, as well as tiny chips, are used[36].

1.1.4.4 Sensing

Many natural events and human practices, such as wildfires, explosives, industrial wastes, automobile exhaust, fossil fuel combustion, plastic, coal, natural gas, food processing, and volcanoes, produce a large amount of pollutants that must be consistently monitored and contained[37, 38]. Sensing has now become a vital aspect of environmental research as a result of environmental issues to detect threats on the surroundings. A device is essentially a manufactured electronic instrument used to determine surface changes when triggered by chemical substances[39]. Semiconductor nanoparticles are widely employed as gas sensors due to their high electron mobility, chemical and thermostability, high surface-volume ratio, ability to confine charges, and crystalline nature. Colloidal quantum dots such as SnO_2, ZnO[39], WO_3[40], and PbS[41] have been utilized to detect compounds or pollutants, including NH_3, NO_2, CH_4, ethanol, and H_2S.

1.1.4.5 Photocatalysis

A catalyst captures solar radiation or artificial UV light and converts it into energy that can decompose a variety of substances[42, 43]. Solvent extraction, reverse osmosis photodegradation, membrane-based filtration chemical precipitation, ion exchange, evaporation, and adsorption have all been used to purify the water for consumption; however, some of the processes are either costly or difficult to discharge the sludge after treatment. Because of the efficient high surface area of semiconductor nanoparticles for adsorption, cost-effectiveness, photocatalytic function, wide bandgap, and eco-friendliness, semiconductor nanomaterials are an appealing choice for removing dyes, heavy metals, and harmful organic compounds from water.

Heller's early work on semiconductor photo-electrochemistry contributed significantly to the development of photocatalysis[44]. There has been an increasing interest in using semiconductor nanocrystals as photosensitizers for the total decomposition of contaminants. Semiconductors can use solar energy to break down organic molecules in wastewater because of their distinctive electronic properties, which include a full valence band and a vacant conduction band. An ideal photocatalyst should be stable in air-saturated and water-rich environments because photocatalytic reactions take place in these conditions. Additionally, the photocatalyst should be physically and chemically stable after numerous uses[45]. The mechanism of photocatalysis is represented in Figure 1.2.

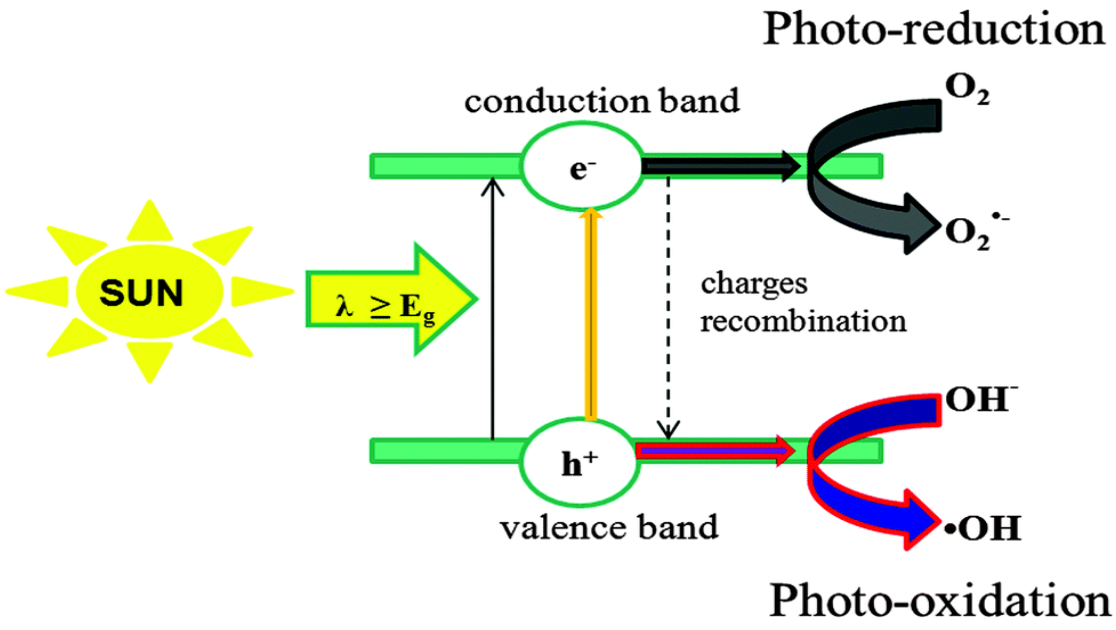

Figure 1.2: Photocatalytic activation of a semiconductor nanoparticle[46]

1.1.5 Growth mechanism of nanoparticles

1.1.5.1 Theory

To make monodispersed particles with tunable size and morphology, researchers used a variety of synthetic approaches. In these syntheses, two basic techniques are being used: top-down and bottom up[47, 48]. The top-down technique uses physical methods to fabricate semiconductor particles, while the bottom-up approach relies on solution-based colloidal chemistry. Top-down approaches can produce large quantities of particles, but they are limited in size and morphological control. On the other hand, Bottom-up approaches have advanced, particularly in synthesizing monodispersed, size- and morphology-controlled particles.

1.1.5.2 The La Mer model for particle formation

La Mer developed this model to describe the generation of colloidal sulfur for the first time in 1950[49, 50]. Many modern procedures are based on this concept. The La Mer model consists of three stages (fig 3): In the first phase, the monomer is formed, and its concentration rises. Phase two begins when the growing monomer concentration reaches supercritical saturation, resulting in fast point nucleation of particles. As the monomer is consumed by nucleation, its concentration drops rapidly, and no additional nucleation events occur once it falls below the critical nucleation level. In phase three, dispersal of the leftover monomer of the precursor onto the particle surface allows the particles to continue to develop.

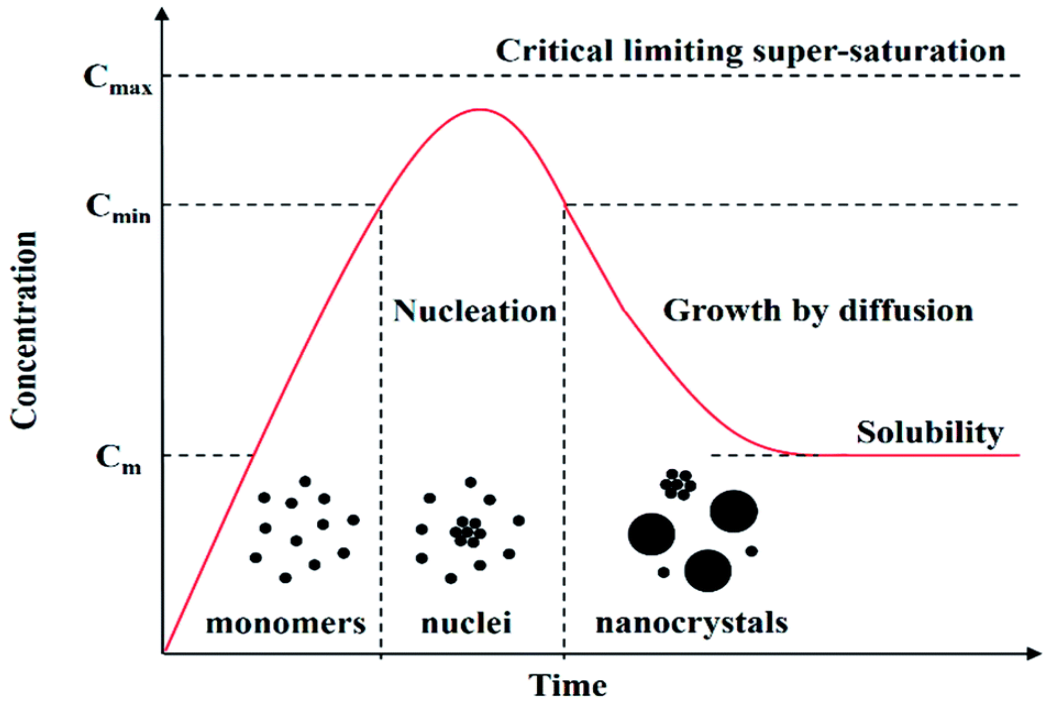

Figure 1.3: Plot of La Mer model[51]

1.1.5.3 Ostwald ripening

Particle ripening takes place after particle growth. Wilhelm Ostwald was the first to describe this phenomenon in 1896. The formation of big particles appears to happen by consuming material from the smaller ones during the Ostwald ripening process, limiting the size distribution[50, 52]. This occurs because it is much more thermodynamically desirable for small particles to shed their monomer, and bigger particles grow from the material drawn from smaller particles. This causes small particles to disappear completely, decreasing the total number of particles in the system. Adding monomers, applying capping agents, or reducing the reaction temperature can all help to prevent this.

1.1.6 General synthetic methods

Thermal evaporation, spray pyrolysis, screen-printing, sputtering, electrodeposition, and solution chemistry methods have been employed to synthesize metal chalcogenides. Nevertheless, these techniques have a number of advantages as well as some drawbacks. Some of these methods are described below.

1.1.6.1 Colloidal route

As detailed in the La Mer model, this approach is based on chemical processes that result in the nucleation and development of nanomaterials in a solution. The colloidal route relies primarily on a controlled precipitation reaction that produces very dilute solutions of monodispersed colloidal particles[53]. Separated nucleation and particle growth, rapid nucleation, and slow growth are the best ways to grow monodispersed nanoparticles with uniform size. As a result, the reaction should

be carried out with stabilizers present to prevent aggregation and additional growth. This synthetic process demands a completely air-free environment due to the high heat and use of extremely hazardous chemicals that are sensitive to air[54].

1.1.6.2 Solvothermal route

The solvothermal reaction is the process of converting reagents in a closed system, commonly an aluminium autoclave, at a specific temperature for a specified period and at high pressure[55, 56]. The reaction requires a temperature that is above the solvent's boiling point. After the autoclave has cooled, the as-prepared sample is collected, left to dry, and then later analysed. The inability to regulate the shape of the nanoparticles is a drawback of this synthetic approach. The procedure is known as hydrothermal when water is utilized for synthesis, and the synthesis is normally carried out below the supercritical temperature of water[57]. Solvothermal reactions can be heterogeneous or homogeneous and occur at subcritical or supercritical conditions, depending on the experimental parameters.

1.1.6.3 Sol-gel

The fabrication of metal oxide nanoparticles has long relied on sol-gel procedures requiring a regulated breakdown of precursors, then after the resultant gels are processed by heat[58]. Precursors produce colloidal solutions, which grow into a gel of solid nanomaterial scattered in a liquid phase over time. Low reaction temperatures, as well as very adjustable conditions such as concentration, reaction duration, pH, and reagent addition rate, enable for regulated nanoparticle formation than the solid-state approaches. Sol-gel approaches generally produce very homogeneous materials

with controlled size and dispersity; nonetheless, the nanoparticles typically have poor crystallinity and contain some impurities, necessitating additional post-synthesis heating processes, which adds costs and time, and the heat treatment[59] could lead to undesirable sintering, lowering the quality of the nanoparticles. Because the regulated nature of the growth needs low concentrations and extended reaction periods, the synthesis route's scalability in an industrial setting is limited[60]. Regardless, sol-gel methods remain a preferred approach to nanomaterials due to the convenience of the approach with regards to the lack of sophisticated instruments and the cost-effectiveness combined with the level of control. NiO[61-63], SiO_2[64], SnO_2[65], TiO_2[66] nanoparticles have been synthesized using this method.

1.1.6.4 Co-precipitation

The aqueous solution of the metal salt is combined with a base that functions as a precipitant in co-precipitation methods, yielding a co-precipitated powder that comes out of the mixture. Similar to sol-gel approaches, the simplicity of the procedure and limited use of specialized tools make this technique popular for nanomaterial fabrication. The precursor employed, the temperature of the reaction, and the solution pH[67] all influence particle size, shape, and composition, with certain situations exhibiting poor size distribution. The nanomaterial product is recovered by rinsing, drying, and calcining the resulting powder. $NiFe_2O_4$[68], ZnO[69, 70], and other nanoparticles[71-74] have been prepared using this method.

1.1.6.5 Single-source precursor

Precursors with two or more constituent elements in a single molecule are known as single-source precursors[75]. The precursors are technologically significant and are intended to comprise all of the necessary components in the proper ratio. The use of a single-source precursor enables nanocrystal formation under favourable reaction conditions with higher synthetic control over particle distribution and crystallite size[76]. Many researchers have been interested in using single-source precursors to synthesize thin films and nanocrystals[77-79]. Many studies on single-source precursors have proven that they are an effective approach to high-quality, crystalline monodispersed semiconducting nanoparticles[77, 80, 81]. A suitable selection of single-source precursors, whose form substantially influences the size, shape, and nanostructure composition of the resulting material, plays a key role in tailoring material attributes.

Single-source precursors have several distinct advantages over other approaches[79]. These properties include a high level of volatility and moisture stability[82]. Preformed bonding can result in particles with less defects and improved stoichiometry[83]. In an inert atmosphere, metal (II) sulfide is generated due to the presence of preformed M-S bonds and the absence of M–C bonds in these precursors[79, 82]. Many of the molecular precursors have appreciable air and moisture stability, making them better to work with and analyse. The potential to lessen the environmental impact of material processing also motivates the utilization of single-source precursors. This is due to the minimal amount of solvent used during synthesis. The thermal decomposition of these precursors produces high-yield nanoparticles[84]. Additionally, because there is only one precursor involved, washing and separation is simple.

Dithiocarbamates complexes are commonly employed as a single-source precursor in the synthesis of metal sulfides[85-89]. Dithiocarbamates have the ability to stabilize a broad range of oxidation states. Moreover, C—S bonds are easier to break than, e.g., P—S bonds, which is vital for precursor decomposition to leave only metal and sulfur when synthesizing nanoparticles. DTC compounds can adopt four structural geometries when no other coordinating ligands are present, i.e., octahedral coordination geometry, square planar coordination geometry, four coordinate dimers, and five-coordinate dimer[90]. The most prevalent structural configurations are square planar and octahedral. The square planar structure is observed in bis(dithiocarbamate) complexes of the type $[M(DTC)_2]$, where M = metal **(a)**. $Cu(DTC)_3$ and $Au(DTC)_3$ are examples of tris(dithiocarbamate)transition metal complexes with an octahedral structure **(b)** in which six sulfur atoms encircle the coordination sphere of the metal ion. In copper and zinc complexes, dimeric forms (**c** and **d**) are common.

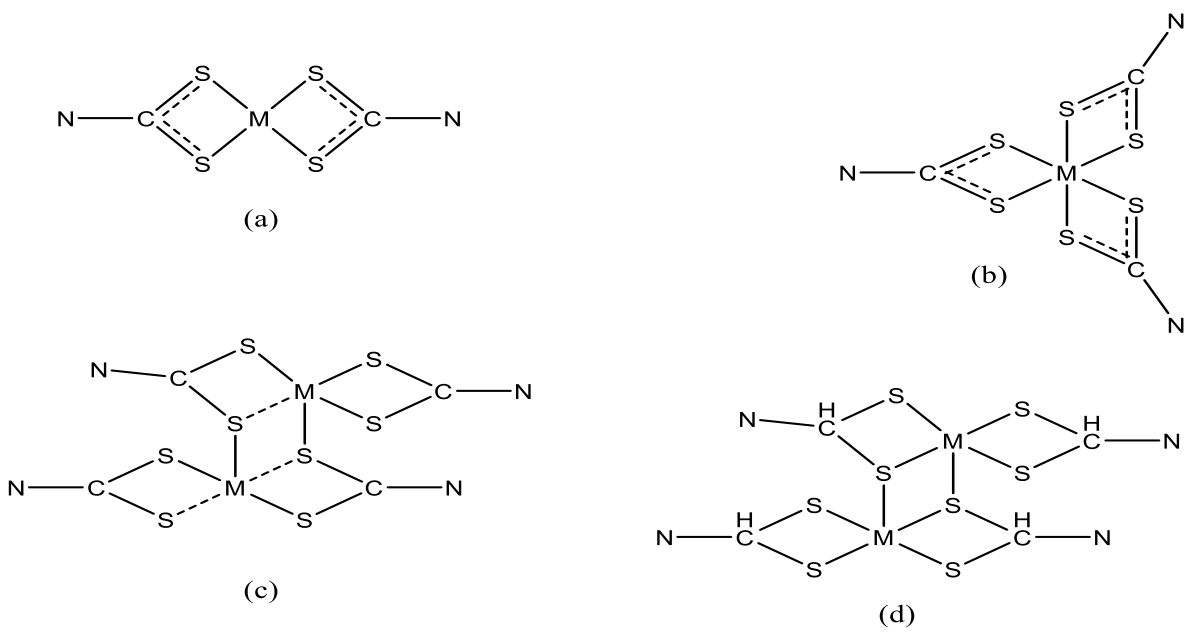

Figure 1.4: Structural configurations of dithiocarbamate complexes[91]

1.2 Literature review

1.2.1 Single-source precursor route

1.2.1.1 Pb(II) dithiocarbamate complexes for the synthesis of PbS nanoparticles

Lead(II) dithiocarbamate complexes $[Pb(S_2CNRR')_2]$ as single-source precursors were first reported by Trindade and co-workers[92]. The effect of experimental factors, such as precursor, growth time, and temperature, on the nanocrystals were investigated. Optical and morphological studies of the lead sulfide nanocrystallites revealed that they greatly depend on the temperature of synthesis rather than on the composition of the precursor.

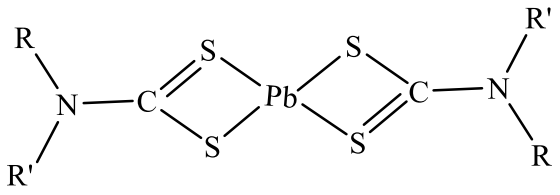

R = Et, Me, Bu^n, Bu^i R' = Et, Pr^i, Bu^n, n-C_6H_{13}

Figure 1.5: R and R' groups used to prepare Pb(II) dithiocarbamate complexes

Nyamen *et al.*[93] reported the synthesis of two dithiocarbamate complexes (illustrated in figure 1.5), as well as their application as single-source precursors for anisotropic PbS nanoparticles synthesis. The complexes were thermolyzed at different temperatures using capping agents such as tri-n-octylphosphine oxide, hexadecylamime, decylamine, and oleylamine. The prepared PbS particles came in a variety of forms, from spheres to cubes and rods, depending on the reaction parameters and compound used.

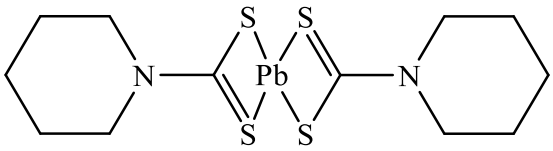

Pb(II) piperidine dithiocarbamate

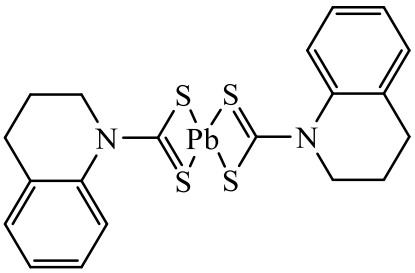

Pb(II) tetrahydroquinoline dithiocarbamate

Figure 1.6: Heterocyclic dithiocarbamate complexes used to synthesize PbS nanoparticles

Sathiyaraj and Thirumaran[94] synthesized and conducted spectral studies on nine Pb(II) dithiocarbamate complexes based on benzyl and furfuryl groups. The spectroscopic studies showed that the carbon-nitrogen bond character in the complexes is enhanced as the length of the alkyl chain attached to the nitrogen is increased. Angeloski *et al*.[95] synthesized and characterized Pb(II) dithiocarbamate complexes. The two single-source precursors exhibited different decomposition properties, with (1) decomposing at a higher temperature than its melting point and (2) decomposing at a temperature where the compound was still solid. The decomposition of the precursors produced PbS nanocrystals. The results show that the size and morphology of the nanocrystals is influenced by the link between the melting point and the temperature at which the precursor decomposes (the DTC ligand has an effect on this).

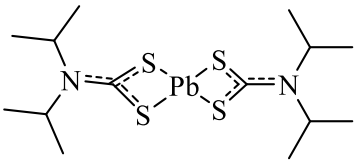

(1) Bis(k^{2}S,S'-di(isopropyl)dithiocarbamato)lead(II)

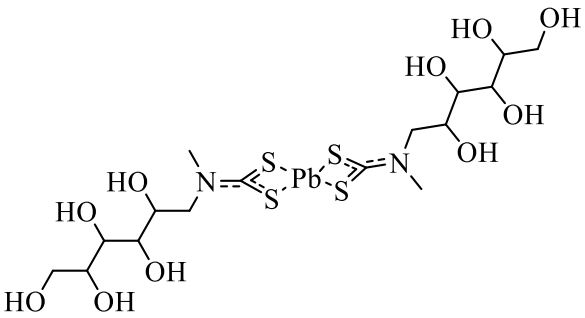

(2) Bis(k^{2}S,S'-N-methyl-N-2,3,4,5,6-pentahydroxyhexyldithiocarbamato)lead(II)

Figure 1.7: Compound (1) and (2) used for the synthesis of PbS nanoparticles

The molecular structure of bis(piperidinedithiocarbamato)lead(II) complex was described by Mlowe *et al.*[96], and it was then used to form thin films. Aerosol-assisted chemical vapour deposition and annealing approaches were used to prepare the PbS films. The deposition at different temperatures revealed that the formation of PbS thin films was dependent on temperature.

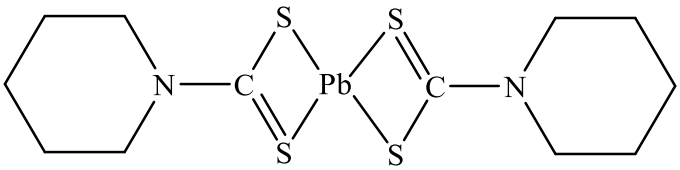

Figure 1.8: Pb(II) dithiocarbamate complex used to prepare PbS thin films

Oluwalana and Ajibade[97] used single-crystal X-ray crystallography to describe two DTC complexes of Pb(II). The compounds' molecular structures showed a distorted tetrahedral geometry around the Pb(II) ions. Bis(N-ethyl-N-phenyldithiocarbamato)Pb(II) formed a dimeric

structure comprising of Pb---Pb and Pb---S contacts, whereas bis(N-benzylmethyldithiocarbamato)Pb(II) formed a monomeric complex having weak C---H contacts.

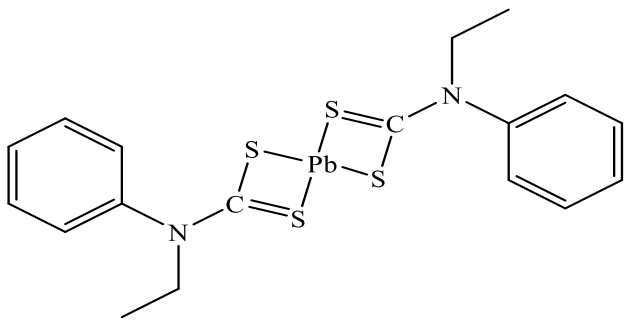

Bis(N-ethyl-N-phenyldithiocarbamato)Pb(II)

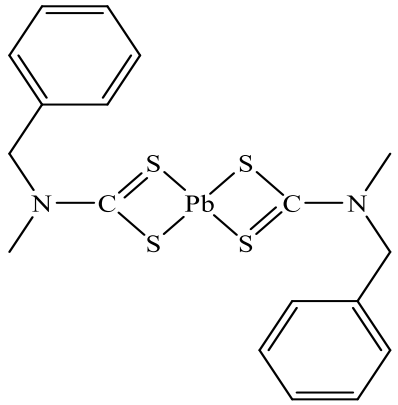

bis(N-benzylmethyldithiocarbamato)Pb(II)

Figure 1.9: Structures of the two Pb(II) dithiocarbamate compounds

Baba *et al*., [98] revealed the crystal structure lead(II) DTC complex (shown in figure 1.7), in which the Pb ion is coordinated in an anisobidentate fashion with the dithiocarbamate. The interaction of the double-bonded S atoms of neighbouring dithiocarbamato groups with the Pb---S contacts raises the four-coordinate geometry to six, resulting in a chain structure for the molecule.

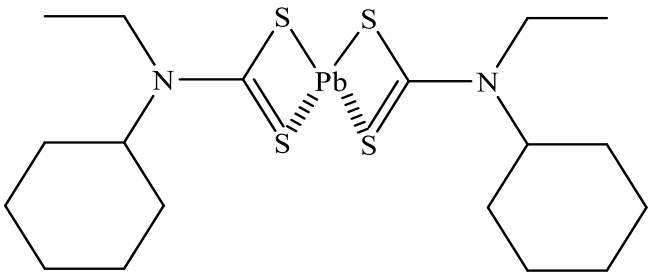

bis(N-cyclohexyl-N-ethyldithiocarbamato-S,S')lead(II)

Figure 1.10: Structure of bis(N-cyclohexyl-N-ethyldithiocarbamato-S,S’)lead(II)

1.2.1.2 Sn(II) dithiocarbamate complexes as single-source precursors

Kevin and colleagues[99] synthesized tin(II) complexes and isolated the crystal of N, N-ethylbutyl amine dithiocarbamate. The structure was described as a distorted square pyramid in which the dithiocarbamate ligands coordinated with the tin(II) ion in a bidentate fashion and the lone pair of electrons at the top of the pyramid.

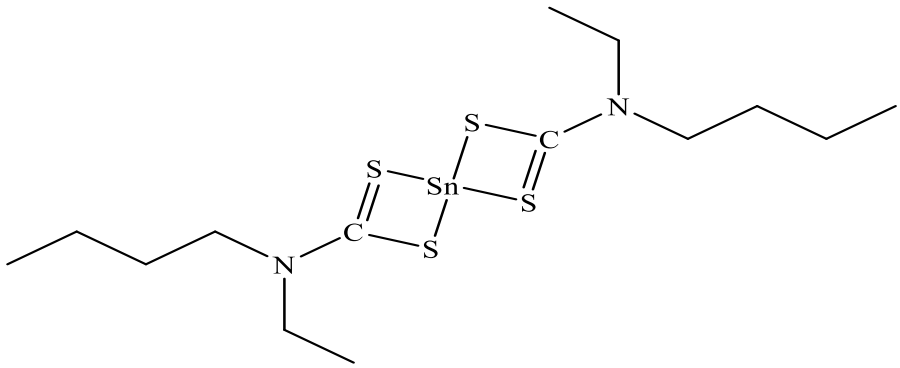

Figure 1.11: Structure of the isolated Tin(II) dithiocarbamate complex

The influence of thermolysis temperature and capping agents on the morphological and optical properties of the SnS nanoparticles from as-prepared bis(phenylpiperazine dithiocarbamato)tin(II) (shown in Scheme 1.1) were studied by Oluwalana and Ajibade[100]. At 150°C, all capping agents produced nanocrystals with sizes ranging from 10 to 28 nm; however, at 230°C, bigger sizes ranging from 35 to 80 nm were obtained. Oleic acid produced monodispersed spherical-shaped SnS nanoparticles, whereas octadecylamine resulted in aggregated cubic nanocrystals.

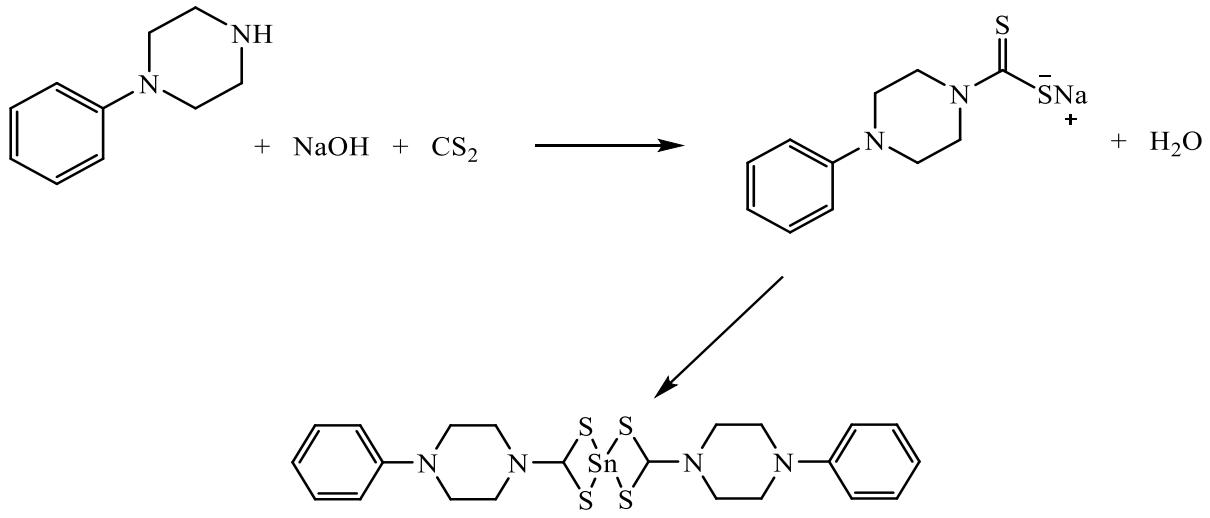

Scheme 1.1: Synthesis of bis(phenylpiperazine dithiocarbamato)tin(II)

Meyer *et al.*[101] prepared SnS nanoparticles from thermal decomposition of mixed-ligands tin(II) complex (shown in figure 1.8). The orthorhombic structure of SnS nanoparticles with an average crystallite diameter of 14 nm was validated by powder X-ray diffraction. The indirect bandgap energy of 1.22 eV and direct bandgap energy of 1.35 eV were obtained, which indicated a redshift when compared to bulk SnS.

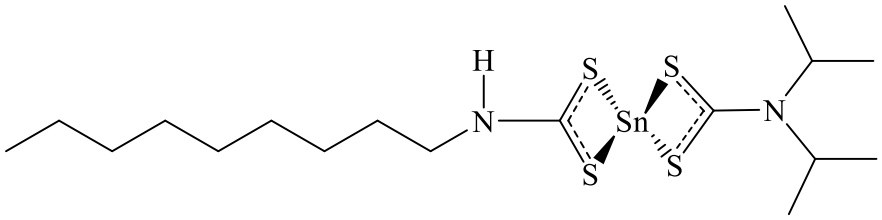

bis(N-di-isopropyl-N-octyl dithiocarbamato)tin(II) complex

Figure 1.12: Tin(II) dithiocarbamate complex used to prepare SnS nanoparticles

Koktysh *et al.*[102] used solvothermal decomposition route to synthesize SnS nanoparticles with an orthorhombic structure from tin(II) dithiocarbamate complex in oleylamine at high temperatures (170 °C or 205 °C). Effects of temperature, time, and capping agents were also studied where it was found that longer reaction time results in bigger nanoparticles, and the size and morphology of the SnS NPs is greatly dependent on the nature of the capping agent.

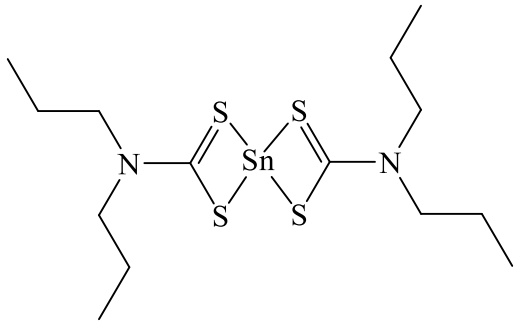

Bis(diethyldithiocarbamato)tin(II)

Figure 1.13: Bis(diethyldithiocarbamato)tin(II) used as a precursor for the synthesis of SnS nanocrystals

1.2.2 Photocatalysis

1.2.2.1 PbS nanoparticles as photocatalysts

The effect of capping agents on the photocatalytic performance of solution-processed PbS films was investigated by Abargues *et al.* [103]. Tetrabutylammonium iodide (TBAI), oleylamine (OA), 3-mercaptopropionic acid (MPA), and 1,2-ethanedithiol (EDT) were among the ligands examined. The research shows that PbS films coated with MPA and EDT have improved photocatalytic performance for methyl orange photodecomposition when exposed to sunlight. It was observed

that the PbS QD films from MPA and EDT were more stable compared to the others, allowing them to work effectively for up to 8 photocatalytic cycles. Wu *et al*.[104] prepared PbS nanoflowers, nanorods, nanodendrites, and nanoplates. The photocatalytic activity test was carried out under visible irradiation on PbS with a particular geometric configuration (dendrites) against nanoparticles for the decomposition of Rhodamine B. Compared to nanoparticles, PbS dendrites showed greater photocatalytic activity.

Pourahmad[105] synthesized PbS nanoparticles by ion exchange route. The nanoparticles were used for the photodegradation of methylene blue, and the effect of parameters such as the amount of catalyst, PbS loading, pH, and dye concentration were investigated. The degradation efficiency of 45% was achieved after an irradiation time of 60 minutes. The degradation rate was found to increase as the amount of catalyst increased, and the photodegradation efficiency of the dye declined as the concentration was increased. The maximum degradation efficiency of over 80% was achieved for methylene blue in an alkaline pH 9. In the recyclability studies, the nanocatalysts' activity declined slightly and steadily after two cycles.

Spherical, cubic, and chain-like nanostructures of lead sulfide are synthesized by simple chemical bath deposition[106]. PbS samples exhibited well a clearly pronounced photocatalytic behavior in the degradation of methylene blue dye solution. The degradation of methylene blue in the presence of chain-like PbS was about 50%, 56% for cubic PbS nanoparticles, and 60% for small spherical PbS nanoparticles in 60 min. This result revealed that PbS nanoparticles of smaller size have greater photocatalytic activity than bigger size PbS nanoparticles.

1.2.2.2 SnS nanoparticles as photocatalysts

Chowdhury *et al.*[107] explored the photodecomposition of brilliant green and eosin yellow dyes using 2.5–3 nm SnS QDs. Complete decomposition was observed after 60 minutes for eosin yellow and 90 minutes for brilliant green. Hedge and co-workers[108] used a wet chemical route to prepare cubic SnS nanoparticles with triethanolamine coordinating agent and orthorhombic phase SnS nanoparticles using ethylene glycol. The photocatalytic properties of the materials were investigated by photodecomposition of methylene blue for 45 min. The degradation efficiencies of 88% for cubic SnS NPs and 98% orthorhombic SnS NPs were reported. Biacchi and coworkers.[109] studied the effect of the shape of the SnS nanoparticles (cubes, sheets, and spherical) used on the photodegradation of methylene blue dye. The cubes were considerably more efficient at methylene blue decomposition than the spherical polyhedra, and sheets were found to be the least effective.

Tang *et al.*[110] synthesized SnS nanoparticles with an average particle size of 5 nm. The photocatalytic activity of SnS nanoparticles was studied by photodecomposition of rhodamine b dye. The adsorption experiment revealed that SnS nanoparticles are much more adsorbent than P25 TiO_2. The as-prepared SnS nanoparticles degraded RhB completely in 90 minutes, but P25 only decomposed 25% of RhB in the same period, suggesting that SnS has a substantially better photocatalytic activity than P25 under visible light. SnS nanoparticles were prepared by Jamali-Sheini *et al.*[111] using a sonochemical method with sonication frequencies of 20 and 50 kHz. In comparison to the nanoparticles produced by 50 kHz sonication, the SnS NPs produced by 20

kHz sonication had a smaller diameter. The study showed that the smaller-sized SnS NPs synthesized at 20 kHz exhibited superior photodegradation of methylene blue.

Zhang *et al*.[21] investigated the photocatalytic activities of SnS nanoflowers and nanoparticles prepared with ethylene glycol solvent and triethanolamine complexing agent. Nanoflowers outperformed nanoparticles in terms of absorption and visible light photocatalytic activity achieving a degradation of 55% of RhB in 180 min. Das et al.[112] used the precipitation method to synthesize orthorhombic structured SnS nanorods. Rapid degradation of trypan blue of more than 95% in 4 h by the nanorods was reported.

1.3 Problem statement

There is a huge range of nanomaterials with attributes that differ from those of bulk counterparts, but finding experimental parameters that yield the preferred nanomaterial for a specific application is still difficult. Researchers have been interested in finding a way to regulate nanoparticles sizes, resulting in a surge of low-cost, and eco-friendly synthetic procedures[113]. This has sparked interest in a cost-effective approach that does not alter the target product but allows for greater control over its phase and size[114]. The cost and safety of starting materials, reaction time, and the exposure of nanomaterials to the environment[115] before and after use are all crucial factors to consider in order to better understand and then explore the prospective applications of these nanomaterials[116].

The content of organic dyes in industrial effluents from the textile, garment and paper manufacturers pollutes the environment significantly. Such dye-polluted wastewater contains cancerous, non-biodegradable, and colour pigments that can harm humans[117]. Dyes are visible in water and adversely degrade aquatic habitats even at trace quantities (below one ppm)[118, 119]. As a result, it is critical to remove organic dyes from waste streams. Adsorption[120] and coagulation[121] are popular strategies for removing organic pigments from industrial effluent in traditional treatment. However, because dyes are typically transformed from a liquid to a solid phase, these procedures result in secondary toxic contamination. As a result, additional treatments are required to address the issue of secondary contamination[122, 123]. Nanomaterials have found functionality in water treatment; however, the typically utilized materials for organic contaminants removal are limited to their large bandgap and UV area, which accounts for a small percentage of solar energy, limiting their application in photocatalysis[124]. This has resulted in the adoption of metal-based semiconductors.

1.4 Motivation and rationale for the study

The adoption of a single-source precursor method is advantageous because it is not time-consuming or energy-intensive since all of the essential atoms are present, implying fewer synthesis steps[82] and the absence of harmful organometallic compounds. This approach produces nanoparticles with enhanced crystallinity and size control, as well as reliable results and a high yield. Nanomaterials have a vital quantum confinement effect, which means they could be used to clean water. Metal sulfide-based semiconductors are the most prevalent photocatalysts for the degradation of dyes in wastewater industries, offering cheap, environmentally benign, and long-term treatment options for pollution control[125]. Also, the use of solar energy, which is a sustainable

and environmentally beneficial alternative, has the potential to alleviate the current societal energy shortage dilemma[126]. By modifying the bandgap of nanostructured materials, we can investigate their potential as photocatalysts. Studying morphological changes to nanomaterials is crucial for developing mechanisms involved from electron-hole pair interactions on the nanomaterial's surface. Amongst metal sulfides, lead sulfide (PbS), and tin sulfide (SnS), the IV-VI semiconductors with distinctive characteristics are extremely promising materials for application in photocatalysis due to their high degradation efficiency, chemical stability, and optical activity in the near-infrared.

1.5 Aim and Objectives of the study

1.5.1 Aim of the study

The aim of study was to prepare PbS and SnS nanoparticles from Pb(II) and Sn(II) dithiocarbamate single source precursors, study their optical and structural properties and evaluate the potentials as photocatalysts for degradation of organic dyes.

1.5.2 Objectives

The objectives of the study are to:

1. Prepare five dithiocarbamate ligands and their corresponding Pb(II) and Sn(II) dithiocarbamate complexes.
2. Characterize the ligands and complexes using NMR, FTIR, mass spectrometry, UV-Vis, and single-crystal X-ray crystallography.

3. Use the Pb(II) and Sn(II) dithiocarbamate complexes as single-source precursors to prepare PbS and SnS nanoparticles.
4. Study the influence of precursor and capping agents on the optical and structural properties of as-prepared PbS and SnS nanoparticles.
5. Study the optical and morphological properties using absorption and emission spectroscopic techniques, XRD, TEM/HRTEM, SEM, and EDS.
6. Evaluate the photocatalytic degradation of methylene blue, rhodamine B, phenol, and brilliant green dyes by the as-prepared PbS and SnS nanoparticles.
7. Evaluate the effect of irradiation time, pH and recyclability of the as-prepared PbS and SnS nanoparticles.

References

1. Dutta, R.; Brahmachary, R., *Natural nanoparticles: an overview*. Lambert academic publishing: **2009**.

2. Lead, J. R.; Wilkinson, K. J., Aquatic Colloids and Nanoparticles: Current Knowledge and Future Trends. *Environ. Chem.* **2006,** *3* (3), 159-171.

3. Hough, R. M.; Noble, R. R. P.; Reich, M., Natural gold nanoparticles. *Ore Geol. Rev.* **2011,** *42* (1), 55-61.

4. Feynman, R. P., There's plenty of room at the bottom *J. Microelectromech. Syst.* **1992,** *1* (1), 60-66.

5. Ijaz, I.; Gilani, E.; Nazir, A.; Bukhari, A., Detail review on chemical, physical and green synthesis, classification, characterizations and applications of nanoparticles. *Green Chem. Lett. Rev.* **2020,** *13* (3), 223-245.

6. Smith, A. M.; Nie, S., Semiconductor nanocrystals: structure, properties, and band gap engineering. *Acc. Chem. Res.* **2010,** *43* (2), 190-200.

7. Burda, C.; Chen, X.; Narayanan, R.; El-Sayed, M. A., Chemistry and Properties of Nanocrystals of Different Shapes. *Chem. Rev.* **2005,** *105* (4), 1025-1102.

8. Cahen, D.; Hodes, G.; Grätzel, M.; Guillemoles, J. F.; Riess, I., Nature of Photovoltaic Action in Dye-Sensitized Solar Cells. *J. Phys. Chem.* **2000,** *104* (9), 2053-2059.

9. Murray, C. B.; Kagan, C. R.; Bawendi, M. G., Synthesis and Characterization of Monodisperse Nanocrystals and Close-Packed Nanocrystal Assemblies. *Annu. Rev. Mater. Sci.* **2000,** *30* (1), 545-610.

10. Chen, X.; Lou, Y.; Dayal, S.; Qiu, X.; Krolicki, R.; Burda, C.; Zhao, C.; Becker, J., Doped semiconductor nanomaterials. *J. Nanosci. Nanotechnol.* **2005,** *5* (9), 1408-1420.

11. Khan, G.; Ahmad, B., Effect of quantum confinement on thermoelectric properties of vanadium dioxide nanofilms. *Appl. Phys. A* **2017,** *123*.

12. Zhang, Q.; Uchaker, E.; Candelaria, S. L.; Cao, G., Nanomaterials for energy conversion and storage. *Chem. Soc. Rev.* **2013,** *42* (7), 3127-3171.

13. Maeda, K., Photocatalytic water splitting using semiconductor particles: History and recent developments. *J. Photochem. Photobiol. C: Photochem. Rev.* **2011,** *12* (4), 237-268.

14. Li, Y.; Kitadai, N.; Nakamura, R., Chemical diversity of metal sulfide minerals and its implications for the origin of life. *Life* **2018,** *8* (4), 46.

15. Terna, A. D.; Elemike, E. E.; Mbonu, J. I.; Osafile, O. E.; Ezeani, R. O., The future of semiconductors nanoparticles: Synthesis, properties and applications. *Mater. Sci. Eng. B* **2021,** *272*, 115363.

16. Obaid, A. S.; Mahdi, M. A.; Hassan, Z.; Bououdina, M., Characterization of nanocrystalline PbS thin films prepared using microwave-assisted chemical bath deposition. *Mater. Sci. Semicond. Process.* **2012,** *15* (5), 564-571.

17. Mamiyev, Z.; Balayeva, N., Preparation and optical studies of PbS nanoparticles. *Opt. Mater.* **2015,** *46*, 522-525.

18. Azadi Motlagh, Z.; Azim Araghi, M. E., Effect of annealing temperature on optical and electrical properties of lead sulfide thin films. *Mater. Sci. Semicond. Process.* **2015,** *40*, 701-707.

19. Santra, A.; Mondal, G.; Acharjya, M.; Bera, P.; Jana, A.; Seok, S. I.; Bera, P., New pyrazole based single precursor for the surfactantless synthesis of visible light responsive PbS nanocrystals: Synthesis, X-ray crystallography of ligand and photocatalytic activity. *Nano-Struct. Nano-Objects* **2017,** *10*, 91-99.

20. Nwofe, P. A.; Reddy, K. T. R.; Sreedevi, G.; Tan, J. K.; Forbes, I.; Miles, R. W., Single phase, large grain, p-conductivity-type SnS layers produced using the thermal evaporation method. *Energy Procedia* **2012,** *15*, 354-360.

21. Zhang, G.; Fu, Z.; Wang, Y.; Wang, H., Facile synthesis of hierarchical SnS nanostructures and their visible light photocatalytic properties. *Adv. Powder Technol.* **2015,** *26* (4), 1183-1190.

22. Adeyemi, J. O.; Oyewo, O. A.; Onwudiwe, D. C., Optical and structural properties of tin sulfide nanoparticles obtained via solvothermal routes. *Z. Anorg. Allg. Chem.* **2019,** *645* (15), 998-1003.

23. Rana, C.; Saha, S., Growth and study of tin sulfide nanocrystals by precipitation technique using triethylamine. *Mater. Today: Proc.* **2019,** *11*, 667-672.

24. Liu, Y.; Li, F.; Shi, G.; Liu, Z.; Lin, X.; Shi, Y.; Chen, Y.; Meng, X.; Lv, Y.; Deng, W.; Pan, X.; Ma, W., PbSe Quantum Dot Solar Cells Based on Directly Synthesized Semiconductive Inks. *ACS Energy Lett.* **2020,** *5* (12), 3797-3803.

25. Sukharevska, N.; Bederak, D.; Goossens, V. M.; Momand, J.; Duim, H.; Dirin, D. N.; Kovalenko, M. V.; Kooi, B. J.; Loi, M. A., Scalable PbS Quantum Dot Solar Cell Production by Blade Coating from Stable Inks. *ACS Appl. Mater. Inter.* **2021,** *13* (4), 5195-5207.

26. Fuke, N.; Hoch, L. B.; Koposov, A. Y.; Manner, V. W.; Werder, D. J.; Fukui, A.; Koide, N.; Katayama, H.; Sykora, M., CdSe Quantum-Dot-Sensitized Solar Cell with ∼100% Internal Quantum Efficiency. *ACS Nano* **2010,** *4* (11), 6377-6386.

27. Shen, H.; Jiao, X.; Oron, D.; Li, J.; Lin, H., Efficient electron injection in non-toxic silver sulfide (Ag_2S) sensitized solar cells. *J. Power Sources* **2013,** *240*, 8-13.

28. Gómez-Ruiz, S.; García-Peñas, A.; Prashar, S.; Rodríguez-Diéguez, A.; Fischer-Fodor, E., Anticancer Applications of Nanostructured Silica-Based Materials Functionalized with Titanocene Derivatives: Induction of Cell Death Mechanism through TNFR1 Modulation. *Materials* **2018,** *11* (2).

29. Hernández-Hernández, A. A.; Aguirre-Álvarez, G.; Cariño-Cortés, R.; Mendoza-Huizar, L. H.; Jiménez-Alvarado, R., Iron oxide nanoparticles: synthesis, functionalization, and applications in diagnosis and treatment of cancer. *Chem. Pap.* **2020,** *74*, 3809 - 3824.

30. Kandasamy, G.; Sudame, A.; Luthra, T.; Saini, K.; Maity, D., Functionalized Hydrophilic Superparamagnetic Iron Oxide Nanoparticles for Magnetic Fluid Hyperthermia Application in Liver Cancer Treatment. *ACS Omega* **2018,** *3* (4), 3991-4005.

31. Sanità, G.; Carrese, B.; Lamberti, A., Nanoparticle Surface Functionalization: How to Improve Biocompatibility and Cellular Internalization. *Front. Mol. Biosci.* **2020,** *7* (381).

32. Kosmala, A.; Wright, R.; Zhang, Q.; Kirby, P., Synthesis of silver nano particles and fabrication of aqueous Ag inks for inkjet printing. *Mater. Chem. Phys.* **2011,** *129* (3), 1075-1080.

33. Hu, Y.; Huang, Y.; Tan, C.; Zhang, X.; Lu, Q.; Sindoro, M.; Huang, X.; Huang, W.; Wang, L.; Zhang, H., Two-dimensional transition metal dichalcogenide nanomaterials for biosensing applications. *Mater. Chem. Front.* **2017,** *1* (1), 24-36.

34. Millstone, J. E.; Kavulak, D. F. J.; Woo, C. H.; Holcombe, T. W.; Westling, E. J.; Briseno, A. L.; Toney, M. F.; Fréchet, J. M. J., Synthesis, properties, and electronic applications of size-controlled poly(3-hexylthiophene) nanoparticles. *Langmuir* **2010,** *26* (16), 13056-13061.

35. Shaalan, M.; Saleh, M.; El-Mahdy, M.; El-Matbouli, M., Recent progress in applications of nanoparticles in fish medicine: A review. *Nanomed. Nanotechnol. Biol. Med.* **2016,** *12* (3), 701-710.

36. Cushing, B. L.; Kolesnichenko, V. L.; O'Connor, C. J., Recent advances in the liquid-phase syntheses of inorganic nanoparticles. *Chem. Rev.* **2004,** *104* (9), 3893-3946.

37. Bai, J.; Zhou, B., Titanium Dioxide Nanomaterials for Sensor Applications. *Chem. Rev.* **2014,** *114* (19), 10131-10176.

38. Hassan, H. S.; Elkady, M. F., Semiconductor Nanomaterials for Gas Sensor Applications. In *Environmental Nanotechnology Volume 3*, Dasgupta, N.; Ranjan, S.; Lichtfouse, E., Eds. Springer International Publishing: Cham, **2020**; pp 305-355.

39. Kumar, R.; Al-Dossary, O.; Kumar, G.; Umar, A., Zinc oxide nanostructures for NO_2 gas–sensor applications: A review. *Nanomicro Lett.* **2015,** *7* (2), 97-120.

40. Dong, C.; Zhao, R.; Yao, L.; Ran, Y.; Zhang, X.; Wang, Y., A review on WO3 based gas sensors: Morphology control and enhanced sensing properties. *J. Alloys Compd.* **2020,** *820*, 153194.

41. Chen, R.; Wang, J.; Xia, Y.; Xiang, L., Near infrared light enhanced room-temperature NO2 gas sensing by hierarchical ZnO nanorods functionalized with PbS quantum dots. *Sens. Actuators B Chem.* **2018,** *255*, 2538-2545.

42. Sunada, K.; Watanabe, T.; Hashimoto, K., Studies on photokilling of bacteria on TiO_2 thin film. *J. Photochem. Photobiol., A* **2003,** *156* (1), 227-233.

43. Paleologou, A.; Marakas, H.; Xekoukoulotakis, N. P.; Moya, A.; Vergara, Y.; Kalogerakis, N.; Gikas, P.; Mantzavinos, D., Disinfection of water and wastewater by TiO_2 photocatalysis, sonolysis and UV-C irradiation. *Catal. Today* **2007,** *129* (1), 136-142.

44. Lewerenz, H. J.; Sharp, I. D., Concepts of Photoelectrochemical Energy Conversion and Fuel Generation. In *Integrated Solar Fuel Generators*, Royal Society of Chemistry: **2018**; pp 1-42.

45. Kumar, S. G.; Devi, L. G., Review on modified TiO_2 photocatalysis under UV/Visible light: Selected results and related mechanisms on interfacial charge carrier transfer dynamics. *J. Phys. Chem.* **2011,** *115* (46), 13211-13241.

46. Colmenares, J. C.; Luque, R., Heterogeneous photocatalytic nanomaterials: prospects and challenges in selective transformations of biomass-derived compounds. *Chem. Soc. Rev.* **2014,** *43* (3), 765-778.

47. Nouailhat, A., *An introduction to nanoscience and nanotechnology*. John Wiley & Sons: 2010; Vol. 10.

48. Hornyak, G. L.; Tibbals, H. F.; Dutta, J.; Moore, J. J., *Introduction to nanoscience and nanotechnology*. CRC press: **2008**.

49. Finney, E. E.; Finke, R. G., Nanocluster nucleation and growth kinetic and mechanistic studies: a review emphasizing transition-metal nanoclusters. *Colloid Inter. Sci.* **2008,** *317* (2), 351-74.

50. Kwon, S. G.; Hyeon, T., Formation mechanisms of uniform nanocrystals via hot-injection and heat-up methods. *Small* **2011,** *7* (19), 2685-702.

51. Chang, J.; Waclawik, E. R., Colloidal semiconductor nanocrystals: controlled synthesis and surface chemistry in organic media. *RSC Adv.* **2014,** *4* (45), 23505-23527.

52. Taylor, P., Ostwald ripening in emulsions. *Adv. Colloid Inter. Sci.* **1998,** *75*, 107-163.

53. Chintso, T. Ni (II) and Pb (II) dithiocarbamate complexes as precursors for the synthesis of HDA-capped NiS and PbS nanoparticles. MSc Dissertation. University of Fort Hare, **2015**.

54. Pradhan, N.; Katz, B.; Efrima, S., Synthesis of high-quality metal sulfide nanoparticles from alkyl xanthate single precursors in alkylamine solvents. *J. Phys. Chem.* **2003,** *107* (50), 13843-13854.

55. Chen, A.; Holt-Hindle, P., Platinum-Based Nanostructured Materials: Synthesis, Properties, and Applications. *Chem. Rev.* **2010,** *110* (6), 3767-3804.

56. Li, J.; Wu, Q.; Wu, J., *Handbook of nanoparticles*. Springer International Publishing: 2015; p 1-28.

57. Feng, S. H.; Li, G. H., Chapter 4 - Hydrothermal and Solvothermal Syntheses. In *Modern Inorganic Synthetic Chemistry (Second Edition)*, Xu, R.; Xu, Y., Eds. Elsevier: Amsterdam, 2017; pp 73-104.

58. Cushing, B. L.; Kolesnichenko, V. L.; O'connor, C. J., Recent advances in the liquid-phase syntheses of inorganic nanoparticles. *Chem. Rev.* **2004,** *104* (9), 3893-3946.

59. Hakuta, Y.; Onai, S.; Terayama, H.; Adschiri, T.; Arai, K., Production of ultra-fine ceria particles by hydrothermal synthesis under supercritical conditions. *J. Mater. Sci. Lett.* **1998,** *17* (14), 1211-1213.

60. Tighe, C. J.; Cabrera, R. Q.; Gruar, R. I.; Darr, J. A., Scale up production of nanoparticles: continuous supercritical water synthesis of Ce–Zn oxides. *Ind. Eng. Chem. Res.* **2013,** *52* (16), 5522-5528.

61. Alagiri, M.; Ponnusamy, S.; Muthamizhchelvan, C., Synthesis and characterization of NiO nanoparticles by sol–gel method. *J. Mater. Sci. Mater. Electron.* **2012,** *23* (3), 728-732.

62. Zorkipli, N. N. M.; Kaus, N. H. M.; Mohamad, A. A., Synthesis of NiO nanoparticles through sol-gel method. *Procedia Chem.* **2016,** *19*, 626-631.

63. Teoh, L. G.; Li, K.-D., Synthesis and characterization of NiO nanoparticles by sol–gel method. *Mater. Trans.* **2012,** *53* (12), 2135-2140.

64. Dubey, R.; Rajesh, Y.; More, M., Synthesis and characterization of SiO_2 nanoparticles via sol-gel method for industrial applications. *Mater. Today: Proc.* **2015,** *2* (4-5), 3575-3579.

65. Aziz, M.; Abbas, S. S.; Baharom, W. R. W., Size-controlled synthesis of SnO_2 nanoparticles by sol–gel method. *Mater. Lett.* **2013,** *91*, 31-34.

66. Sharma, A.; Karn, R.; Pandiyan, S., Synthesis of TiO2 nanoparticles by sol-gel method and their characterization. *Basic Appl. Eng. Res.* **2014,** *1* (9), 1-5.

67. Hui, B. H.; Salimi, M. N., Production of Iron Oxide Nanoparticles by Co-Precipitation method with Optimization Studies of Processing Temperature, pH and Stirring Rate. *IOP Conf. Ser.: Mater. Sci. Eng.* **2020,** *743*, 012036.

68. Sagadevan, S.; Chowdhury, Z. Z.; Rafique, R. F., Preparation and characterization of nickel ferrite nanoparticles via co-precipitation method. *Mater. Res.* **2018,** *21*.

69. Ahamed, A. J.; Kumar, P. V., Synthesis and characterization of ZnO nanoparticles by co-precipitation method at room temperature. *J. Chem. Pharm. Res.* **2016,** *8* (5), 624-628.

70. Adam, R. E.; Pozina, G.; Willander, M.; Nur, O., Synthesis of ZnO nanoparticles by co-precipitation method for solar driven photodegradation of Congo red dye at different pH. *Photonics Nanostruct. Fundam. Appl.* **2018,** *32*, 11-18.

71. Tazikeh, S.; Akbari, A.; Talebi, A.; Talebi, E., Synthesis and characterization of tin oxide nanoparticles via the Co-precipitation method. *Mater. Sci.* **2014,** *32* (1), 98-101.

72. Farahmandjou, M.; Soflaee, F., Synthesis and characterization of α-$Fe2O_3$ nanoparticles by simple co-precipitation method. *Phys. Chem. Res.* **2015,** *3* (3), 191-196.

73. Vaidyanathan, G.; Sendhilnathan, S., Characterization of Co_1− xZnxFe_2O_4 nanoparticles synthesized by co-precipitation method. *Physica B.* **2008,** *403* (13-16), 2157-2167.

74. Al-Alawy, A. F.; Al-Abodi, E. E.; Kadhim, R. M., Synthesis and characterization of magnetic iron oxide nanoparticles by co-precipitation method at different conditions. *J. Eng.* **2018,** *24* (10), 60-72.

75. Malik, M. A.; Afzaal, M.; O'Brien, P., Precursor chemistry for main group elements in semiconducting materials. *Chem. Rev.* **2010,** *110* (7), 4417-4446.

76. Davidovich, R. L.; Stavila, V.; Whitmire, K. H., Stereochemistry of lead (II) complexes containing sulfur and selenium donor atom ligands. *Coord. Chem. Rev.* **2010,** *254* (17-18), 2193-2226.

77. Akhtar, J.; Malik, M. A.; O'Brien, P.; Helliwell, M., Controlled synthesis of PbS nanoparticles and the deposition of thin films by Aerosol-Assisted Chemical Vapour Deposition (AACVD). *J. Mater. Chem.* **2010,** *20* (29), 6116-6124.

78. Lazell, M.; O'Brien, P., A novel single source precursor route to self capping CdS quantum dots. *Chem. Commun.* **1999,** (20), 2041-2042.

79. Fan, D.; Afzaal, M.; Mallik, M. A.; Nguyen, C. Q.; O'Brien, P.; Thomas, P. J., Using coordination chemistry to develop new routes to semiconductor and other materials. *Coord. Chem. Rev.* **2007,** *251* (13-14), 1878-1888.

80. Akhtar, J.; Afzaal, M.; Vincent, M. A.; Burton, N. A.; Hillier, I. H.; O'Brien, P., Low temperature CVD growth of PbS films on plastic substrates. *Chem. Commun.* **2011,** *47* (7), 1991-1993.

81. Adeyemi, J. O.; Onwudiwe, D. C., PbS nanoparticles prepared Using 1, 10-phenanthroline adduct of lead(II) bis(N-alkyl-N-phenyl dithiocarbamate) as single source precursors. *Molecules* **2020,** *25* (9).

82. Barreca, D.; Gasparotto, A.; Maragno, C.; Seraglia, R.; Tondello, E.; Venzo, A.; Krishnan, V.; Bertagnolli, H., Cadmium O-alkylxanthates as CVD precursors of CdS: a chemical characterization. *Appl. Organomet. Chem.* **2005,** *19* (1), 59-67.

83. Ritch, J. S.; Chivers, T.; Ahmad, K.; Afzaal, M.; O'Brien, P., Synthesis, structures, and multinuclear NMR spectra of tin (II) and lead (II) complexes of tellurium-containing imidodiphosphinate ligands: preparation of two morphologies of phase-pure PbTe from a single-source precursor. *Inorg. Chem.* **2010,** *49* (3), 1198-1205.

84. Duan, T.; Lou, W.; Wang, X.; Xue, Q., Size-controlled synthesis of orderly organized cube-shaped lead sulfide nanocrystals via a solvothermal single-source precursor method. *Colloids Surf A: Physiochem. Eng. Asp* **2007,** *310* (1-3), 86-93.

85. Paca, A. M.; Ajibade, P. A., Bis-(N-ethylphenyldithiocarbamato)palladium(II) as molecular precursor for palladium sulfide nanoparticles. *J. Mol. Struct.* **2021,** *1243*, 130777.

86. Roffey, A.; Hollingsworth, N.; Hogarth, G., Synthesis of ternary sulfide nanomaterials using dithiocarbamate complexes as single source precursors. *Nanoscale Adv.* **2019,** *1* (8), 3056-3066.

87. Sathiyaraj, E.; Gurumoorthy, G.; Thirumaran, S., Nickel(ii) dithiocarbamate complexes containing the pyrrole moiety for sensing anions and synthesis of nickel sulfide and nickel oxide nanoparticles. *New J. Chem.* **2015,** *39* (7), 5336-5349.

88. Dar, S. H.; Thirumaran, S.; Selvanayagam, S., Synthesis, spectral and X-ray structural studies on Hg(II) dithiocarbamate complexes: A new precursor for HgS nanoparticles. *Polyhedron* **2015,** *96*, 16-24.

89. Bobinihi, F. F.; Onwudiwe, D. C.; Hosten, E. C., Synthesis and characterization of homoleptic group 10 dithiocarbamate complexes and heteroleptic Ni(II) complexes, and the use of the homoleptic Ni(II) for the preparation of nickel sulphide nanoparticles. *J. Mol. Struct.* **2018,** *1164*, 475-485.

90. Karlin, K. D., *Progress in inorganic chemistry*. John Wiley & Sons: 2011; Vol. 113.

91. Sarker, J. C.; Hogarth, G., Dithiocarbamate complexes as single source precursors to nanoscale binary, ternary and quaternary metal sulfides. *Chem. Rev.* **2021,** *121* (10), 6057-6123.

92. Trindade, T.; Brien, P. O., Lead(II) dithiocarbamato complexes as precursors for the LP-MOCVD of lead sulfide. *Chem. Vap. Depos.* **1997,** *3* (2), 75-77.

93. Nyamen, L. D.; Rajasekhar Pullabhotla, V. S. R.; Nejo, A. A.; Ndifon, P. T.; Warner, J. H.; Revaprasadu, N., Synthesis of anisotropic PbS nanoparticles using heterocyclic dithiocarbamate complexes. *Dalton Trans.* **2012,** *41* (27), 8297-8302.

94. Sathiyaraj, E.; Thirumaran, S., Synthesis and spectral studies on Pb(II) dithiocarbamate complexes containing benzyl and furfuryl groups and their use as precursors for PbS nanoparticles. *Spectrochimica Acta A* **2012,** *97*, 575-581.

95. Angeloski, A.; Gentle, A. R.; Scott, J. A.; Cortie, M. B.; Hook, J. M.; Westerhausen, M. T.; Bhadbhade, M.; Baker, A. T.; McDonagh, A. M., From Lead(II) Dithiocarbamate precursors to a fast response PbS positive temperature coefficient thermistor. *Inorg. Chem.* **2018,** *57* (4), 2132-2140.

96. Mlowe, S.; Shombe, G. B.; Akerman, M. P.; Mubofu, E. B.; O'Brien, P.; Mashazi, P.; Nyokong, T.; Revaprasadu, N., Morphological influence of deposition routes on lead sulfide thin films. *Inorg. Chim. Acta* **2019,** *498*, 119116.

97. Oluwalana, A. E.; Ajibade, P. A., Synthesis and crystal structures of Pb(II) dithiocarbamates complexes: precursors for PbS nanophotocatalyst. *J. Sulfur Chem.* **2020,** *41* (2), 182-199.

98. Baba, I.; Farina, Y.; Othman, A. H.; Razak, I. A.; Fun, H.-K.; Ng, S. W., Bis(N-cyclo-hexyl-N-ethyl-di-thio-carbamato-S,S′)-lead(II). *Acta Cryst. E.* **2001,** *57* (1), m35-m36.

99. Kevin, P.; Lewis, D. J.; Raftery, J.; Azad Malik, M.; O'Brien, P., Thin films of tin(II) sulphide (SnS) by aerosol-assisted chemical vapour deposition (AACVD) using tin(II) dithiocarbamates as single-source precursors. *J. Cryst. Growth* **2015,** *415*, 93-99.

100. Oluwalana, A. E.; Ajibade, P. A., Effect of temperature and capping agents on structural and optical properties of tin sulphide nanocrystals. *J. Nanotechnol.* **2019,** *2019*, 8235816.

101. Meyer, E. L.; Mbese, J. Z.; Agoro, M. A.; Taziwa, R., Optical and structural-chemistry of SnS nanocrystals prepared by thermal decomposition of bis(N-di-isopropyl-N-octyl dithiocarbamato)tin(II) complex for promising materials in solar cell applications. *Opt. Quantum Electron.* **2020,** *52* (2), 90.

102. Koktysh, D. S.; McBride, J. R.; Rosenthal, S. J., Synthesis of SnS nanocrystals by the solvothermal decomposition of a single source precursor. *Nanoscale Res. Lett.* **2007,** *2* (3), 144.

103. Abargues, R.; Navarro, J.; Rodríguez-Cantó, P. J.; Maulu, A.; Sánchez-Royo, J. F.; Martínez-Pastor, J. P., Enhancing the photocatalytic properties of PbS QD solids: the ligand exchange approach. *Nanoscale* **2019,** *11* (4), 1978-1987.

104. Wu, W.; He, Y.; Wu, Y.; Wu, T., Self-template synthesis of PbS nanodendrites and its photocatalytic performance. *J. Alloys Compd.* **2011,** *509* (38), 9356-9362.

105. Pourahmad, A., Fabrication of nanocatalyst in aqueous solution with photocatalytic activity of methylene blue. *Synth. React. Inorg. Met. Org. Chem.* **2015,** *45* (7), 1080-1086.

106. Mishra, A.; Saha, S., Comparison of photocatalytic activity of methylene blue in the presence of different shape lead sulfide nanoparticles. *Int. J. Miner. Met. Mater.* **2020,** *10* (1), 13-20.

107. Chowdhury, A. P.; Shambharkar, B. H.; Ghugal, S. G.; Umare, S. S.; Shende, A. G., Ethylene glycol mediated synthesis of SnS quantum dots and their application towards degradation of eosin yellow and brilliant green dyes under solar irradiation. *RSC Adv.* **2016,** *6* (110), 108290-108297.

108. Hegde, S. S.; Surendra, B. S.; Talapatadur, V.; Murahari, P.; Ramesh, K., Visible light photocatalytic properties of cubic and orthorhombic SnS nanoparticles. *Chem. Phys. Lett.* **2020,** *754*, 137665.

109. Biacchi, A. J.; Vaughn, D. D.; Schaak, R. E., Synthesis and Crystallographic Analysis of Shape-Controlled SnS Nanocrystal Photocatalysts: Evidence for a Pseudotetragonal Structural Modification. *J. Am. Chem. Soc.* **2013,** *135* (31), 11634-11644.

110. Tang, P.; Chen, H.; Cao, F.; Pan, G.; Wang, K.; Xu, M.; Tong, Y., Nanoparticulate SnS as an efficient photocatalyst under visible-light irradiation. *Mater. Lett.* **2011,** *65* (3), 450-452.

111. Jamali-Sheini, F.; Yousefi, R.; Ali Bakr, N.; Cheraghizade, M.; Sookhakian, M.; Huang, N. M., Highly efficient photo-degradation of methyl blue and band gap shift of SnS nanoparticles under different sonication frequencies. *Mater. Sci. Semicond. Process.* **2015,** *32*, 172-178.

112. Das, D.; Dutta, R. K., A novel method of synthesis of small band gap SnS nanorods and its efficient photocatalytic dye degradation. *J. Colloid Inter. Sci.* **2015,** *457*, 339-344.

113. Odularu, A. T.; Ajibade, P. A., Dithiocarbamates: Challenges, control, and approaches to excellent yield, characterization, and their biological applications. *Bioinorg. Chem. Appl.* **2019,** *2019*, 8260496.

114. Yadav, S.; Shrivas, K.; Bajpai, P. K., Role of precursors in controlling the size, shape and morphology in the synthesis of copper sulfide nanoparticles and their application for fluorescence detection. *J. Alloys Compd.* **2019,** *772*, 579-592.

115. Shanker, U.; Jassal, V.; Rani, M.; Kaith, B. S., Towards green synthesis of nanoparticles: From bio-assisted sources to benign solvents. A review. *Int. J. Environ. Anal. Chem.* **2016,** *96* (9), 801-835.

116. Hussain, I.; Singh, N. B.; Singh, A.; Singh, H.; Singh, S. C., Green synthesis of nanoparticles and its potential application. *Biotechnol. Lett* **2016,** *38* (4), 545-560.

117. Chen, S.; Zhang, J.; Zhang, C.; Yue, Q.; Li, Y.; Li, C., Equilibrium and kinetic studies of methyl orange and methyl violet adsorption on activated carbon derived from Phragmites australis. *Desalination* **2010,** *252* (1), 149-156.

118. Daneshvar, N.; Salari, D.; Khataee, A. R., Photocatalytic degradation of azo dye acid red 14 in water: investigation of the effect of operational parameters. *J. Photochem. Photobiol., A* **2003,** *157* (1), 111-116.

119. Grzechulska, J.; Morawski, A. W., Photocatalytic decomposition of azo-dye acid black 1 in water over modified titanium dioxide. *Appl. Catal. B.* **2002,** *36* (1), 45-51.

120. Haque, E.; Jun, J. W.; Jhung, S. H., Adsorptive removal of methyl orange and methylene blue from aqueous solution with a metal-organic framework material, iron terephthalate (MOF-235). *J. Hazard. Mater.* **2011,** *185* (1), 507-511.

121. Shi, B.; Li, G.; Wang, D.; Feng, C.; Tang, H., Removal of direct dyes by coagulation: The performance of preformed polymeric aluminum species. *J. Hazard. Mater.* **2007,** *143* (1), 567-574.

122. Galindo, C.; Jacques, P.; Kalt, A., Photooxidation of the phenylazonaphthol AO20 on TIO2: kinetic and mechanistic investigations. *Chemosphere* **2001,** *45* (6), 997-1005.

123. Aleboyeh, A.; Aleboyeh, H.; Moussa, Y., "Critical" effect of hydrogen peroxide in photochemical oxidative decolorization of dyes: Acid Orange 8, Acid Blue 74 and Methyl Orange. *Dyes Pigm.* **2003,** *57* (1), 67-75.

124. Ain, N. u.; Zia ur, R.; Aamir, A.; Khan, Y.; Rehman, M.-u.; Lin, D.-J., Catalytic and photocatalytic efficacy of hexagonal CuS nanoplates derived from copper(II) dithiocarbamate. *Mater. Chem. Phys.* **2020,** *242*, 122408.

125. Raja, V. R.; Rosaline, D. R.; Suganthi, A.; Rajarajan, M., Facile fabrication of PbS/MoS_2 nanocomposite photocatalyst with efficient photocatalytic activity under visible light. *Solid State Sci.* **2017,** *67*, 99-108.

126. Mohamed, R. M.; McKinney, D. L.; Sigmund, W. M., Enhanced nanocatalysts. *Mater. Sci. Eng.* **2012,** *73* (1), 1-13.

CHAPTER TWO

EXPERIMENTAL

2.1 Materials

Sodium hydroxide, potassium hydroxide, carbon disulfide, morpholine, thiomorpholine, N-(2-hydroxyethyl aniline), 4-methylpiperidine, 4-benzylpiperidine, lead nitrate, tin chloride dihydrate, diethyl ether, methanol, hexane, chloroform, DCM, toluene, acetonitrile, deuterated dimethyl sulfoxide, deuterated water and DMSO are analytical grade reagents purchased from Sigma Aldrich, and they were used without any further purifications.

2.2 Physical Measurements

The colour, percentage yield and melting points of the compounds were determined and summarized under each ligand.

2.2.1 Solubility

The solubility of the dithiocarbamate ligands was determined using water and alcohols and different solvents like DMSO, DCM, toluene, chloroform, and acetonitrile were used for the complexes. In most solvents, the complexes were only partly soluble. Therefore, DMSO was used to dissolve the complexes for further analysis since it does not interfere with important characterization peaks.

2.2.2 ^{1}H and ^{13}C NMR spectroscopy

Bruker 400 MHz and 100 MHz spectrometers were used to acquire ^{1}H and ^{13}C NMR spectra, respectively. The chemical shift results were expressed in ppm in comparison to the internal standard, tetramethylsilane reference in D_2O and d_6-DMSO, respectively.

2.2.3 FTIR spectroscopy

Data was collected using an Agilent Cary 630 spectrometer with Agilent MicroLab PC 5.1.22 equipped with ATR Diamond-1 Bounce with 30 background scans and 30 sampling scans in the range 4000 – 650 cm^{-1} with a resolution of 4 cm^{-1}. The data processing for peaks and smoothing was done using ResolutionPro 5.0.0.395.

2.2.4 UV-Vis spectroscopy

A Perkin Elmer Lamda 25 spectrophotometer was used to measure the absorption spectra of the ligands and complexes in the region of 200-700 nm. The samples were loaded in 1-centimeter quartz cuvettes. The solvents selected were determined by the compounds' solubility and stability in each solvent. For all solution measurements, analytical grade solvents were utilized.

2.2.5 Mass spectrometry

The molecular mass and purity of the as-synthesized ligands and complexes was determined using mass spectrometry. The LC Premier micro-mass spectrometer was used to collect mass spectra.

2.2.6 Single-crystal X-ray crystallography

The crystals were grown by slow evaporation of chloroform/hexane. Suitable crystals were selected and placed in paratone oil on an MITIGEN holder attached to a Bruker APEX-II CCD diffractometer (Billerica, MA, USA). The crystals were kept at 102 K throughout the analysis. Olex2[1] and structure solution program SHELXS[2] were used to analyse the structure using direct methods and simplified with the refinement programme SHELXL[3] by least squares minimization.

2.3 Preparation of dithiocarbamate ligands

2.3.1 Preparation of sodium morpholine dithiocarbamate L1

A procedure from the published works[4] was adopted as presented in Scheme 2.1. The solution was prepared by dissolving sodium hydroxide (2 g, 0.05 mol) in a small volume of distilled water, followed by the addition of morpholine (4.37 mL, 0.05 mol), while stirring at room temperature. After 30 minutes, cold carbon disulfide (3.00 mL, 0.05 mol) was introduced. The resultant solution was agitated for 4 h in an ice bath. A pure white flocculate was suction filtered and splashed with diethyl ether. Yield = 79%, 7.3098 g. FTIR (cm^{-1}): 1457 (νC—N), 970 (ν_sC—S), 1018 (ν_{as}C—S). ^{1}H NMR (D_2O): δ 3.75 (t, 4H); δ 4.38 (t, 4H). ^{13}C NMR (D_2O): δ 209 (C—S); δ 66 (N—CH_2); δ 51 (O—CH_2). Anal. Calc. for $C_5H_8NOS_2$ (%): C: 27.14, H: 5.47, N: 6.33. Found: C: 26.69, H: 5.47, N: 6.06. MS: *m/z* [M^+] 162.

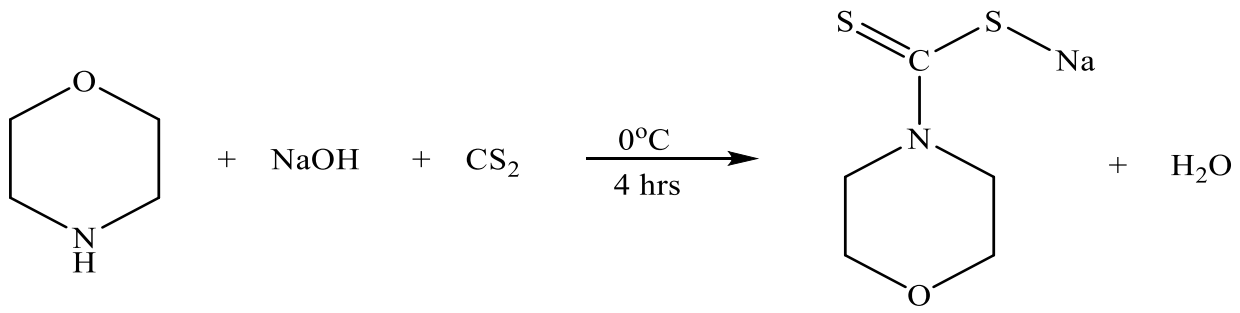

Scheme 2.1: Preparation of sodium morpholine dithiocarbamate

2.3.2 Preparation of sodium thiomorpholine dithiocarbamate L2

Scheme 2.2 showed the synthetic procedure used to prepare the ligand[5]. An amount of 5.03 mL (0.05 mol) thiomorpholine was introduced into an aqueous solution of 2.00 g (0.05 mol) sodium hydroxide, followed by the addition of 3.00 mL (0.05 mol) cold carbon disulfide, and the reaction was stirred over 4 h. A cream-white precipitate was vacuum filtered and washed with diethyl ether. Yield = 91%, 9.1930 g. FTIR $\upsilon(cm^{-1})$: 1458 (νC—N), 923 (ν_sC—S), 996 (ν_{as}C—S). ^{1}H NMR (D_2O): δ 3.50 (t, 4H); δ 1.63 (t, 4H). ^{13}C NMR (D_2O): δ 209 (C—S); δ 54 (N—CH_2); δ 27 (S—CH_2). Anal. Calc. for $C_5H_8NS_3$ (%): C: 25.30, H: 5.10, N: 5.90. Found: C: 26.99, H: 5.34, N: 5.95. MS: *m/z* [M^+] 178.

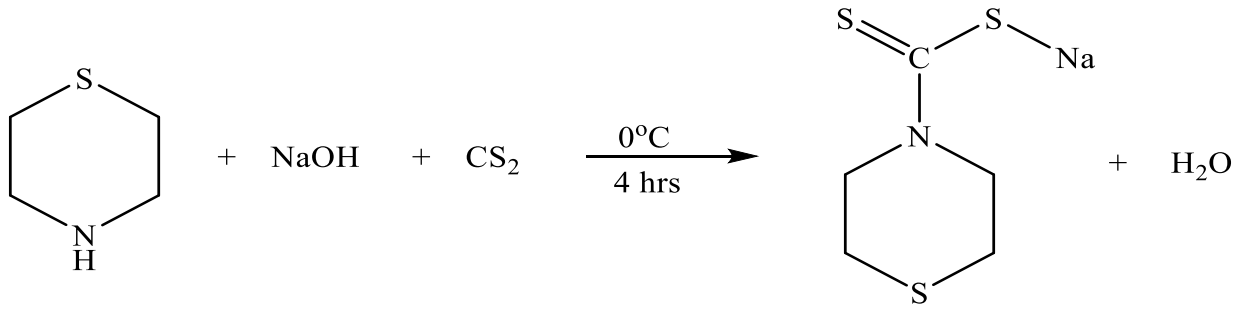

Scheme 2.2: Preparation of sodium thiomorpholine dithiocarbamate

2.3.3 Preparation of potassium N-(2-hydroxyethyl)phenyl dithiocarbamate L3

Scheme 2.3 shows the synthesis of N-(hydroxyethyl)phenyl dithiocarbamate ligand. Carbon disulfide (3.00 mL, 0.05 mol) was introduced into a cold mixture of N-(hydroxyethyl)aniline (6.27 mL, 0.05 mol) dispersed in 10 mL of tetrahydrofuran and aqueous potassium hydroxide (2.80 g, 0.05 mol). The resulting yellow precipitate was suction filtered, splashed with diethyl ether. Yield = 47%, 5.9569 g. FTIR $\upsilon(cm^{-1})$: 1496 (νC—N), 988 (ν_sC—S), 1050 (ν_{as}C—S). ^{1}H NMR (D_2O): δ 3.48 (t, 2H); δ 4.59 (t, 2H); δ 6.88 (t, 1H); δ 7.27 (t, 2H); δ 7.52 (d, 2H). $C_9H_{10}NOS_2$ (%): C: 37.61, H: 4.91, N: 4.87. Found: C: 36.32, H: 3.90, N: 4.55. MS: *m/z* [M^+] 212.

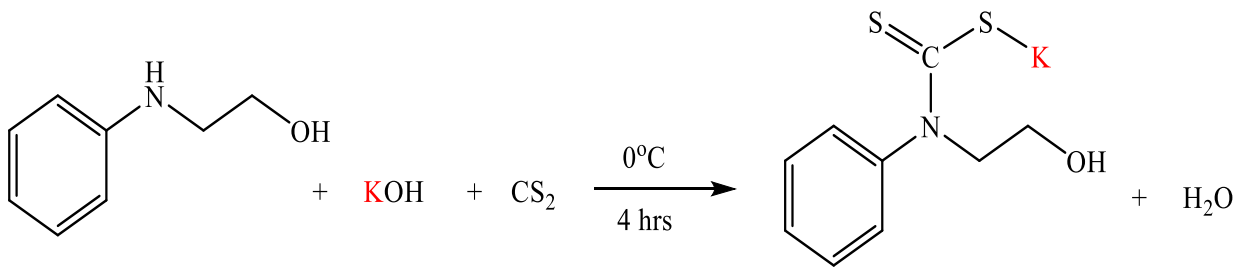

Scheme 2.3: Preparation of potassium N-(2-hydroxyethyl)phenyl dithiocarbamate

2.3.4 Preparation of sodium 4-methylpiperidine dithiocarbamate L4

The ligand was prepared following a literature procedure[6]. In an ethanolic solution of 0.05 mol (4.9585 g) 4-methylpiperidine and 0.05 mol (2.00 g) sodium hydroxide, carbon disulfide (3.00 mL, 0.05 mmol) was gently introduced. The mixture was agitated for 4 h, resulting in a white precipitate that was separated by suction filtration and splashed multiple times with cold diethyl ether. Yield: 6.9112 g, 70.15%. Mp: 139.6°C – 143.3°C. FTIR $\upsilon(cm^{-1})$: 1468 (νC—N), 945 (νC—S), 1017 (ν_{asy}C—S). ^{1}HNMR (D_2O): δ 0.91 (3H, d, CH_3), δ 1.69-1.73 (1H, s, CH), δ 1.11-1.21

(4H, s, CH_2), δ 3.11-3.18 (4H, s, CH_2). ^{13}C-NMR (D_2O): δ 20.5 (CH_3), δ 30.1 (CH), δ 33.6 (CH_2), δ 52.2 (CH_2), δ 205.5 (CS_2).

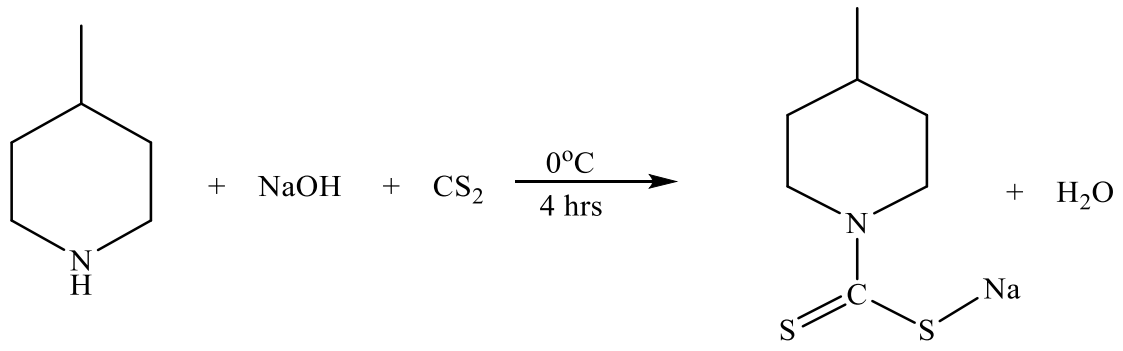

Scheme 2.4: Preparation of sodium 4-methylpiperidine dithiocarbamates

2.3.5 Preparation of sodium 4-benzylpiperidine dithiocarbamate L5

A procedure from the published works[7] was adopted as presented in Scheme 2.5. Carbon disulfide 0.03 mol (1.80 mL) was slowly introduced to an equimolar mixture of sodium hydroxide 0.03 mol (1.20 g) and 4-benzylpiperidine 0.03 mol (5.2581 g). The resulting white product was isolated, splashed with diethyl ether, and suction dried. Yield: 3.0452 g, 37.17%. Mp: 128.2°C – 131.4°C. FTIR υ(cm^{-1}): 1417 (νC—N), 945 ($ν_s$C—S), 1017 ($ν_{asy}$C—S). ^{1}H-NMR (D_2O): δ 1.19-1.31 (2H, m, CH_2), δ 1.67-1.70 (2H, d, CH_2), δ 3.05-3.12 (2H, s, CH_2), δ 5.35-5.38 (2H, d, CH_2), δ 1.86-1.97 (1H, m, CH), δ 2.56-2.58 (2H, d, CH_2), δ 7.22-7.36 (5H, m, C_6H_5). ^{13}C-NMR (D_2O): δ 126.1-129.2 (C_6H_5), δ 141.4 (C—C_6H_5), 41.7 (CH_2), δ 37.8 (CH), δ 31.7 (CH_2), δ 52.0 (CH_2), δ 205.9 (CS_2).

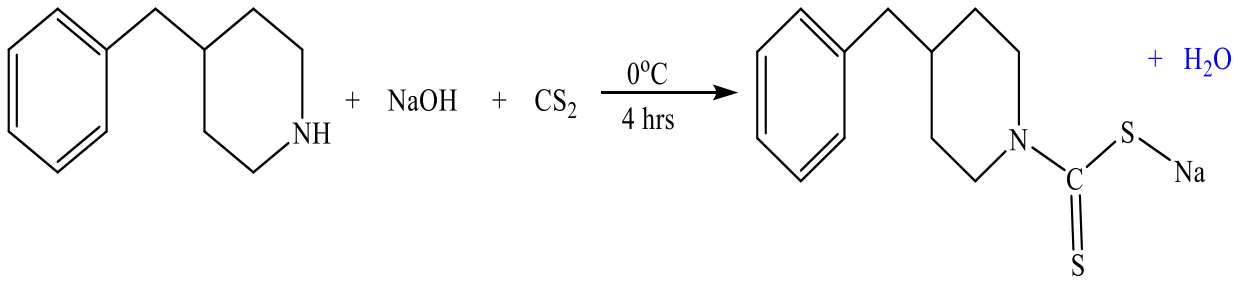

Scheme 2.5: Preparation of sodium 4-benzylpiperidine dithiocarbamate ligand

2.4 Preparation of Pb(II) and Sn(II) dithiocarbamate complexes

2.4.1 Preparation of bis(morpholinyldithiocarbamato)Pb(II)

To a 30 mL aqueous solution of morpholinyldithiocarbamate sodium salt (0.93 g, 0.005 mol), aqueous $Pb(NO_3)_2$ (0.83 g, 0.0025 mol) was introduced. A white product appeared instantly and was agitated for 2 h. The product was removed by suction filtration and splashed with a 3:1 mixture of methanol and distilled water. The reaction Scheme is shown in Scheme 2.6. Yield: 81%, 1.1067 g; Melting point: 313.7 – 315.3 ℃. ^{1}H-NMR (D_6): δ 3.61 – 3.63 (t, 8H, O—CH_2), δ 4.04 – 4.06 (t, 8H, N—CH_2). FTIR υ(cm^{-1}): 989 (νC—S) and 1428 (νN—CS_2). TOF MS ES$^+$ (m/z): 552.93.

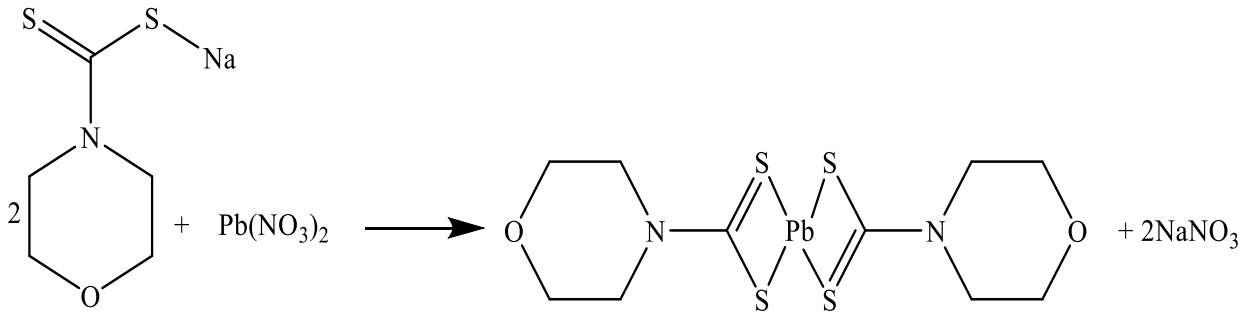

Scheme 2.6: Preparation of bis(morpholinyldithiocarbamato)Pb(II)

2.4.2 Preparation of bis(thiomorpholinyldithiocarbamato)Pb(II)

$Pb(NO3)_2$ (0.83 g, 0.0025 mol) was dispersed in 20 mL of water and gently introduced to thiomorpholine dithiocarbamate (1.01 g, 0.005 mol) in 30 mL of water with continuous stirring as shown in Scheme 2.7. The white precipitate that formed instantaneously was agitated for 2 h at ambient temperature. The product was isolated by vacuum filtration and rinsed with a 3:1 solution of methanol and water. Yield: 89 %, 1.2576 g; Melting point: 271.2 – 274.9 ℃. ^{1}H-NMR (D_6): δ 2.69 – 2.71 (t, 8H, S—CH_2), δ 4.29 – 4.31 (t, 8H, N—CH_2). FTIR υ(cm^{-1}): 948 (νC—S_2) and 1451 (νN—CS_2). TOF MS ES+ (m/z): 564.07.

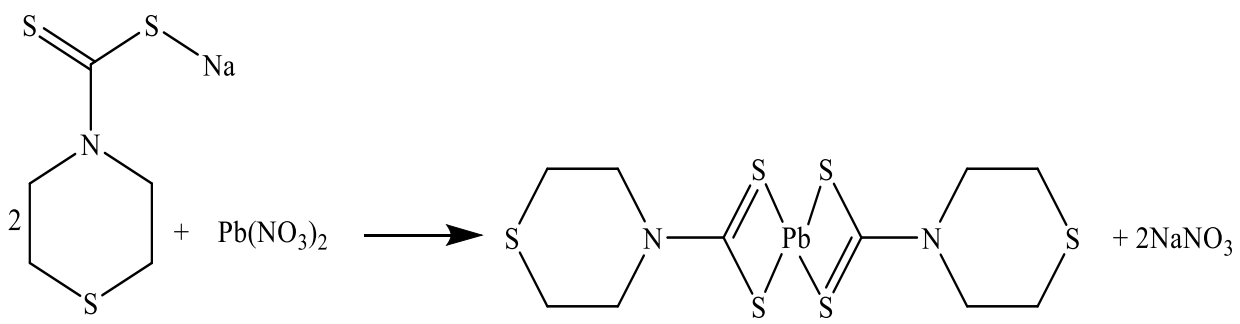

Scheme 2.7: Preparation of bis(thiomorpholinyldithiocarbamato)Pb(II)

2.4.3 Preparation of bis(N-(2-hydroxyethyl)phenyldithiocarbamato)Pb(II)

As illustrated in Scheme 2.8, 10 mL of $Pb(NO_3)_2$ (0.07 g, 0.00020 mol) was mixed with 15 mL of N-(2-hydroxyethyl) phenyl dithiocarbamate (0.10 g, 0.00040 mol). The instantly formed black product was agitated for 2 h. After filtering and rinsing with distilled water, the product was kept at room temperature to dry. Yield: 93 %, 0.1163 g; Melting point: 103.1-104.7℃. ^{1}H-NMR (D_6): δ 3.07 – 3.10 (t, 4H, CH_2), δ 4.29 – 4.33 (t, 4H, CH_2), δ 4.83 (s, 2H, OH), δ 7.07 – 7.11 (t, 2H,

CH), δ 7.33 – 7.38 (t, 4H, CH), δ 7.66 – 7.68 (d, 4H, CH). FTIR υ(cm^{-1}): 1059 (νC—S_2) and 1592 (νN—CS_2). TOF MS ES+ (m/z): 664.05.

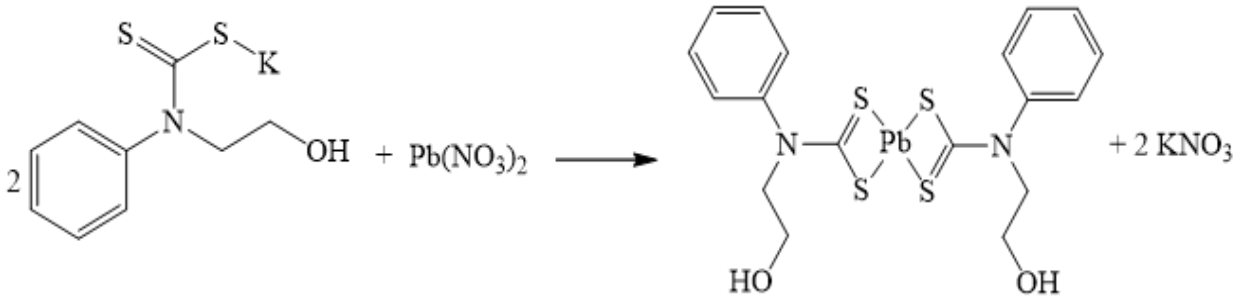

Scheme 2.8: Preparation of bis(N-(2-hydroxyethyl)phenyldithiocarbamato)Pb(II)

2.4.4 Preparation of bis(4-methylpiperidinedithiocarbamato)Pb(II)

Bis(4-methylpiperidine-1-carbodithioato)-lead(II) complex was synthesized using a previously reported method[8]. $Pb(NO_3)_2$ (0.8280 g, 0.0025 mol) dispersed in 20 mL of distilled water was gently introduced to 4-methylpiperidine dithiocarbamate (0.9852 g, 0.005 mol) in 30 mL of water. The precipitate formed instantly, and it was agitated for 2 h. The white precipitate was removed by vacuum filtration and rinsed with distilled water. Yield: 1.5731g, 91.58%. Mp: 261.5-263.4℃. ^{1}H-NMR (DMSO): δ 0.90 (6H, d, CH_3), δ 1.71-1.74 (2H, t, CH), δ 1.03-1.12 (8H, q, CH_2), δ 2.99-3.05 (8H, q, CH_2). FTIR υ(cm^{-1}): 958 (νC—S_2) and 1429 (νN—CS_2).

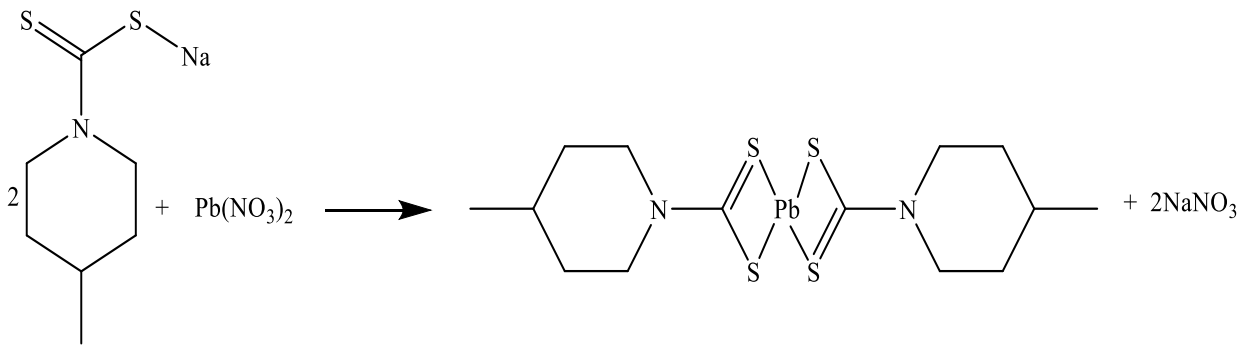

Scheme 2.9: Preparation of bis(4-methylpiperidinedithiocarbamato)Pb(II)

2.4.5 Preparation of bis(4-benzylpiperidinedithiocarbamato)Pb(II)

The bis(4-benzylpiperidine-1-carbodithioato)-lead(II) complex was prepared as presented in Scheme 2.10. $Pb(NO_3)_2$ (0.8280 g, 0.0025 mol) was dispersed in 20 mL of distilled water and gently introduced to 4-benzylpiperidine dithiocarbamate (1.3653g, 0.005 mol) in 30 mL of water. The product formed instantaneously, and it was agitated for 2 h to ensure a complete reaction. The resulting white product was removed by vacuum filtration and splashed with distilled water. Yield: 1.6316 g, 92.16%. Mp: 211.2°C – 214.6°C. Selected FTIR $\upsilon(cm^{-1})$: 1478 (νC—N), 961 (νC—S). ^{1}H-NMR (D_6): δ 1.19-1.31 (2H, m, CH_2), δ 1.67-1.70 (2H, d, CH_2), δ 3.05-3.12 (2H, s, CH_2), δ 5.35-5.38 (2H, d, CH_2), δ 1.86-1.97 (1H, m, CH), δ 2.56-2.58 (2H, d, CH_2), δ 7.22-7.36 (5H, m, C_6H_5).

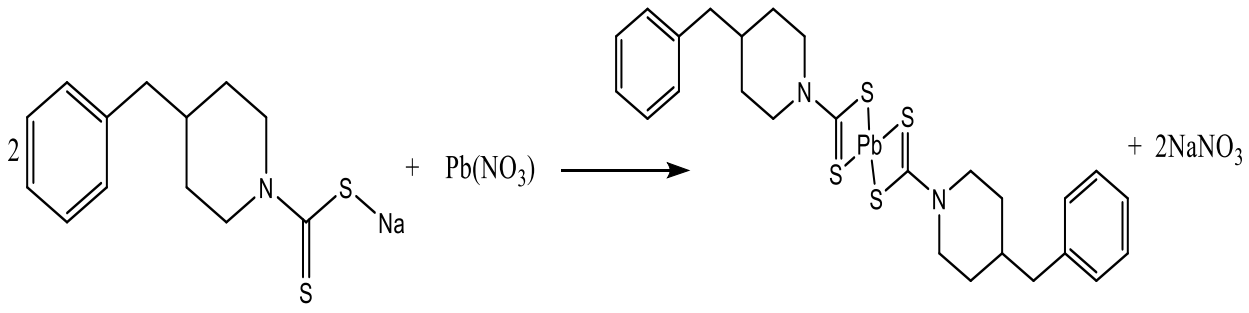

Scheme 2.10: Preparation of bis(4-benzylpiperidinedithiocarbamato)Pb(II**)**

2.4.6 Preparation of bis(morpholinyldithiocarbamato)Sn(II)

To a 20 mL methanolic solution of morpholine dithiocarbamate (0.9260 g, 5 mmol), cold 0.5641 g of $SnCl_2{\cdot}2H_2O$ (2.5 mmol) was introduced. A pale yellow product formed instantly and was agitated for 2 h under nitrogen. The fine powder product was removed by suction filtration and splashed with a 3:1 solution of methanol and distilled water. The reaction is illustrated in Scheme 2.11. Yield: 59%, 0.6590 g; Melting point: 248.1 -250.0 ℃. ^{1}H-NMR (D_6): δ 3.83 – 3.86 (t, 8H -O—CH_2), δ 3.93 – 3.95 (t, 8H -N—CH_2). FTIR υ(cm^{-1}): 985 (νC—S_2) and 1499 (νN—CS_2).

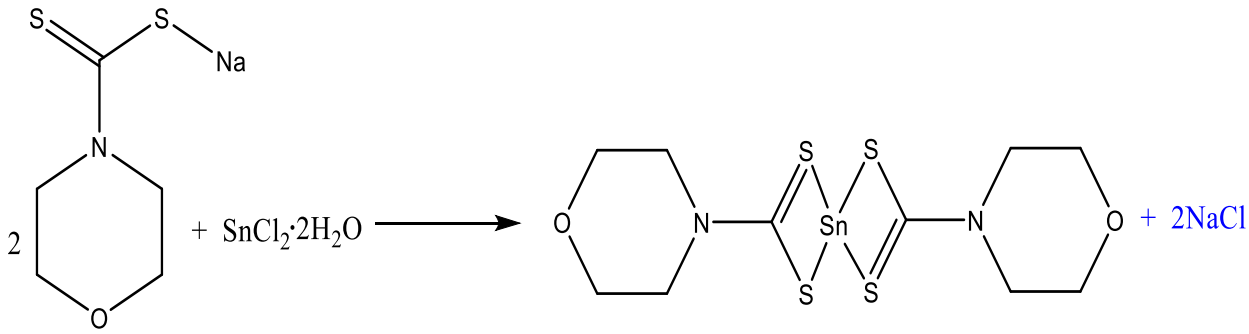

Scheme 2.11: Preparation of bis(morpholinyldithiocarbamato)Sn(II)

2.4.7 Preparation of bis(thiomorpholinyldithiocarbamato)Sn(II)

$SnCl_2 \cdot 2H_2O$ (2.5 mmol, 0.5641 g) was dropwise introduced to a 30 mL methanolic solution of thiomorpholine dithiocarbamate (1.0060 g, 5 mmol) with continuous stirring under nitrogen as shown in Scheme 2.12. The orange precipitate that formed instantaneously was agitated for 2 h at ambient temperature. The product was vacuum filtered and rinsed with a 3:1 solution of methanol and water. Yield = 58%, 0.6896 g. Melting point: 214.3 - 217.1 ℃. ^{1}H-NMR (D_6): δ 2.80 – 2.82 (t, 8H -S—CH_2), δ 3.25 – 3.27 (t, 8H -N—CH_2). FTIR υ(cm^{-1}): 939 (νC—S_2) and 1497 (νN—CS_2).

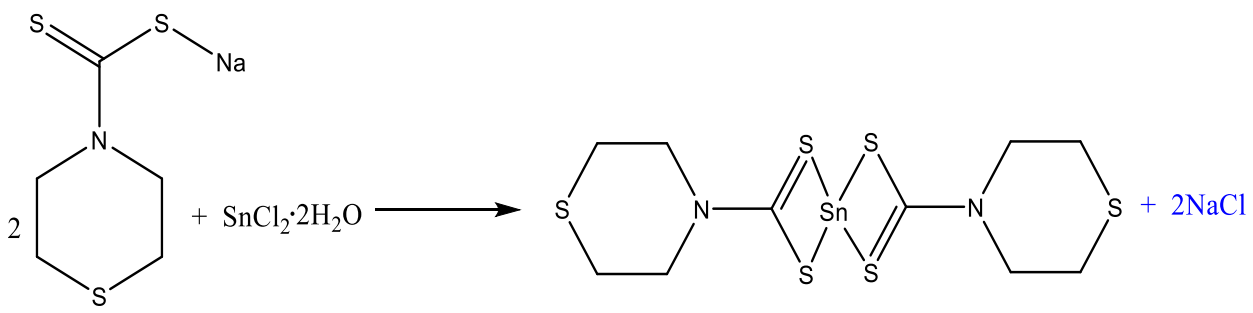

Scheme 2.12: Preparation of bis(thiomorpholinyldithiocarbamato)Sn(II)

2.4.8 Preparation of bis(N-(2-hydroxyethyl)phenyldithiocarbamato)Sn(II)

Scheme 2.3.3 shows the synthesis of the Sn(II) N-(hydroxyethyl)phenyl dithiocarbamate complex. 0.5189 g of $SnCl_2 \cdot 2H_2O$ (2.3 mmol) was introduced N-(hydroxyethyl)phenyl dithiocarbamate (4.6 mmol, 1.1479 g) in 20 mL of methanol. A light-yellow product formed instantly and was agitated for 2 h under nitrogen. The fine powder was suction filtered and rinsed with distilled water followed by diethyl. Yield = 21%, 0.2588 g. Melting point: 223.4 - 226.5 ℃. FTIR υ(cm^{-1}): 996 (νC—S_2) and 1489 (νN—CS_2). ^{1}H-NMR (D_6): δ 3.07 – 3.10 (t, 4H, CH_2), δ 4.29 – 4.32 (t, 4H,

CH_2), δ 4.53 (s, 2H, OH), δ 7.06 – 7.09 (t, 2H, CH), δ 7.31 – 7.37 (t, 4H, CH), δ 7.42 – 7.50 (d, 4H, CH).

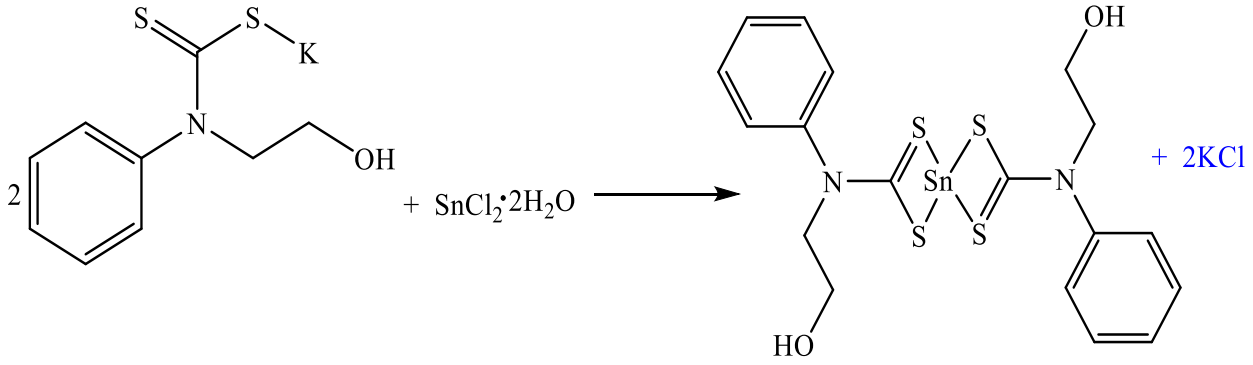

Scheme 2.13: Preparation of bis(N-(2-hydroxyethyl)phenyldithiocarbamato)Sn(II)

2.4.9 Preparation of bis(4-methylpiperidinedithiocarbamato)Sn(II)

The Sn(II) 4-methylpiperidine dithiocarbamate complex was synthesized at room temperature (Scheme 2.14). In separate beakers, $SnCl_2{\cdot}2H_2O$ (2.5 mmol, 0.5641 g) and sodium 4-methylpiperidine dithiocarbamate (5 mmol, 0.9852 g) were dissolved in 20 mL of distilled water. Thereafter, the aqueous solutions were gently combined and agitated for around 2 h to make sure that the reaction was complete. The filtered yellow fine powder was splashed with distilled water. Yield: 1.0243 g, 76%. ^{1}H-NMR (DMSO): δ 0.992 (6H, d, CH_3), δ 1.58-1.64 (2H, t, CH), δ 1.01-1.10 (8H, q, CH_2), δ 2.84-3.03 (8H, q, CH_2). FTIR υ(cm^{-1}): 945 (νC—S_2) and 1468 (νN—CS_2).

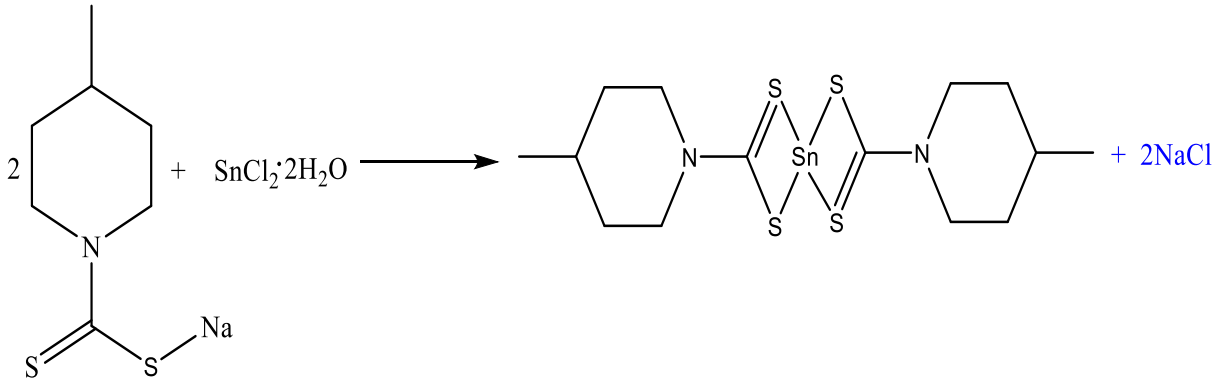

Scheme 2.14: Preparation of bis(4-methylpiperidinedithiocarbamato)Sn(II)

2.4.10 Preparation of bis(4-benzylpiperidinedithiocarbamato)Sn(II)

The tin(II) 4-benzylpiperidine dithiocarbamate complex was prepared according to Scheme 15. The tin salt, $SnCl_2{\cdot}2H_2O$ (2.5 mmol, 0.5641 g) dispersed in 20 mL of water was gently introduced to the sodium 4-benzylpiperidine dithiocarbamate (5 mmol, 1.3653 g) in 20 mL of water and agitated for 2 h. The filtered orange fine powder was splashed with distilled water. Yield: 1.7001 g, 84.21%. FTIR ν(cm^{-1}): 1422 (νC—N), 945 (νC—S). ^{1}H-NMR (D_6): δ 1.19-1.31 (2H, m, CH_2), δ 1.63-1.69 (2H, d, CH_2), δ 3.09-3.13 (2H, s, CH_2), δ 5.35-5.38 (2H, d, CH_2), δ 1.79-1.88 (1H, m, CH), δ 2.77-2.81 (2H, d, CH_2), δ 7.15-7.32 (5H, m, C_6H_5).

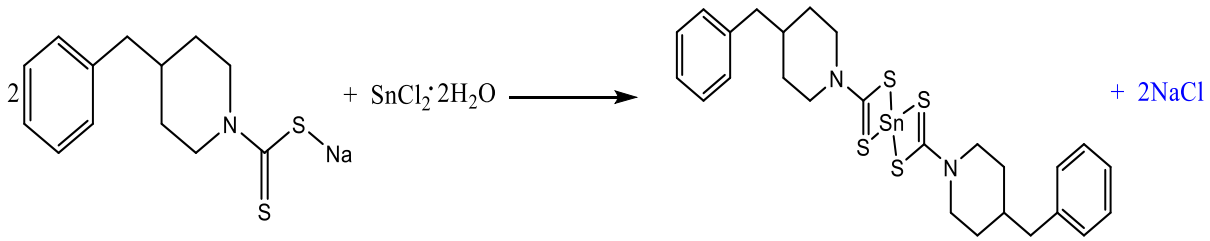

Scheme 2.15: Preparation of bis(4-benzylpiperidinedithiocarbamato)Sn(II)

References

1. Dolomanov, O. V.; Bourhis, L. J.; Gildea, R. J.; Howard, J. A.; Puschmann, H., OLEX2: a complete structure solution, refinement and analysis program. *J. Appl. Crystallogr.* **2009,** *42* (2), 339-341.

2. Sheldrick, G. M., A short history of SHELX. *Acta Crystallogr. A.* **2008,** *64* (1), 112-122.

3. Sheldrick, G. M., Crystal structure refinement with SHELXL. *Acta Crystallogr. C.* **2015,** *71* (1), 3-8.

4. Balakrishnan, S.; Duraisamy, S.; Kasi, M.; Kandasamy, S.; Sarkar, R. P.; Kumarasamy, A., Syntheses, physicochemical characterization, antibacterial studies on potassium morpholine dithiocarbamate nickel (II), copper (II) metal complexes and their ligands. *Heliyon* **2019,** *5*.

5. Solomane, N.; Ajibade, P. A., Synthesis and crystal structure of bis(thiomorpholinyldithiocarbamato)Cu(II) complex and its use as precursor for CuS nanoparticles photocatalyst for the degradation of organic dyes. *J. Sulfur Chem.* **2021,** *42* (2), 167-179.

6. Nath, P.; Bharty, M. K.; Prasad, L. B.; Butcher, R. J.; Jasinski, J. P., A piperidinium-carbodithioate salt: Synthesis, crystal structure, spectral, cation-interaction and electrochemical studies. *J. Mol. Struct.* **2019,** *1189*, 51-56.

7. Paca, A. M.; Ajibade, P. A.; Andrew, F. P.; Nundkumar, N.; Singh, M., Synthesis, X-ray crystal structures and anticancer studies of four Pd(II) dithiocarbamate complexes. *Arab. J. Chem.* **2021,** *14* (9), 103326.

8. Sathiyaraj, E.; Thirumaran, S.; Selvanayagam, S., Bis[N-benzyl-N-(2-phenylethyl)dithiocarbamato-k^2S,S']lead(II). *Acta Cryst. E.* **2012,** *68* (9), m1217.

CHAPTER THREE

SPECTROSCOPIC CHARACTERIZATION OF DITHIOCARBAMATE LIGANDS, Pb(II) AND Sn(II) COMPLEXES

3.1 Introduction

Dithiocarbamates are organosulfur compounds that are classified as monoanionic 1,1-dithiolate ligands[1]. Other commonly used ligands include dithiophosphinates[2], dithiophosphates[3], dithiocarbimates[4], and xanthates[5]. Dithiocarbamates are a well-studied group of compounds with a broad variety of applications. These applications include vulcanization accelerators in agriculture[6] and rubber industry[7], antifungal[8], antimicrobial[9], pharmaceuticals, and electrochemical sensors[10]. The extensive use of the dithiocarbamates is due to their ability to form strong bonds with both main and transition metal ions. The dithiocarbamate exists in two resonance form; hence it can stabilize metals of both high and low oxidation states[11].

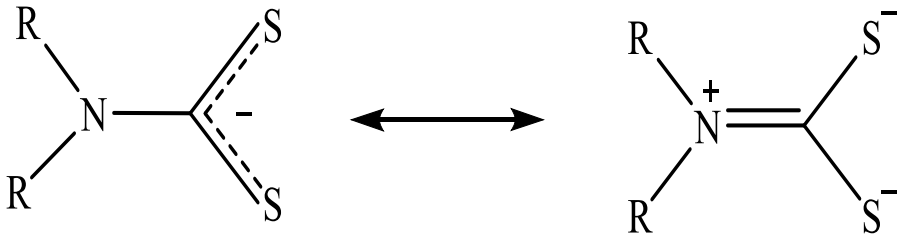

Dithiocarbamate Thioureide

Scheme 3.1: Resonance forms of the dithiocarbamate ligand

The dithiocarbamate resonance form consists of a single bond between the nitrogen atom and the sulfur-bearing carbon, and the -1 charge is delocalised between carbon and the two sulfur atoms. In the thioureide form (Scheme 16), the nitrogen is sp^2 hybridized. The former resonance best suited to stabilize soft metals at lower oxidation states[12]. In contrast, the latter type is labelled a hard ligand, stabilizing metal centers with high oxidation states. Dithiocarbamates complexes find extensive use as single-source precursors for the fabrication of metal sulfide nanoparticles[13-16]. This chapter presents the characterization of the dithiocarbamate ligands, Pb(II) and Sn(II) complexes by ^{1}H and ^{13}C-NMR spectroscopy, mass spectrometry, UV-Vis, FTIR and single crystal X-ray crystallography.

3.2 NMR spectra studies

The ligands were dissolved in deuterated water for NMR analysis; therefore, all of the ligands' ^{1}H NMR showed a solvent peak at 4.7 ppm. There are no specific shifts expected from proton NMR. The peak of the carbon atom in the NCS_2 group of the dithiocarbamate ligands which appeared downfield around 200 ppm[6] on the ^{13}C NMR. These position of these chemical shifts vary depending on the compound structural arrangement of R group coordinated to the nitrogen atom. The signal intensity is quite low, which is typical of quaternary carbon signals[17]. Due to the poor solubility of the complexes, ^{13}C-NMR could not be done.

3.2.1 NMR spectra of sodium morpholine dithiocarbamate and its lead(II) and tin(II) complexes

The ^{1}H NMR spectrum of morpholine dithiocarbamate ligand in Figure 3.1(c) shows the methylene protons of carbon bonded directly to thioureide nitrogen (N—CH_2) in the range 4.36–4.39 ppm, and the methylene protons of carbon directly bonded to an oxygen atom (O—CH_2)

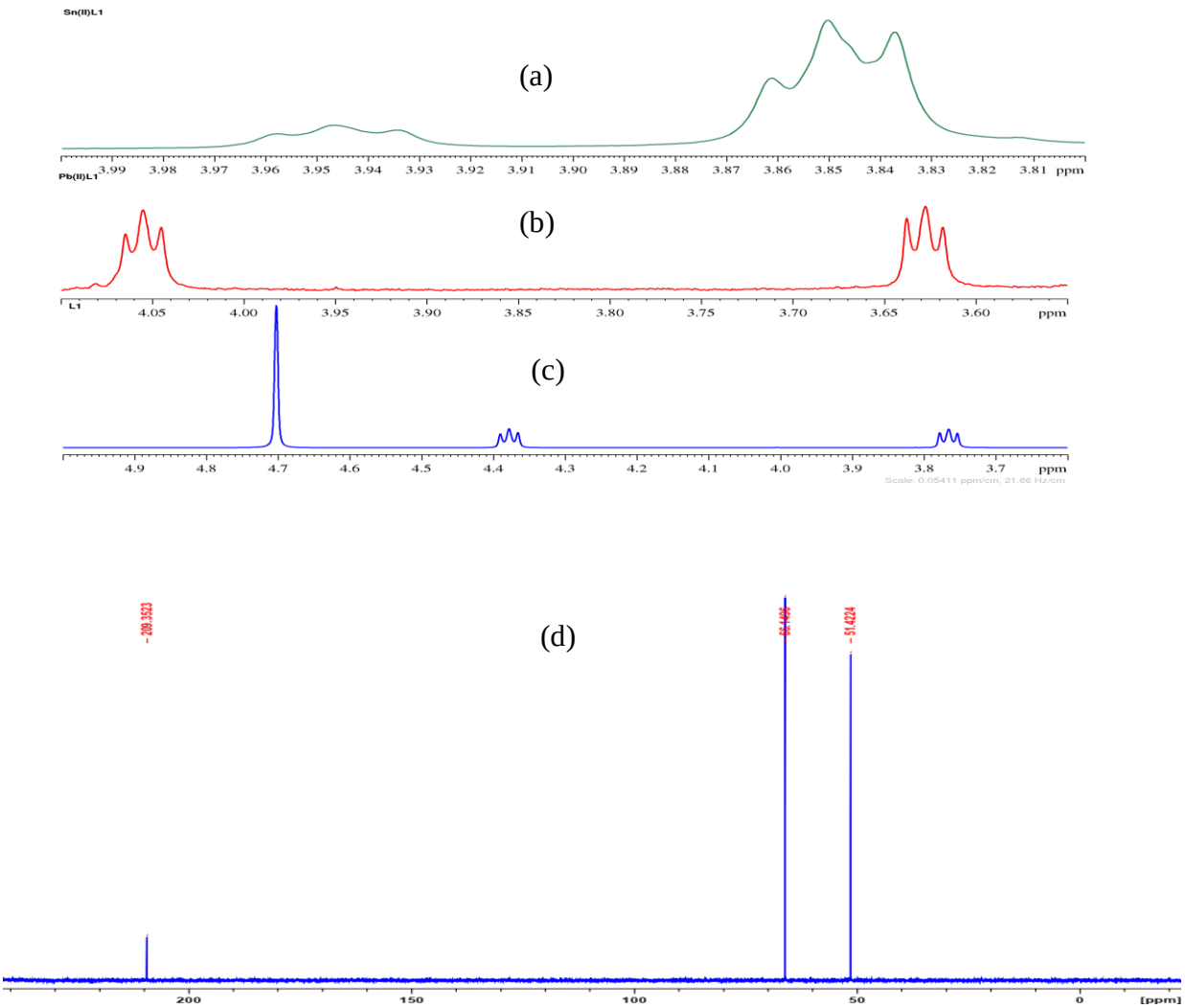

Figure 3.1. ^{1}H NMR spectra of sodium morpholine dithiocarbamate ligand (a), its Pb(II) (b), Sn(II) complexes (c) and ^{13}C NMR of sodium morpholine dithiocarbamate (d)

appeared between 3.83– 3.85 ppm[18]. The deuterated solvent peak was found at 4.7 ppm. In the spectrum of Pb(II) morpholine dithiocarbamate (Fig. 3.1(b)), a downfield shift was observed for methylene protons of O—CH_2 and N—CH_2 peaks at 3.62 ppm (t, 8H) and 4.05 ppm (t,8H), respectively. The proton NMR spectrum of Sn(II) morpholine dithiocarbamate (Fig. 3.1(a)) also showed a triplet at 3.83-3.86 ppm that is due to O—CH_2. The second triplet appeared at 3.75-3.77 ppm, which is for N—CH_2. The peaks are also down-shifted compared to those of the plain ligand due to the bonding of the ligand to the metal center. The ^{13}C NMR of morpholine dithiocarbamate (Fig. 3.1(d)) showed a peak assigned to the O—CH_2 carbon at 51.42 ppm, the N—CH_2 carbon peak at 66.15 ppm, and the signal assigned to –CS2 appeared at 209.35 ppm[19].

3.2.2 NMR spectra of sodium thiomorpholine dithiocarbamate and its lead(II) and tin(II) complexes

^{1}H NMR spectrum of thiomorpholine (Fig. 3.2(c)) displays two triplets around 3.50 – 3.48 ppm (t, 4H) and around 1.65 – 1.62 ppm (t, 4H) corresponding to the -CH_2 of N—CH_2 and S—CH_2, respectively. Pb(II) thiomorpholine dithiocarbamate (Fig. 3.2(b)) also showed two downfield shifted methylene protons of S—CH_2 and N—CH_2 at 2.7 ppm (t, 8H) and 4.3 ppm (t, 8H), respectively. The spectrum of the Sn(II) thiomorpholine dithiocarbamate (Fig. 3.2(a)) showed the N—CH_2 protons upfield as a triplet at 3.25-3.27 ppm and S—CH_2 protons signals at 2.80-2.82 ppm, which is a downfield shift compared to that of the ligand. In the ^{13}C NMR of the ligand shown in Figure 3.2(d), the peak at 26.79 ppm is due to the C atom in the S—CH_2, while 53.85 ppm peak is ascribed to the C atom in N—CH_2[19]. The signal observed at 208.90 is due to –CS_2.

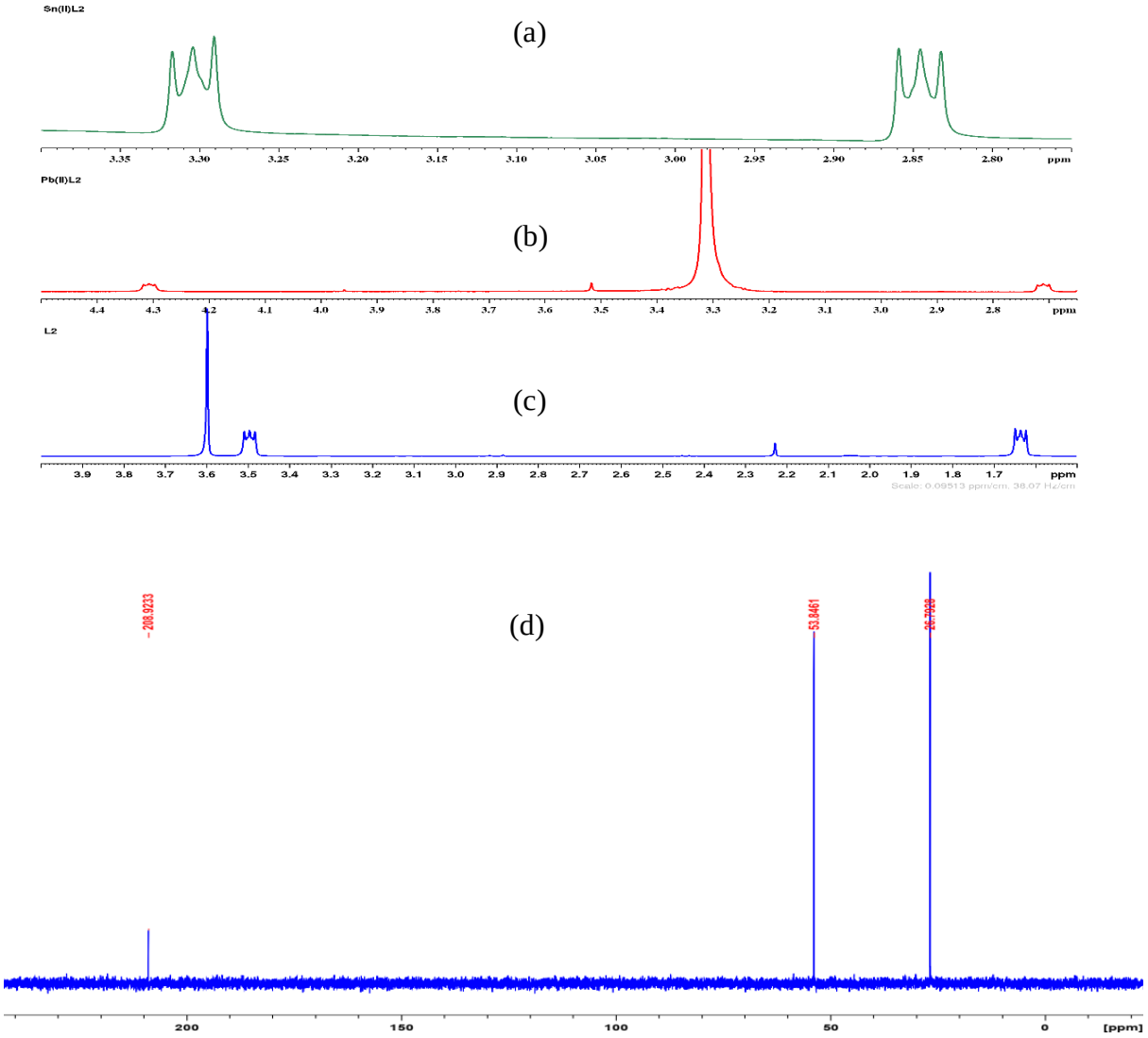

Figure 3.2. ^{1}H NMR spectra of sodium thiomorpholine dithiocarbamate ligand (a), its Pb(II) (b), Sn(II) complexes (c) and ^{13}C NMR of sodium thiomorpholine dithiocarbamate.

3.2.3 NMR spectra of N-(2-hydroxyethyl) phenyl dithiocarbamate and its lead(II) and tin(II) complexes

The ^{1}H NMR spectrum of K(hepdtc) (Fig 3.3 (c))shows two triplets for the alkyl chain protons at 3.46-3.49 ppm for methylene protons on the carbon bonded to the hydroxyl the other at 4.56-4.59 ppm assigned to the methylene protons directly bonded to the nitrogen. The peak observed at 4.76 is due to the proton of the OH group, and the peaks at 6.86-7.50 ppm are attributed to the protons of the phenyl group. In the proton NMR spectrum of Pb(II) N-(2-hydroxyethyl) phenyl dithiocarbamate (Fig 3.3 (b)), two methylene protons of the alkyl chain split into triplets at 3.06 ppm and 4.28 pm, and the aromatic protons are observed around 7.07-7.67 ppm. The proton of the OH group appeared as a singlet at δ 4.82 ppm in the free ligands as well as in the complex which confirmed that that the OH group of the ligand is not coordinated to the metal ion. For the Sn(II) complex (Fig 3.3 (a)), the alkyl chain protons were also split into triplets and deshielded to 3.07 and 4.29 ppm. The protons assigned to the phenyl appeared at 7.32-7.46 ppm. The deshielding effect upon coordination is caused by the lone pair electron distribution from the nitrogen to the sulfurs, and electronegativity of the protons is increased as a result.

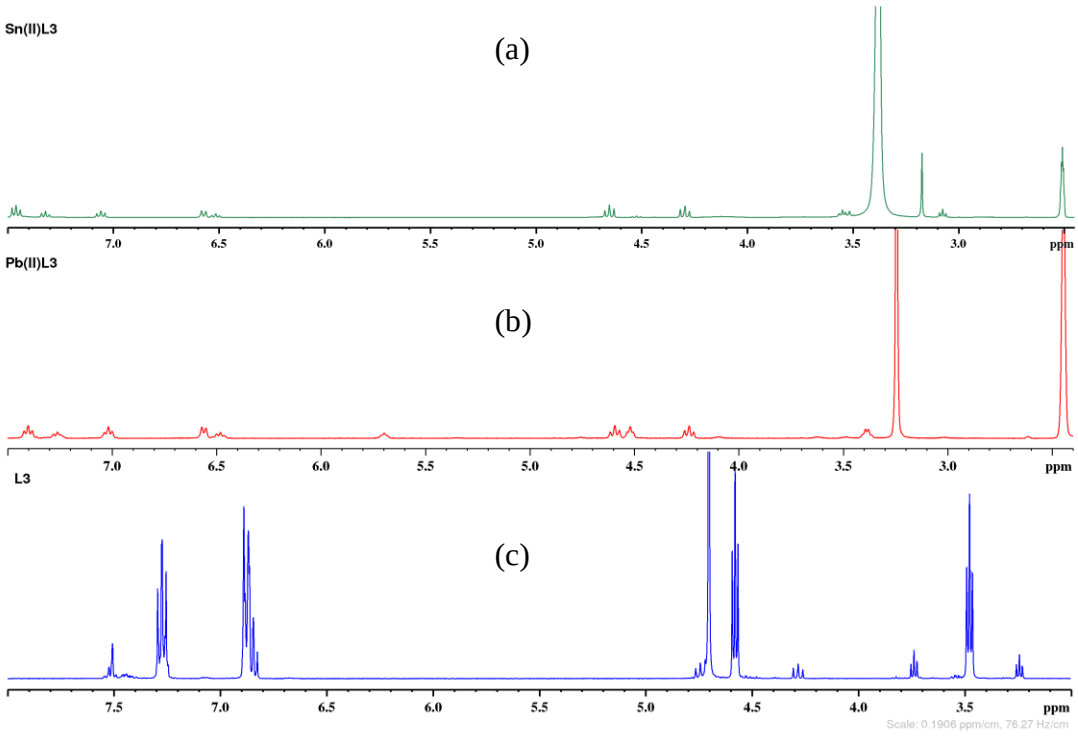

Figure 3.3. ^{1}H NMR spectra of potassium N-(2-hydroxyethyl)phenyl dithiocarbamate ligand (a), its Pb(II) (b) and Sn(II) complexes (c).

3.2.4 NMR spectra of sodium 4-methylpiperidine dithiocarbamate and its lead(II) and tin(II) complexes

The free 4-methylpiperidinyl dithiocarbamate ligand proton spectrum (Fig 3.4(c)) shows a doublet due to the methyl group at 0.91 ppm the multiplet at 1.69-1.78 ppm due to the hydrogen between the piperidine and the methyl group. The N—CH_2 protons are also observed around 3.11–3.18 ppm. The methyl group protons were upfield shifted to 0.90 ppm and 0.86 ppm in the Pb(II) and

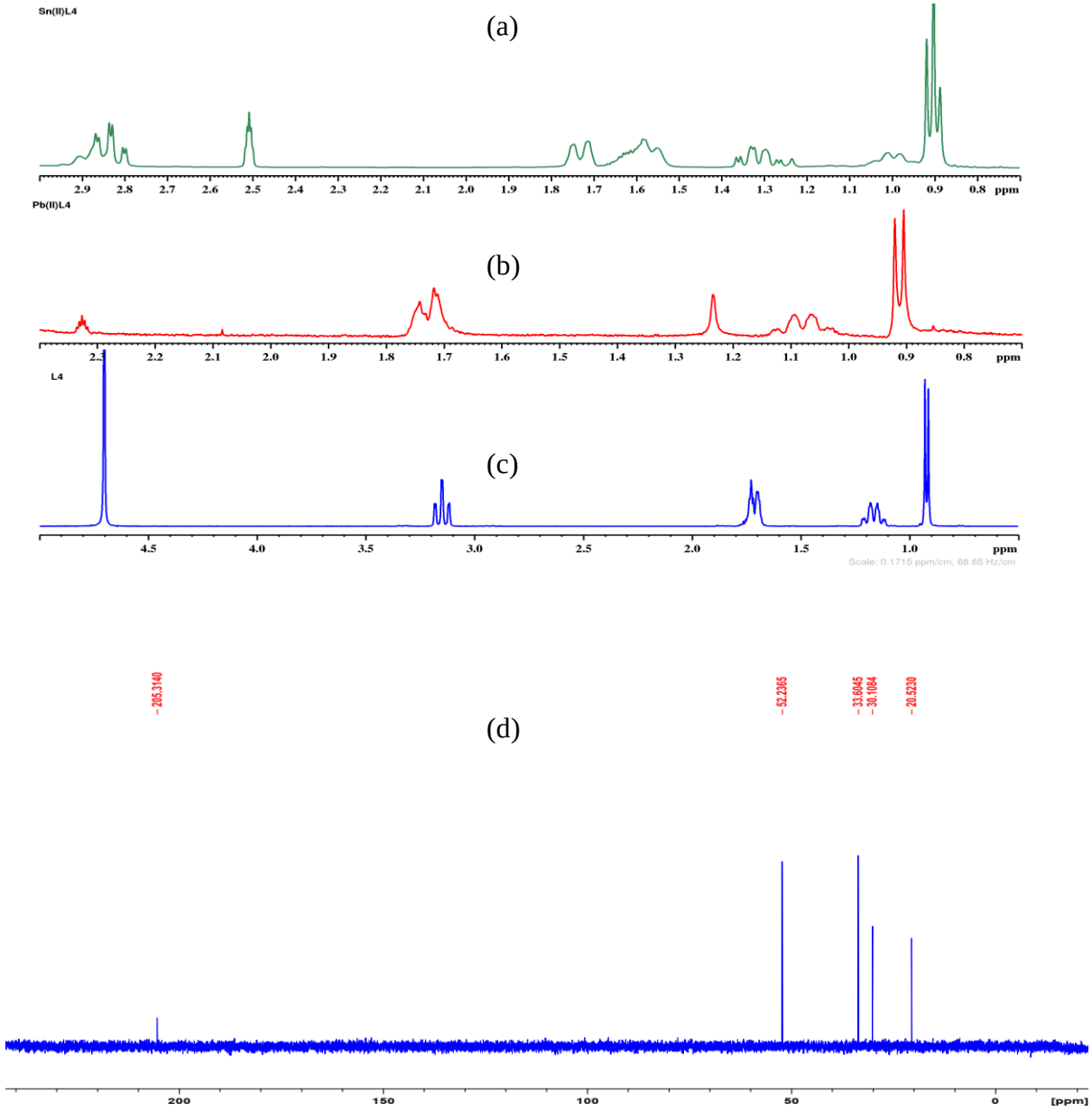

Figure 3.4. ^{1}H NMR spectra of sodium 4-methylpiperidine dithiocarbamate ligand (a), its Pb(II) (b), Sn(II) complexes (c) and ^{13}C NMR of sodium 4-methylpiperidine dithiocarbamate

Sn(II) complexes, respectively. A shielding effect was also observed for the N—CH_2 protons in both complexes. This may be due to the electron delocalization upon complexation. The ^{13}C NMR spectrum of the ligand (Fig 3.4(d)) reveals the significant peak attributed to the $-CS_2$ at 205 ppm.

3.2.5 NMR spectra of sodium 4-benzylpiperidine dithiocarbamate and its lead(II) and tin(II) complexes

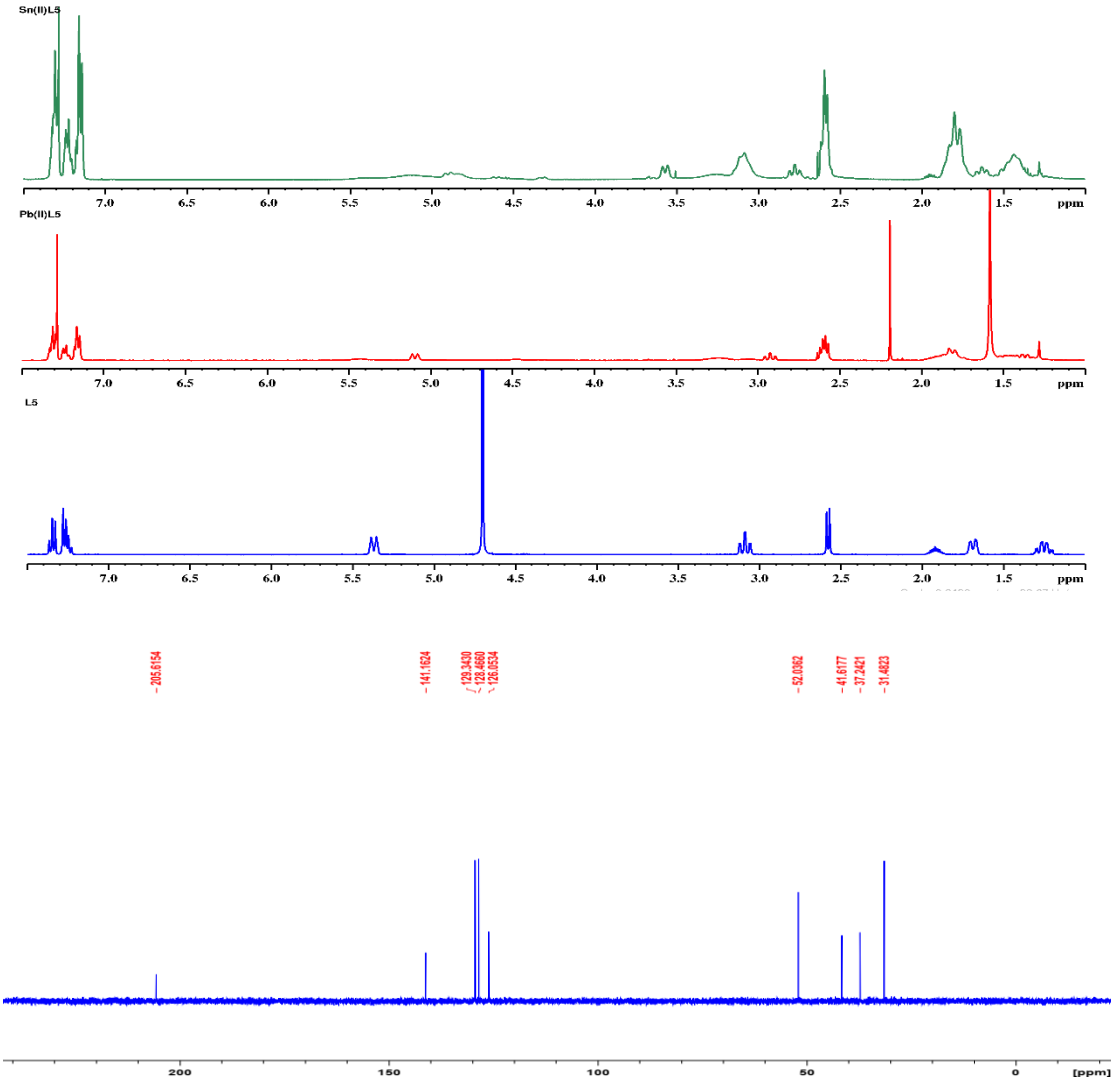

Figure 3.5. ^{1}H NMR spectra of sodium 4-benzylpiperidine dithiocarbamate ligand (a), its Pb(II) (b) and Sn(II) complexes (c) and ^{13}C NMR sodium 4-benzylpiperidine dithiocarbamate

The ^{1}H NMR data of Na(4-Bpipdtc) in Figure 3.4 (c) shows a multiplet for the aromatic ring at 7.22-7.36 ppm and a doublet at 1.67- 1.70 ppm ascribed to the methylene protons directly bonded to the benzyl. The multiplet at 1.86-1.97 ppm is ascribed to the hydrogen on the carbon between the methylene group and piperidine, and the peaks around 3.05-3.12 ppm are attributed to the N—CH_2 of the piperidine[20]. Upon complexation with Pb(II) metal ion, the aromatic ring peaks were shifted to about 7.11-7.30 ppm and 7.15-7.31 ppm for Sn(II). The N—CH_2 protons were also significantly upfield shifted around to 2.77-3.10 for Sn(II) complex and 2.87-2.93 ppm for the Pb(II) complex. The ^{13}C NMR of a free ligand in Figure 3.5(d) exhibits the $–CS_2$ peak at 205 ppm.

3.3 Mass spectrometry of the dithiocarbamate ligands and lead(II) and tin(II) dithiocarbamate complexes

The molecular ion base peaks for all the dithiocarbamate ligands appeared in the negative ESI spectra. N-(2-hydroxyethyl)phenyl dithiocarbamate has a molar mass of 250.42 g/mol and the M^{-} of 212 m/z when K^{+} is excluded. Na^{+} was also not observed in the base peaks of morpholine dithiocarbamate (185.23 g/mol) and thiomorpholine dithiocarbamate (201.30 g/mol), and their M^{-} was 162 m/z and 178 m/z, respectively. The TOF mass spectrometry of all the Pb(II) and Sn(II) complexes was also done and the complexes might have been unstable or decomposed which resulted in mass spectra with unexpected M^{+}.

3.4 Absorption spectra studies of the lead(II) complexes

3.4.1 Absorption spectra of morpholine dithiocarbamate and its lead(II) and tin(II) complexes

The electronic spectrum of the morpholine dithiocarbamate showed three characteristic absorption bands[21]. The band at 207 nm is attributed to $\pi \rightarrow \pi^*$ transition of the N-C=S group, another $\pi \rightarrow \pi^*$ transition of the S-C=S dithiocarbamate moiety is found at 260 nm, and the band at 286 nm is ascribed to $n \rightarrow \pi^*$ transition of the sulfur atoms. Upon complexation, the LMCT transitions for [Pb(morph)$_2$] and [Sn(morph)$_2$] were found at 270 and 359 nm, respectively. The complexes have no observable *d-d* transition, since they are d^{10} system.

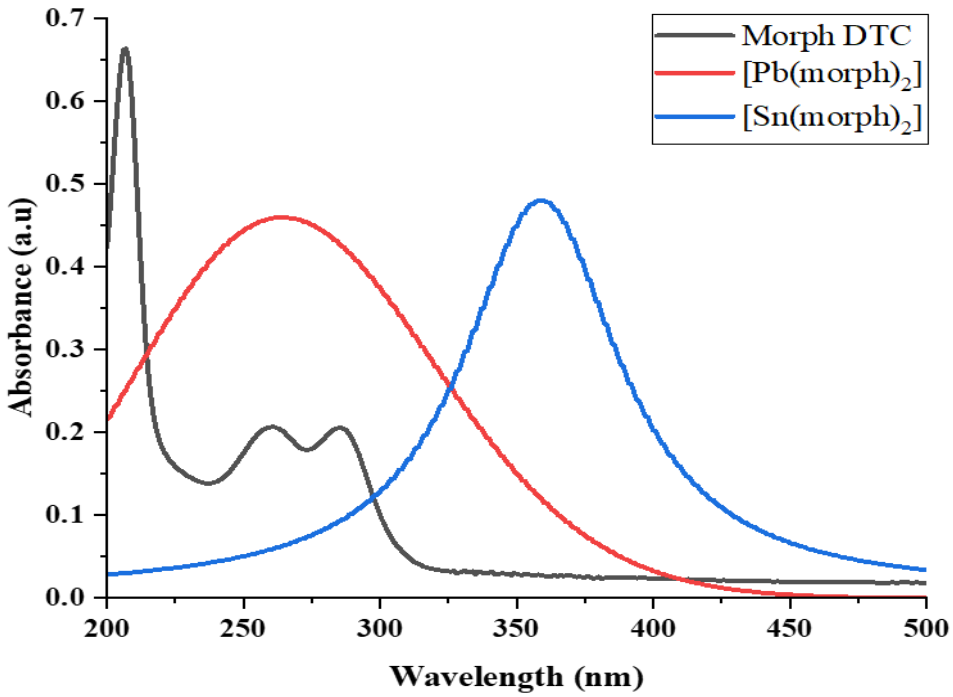

Figure 3.6 Absorption spectra of morpholine dithiocarbamate and its Pb(II) and Sn(II) complexes

3.4.2 Absorption spectra of thiomorpholine dithiocarbamate and its lead(II) and tin(II) complexes

Thiomorpholine dithiocarbamate and its corresponding complexes absorption spectra are presented in Figure 3.7. The ligand spectrum exhibited π→π* transitions[15] at 204 and 262 nm, owing to the N–C=S and S–C=S of the dithiocarbamate moiety, respectively. The third band at 286 nm is ascribed to $n \rightarrow \pi^*$ transition on the sulfur atoms. Both complexes exhibited only one band each ascribed to LMCT transitions at 272 nm for $[Pb(Tmorph)_2]$ and 370 nm for $[Sn(Tmorph)_2]$.

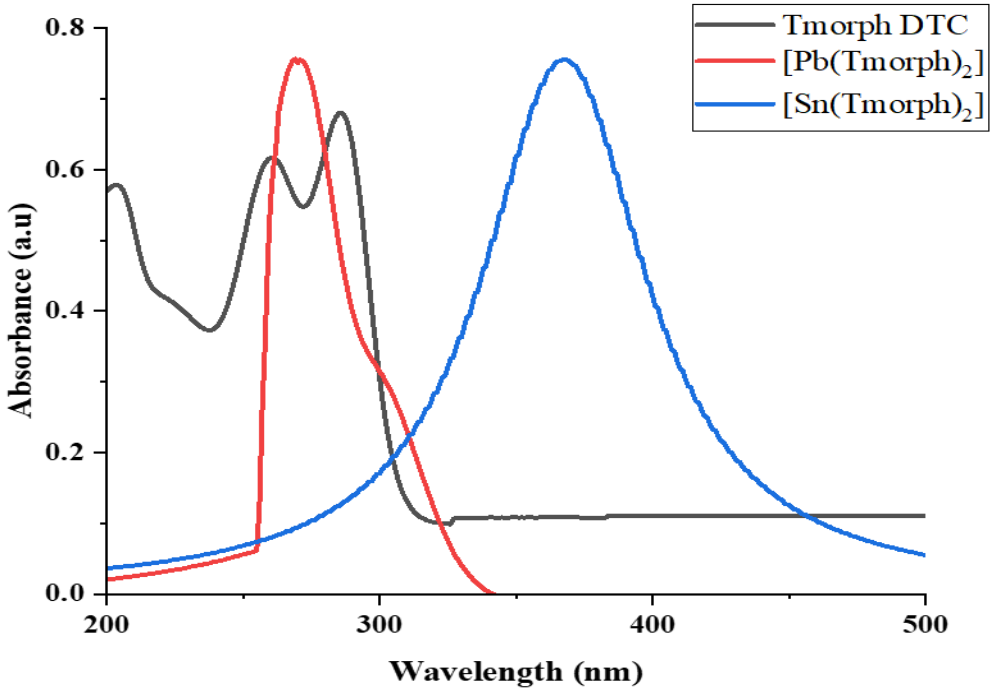

Figure 3.7 Absorption spectra of thiomorpholine dithiocarbamate and its Pb(II) and Sn(II) complexes

3.4.3 Absorption spectra of N-(2-hydroxyethyl)phenyl dithiocarbamate and its lead(II) and tin(II) complexes

The spectrum of the ligand in Figure 3.8 exhibited two absorption bands at 234 and 301 nm, which are assigned to π→π* and n→π* transitions[22], respectively. The absorption spectra of the Pb(II) and Sn(II) complexes exhibit broad bands at 261 nm and 377 nm, respectively, which is attributed to the active LMCT transition. Being a d^{10} system, the Pb(II) and Sn(II) complexes show no *d-d* transition in the visible region.

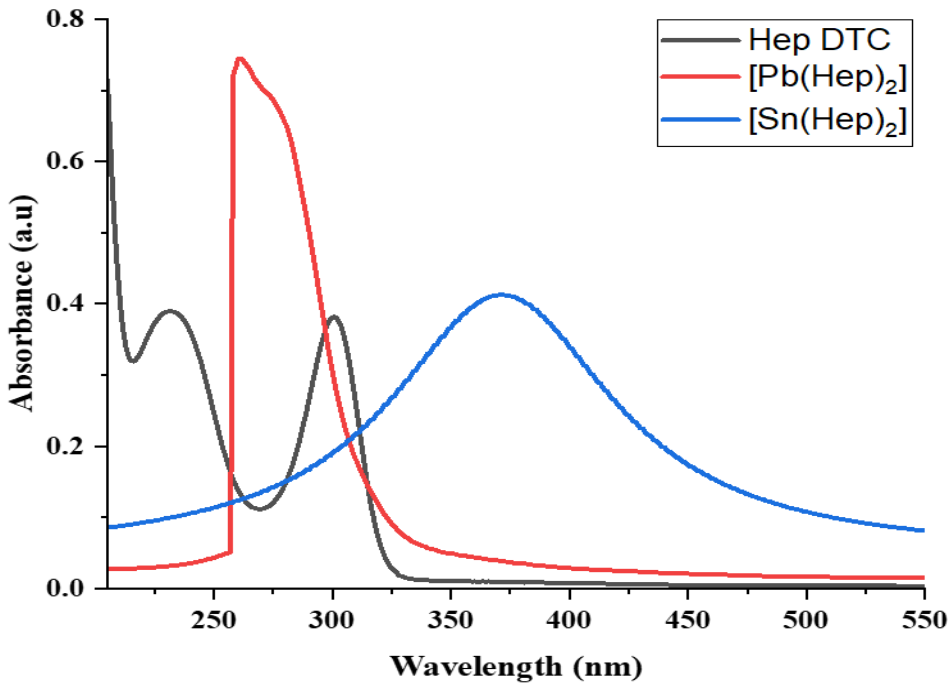

Figure 3.8 Absorption spectra of N-(2-hydroxyethyl)phenyl dithiocarbamate and its Pb(II) and Sn(II) complexes

3.4.4 Absorption spectra of 4-methylpiperidine dithiocarbamate and its lead(II) and tin(II) complexes

The electronic spectrum of 4-methylpiperidinecarbodithioate in Figure 3.9 showed $\pi \rightarrow \pi^*$ transitions at 204 nm and 258 nm corresponding to -NCS and -SCS systems[10], respectively. The peak at 281 nm corresponds to $n \rightarrow \pi^*$ transition owing to the sulfur atoms' lone electron pairs. The prominent LMCT transitions are seen in the absorption spectra of the Pb(II) and Sn(II) complexes at 266 nm and 267 nm, respectively. The complexes have no observable *d-d* transition since they are a d^{10} system.

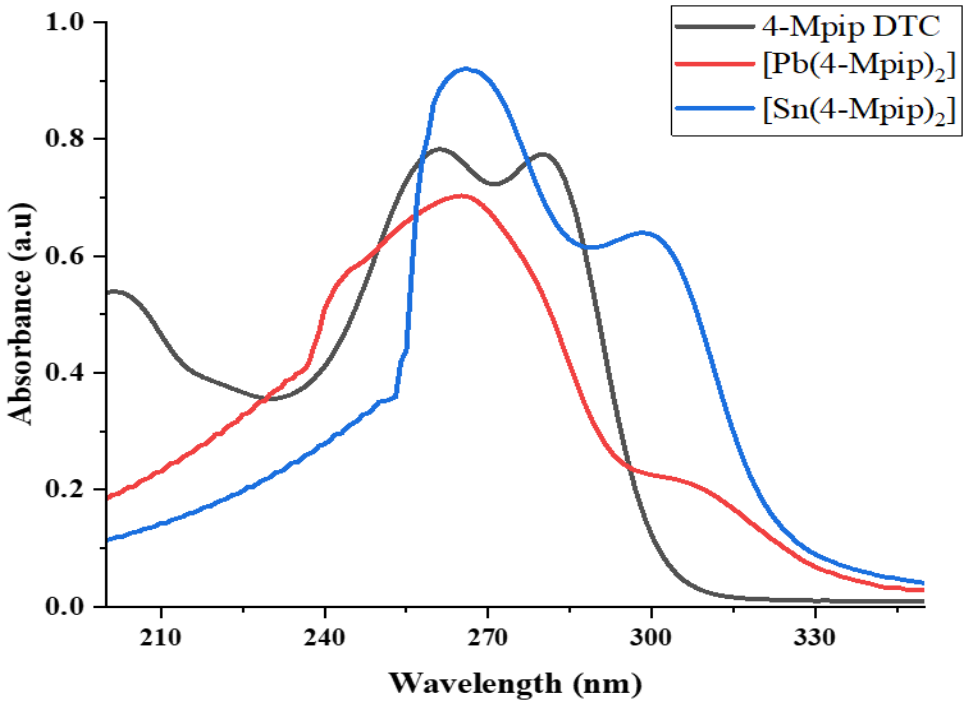

Figure 3.9 Absorption spectra of 4-methylpiperidine dithiocarbamate and its Pb(II) and Sn(II) complexes

3.4.5 Absorption spectra of 4-benzylpiperidine dithiocarbamate ligand and its lead(II) and tin(II) complexes

The ligand's absorption spectrum in Figure 3.10 revealed three distinct absorption bands. The π→π* transition on the -NCS group is responsible for the band at 205 nm. The 262 nm band is also attributed to π→π* transitions; however, this instance is within the -SCS dithiocarbamate group[23]. The band at 282 nm is assigned to the n→π* transition on sulfur atoms. After complexation, absorption peaks for [Pb(4-Bpip)$_2$] and [Sn(4-Bpip)$_2$] were found at 263 and 258 nm, respectively. This band is ascribed to a LMCT transition.

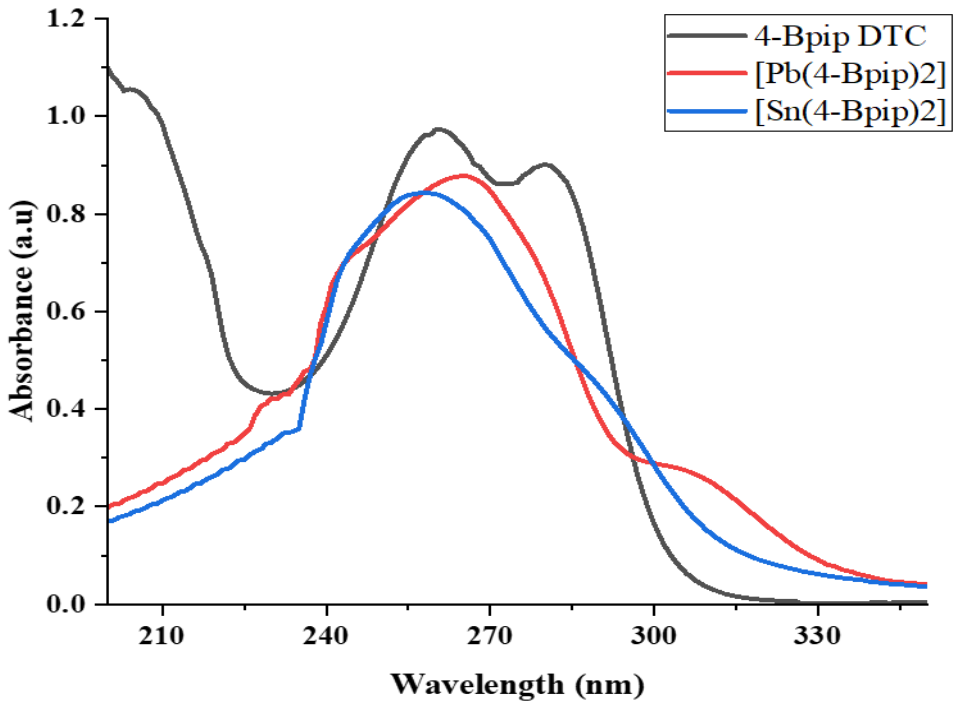

Figure 3.10 Absorption spectra of 4-benzylpiperidine dithiocarbamate and its Pb(II) and Sn(II) dithiocarbamate complexes

3.5 Fourier-transform infrared spectroscopy of the dithiocarbamate ligands and Pb(II) and Sn(II) dithiocarbamate complexes

Free dithiocarbamate ligands normally exhibit distinct v(C-S) bands around 1055 cm^{-1} and 961 cm^{-1} due to $v(CS_2)_{asym}$ and $v(CS_2)_{sym}$, respectively. These bands determine the binding form of the dithiocarbamate to the metal ion. In the instance of a bidentate complex formation, these are supplanted by a single sharp peak at roughly 1000 ± 70 cm^{-1}. Conversely, the split of a band with a gap of about 20 cm^{-1} over the same area indicates the dithiocarbamate ligand's monodentate configuration.[12]. The infrared spectra of dithiocarbamate complexes exhibited three diagnostic bands, namely, the thioureide v(C=N), the v(C-S), and v(M-S), and they have direct structural relevance[12, 24]. The band around 1450-1550 cm^{-1} is associated with v(C-N) thioureide vibration representing the partial double bond behavior. The v(C-S) vibration is usually observed in the 950-1050 cm^{-1} area, whereas the v(M-S) band appears in the far-infrared region of 350-450 cm^{-1} which indicates the complexation.

3.5.1 Infrared spectra of morpholine dithiocarbamate and its lead(II) and tin(II) complexes.

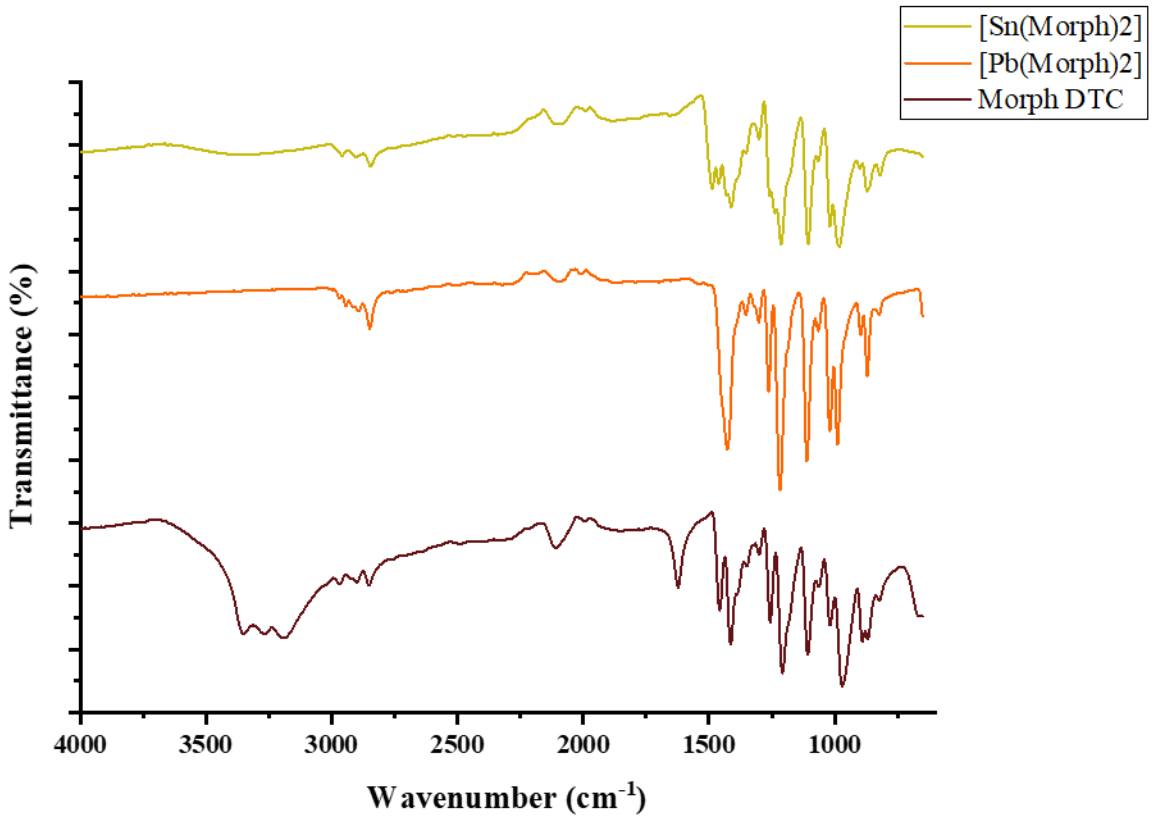

Figure 3.11 Infrared spectra of morpholine DTC and its lead(II) and tin(II) complexes

The superimposed spectra of the morpholine dithiocarbamate ligand, lead(II), and tin(II) complexes are shown in Figure 3.11. The dithiocarbamate ligand showed two vibrations assigned to $v(CS_2)_{sym}$ and $v(CS_2)a_{sym}$ at 970 and 1018 cm^{-1}, which merged and moved to 984 and 988 cm^{-1} upon complexation with tin(II) and lead(II), respectively. The bare ligand spectrum also displays C-N vibration at 1457 cm^{-1}; however, this band moved to 1428 cm^{-1} and 1498 cm^{-1} in the lead(II) and tin(II) complexes which fall in between C-N and C=N infrared absorption bands, demonstrating the partial double bond nature.

3.5.2 Infrared spectra of thiomorpholine dithiocarbamate and its lead(II) and tin(II) complexes.

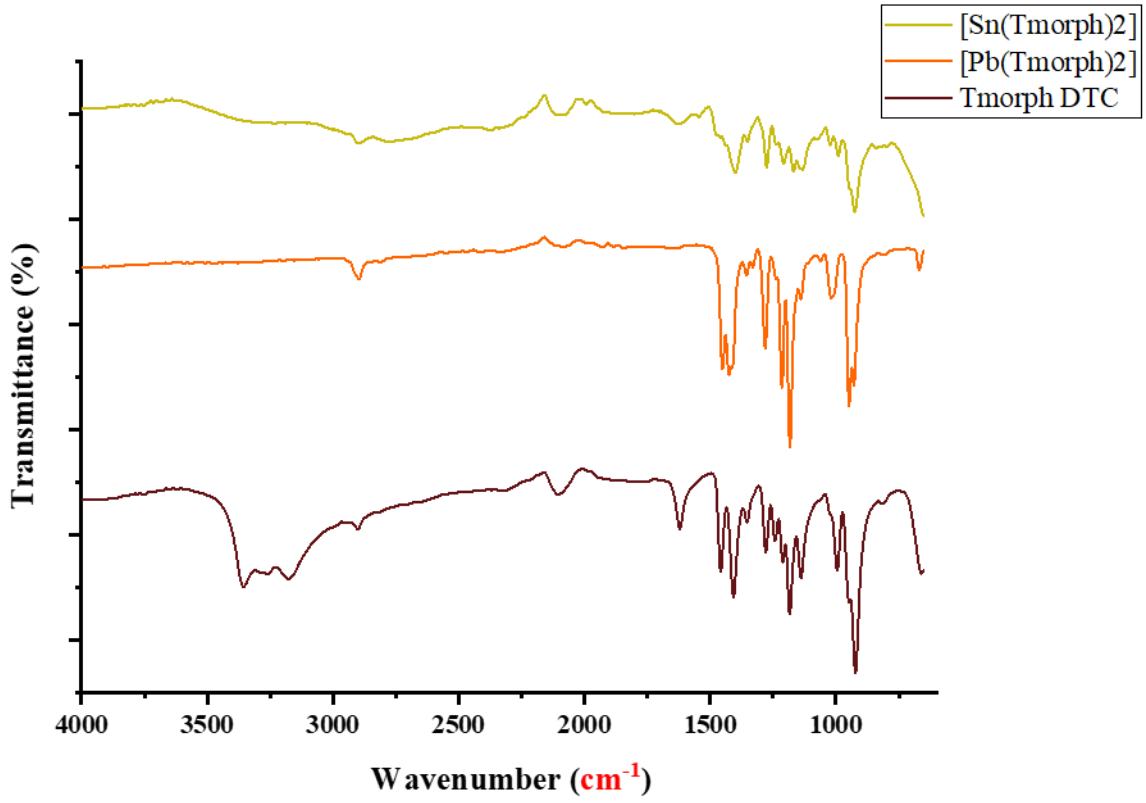

Figure 3.12 Infrared spectra of thiomorpholine dithiocarbamate and its lead(II) and tin(II) complexes

Figure 3.12 depicts the overlaid spectra of thiomorpholine dithiocarbamate and its corresponding lead(II) and tin(II) complexes. The bare ligand exhibits two v(C-S) vibrations at 922 cm^{-1} and 995 cm^{-1}. In the spectra of the complexes, the v(C–S) vibrational band appeared as a single band, suggesting that the ligands are coordinated to the metal centers in a symmetrical bidentate fashion. Tmorph DTC also displays the C-N stretching vibration at 1458 cm^{-1}.

[Sn(Tmorph)$_2$] and [Pb(Tmorph)$_2$] complexes spectra exhibit bands corresponding to the thioureide moiety at 1497 and 1451 cm^{-1}, respectively. These frequencies are in the middle of a C-N (1250-1350 cm^{-1}) and a C=N (1640-1690 cm^{-1}), implying a partial double-bond nature and consequently π-electron density distribution around the dithiocarbamate group.

3.5.3 Infrared spectra of N-(2-hydroxyethyl)phenyl dithiocarbamate and its lead(II) and tin(II) complexes

N-(2-hydroxyethyl)phenyl dithiocarbamate and its corresponding tin (II) and lead(II) complexes infrared spectra are presented in Figure 3.13. All spectra exhibit significant vibrations of the dithiocarbamate moiety. The C–S vibration was identified as a broad single band in the ligand spectrum about 990-1040 cm^{-1}, and it emerged at notably lower frequencies in the complexes. The single band suggested that the ligands were coordinated to the metal ions in a bidentate fashion. Hep DTC revealed the C-N vibration at 1496 cm^{-1} which dropped to 1484 cm^{-1} and 1488 cm^{-1} in the lead(II) and tin(II) complexes. The apparent drop in stretching vibrations of the thioureide bands of [Pb(Hep)$_2$] and [Sn(Hep)$_2$] compared to those obtained in the bare ligand spectrum could be attributable to sulfur atoms binding to metal ions, which enhances the C=N double-bond character.

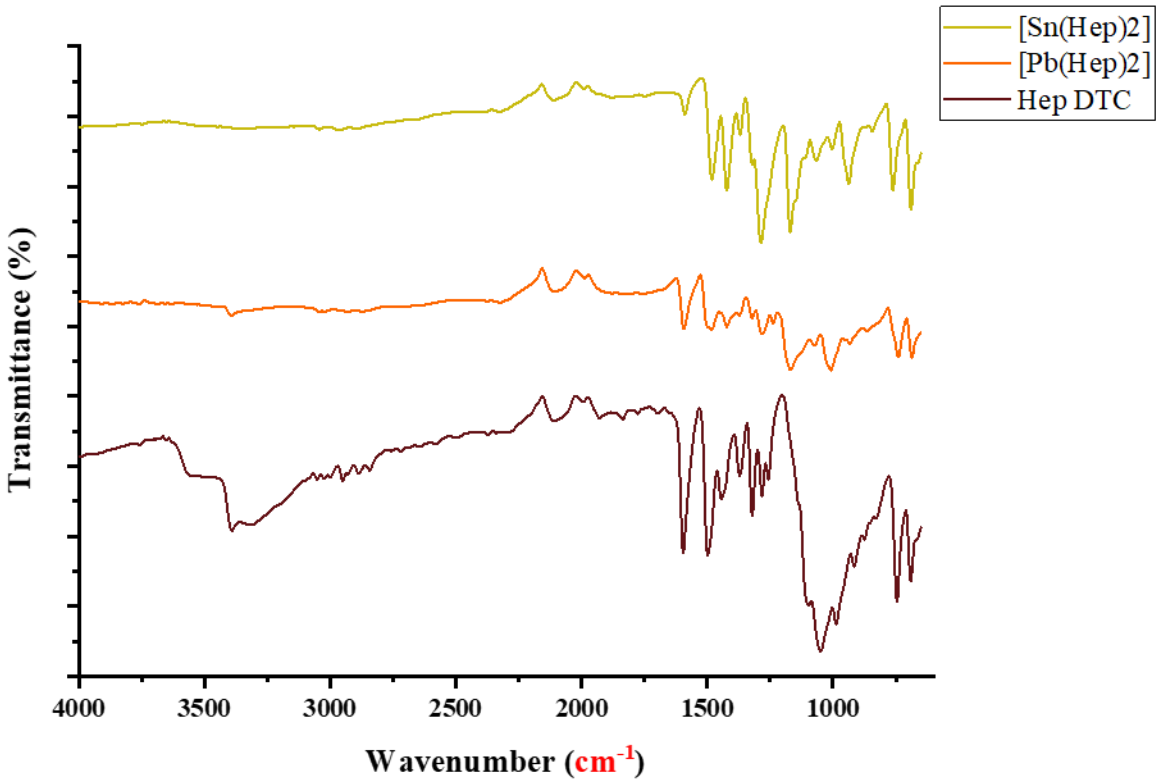

Figure 3.13 Infrared spectra of N-(2-hydroxyethyl)phenyl dithiocarbamate and its lead(II) and tin(II) complexes

3.5.4 Infrared spectra of 4-methylpiperidine dithiocarbamate and its lead(II) and tin(II) complexes.

All of the spectra showed significant dithiocarbamate moiety vibrations. The 4-methylpiperidinyl ligand exhibited the C-N vibration at 1468 cm^{-1}, which downshifted to 1430 cm^{-1} and 1417 cm^{-1} in the lead(II) and tin(II) complexes, respectively, owing to ligand chelation to the metal ion. The symmetric and asymmetric (C-S) vibrations are responsible for the bands found in the ligand spectrum at 945 cm^{-1} and 1018 cm^{-1}. Lead(II) and tin(II) complexes each had a single peak at 958

cm^{-1} and 947 cm^{-1}, respectively. This is attributable to the ligand's bidentate coordination with the metal ions.

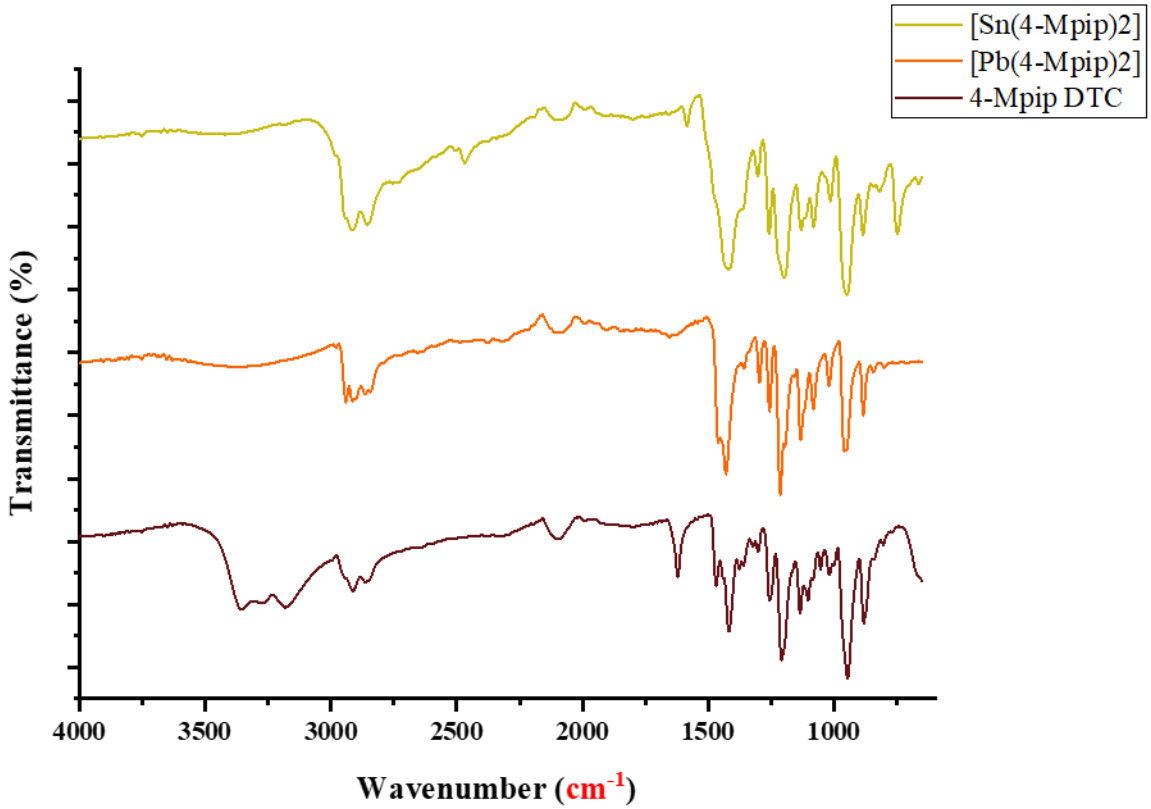

Figure 3.14 Infrared spectra of 4-methylpiperidine dithiocarbamate and its lead(II) and tin(II) complexes

3.5.5 Infrared spectra of 4-benzylpiperidine dithiocarbamate and its lead(II) and tin(II) complexes.

The overlay spectra of the 4-benzylpiperidine dithiocarbamate ligand, lead(II), and tin(II) dithiocarbamate complexes are presented in Figure 3.15. All three spectra exhibited the significant

vibrations of the dithio-moiety. At 945 cm^{-1} and 1017 cm^{-1}, the bare ligand spectrum revealed $v(CS_2)_{sym}$ and $v(CS_2)a_{sym}$. For the tin(II) and lead(II) complexes, these were combined into single peaks at 962 cm^{-1} and 961 cm^{-1}, respectively, suggesting bidentate coordination. In the 4-Bpip DTC, the C-N vibration was found at 1469 cm^{-1}, but in the $[Sn(4\text{-Bpip})_2]$ and $[Pb(4\text{-Bpip})_2]$ this was detected in relatively lower frequencies.

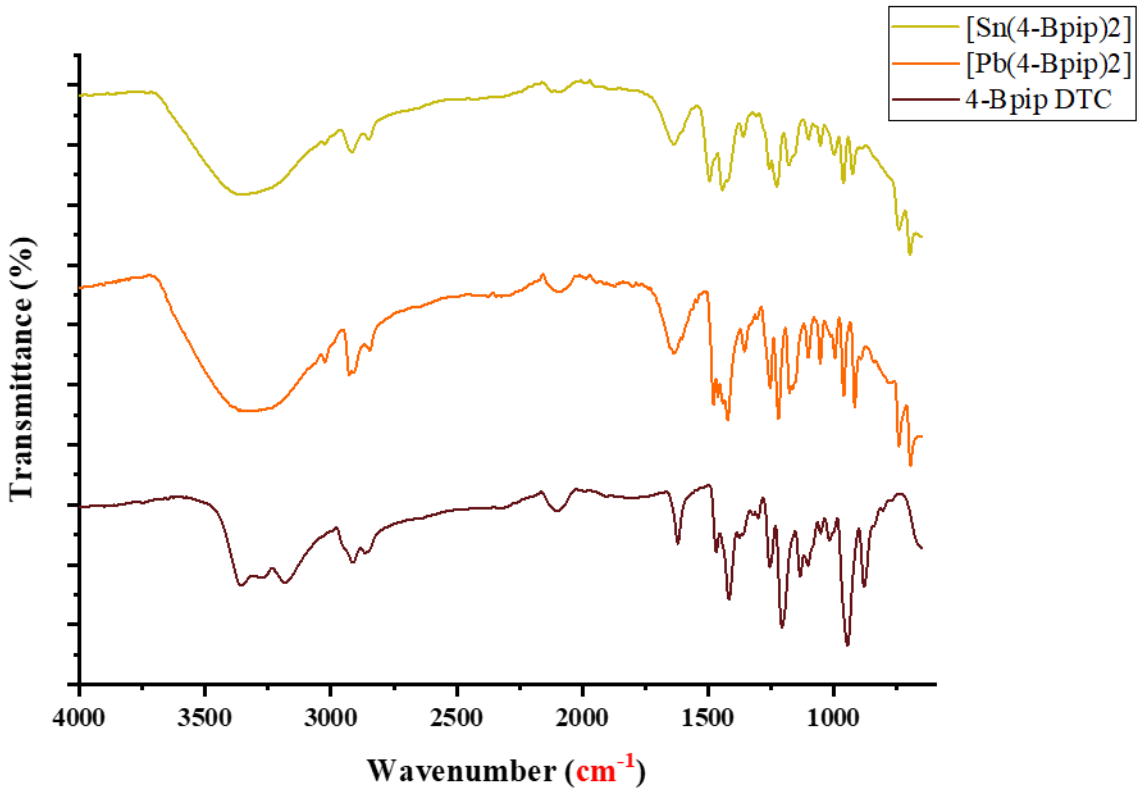

Figure 3.15 Infrared spectra of 4-benzylpiperidine dithiocarbamate and its lead(II) and tin(II) complexes

3.6 Molecular structures of the complexes

3.6.1 Molecular structure of bis(4-methylpiperidine-1-carbothioato)-lead(II)

The structure crystallizes in the C2/c space group of the monoclinic crystal system. The compound is four-coordinate with two bidentate monoanionic piperidinyl ligands chelating the lead(II) ion, forming a neutral chelate. The distorted configuration (illustrated in Fig. 3.16) indicates the existence of a stereochemically active $6s^2$ lone pair[25, 26]. Identical coordination arrangements have

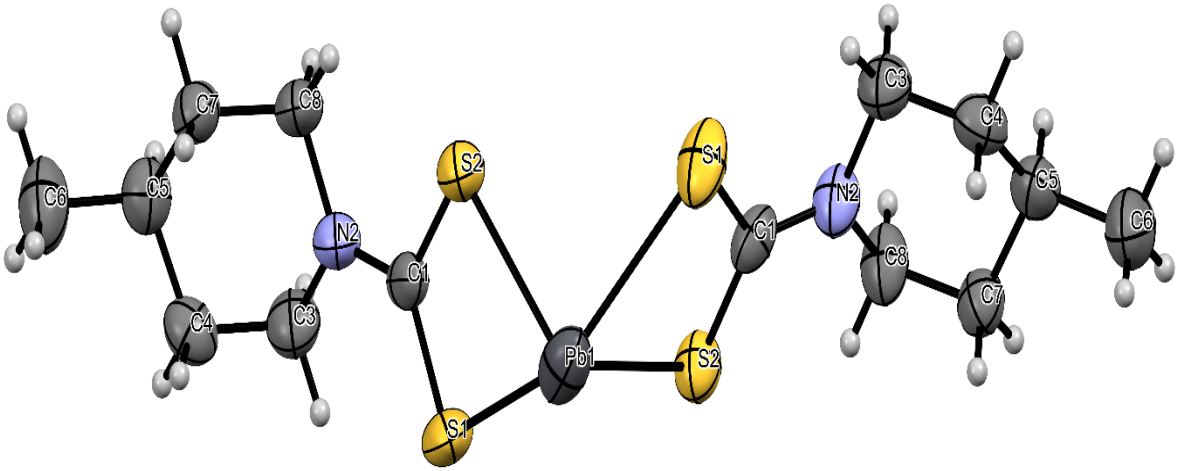

Figure 3.16: The molecular structure of bis(4-methylpiperidine-1-carbothioato)-lead(II)

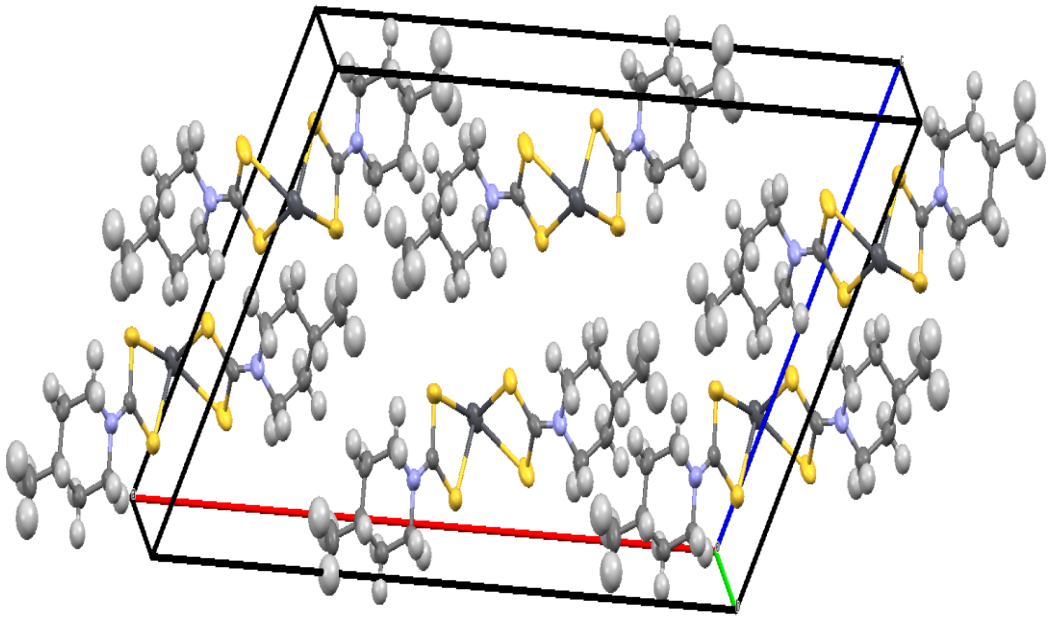

Figure 3.17: Crystal packing of bis(4-methylpiperidine-1-carbothioato)-lead(II)

been observed for related molecules[27, 28]. The data in Table 3.2 depicted a few significant aspects of the molecular structure, and the relevant bond distances and angles are listed in table 3.1. The S1–Pb1–S2 bond angles within the ligand are quite acute, averaging 64.02°. The S1–Pb1–S21 bond angles are not restricted by the ligand and hence exhibit a greater angle of 83.57°, which deviates from that of a perfect tetrahedron. The Pb–S bonds are not equal in length, as is common in chelates of this type, displaying a short and one greater bond distance per ligand. The lengths of the S-C bonds are nearly equal, indicating that electrons are delocalized over this region of the ligand. The crystal packing of the compound (Figure 3.17) shows six molecules within the crystal packing arranged in group of three molecules that are parallel to each other.

Table 3.1: Bond lengths and angles for bis(4-methylpiperidine-1-carbothioato)-lead(II)

Bond Length		Bond Angles	
Bond	**Length(Å)**	**Bonds**	**Angle(°)**
Pb1–S2	2.7097(10)	S2–Pb1–S21	97.63(5)
Pb1–S21	2.7097(10)	S2–Pb1–S1	64.02(3)
Pb1–S1	2.8831(13)	S21–Pb1–S1	83.57(3)
Pb1–S11	2.8831(13)	S2–Pb1–S11	83.57(3)
S2–C1	1.736(4)	S21–Pb1–S11	64.02(3)
S1–C1	1.705(4)	S1–Pb1–S11	130.63(5)
C1–N2	1.338(6)	C1–S2–Pb1	90.67(14)
		C1–S1–Pb1	85.60(15)

Table 3.2: Summary of crystal data and structure refinement of bis(4-methylpiperidine-1-carbothioato)-lead(II)

Compound	$[Pb(4\text{-mpipdtc})_2]$
Formula	$C_{14}H_{24}N_2PbS_4$
$D_{calc.}$/ g cm^{-3}	1.951
μ/mm^{-1}	21.417
Formula Weight	555.78
Size/mm^3	0.505x0.190x 0.055
T/K	102(2)
Crystal System	Monoclinic
Space Group	C2/c
a/Å	29.5086(10)
b/Å	4.6830(2)
c/Å	15.6621(5)

α/°	90
β/°	119.0530(10)
γ/°	90
V/Å^3	1891.99(12)
Z	4
Θ_{min}/°	3.427
Θ_{max}/°	72.650
Measured Refl.	16061
Independent Refl.	1838
Reflections Used	100
R_{int}	0.0547
Parameters	97
Largest Peak	0.452
Deepest Hole	-2.382
GooF	1.108
wR_2 (all data)	0.0870
wR_2	0.0856
R_1 (all data)	0.0349
R_1	0.0338

3.6.2 Molecular structure of bis(4-benzylpiperidine-1-carbothioato)-lead(II)

[Pb(4-Bpip)$_2$] crystallized in the monoclinic C2/n space group. The crystallographic data is listed in Table 3.3, and relevant bond distances and bond angles are presented in Table 3.4. The lead(II) ion is coordinated to the sulfur atoms of the benzylpiperidinyl ligands, forming a distorted tetrahedron in the PbS_4 core. The Pb–S bond lengths are not equivalent and range between 2.6614(7) and 2.8779(8) A. In the constrained PbS_4 core, the S1–Pb1–S2 bond angles

average to 64.68° while the remaining trans-intraligand S1–Pb1–S11 and S2–Pb1–S21 bond angles are 136.31°and 91.56°, respectively. The results are consistent with previous findings for various lead(II) complexes[29-31]. Both NCS_2 moieties have N–C bonds equal to 1.323(4) and are shorter than a typical N–C bond. The S–C bond lengths reveal no measurable variation with a mean of 1.724(3), signifying the existence of a partial double-bond nature. The crystal packing of the Pb(II) compound is balanced by inter C–H⋯S interactions, as presented in Figure 3.19.

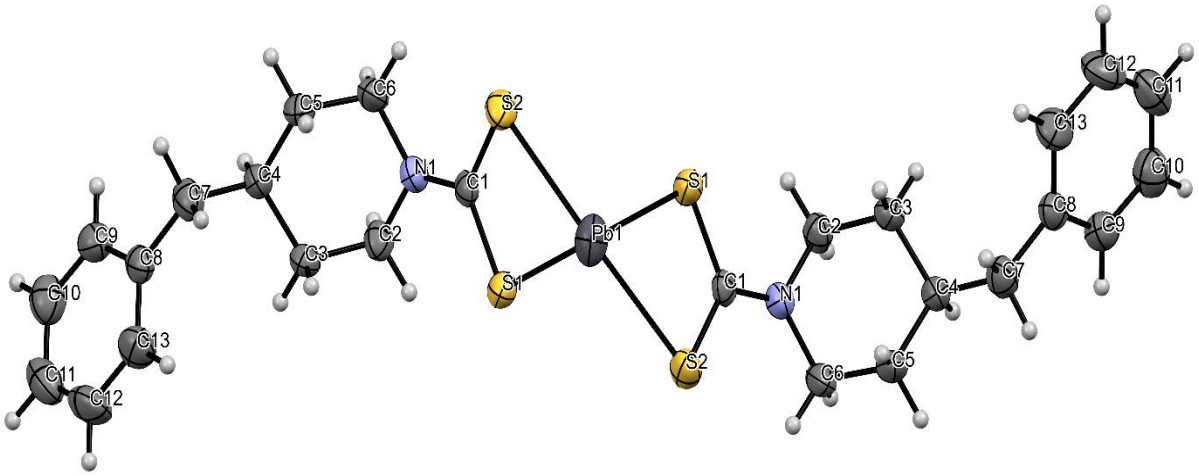

Figure 3.18: The molecular structure of bis(4-benzylpiperidine-1-carbothioato)-lead(II)

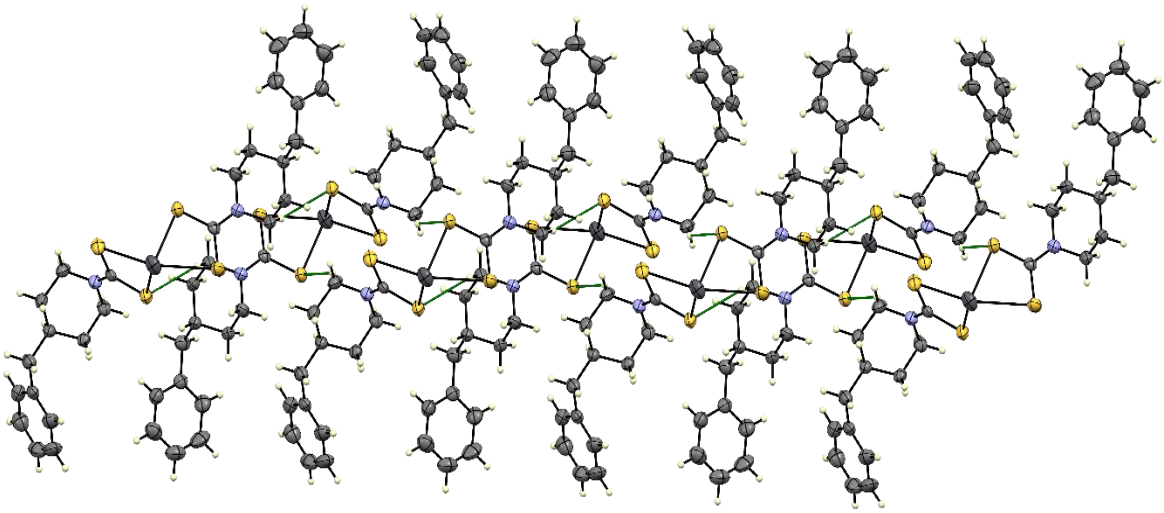

Figure 3.19: Intermolecular (green lines) C–H⋯S interactions of $[Pb(4\text{-}Bpip)_2]$

Table 3.3: Crystallographic data for bis(4-benzylpiperidine-1-carbothioato)-lead(II)

Compound	$[Pb(4\text{-}bpipdtc)_2]$
Formula	$C_{26}H_{32}N_2PbS_4$
$D_{calc.}$/ g cm^{-3}	1.724
μ/mm^{-1}	15.012
Formula Weight	707.96
Size/mm^3	0.335 x 0.270 x 0.120
T/K	102(2)
Crystal System	Monoclinic
Space Group	C2/n
a/Å	25.5177(17)
b/Å	9.1660(5)
c/Å	12.0217(7)
α/°	90
β/°	104.015(4)

γ/°	90
V/Å^3	2728.1(3)
Z	4
Θ_{min}/°	0.335
Θ_{max}/°	72.234
Measured Refl.	26753
Independent Refl.	2679
Reflections Used	123
R_{int}	0.0461
Parameters	150
Largest Peak	0.399
Deepest Hole	-1.393
GooF	1.138
wR_2 (all data)	0.0563
wR_2	0.561
R_1 (all data)	0.0229
R_1	0.0227

Table 3.4: Bond lengths and angles for bis(4-benzylpiperidine-1-carbothioato)-lead(II)

Bond Lengths		**Bond Angles**	
Bond	**Length(Å)**	**Bonds**	**Angle(°)**
Pb1–S1	2.6614(7)	S1–Pb1–S11	91.56(3)
Pb1–S11	2.6614(7)	S1–Pb1–S21	84.75(2)
Pb1–S21	2.8778(8)	S11–Pb1–S21	64.68(2)
Pb1–S2	2.8779(8)	S1–Pb1–S2	64.68(2)
S2–C1	1.710(3)	S11–Pb1–S2	84.76(2)
S1–C1	1.738(3)	S21–Pb1–S2	136.31(3)
N1–C1	1.323(4)	C1–S1–Pb1	91.46(9)

C1–S2–Pb1	84.94(9)	

References

1. Hogarth, G., Transition metal dithiocarbamates: 1978–2003. In *Prog. Inorg. Chem.*, Karlin, K. D., Ed. 2005; pp 71-561.

2. Tercero, N.; Nagaraj, D.; Farinato, R., A Critical Overview of Dithiophosphinate and Dithiophosphate Interactions with Base Metal Sulfides and Precious Metals. *Mining Metall. Explor.* **2019,** *36*, 1-12.

3. Nicholls, M.; Do, T.; Norton, P.; Kasrai, M.; Bancroft, G., Review of the lubrication of metallic surfaces by zinc dialkyl-dithiophosphates. *Tribol. Int.* **2005,** *38*, 15-39.

4. Castro, R. A.; Oliveira, M. R. L.; Janczak, J.; Rubinger, M. M. M., Syntheses and characterization of novel heteroleptic nickel complexes with dithiocarbimates and trithiocarbimates. *Inorg. Chim. Acta* **2017,** *462*, 195-203.

5. Al-Shakban, M.; Matthews, P. D.; Deogratias, G.; McNaughter, P. D.; Raftery, J.; Vitorica-Yrezabal, I.; Mubofu, E. B.; O'Brien, P., Novel xanthate complexes for the size-controlled synthesis of copper sulfide nanorods. *Inorg. Chem.* **2017,** *56* (15), 9247-9254.

6. Adeyemi, J. O.; Onwudiwe, D. C., Chemistry and some biological potential of bismuth and antimony dithiocarbamate complexes. *Molecules* **2020,** *25* (2).

7. Alam M. N. and Debnath, S. C., Effect of zinc dithiocarbamates and thiazole-based accelerators on the vulcanization of natural rubber. *Rubber Chem. Technol.* **2012,** *85* (1), 120-131.

8. Rafin, C.; Veignie, E.; Sancholle, M.; Postel, D.; Len, C.; Villa, P.; Ronco, G., Synthesis and Antifungal Activity of Novel Bisdithiocarbamate Derivatives of Carbohydrates against Fusarium oxysporum f. sp. lini. *J. Agric. Food. Chem.* **2000,** *48* (11), 5283-5287.

9. Islam, S. I.; Das, S. B.; Chakrabarty, S.; Hazra, S.; Pandey, A.; Patra, A., Synthesis, Characterization, and Biological Activity of Nickel (II) and Palladium (II) Complex with Pyrrolidine Dithiocarbamate (PDTC). *Adv. Chem.* **2016,** *2016*, 4676524.

10. Tiwari, S.; Reddy, K.; Bajpai, A.; Khare, K.; Nagaraju, V., Synthesis and Characterization of Bisdithiocarbamates from Weak Nitrogen Bases and Its Metal Complexes. *Int. Res. J. Pure Appl. Chem.* **2015,** *7*, 78-91.

11. Hogarth, G., ChemInform Abstract: Metal-dithiocarbamate complexes: chemistry and biological activity. *Mini Rev. Med. Chem.* **2013,** *12*, 1202-15.

12. Adeyemi, J. O.; Onwudiwe, D. C., Organotin(IV) dithiocarbamate complexes: Chemistry and biological activity. *Molecules* **2018,** *23* (10).

13. Adeyemi, J. O.; Onwudiwe, D. C., PbS nanoparticles prepared Using 1, 10-phenanthroline adduct of lead(II) bis(N-alkyl-N-phenyl dithiocarbamate) as single source precursors. *Molecules* **2020,** *25* (9).

14. Lewis, E. A.; McNaughter, P. D.; Yin, Z.; Chen, Y.; Brent, J. R.; Saah, S. A.; Raftery, J.; Awudza, J. A. M.; Malik, M. A.; O'Brien, P.; Haigh, S. J., In Situ Synthesis of PbS Nanocrystals in Polymer Thin Films from Lead(II) Xanthate and Dithiocarbamate Complexes: Evidence for Size and Morphology Control. *Chem. Mater.* **2015,** *27* (6), 2127-2136.

15. Solomane, N.; Ajibade, P. A., Synthesis and crystal structure of bis(thiomorpholinyldithiocarbamato)Cu(II) complex and its use as precursor for CuS nanoparticles photocatalyst for the degradation of organic dyes. *J. Sulfur Chem.* **2021,** *42* (2), 167-179.

16. Nyamen, L. D.; Rajasekhar Pullabhotla, V. S. R.; Nejo, A. A.; Ndifon, P. T.; Warner, J. H.; Revaprasadu, N., Synthesis of anisotropic PbS nanoparticles using heterocyclic dithiocarbamate complexes. *Dalton Trans.* **2012,** *41* (27), 8297-8302.

17. Sarker, J. C.; Hogarth, G., Dithiocarbamate complexes as single source precursors to nanoscale binary, ternary and quaternary metal sulfides. *Chem. Rev.* **2021,** *121* (10), 6057-6123.

18. Mphahlele, L. L. R.; Ajibade, P. A., Synthesis and crystal structure of bis(morpholino dithiocarbamato) Cd(II) complex and its use as precursor for CdS quantum dots using different capping agents. *J. Sulfur Chem.* **2019,** *40* (6), 648-663.

19. Ajibade, P. A.; Solomane, N., Synthesis and crystal structure of bis(thiomorpholinyldithiocarbamato) Zn(II): structural, optical, and photocatalytic studies of ZnS nanoparticles from the complex. *J. Coord. Chem.* **2020,** *73* (8), 1292-1305.

20. Paca, A. M.; Ajibade, P. A.; Andrew, F. P.; Nundkumar, N.; Singh, M., Synthesis, X-ray crystal structures and anticancer studies of four Pd(II) dithiocarbamate complexes. *Arab. J. Chem.* **2021,** *14* (9), 103326.

21. Odularu, A. T.; Ajibade, P. A., Dithiocarbamates: Challenges, control, and approaches to excellent yield, characterization, and their biological applications. *Bioinorg. Chem. Appl.* **2019,** *2019*, 8260496.

22. Oluwalana, A. E.; Ajibade, P. A., Effect of temperature and capping agents on structural and optical properties of tin sulphide nanocrystals. *J. Nanotechnol.* **2019,** *2019*, 8235816.

23. Paca, A. M.; Ajibade, P. A., Effect of temperature on structural and optical properties of iron sulfide nanocrystals prepared from tris(N-methylbenzyldithiocarbamato) iron(III) complex. *Inorg. Nano-Met. Chem.* **2020**, 1-10.

24. Onwudiwe, D. C.; Ajibade, P. A., Synthesis, characterization and thermal studies of Zn(II), Cd(II) and Hg(II) complexes of N-methyl-N-phenyl dithiocarbamate: the single crystal structure of $[(C_6H_5)(CH_3)NCS_2]_4Hg_2$. *Int J Mol Sci* **2011,** *12* (3), 1964-1978.

25. Wu, X.-S.; Tang, Y.-R.; Liu, J.-L.; Wang, L.; Ren, X.-M., Comprehensively understanding the steric hindrance effect on the coordination sphere of Pb^{2+} ions and photophysical nature of two luminescent Pb(II)-coordination polymers. *Dalton Trans.* **2019,** *48* (36), 13841-13849.

26. Claudio, E. S.; Goldwin, H.; Magyar, J. S., Fundamental coordination chemistry, environmental chemistry, and biochemistry of lead (II). *Prog. Inorg. Chem.* **2003,** *51*, 1-144.

27. Mlowe, S.; Shombe, G. B.; Akerman, M. P.; Mubofu, E. B.; O'Brien, P.; Mashazi, P.; Nyokong, T.; Revaprasadu, N., Morphological influence of deposition routes on lead sulfide thin films. *Inorg. Chim. Acta* **2019,** *498*, 119116.

28. Iwasaki, H.; Hagihara, H., The crystal structure of lead(II) diethyldithiocarbamate. *Acta Crystallogr. B* **1972,** *28* (2), 507-513.

29. Ito, M.; Iwasaki, H., Structure of lead(II) N,N-diisopropyldithiocarbamate [bis(N,N-diisopropyldithiocarbamato)lead(II)]. *Acta Crystallogr. B* **1980,** *36* (2), 443-444.

30. Akhtar, J.; Malik, M. A.; O'Brien, P.; Helliwell, M., Controlled synthesis of PbS nanoparticles and the deposition of thin films by Aerosol-Assisted Chemical Vapour Deposition (AACVD). *J. Mater. Chem.* **2010,** *20* (29), 6116-6124.

31. Afzaal, M.; Ellwood, K.; Pickett, N. L.; O'Brien, P.; Raftery, J.; Waters, J., Growth of lead chalcogenide thin films using single-source precursors. *J. Mater. Chem.* **2004,** *14* (8), 1310-1315.

CHAPTER FOUR

SYNTHESIS AND CHARACTERIZATION OF METAL SULFIDE NANOPARTICLES

4.1 Introduction

Nano sized semiconductors have been explored among several classes of materials due to their new features and possible application. With the decrease of dimension to the nanoscale range, physical and chemical attributes of materials diverge from the bulk[1-3]. The remarkable change in characteristics of nanomaterials compared to the bulk is caused by two factors: a large surface area to volume ratio, which favours surface and interface effects over volume effects, and an alteration in electronic properties, which results in an increase in energy bandgap[4]. A great deal of work has gone into controlling the size, shape, and crystallinity of these materials in order to tailor their properties. The use of organometallic compounds for controlled synthesis of semiconductor nanoparticles was introduced by Murray and colleagues[5], however the harmful nature of the starting materials necessitates the development of simpler and better synthetic approaches. As a result, a single source precursor approach for the fabrication of semiconductor nanoparticles was developed. This approach eliminates the usage of volatile and toxic chemicals at elevated temperatures, resulting in nanomaterials with a uniform metal ion distribution at the molecular level[6, 7]. The goal of nanochemistry is to develop a low-cost, easy-to-manage, safe, and high-yielding pathway to nanoparticle fabrication. Metal dithiocarbamate compounds are well-known single-source precursors for metal sulfide nanoparticles synthesis[8, 9]. Amount of precursor, temperature[10], and capping agents[9] all have a significant impact on the structural properties of the resulting nanoparticles. This chapter presents the use of Pb(II) and Sn(II) dithiocarbamate

complexes as single-source precursor for the synthesis of PbS and SnS nanoparticles, the study of the effect of precursor and capping agents on the morphology and optical properties of the as-prepared nanoparticles and the characterization of the PbS and SnS nanoparticles by powder X-ray diffraction (p-XRD), high-resolution transmission electron microscopy (HRTEM), scanning electron microscopy (SEM), UV-Visible spectroscopy, photoluminescence (PL) and fourier-transform infrared spectroscopy (FTIR).

4.2 Materials

4.2.1 Chemicals

Oleic acid, hexadecylamine, tri-n-octylphosphine, octadecylamine, trioctylphosphine oxide, methanol were purchased from Sigma Aldrich and used without purification. The precursors bis(morpholinyldithiocarbamato)Pb(II), bis(thiomorpholinyldithiocarbamato)Pb(II), bis(N-(2-hydroxyethyl)phenyldithiocarbamato)Pb(II), bis(4-methylpiperidinedithiocarbamato)Pb(II) and bis(4-benzylpiperidinedithiocarbamato)Pb(II) were prepared and characterized as reported in Chapters Two and Three.

4.2.2 Characterization techniques

4.2.2.1 UV-Vis spectroscopy

A Perkin Elmer Lamda 25 spectrophotometer was used to measure the absorption spectra of the nanoparticles in the region of 200-700 nm. The samples were loaded in 1-centimeter quartz cuvettes. The nanoparticles were dispersed in hexane for analysis.

4.2.2.2 Photoluminescence Spectroscopy

The analysis was done on the florescence L45 Perkin Elmer equipped with Win lab software. The samples were loaded in a 10 mm path length cuvette. The nanoparticles were dispersed in hexane for analysis. The analysis was carried out at ambient condition at an excitation wavelength of 350 nm.

4.2.2.3 Powder X-ray diffraction

Powder X-ray diffraction method is used to determine the purity and crystallinity of a substance. It is a straightforward approach based on the constructive interference of X-rays and material. Powder X-ray diffraction (p-XRD) was performed on a Bruker D8 Advance using monochromatic CuKα (λ = 1.5406) radiation in the 20°-80° range.

4.2.2.4 Transmission Electron Microscopy (TEM)

The morphology and size distribution of nanomaterials are determined using transmission electron microscopy (TEM). JEOL HRTEM-2100 was used to obtain images, lattice fringes, and selected area electron diffraction (SAED) patterns of the nanoparticles.

4.2.2.5 Scanning Electron Microscopy (SEM)

The scanning electron microscope (SEM) is a useful tool for evaluating the surface features of materials as well as revealing information about their chemical components. SEM micrographs and EDX spectra were obtained from Zeiss EVO LS 15 scanning electron microscope equipped with EDX INCA software.

4.2.2.6 FTIR spectroscopy

This is used to determine which functional groups are present in the compounds. Data was collected using an Agilent Cary 630 spectrometer with Agilent MicroLab PC 5.1.22. The data processing for peaks and smoothing was done using ResolutionPro 5.0.0.395. The data was collected using ATR Diamond-1 Bounce with 30 background scans and 30 sampling scans in the range 4000 – 650 cm^{-1} with a resolution of 4 cm^{-1}.

4.2.3 Synthesis of PbS nanoparticles

4.2.3.1 Synthesis of hexadecylamine capped PbS nanoparticles

PbS nanoparticles were prepared from bis(morpholinedithiocarbamato)Pb(II), bis(thiomorpholinedithiocarbamato)Pb(II) and bis(N-(2-hydroxyethyl)phenyldithiocarbamato)Pb(II) complexes by adopting a literature procedure[11]. Each respective lead(II) complex (0.3 g, 0.05 mmol) was dispersed in 5 mL oleic acid and injected into 3.0 g of hot HDA at 180°C and the temperature drop of about 15°C was observed. A constant temperature of 180°C was maintained for a period of 1 h under the flow of nitrogen while stirring. The mixture was cooled to room temperature and excess cold methanol was added to precipitate the nanoparticles and remove excess HDA. The precipitates were separated by centrifugation and washed with methanol and the resulting solid precipitates of HDA capped PbS nanoparticles were dried at room temperature.

4.2.3.2 Synthesis of hexadecylamine, octadecylamine and trioctylphosphine oxide capped PbS nanoparticles

0.25 g of each bis(4-methylpiperidinedithiocarbamato)Pb(II) and bis(4-benzylpiperidinedithiocarbamato)Pb(II) complex was dispersed in 1mL trioctylphosphine (TOP). The resulting solution was introduced into hot 4 g of octadecylamine (ODA) in a three-necked round bottom flask at 180°C under inert atmosphere. The mixture was allowed to stabilize at the desired temperature after a 12–18°C temperature drop, and then stirred for 1 h. The reaction was allowed to cool to 70°C before adding cold methanol. The flocculate was then centrifuged for 30 minutes at 3500 rpm, with the supernatant decanted and washed several times to remove excess ODA. To study the effects of capping agents, the same procedure was repeated using hexadecylamine (HDA), and trioctylphosphine oxide (TOPO).

4.2.3.3 Synthesis of dodecylamine capped SnS nanoparticles

Each of the five Sn(II) dithiocarbamate complexes (0.40 g) was dispersed in 2 mL of oleic acid and injected into 2 g of hot dodecylamine in a three necked round-bottom flask. A temperature drop of 8-13℃ was noted, thereafter the temperature was allowed to stabilize at 180℃ for 1 hour. The resulting mixture was cooled to about 70℃ and washed with methanol several times.

4.3 Results and discussion

4.3.1 Effect of precursor on structural and optical properties of PbS nanoparticles

4.3.1.1 Powder X-ray diffraction of PbS nanoparticles

Figure 4.1 showed the powder X-ray diffraction (XRD) patterns of as-prepared PbS NPs using three different precursors at 180 °C. The diffraction patterns shows sharp peaks, indicating that the particles are crystalline. The distinctive diffraction peaks correspond with the Bragg's reflections of the standard XRD lines of face-centered cubic rock-salt structure of PbS (JCPDS: 05-0592)[12]. The diffraction peaks at 2θ values 30.22°, 35.06°, 39.57°, 46.94°, 50.44°, 59.92°, 62.85°, 74.09° correspond to reflections from (111), (200), (220), (311), (222), (400), (420) and (422) diffraction planes. Furthermore, no peaks other than those related to PbS were found, indicating the PbS nanoparticles formed in pure crystalline phase. The estimated particle sizes were 27.99 nm for PbS**1** prepared from bis(morpholinedithiocarbamato)Pb(II), 24.51 nm for PbS**2** prepared from bis(thiomorpholinedithiocarbamato)Pb(II) and 31.74 nm for PbS**3** prepared from bis(N-(2-hydroxyethyl)phenyldithiocarbamato)Pb(II)

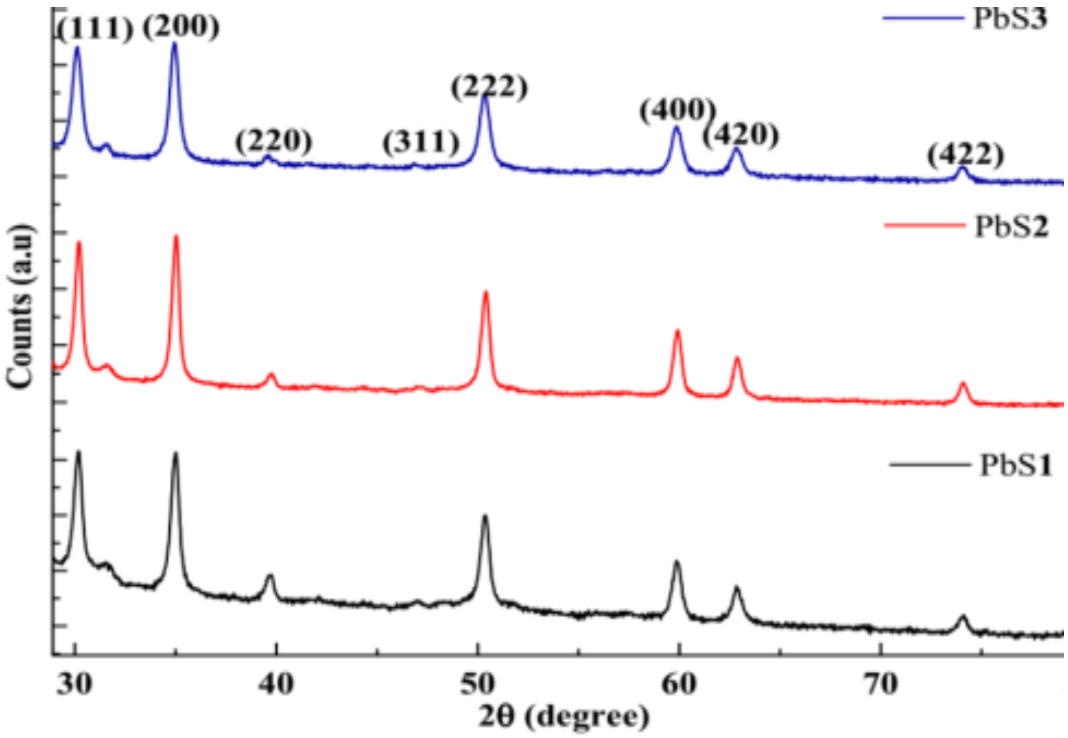

Figure 4.1: p-XRD patterns of HDA capped PbS**1**, PbS**2** and PbS**3** nanoparticles synthesized at 180°C.

4.3.1.2 High-resolution transmission electron Microscopy (HRTEM) studies of HDA capped PbS1, PbS2 and PbS3 nanoparticles

The size, *d*-spacing, and crystalline/amorphous nature of the PbS nanoparticles were investigated using HRTEM. Figure 4.2 shows high-resolution TEM (HRTEM) images, lattice fringes, and SAED of PbS**1**, PbS**2**, and PbS**3**. The nanoparticles were synthesized using different precursors while other reaction parameters were kept the same. The PbS nanoparticles are agglomerated, as per the HRTEM images. PbS**1**, PbS**2**, and PbS**3** nanoparticles all show semi-spherically shaped

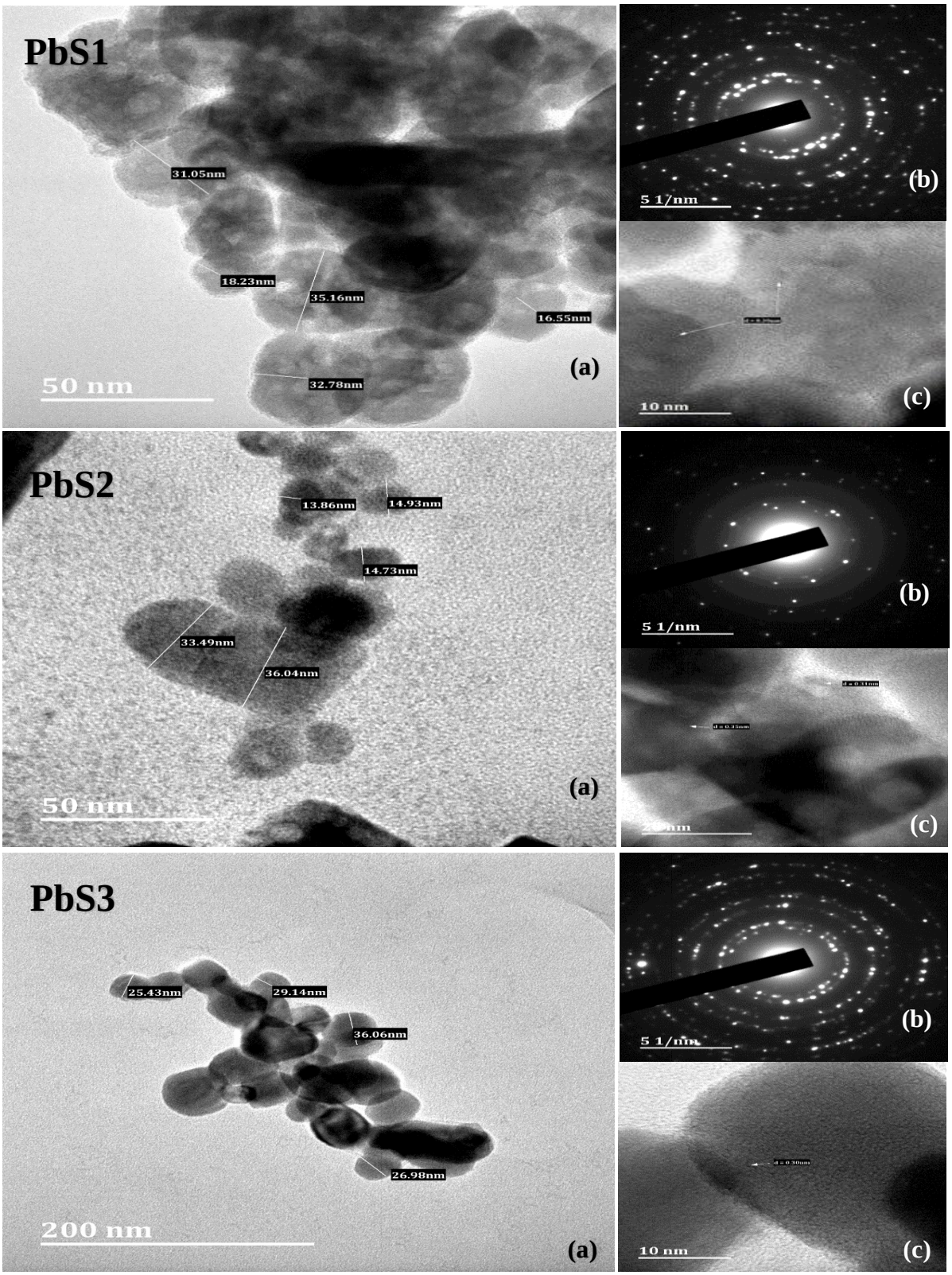

Figure 4.2: (a) HRTEM images, (b) lattice fringes and (c) SAED patterns of the PbS nanoparticles

nanoparticles and some rectangular shaped particles for PbS**2**. However, the nanoparticles come in different sizes with the diameter range of 16.55–35.16 nm for PbS**1**, 13.86–36.04 nm for PbS**2**, and 25.43–36.06 nm for PbS**3**. PbS**1** and PbS**3** lattice fringes have a distinct space between the planes of 0.30 nm, indicating the (200) reflection plane, while PbS**2** lattice fringes have two *d*-spacings of 0.35 and 0.31 nm, indicating the (111) and (200) planes, respectively. The concentric rings observed on the selected area electron diffraction pattern imply crystalline nature of the nanoparticles, as evidenced by the strong XRD diffraction peaks. The results show that the precursor used influences the size, shape, lattice fringes and degree of crystallinity of the as-prepared PbS nanoparticles produced.

4.3.1.3 Scanning electron microscopy studies of HDA capped PbS1, PbS2 and PbS3 nanoparticles

SEM micrographs of PbS nanoparticles (Fig. 4.3) revealed flaky, spherical, and rough surface morphology for PbS**1**, PbS**2**, and PbS**3**, respectively, indicating that precursors have an influence on morphological properties. The appearance of lead and sulfur in the EDX spectra confirms a successful synthesis of lead sulfide nanoparticles. The surfactant and capping agents used are the sources of the carbon and oxygen observed in the EDX spectra.

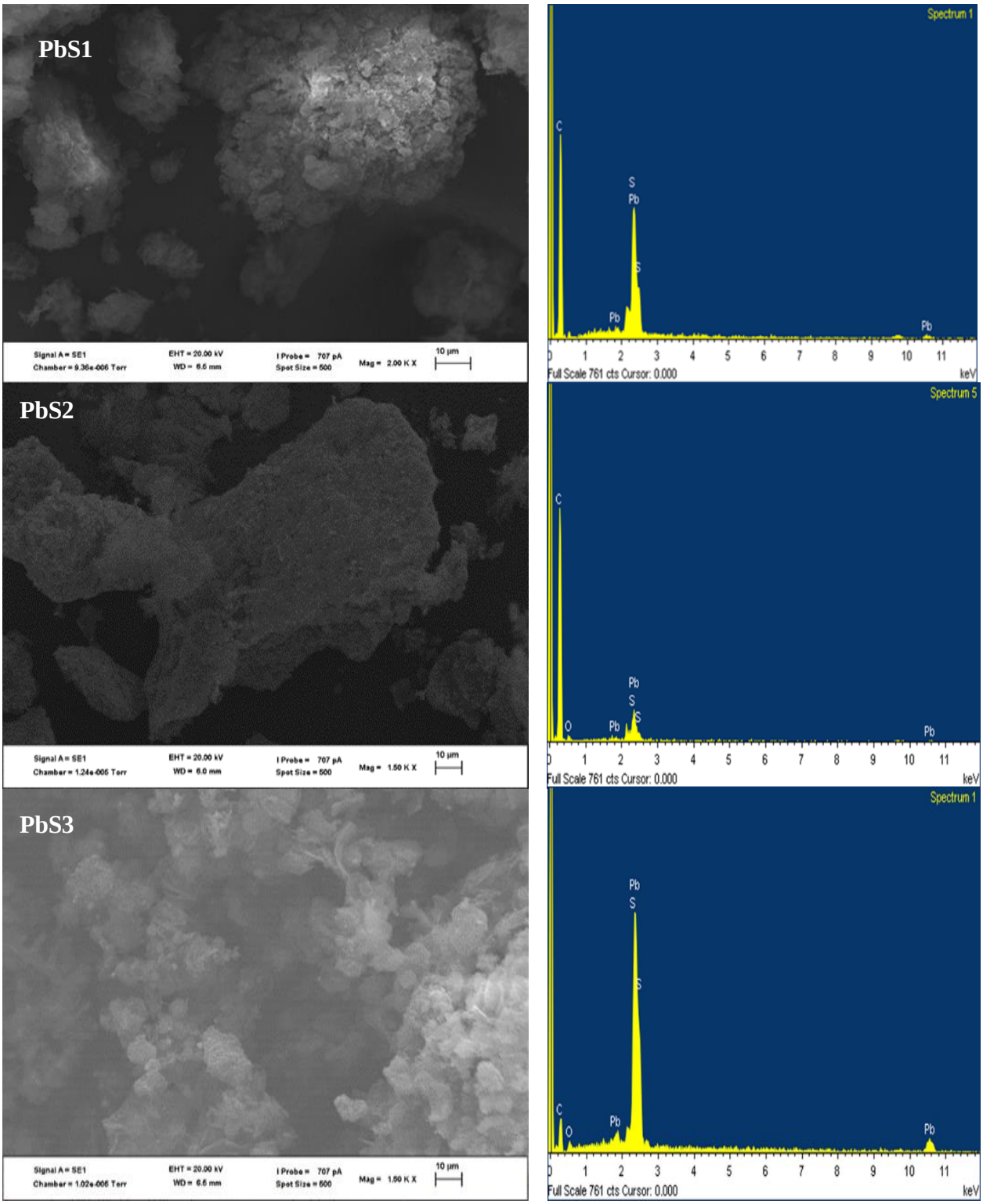

Figure 4.3: SEM images of PbS**1**, PbS**2** and PbS**3** nanoparticles

4.3.1.4 Fourier Transform Infrared Spectroscopy of HDA capped PbS1, PbS2 and PbS3 nanoparticles

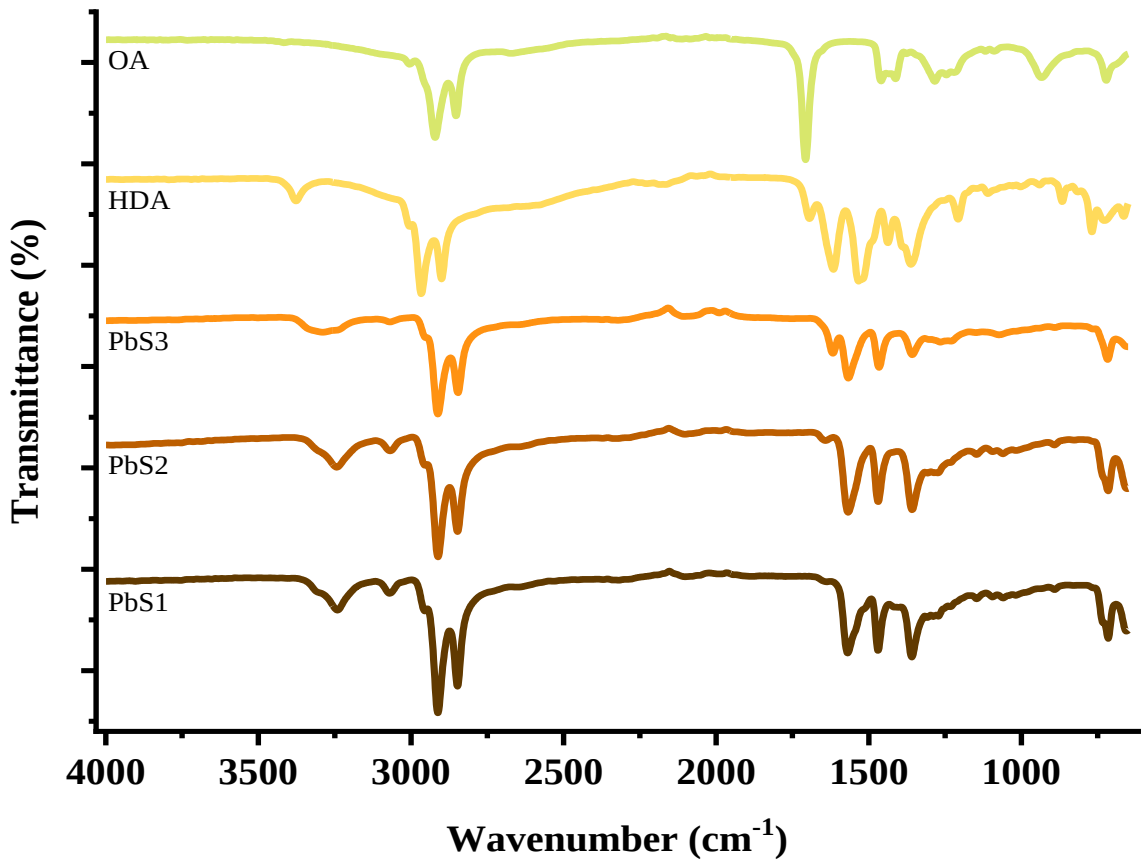

Figure 4.4: FTIR spectra of HDA capped PbS**1**, PbS**2** and PbS**3** nanoparticles

The HDA exhibits a peak at 3375 cm^{-1} that broadened and shifted to 3315 cm^{-1} in the spectra of the lead sulfide nanoparticles, and this peak is attributable to v(N-H) from the hexadecylamine (HDA). This distinct peak is the primary functional group of HDA, showing that the nanoparticles successfully interacted with HDA[13]. The FTIR spectra of the PbS nanoparticles exhibited strong peaks at 2843 and 2907 cm^{-1} for PbS**1**, 2851 and 2918 cm^{-1} for PbS**2** and 2843 and 2907 cm^{-1} for PbS**3** which are attributed to asymmetric CH_2 and CH_3 of the hexadecylamine capping agent[14].

The band at 1710 cm^{-1}, assigned to v(C=O) from the carboxylic group of oleic acid (OA), is absent in the spectra of the PbS nanoparticles indicating that OA is not present on the nanoparticles' surface as a capping agent.

4.3.1.5 Optical properties of HDA capped PbS nanoparticles

The absorption spectra of PbS nanoparticles prepared from three different precursors, emission spectra, and their Tauc plots, are shown in Figure 4.5. The UV-Vis spectra of lead sulfide nanoparticles exhibited sharp absorption bands at 285 nm for PbS**1**, 284 nm for PbS**2** and 286 for PbS**3**. The energy bandgap (eV) was calculated directly from the absorption spectra band edges using Tauc's equation[15]. Extrapolation of $(\alpha hv)^2$ versus (hv) provided the band gap of the as-prepared PbS nanoparticles, where α and hv denote the absorption coefficient and incident beam frequency, respectively. The estimated band gap energies from Tauc plots for PbS**1**, PbS**2**, and PbS**3** are 2.48 eV, 3.06 eV, and 2.25 eV, respectively. The calculated band gap energy values are higher than the 0.41 eV band gap of bulk PbS. The decrease in the crystallite size, which is attributed to quantum confinement, may be responsible for the increase in the energy bandgap of the as-prepared PbS nanoparticles. The photoluminescence of the PbS nanoparticles exhibit broad emission peaks at 378 nm, which may be due to aggregation and electronic passivation of the nanoparticles.

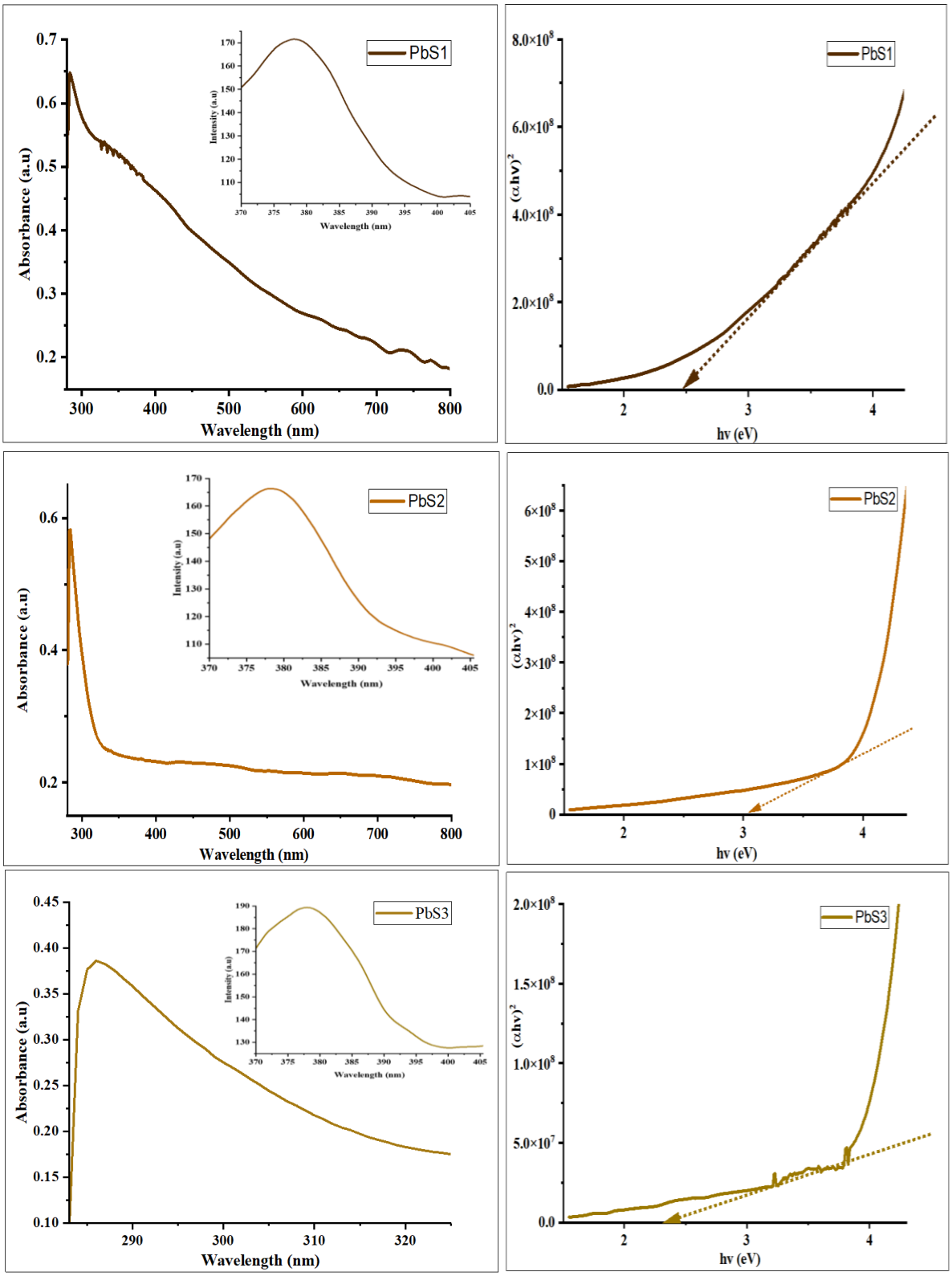

Figure 4.5**:** UV-Vis, emission spectra and Tauc plot of PbS nanoparticles

4.3.2 Effect of capping agents on structural and optical properties of PbS nanoparticles

4.3.2.1 Powder X-ray diffraction of PbS4 and PbS5 nanoparticles

Powder X-ray diffraction was used to study the structural properties of the as-prepared PbS nanoparticles. The diffraction patterns of HDA, ODA, and TOPO capped PbS nanoparticles are shown in Figure 4.6. The JCPDS file No. 5–0592 was used to identify the peaks[16], which confirmed cubic crystalline phase of PbS. The diffraction patterns of PbS**4** and PbS**5** nanoparticles are similar except that PbS**4** does not contain (311) plane. The diffractograms of HDA-capped PbS nanoparticles exhibited significant peaks at 2θ values of 30.29°, 35.10°, 50.49°, 60.01°, 62.98°, and 74.19°, which correspond to lattice planes (111), (200), (220), (311), (222), (400), (420) and (422) respectively. The sharp peaks indicate the crystalline nature of the PbS nanoparticles. ODA-capped PbS XRD patterns also revealed distinct peaks at 30.30°, 35.12°, 50.48°, 60.59°, 62.96° and 74.14° which can be indexed to (111), (200), (220), (311), (222), (400), (420) and (422) planes of PbS with JCPDS card No. 05-0592[17]. Except for the absence of a (220) plane in ODA-PbS**1**, the patterns are comparable. This could be due to slight difference in the PbS nanoparticles morphology. p-XRD patterns of TOPO-capped nanoparticles were also indexed to the (111), (200), (220), (311), (222), (400), (420) and (422) lattice planes. The peaks of TOPO-capped PbS nanoparticles are broader compared to those of HDA and ODA-capped PbS nanoparticles.

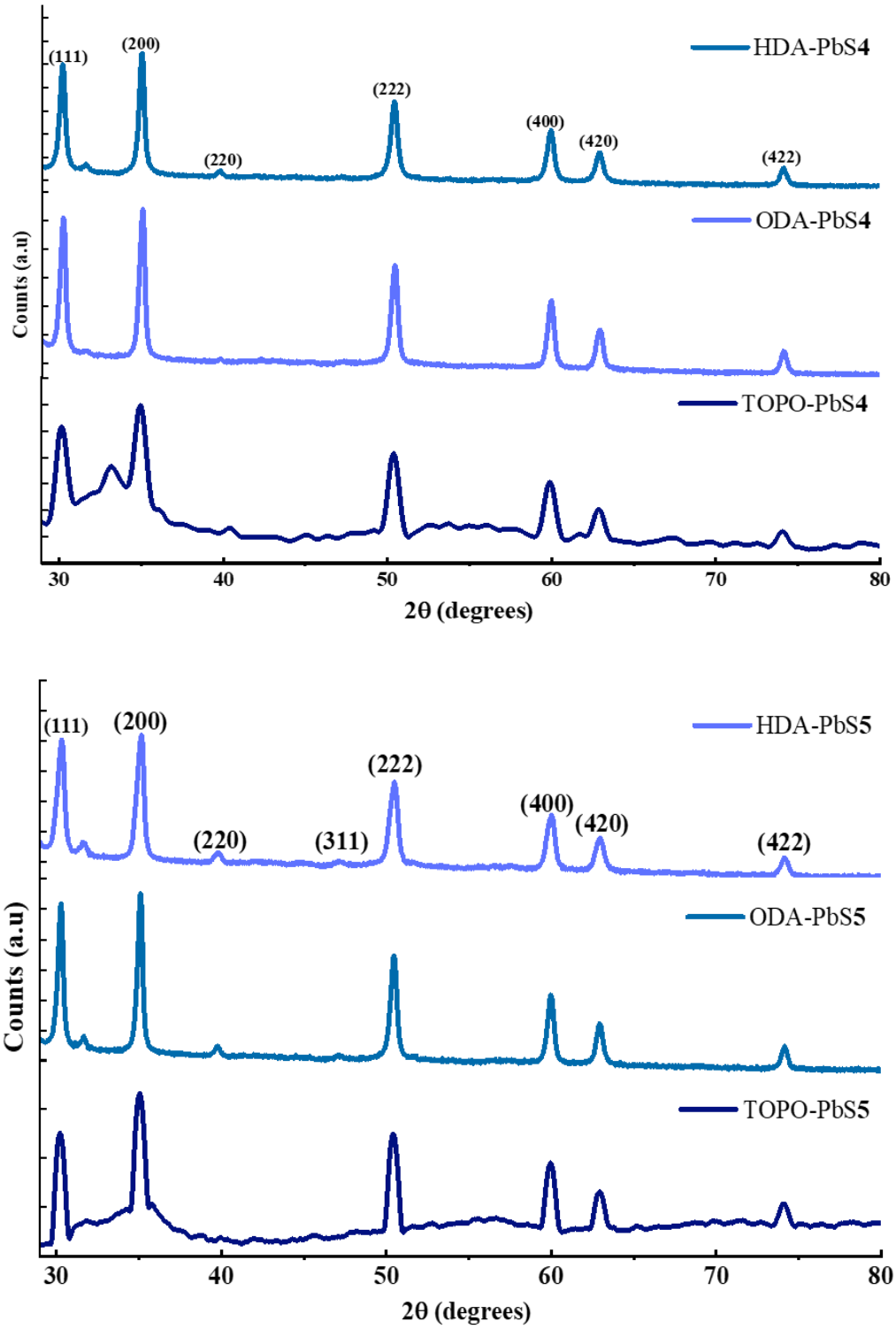

Figure 4.6: XRD diffraction patterns of PbS**4** and PbS**5** nanoparticles prepared from different precursors and capped with HDA, ODA and TOPO.

4.3.2.2 High-resolution transmission electron microscopy (HRTEM) studies of HDA, ODA and TOPO capped PbS4 and PbS5 nanoparticles

Figure 4.7 shows HRTEM images of PbS**4** and PbS**5** nanoparticles prepared from bis(4-methylpiperidine-1-carbodithioato)Pb(II) and bis(4-benzylpiperidine-1-carbodithioato)Pb(II), respectively. The HRTEM images of HDA capped PbS**4** and PbS**5** nanoparticles shows agglomerated cubic shaped particles with an average particle size of 58.88 nm for PbS**4** and 66.52 nm for PbS**5**. The difference in the average particle sizes may be due to the different precursors used. The sizes of HDA capped PbS nanoparticles obtained in this study are larger compared to other HDA capped PbS nanoparticles in literature[11, 18-20] but similar in shape. ODA capped PbS**4** and PbS**5** nanoparticles also show cubic shaped nanoparticles with some degree of agglomeration and the mean particle size of PbS**4** is 47.29 nm and 67.51 nm for PbS**5**. The average size range and agglomerated cubic shaped ODA capped PbS nanoparticles obtained in this study are comparable to that of PbS nanoparticles prepared from (N-phenyl piperazine dithiocarbamate) lead(II)[21]. The HRTEM images of TOPO capped PbS**4** and PbS**5** nanoparticles show densely packed agglomerates with some small spherical nanoparticles. The agglomeration observed could be due to the increased steric hindrance of TOPO resulting in a low capping density for the particles[18, 22]. The average particle sizes of TOPO-PbS**4** and TOPO-PbS**5** are 61.32 nm and 58.21 nm, respectively. The SAED patterns also show that the nanoparticles are crystalline which is in agreement with the XRD patterns.

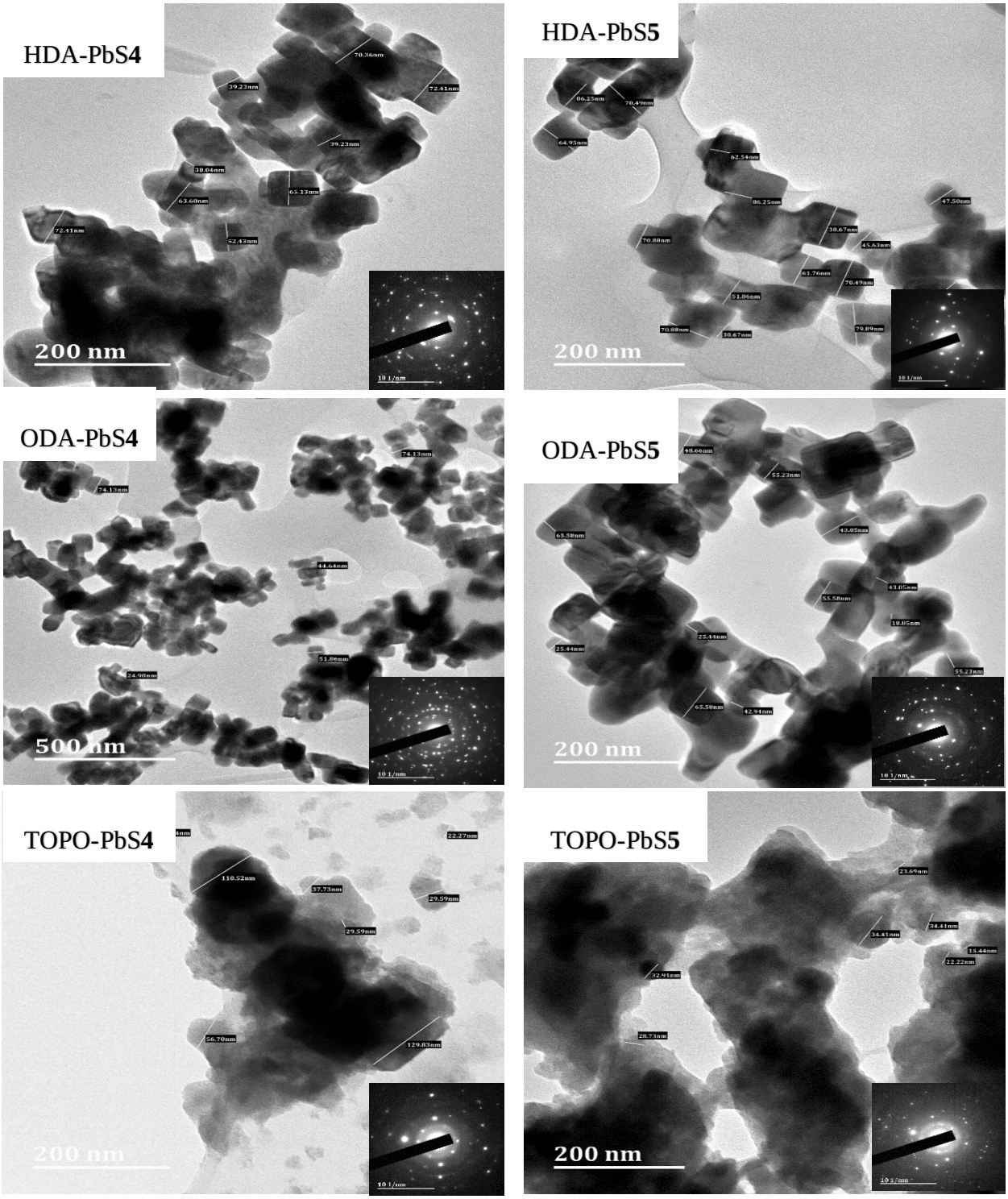

Figure 4.7: HRTEM images and SAED patterns of HDA, ODA and TOPO capped PbS**4** and PbS**5** nanoparticles

4.3.2.3 Scanning electron microscopy studies of HDA, ODA and TOPO capped PbS4 and PbS5 nanoparticles

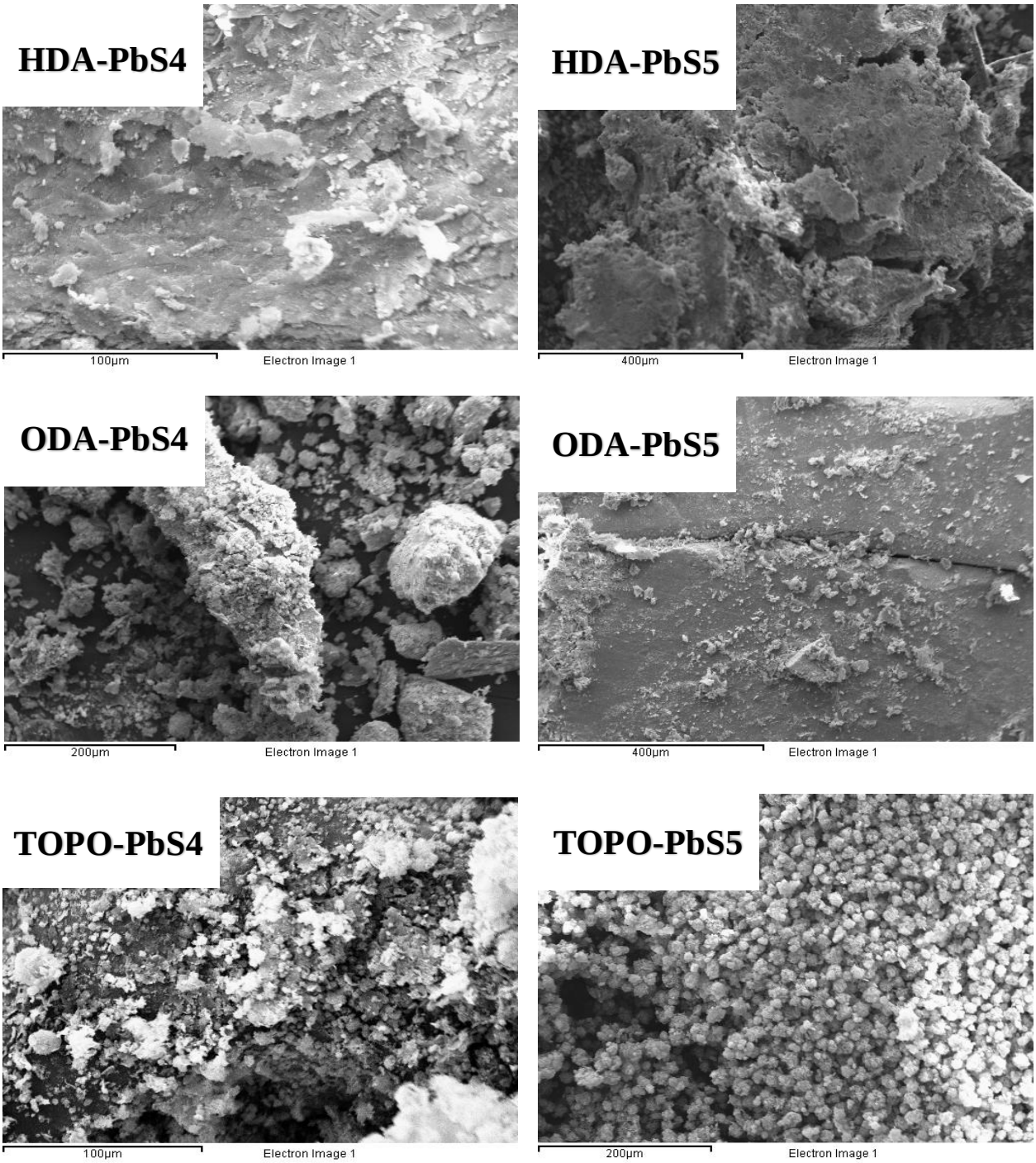

Figure 4.8: SEM images of HDA, ODA and TOPO capped PbS**4** and PbS**5** nanoparticles

The surface of the nanoparticles was studied using scanning electron microscopy (SEM) and the elemental composition of the PbS nanoparticles were confirmed with energy dispersive X-ray (EDX). HDA capped nanoparticles show irregular densely packed agglomerates with smooth surfaces. ODA-PbS**4** shows scattered particles with rough surface morphology while ODA-PbS**5** exhibits a solid smooth surface. TOPO-PbS**4** shows a flaky surface whereas TOPO-PbS**5** exhibit small closely packed spherical surface morphology. The EDX patterns show lead and sulfur confirming the formation of PbS nanoparticles. The additional peaks of carbon and gold observed in the EDX spectra are due to the coating used for the analysis.

4.3.2.4 Fourier transform infrared spectroscopy of HDA, ODA and TOPO capped PbS4 and PbS5 nanoparticles

The Infrared spectra were measured in the range of 4000 to 500 cm^{-1}. The stretching vibrations of TOPO-capped PbS were compared to the peaks of a clean TOPO spectrum. The peaks at 2915 and 2847 cm^{-1} are assigned to the asymmetric and symmetric stretching vibrations of CH_2 of TOPO. With the exception of the P=O stretch, the spectra of PbS nanoparticles aligned with all of the TOPO peaks in frequency. The stretching vibrational band of P=O observed at 1145 cm^{-1} in clean TOPO[23],shifted from 1145 cm^{-1} to 965 cm^{-1} in the spectra of PbS nanoparticles. The chemical interactions of TOPO molecules with PbS nanoparticles occurred through the O atom of the P=O group is responsible for the observed shift of this peak. The P=O frequency shifts to a lower energy after interactions with the PbS nanoparticles, signifying an electron density transition from P to O, effectively reducing the frequency of the P=O stretching mode, as a result, a lower absorption frequency and red shift is observed[24]. The asymmetric CH_3 and CH_2 vibrations observed at 2916 cm^{-1} and 2849 cm^{-1} in HDA-capped PbS nanoparticles spectra are attributed to HDA's alkyl chain.

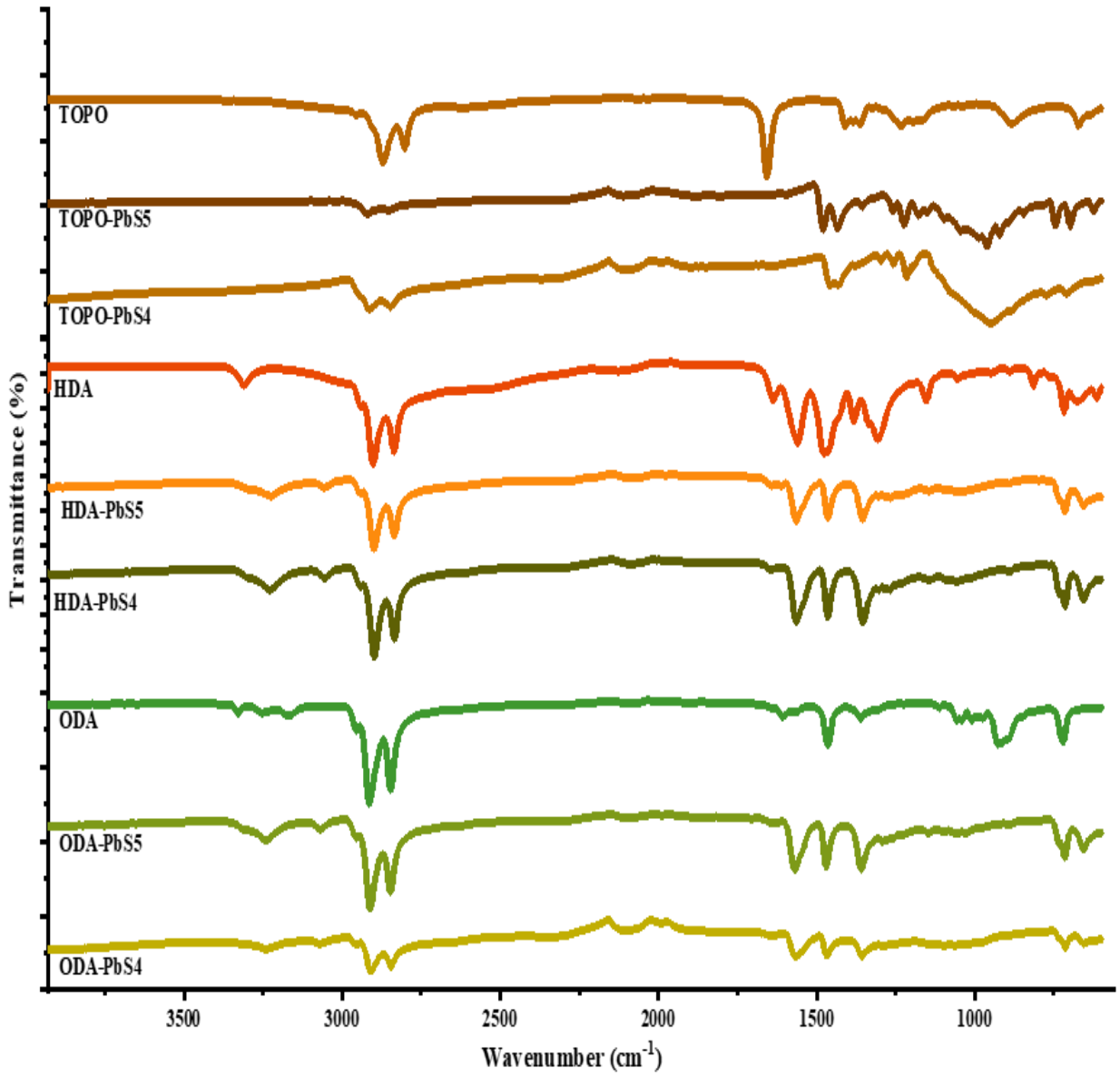

Figure 4.9: FTIR spectra of HDA, ODA, and TOPO capped as-prepared PbS**4** and PbS**5** nanoparticles.

The HDA characteristic peaks of N–H stretching vibrations at 3243 cm^{-1} and bending vibrations at 1630 cm^{-1} indicate that PbS nanoparticles are capped through $–NH_2$ group interactions[19].

Furthermore, the absence of C–P stretching vibrations at 1170, 1010, and 1037 cm^{-1} confirms that the PbS nanoparticles are free of TOP.[25] ODA capped PbS nanoparticles and pure ODA spectra were also compared. The spectra differ just slightly, implying that the PbS nanoparticles interact with the capping agent. v(N–H) stretching vibrations are responsible for the three absorption bands[26] present in the spectra of ODA at 3326, 3248, and 3166 cm^{-1}. The varied intensities of stretching vibrations in the PbS nanoparticles spectra show that nanoparticles prepared from different compounds interact with the capping agent in distinct ways.

4.3.2.5 Optical properties of HDA, ODA and TOPO capped PbS4 and PbS5 nanoparticles

The absorption spectra of the lead sulfide nanoparticles and their Tauc plots are presented in Figure 4.10. The UV-Vis spectra shows absorption bands at 261 nm for both HDA-PbS**4** and HDA-PbS**5**. Sharp absorption maxima were observed at 259 nm for ODA-PbS**4** and 261 nm for ODA-PbS**5**. The absorption spectra of TOPO capped PbS nanoparticles shows absorption band edges at 276 and 259 nm for PbS**4** and PbS**5**, respectively. The intensity of absorption maxima was higher for PbS**4** nanoparticles than that of PbS**5** nanoparticles for all capping agents. The energy band gaps of the PbS nanoparticles was calculated using Tauc's formula[27]. HDA capped PbS nanoparticles have the same absorption maxima but different band gap energies of 3.57 eV for PbS**4** and 3.98 eV for PbS**5**. ODA-PbS**5** has a band gap energy of 4.37 eV, whereas ODA-PbS**4** has a higher bandgap of 4.50 eV despite having absorption band at a lower wavelength than ODA-PbS**5**. The same is observed for TOPO capped PbS nanoparticles with PbS**5** having higher band gap energy of 3.50 eV and a lower band gap energy of 3.43 eV for PbS**4**. The band gap energies indicate a significant blue shift relative to bulk PbS (0.41 eV) as a result of quantum size effect[28].

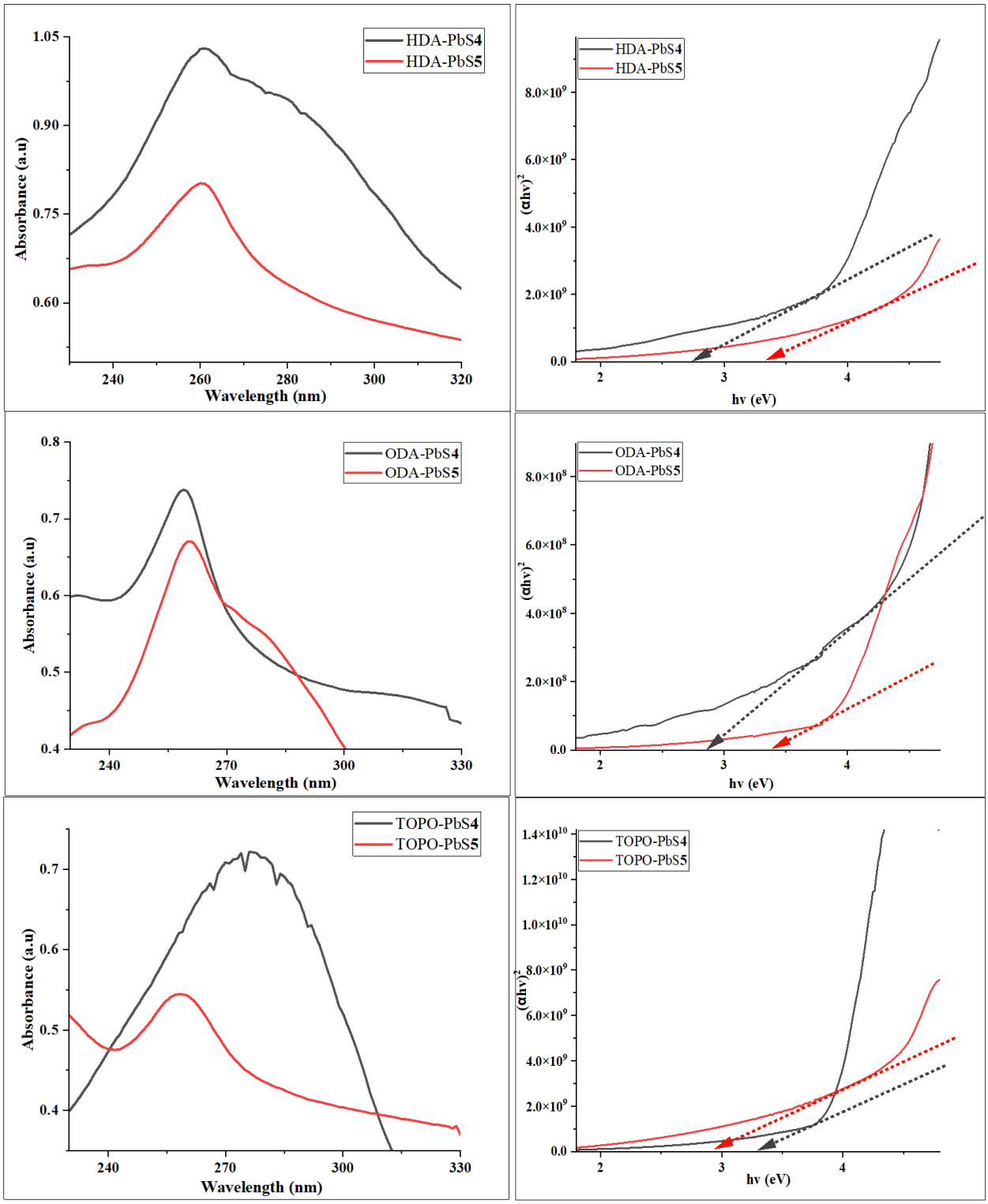

Figure 4.10: UV-Vis spectra and Tauc plots of HDA, ODA and TOPO capped PbS**4** and PbS**5** nanoparticles

The emission spectra of PbS nanoparticles were recorded at excitation wavelength of 300 nm. The PL spectra in Figure 4.11 showed broad emission peaks with varying intensities at 516 nm for all PbS nanoparticles. This emission could be due to the recombination of electron-hole pair[18]. The PbS nanoparticles emission is blue shifted relative to bulk PbS.

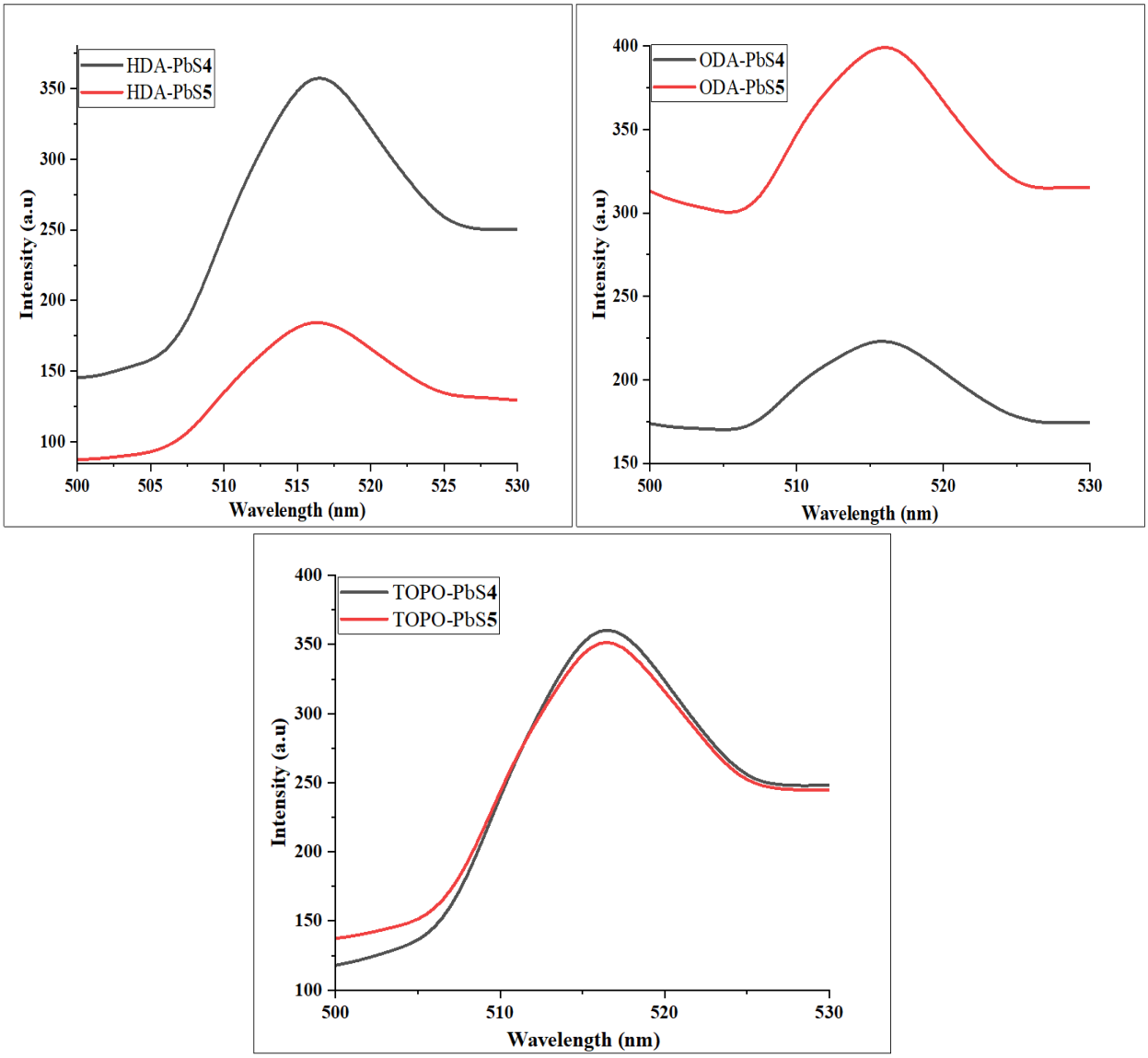

Figure 4.11: Emission spectra of HDA, ODA and TOPO capped PbS**4** and PbS**5** nanoparticles

4.3.3 Effect of precursor on morphological and optical properties of SnS nanoparticles

4.3.3.1 Powder x-ray diffraction of SnS nanoparticles prepared from different precursors

Powder X-ray diffraction patterns of the as-synthesized SnS nanoparticles are presented in Figure 4.12. The peaks were indexed to the Herzenbergite orthorhombic structure of SnS (JCPDS: 39-0354)[29, 30] for all samples. The X-ray diffraction patterns for SnS**1** showed eight broad peaks at 2θ values of 21.07°, 30.94°, 33.03°, 39.57°, 44.08°, 49.16°, 60.60° and 68.76°. These correspond to (110), (111), (040), (131), (141), (211), (250) and (080). The broad diffraction peaks indicate smaller particle sizes. In the diffraction pattern of SnS**2**, a broad prominent peak is observed at 2θ = 60.02° which correlates to the (250) reflection plane; three moderate intensity peaks at 2θ = 30.99° (111), 33.02° (040) and 39.57° (131) and nine low intensity peaks at 2θ = 25.95°, 44.54°, 46.28°, 49.18°,50.88°, 53.34°, 54.90°, 67.24° and 69.15° corresponding to (120), (141), (002), (211), (151), (122), (231), (171) and (080), respectively. SnS**3** diffractogram also showed peaks at 21.33°, 24.44°, 27.47°, 30.46°, 33.04°, 39.74°, 44.15°, 45.31°, 47.29°, 49.42°, 52.00°, 54.18°, 59.15° and 69.42° corresponding to (110), (120), (021), (111), (040), (131), (210), (141), (002), (211), (151), (231), (250), and (080) planes. The presence of well-defined sharp peaks with significant intensity suggests the crystallinity of pure SnS**3** nanoparticles. SnS**4** nanoparticles showed nine broad peaks at 22.94°, 25.25°, 31.01°, 33.30°, 39.14°, 48.97°, 50.62°, 60.62° and 69.25° corresponding to (110), (120), (111), (040), (131), (211), (151), (250), and (080) planes, respectively. The high intensity of the peaks may be attributed to the crystalline nature of the SnS nanoparticles. SnS**5** diffractogram exhibits two sharp and intense peaks at 33.10° and 58.88° correlating to (040) and (042) planes and other broad peaks with low intensity at 20.01°, 28.79°, 31.01°, 39.13°, 44.39°, 47.51°, 50.55°, 52.57°, 54.25°, 60.78°, 64.43°, 66.56° and 69.31°

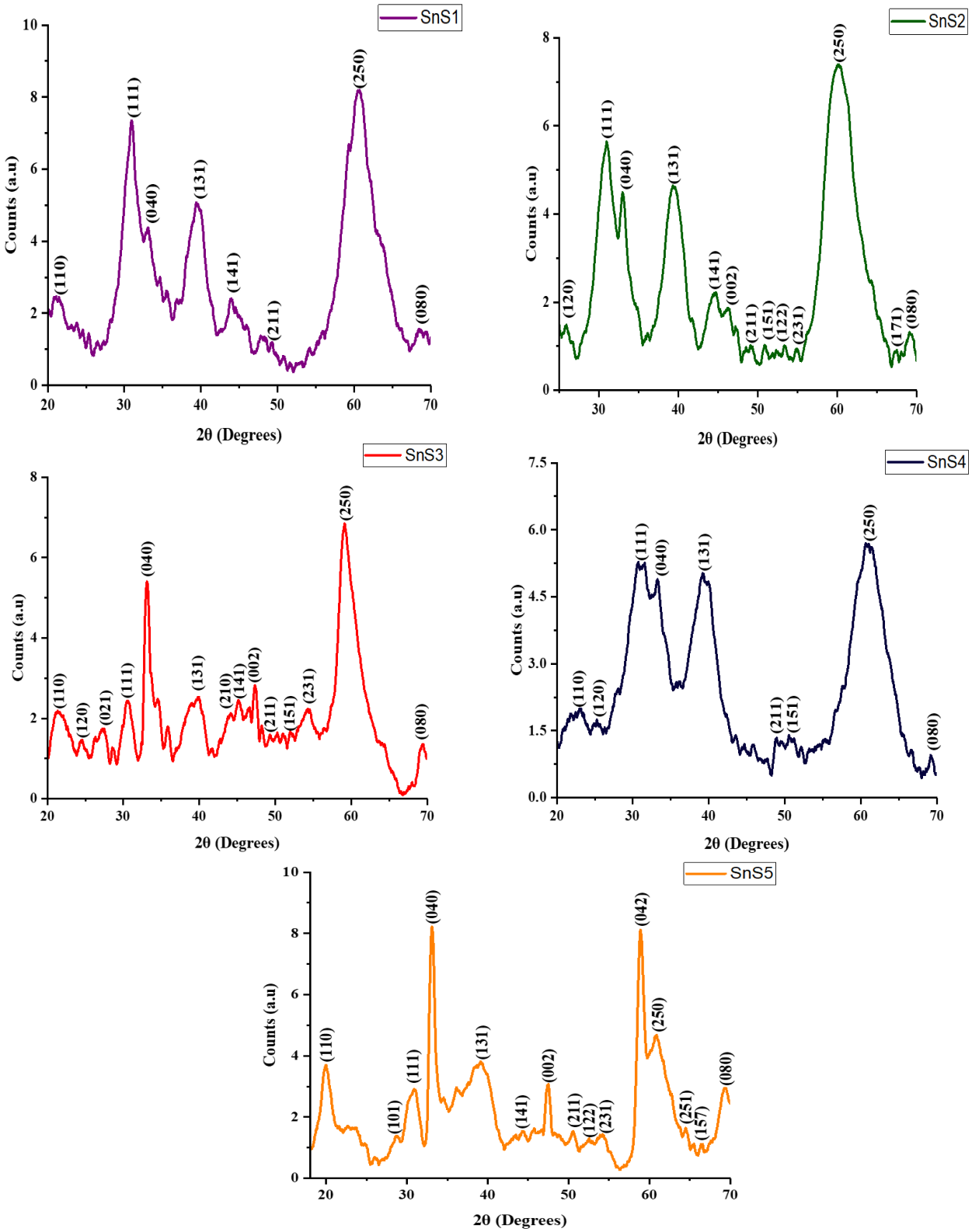

Figure 4.12: p-XRD patterns of SnS nanoparticles prepared from different precursors

corresponding to (110), (101), (111), (131), (141), (002), (211), (122), (231), (250), (251), (157) and (080). The peaks are slightly shifted to the left which may be due to the different precursor used to prepare SnS**5** nanoparticles.

4.3.3.2 Scanning electron microscope of SnS nanoparticles

Scanning electron microscopy images and energy dispersive spectroscopy EDS spectra of SnS nanoparticles are presented in Fig. 4.13. The SEM image of SnS**1** nanoparticles shows a moss-like morphology with rough surface. SEM image of SnS**2** nanoparticles shows smooth surface morphology with some cracks with no distinct patterns. SnS**3** nanoparticles SEM image shows loosely stacked large particles with smooth surface morphology and some flaky agglomerates are also observed on top and around the large particles. SEM image of SnS**4** reveals a mixture of big and small sized irregular shaped nanoparticles with smooth surface and no distinct arrangement is observed. SnS**5** nanoparticles SEM image shows asphalt crush-like morphology with rough surface. The SEM images revealed varying morphology due to the different precursors used in the synthesis of SnS nanoparticles. EDS spectra shows the presence of Au, C, O, Sn and S elements indicating the successful synthesis of SnS nanoparticles with capping agent. The C and O atoms observed are from the dodecylamine and oleic acid used to prepare the SnS nanoparticles and the Au is from the coating used for analysis.

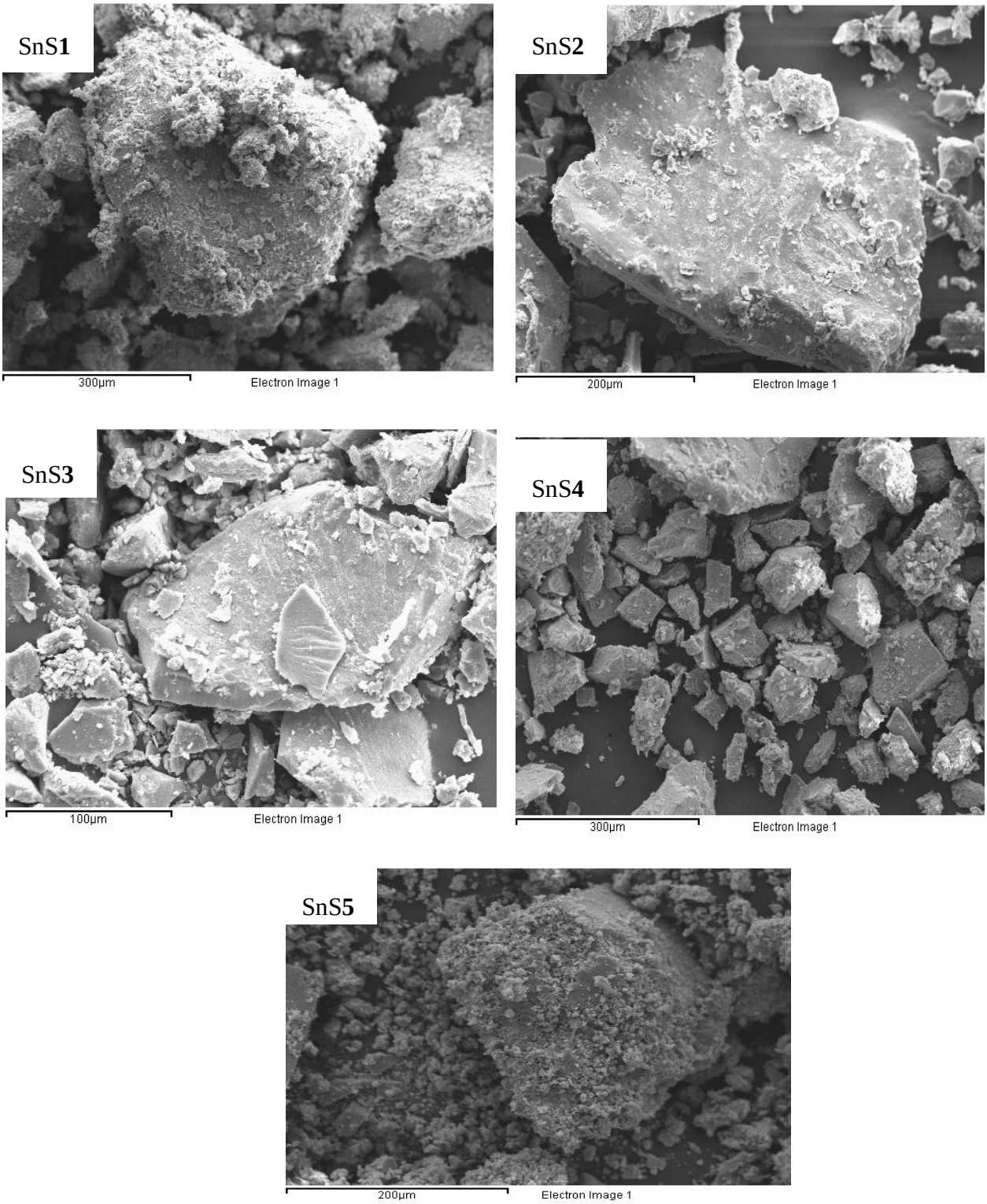

Figure 4.13: SEM images of SnS nanoparticles prepared from different precursors

4.3.3.3 Fourier transform infrared spectroscopy of dodecylamine capped SnS nanoparticles

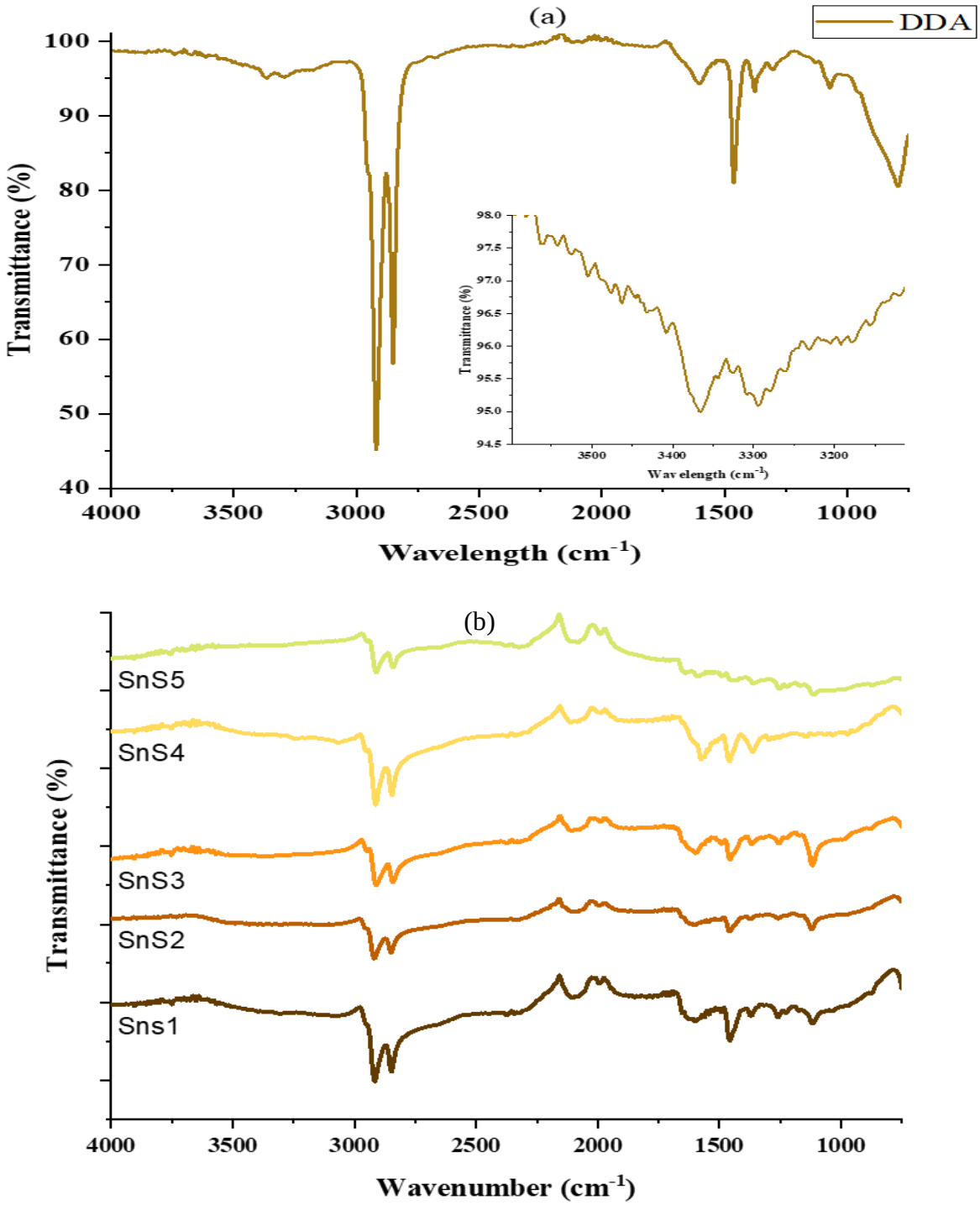

Figure 4.14: FTIR spectra of (a) dodecylamine and (b) dodecylamine capped SnS nanoparticles

FTIR spectra of pure dodecylamine and SnS nanoparticles were compared. Dodecylamine spectrum (Fig. 4.14(a)) exhibits two weak bands at 3367 and 3294 cm^{-1} ascribed to v(N—H) stretching vibrations[31]. These bands are not visible on the SnS nanoparticles spectra (Fig. 4.14(b)), suggesting that the interaction of the capping agent and SnS nanoparticles occurred through the –NH_2 group of dodecylamine. The asymmetric and symmetric C–H stretching vibrations of dodecylamine are observed at 2916 and 2842 cm^{-1} and are also evident but shifted to 2911 and 2847 cm^{-1} in the spectra of SnS nanoparticles. Pure dodecylamine spectrum also shows N– H and C–H bending bands at 1600 and 1466 cm^{-1}, respectively, which were shifted by 26 and 9 cm^{-1} to lower wavenumbers in the spectra of SnS nanoparticles. The significant peaks evident in the spectra of SnS nanoparticles indicate the presence of dodecylamine on the surface of the SnS nanoparticles.

4.3.3.4 Optical properties of SnS nanoparticles

Figure 4.15 shows absorption and emission spectra of SnS nanoparticles. UV-Vis spectra shows absorption bands at 250 nm for SnS**1** and SnS**3**, 248 nm for SnS**2** and 254 nm for SnS**4** and SnS**5**. The fluorescence spectra of the as-prepared SnS nanoparticles recorded at excitation wavelength of 350 nm show a red-shift compared to the absorption band edges. SnS**1** shows a broad emission peak at 425.5 nm, while SnS**2** shows a sharp emission at 462 nm and SnS**3**, SnS**4** and SnS**5** all show a strong emission at 516.5 nm and these may be attributed to tin and sulfur vacancies associated to interstitial defects[32].The absorption band edges were used to calculate the band gap energies of the as-prepared SnS nanoparticles using Tauc formula[33] and the Tauc plots are presented in Figure 4.16.

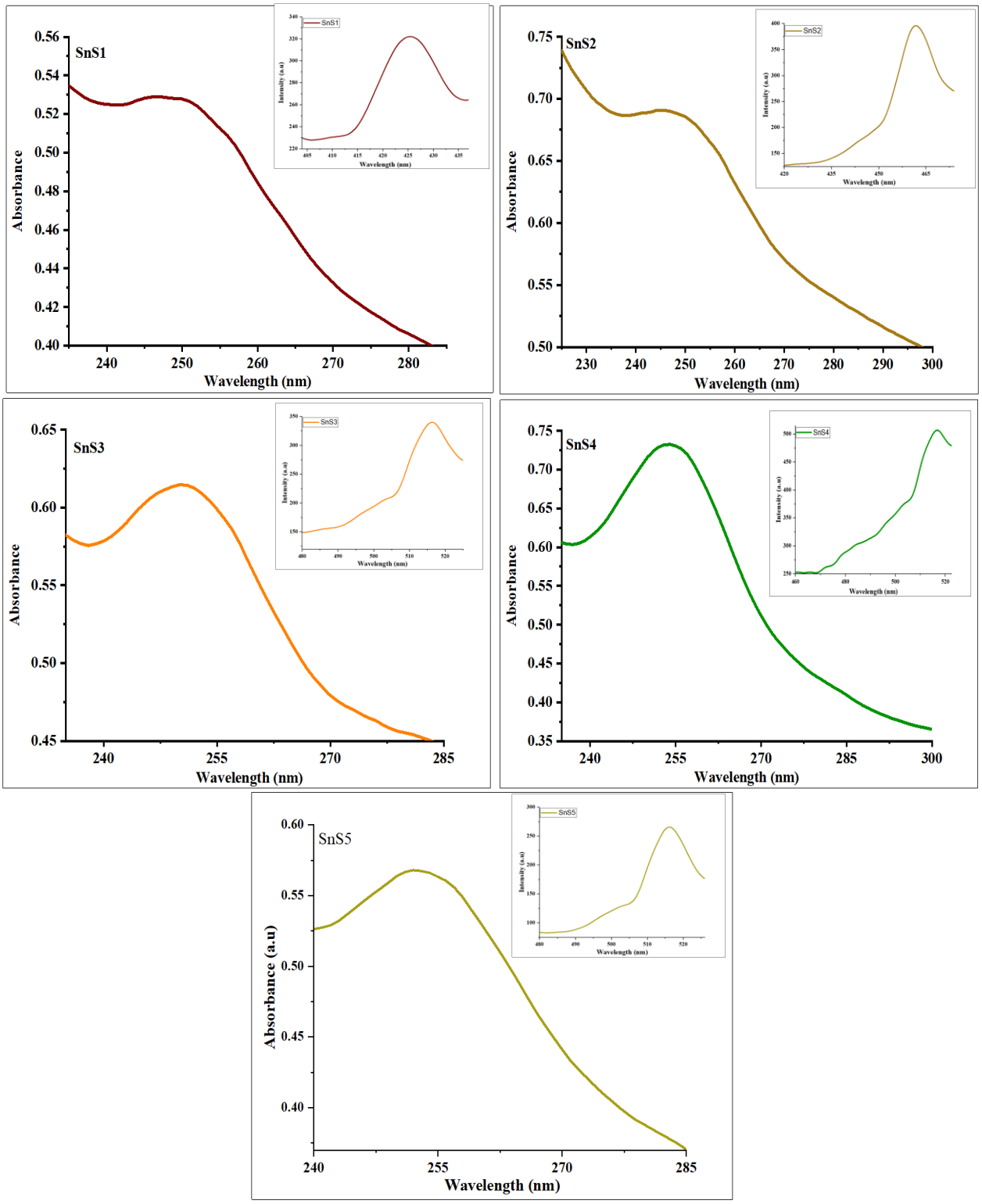

Figure 4.15: UV-Vis and emission spectra of SnS nanoparticles

The highest bandgap energy of 3.97 eV was obtained for SnS**2**, while the lowest bandgap energy of 3.42 eV was obtained for SnS**3** and the band gap energies of SnS**1**, SnS**4** and SnS**5** are 3.85 eV, 3.82 eV and 3.60 eV, respectively. The SnS nanoparticles prepared from bulky precursors have a smaller energy bandgap compared the ones prepared from small sized precursors. The direct bandgap energies show a significant blue-shift relative to bulk SnS (1.5 eV) [34], indicating a quantum size effect in SnS nanoparticles.

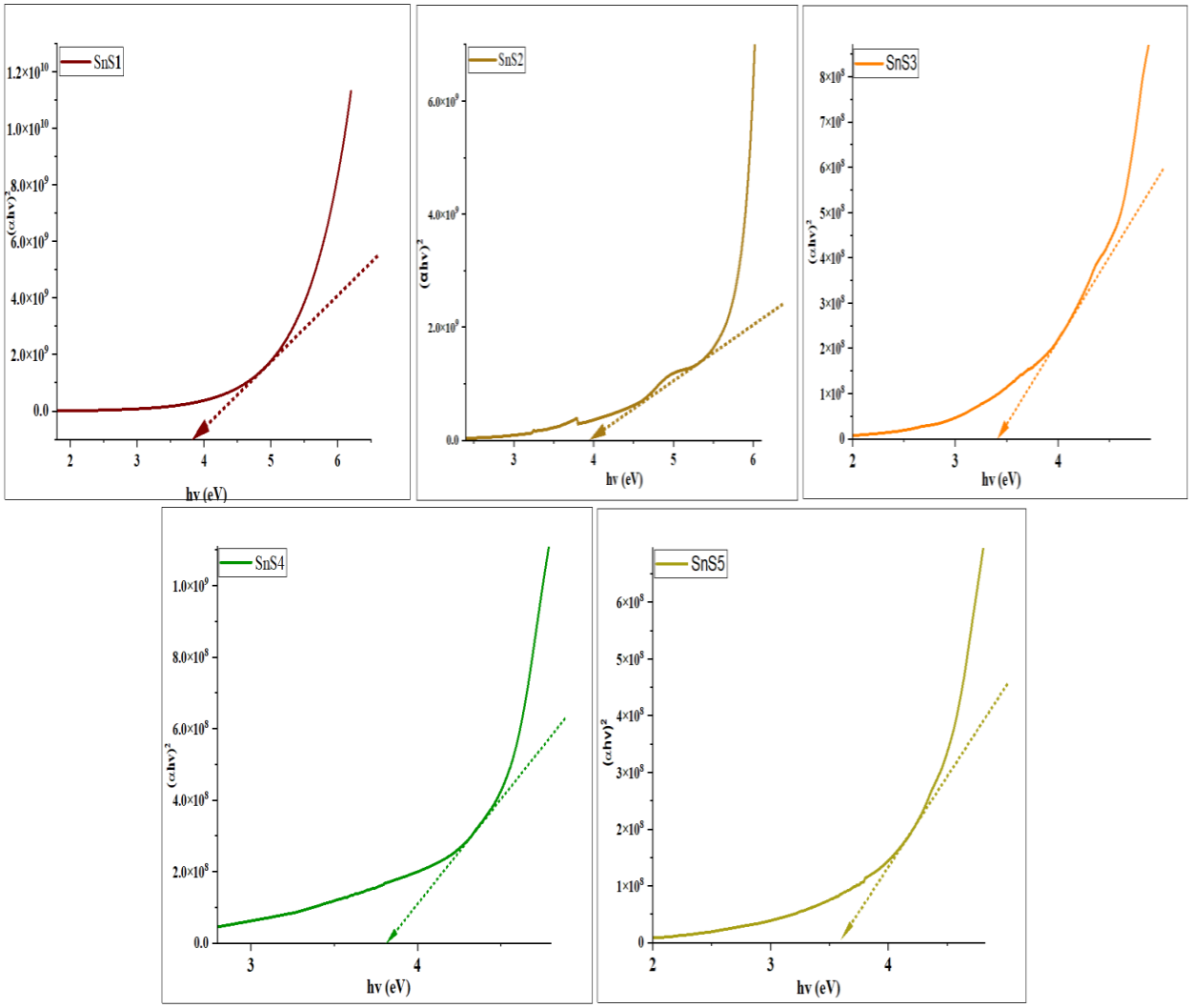

Figure 4.16: Tauc plots of SnS nanoparticles prepared from different precursors

References

1. Malik, M. A.; Revaprasadu, N.; O'Brien, P., Air-stable single-source precursors for the synthesis of chalcogenide semiconductor nanoparticles. *Chem. Mater.* **2001,** *13* (3), 913-920.

2. Trindade, T.; O'Brien, P.; Zhang, X.-M., Synthesis of CdS and CdSe nanocrystallites using a novel single-molecule precursors approach. *Chem. Mater.* **1997,** *9* (2), 523-530.

3. Green, M.; Prince, P.; Gardener, M.; Steed, J., Mercury(II) N,N′-methyl-phenylethyl-dithiocarbamate and its use as a precursor for the room-temperature solution deposition of β-HgS thin films. *Adv. Mater.* **2004,** *16* (12), 994-996.

4. Alivisatos, A. P., Perspectives on the Physical Chemistry of Semiconductor Nanocrystals. *J. Phys. Chem.* **1996,** *100* (31), 13226-13239.

5. Murray, C. B.; Norris, D. J.; Bawendi, M. G., Synthesis and characterization of nearly monodisperse CdE (E = sulfur, selenium, tellurium) semiconductor nanocrystallites. *J. Am. Chem. Soc.* **1993,** *115* (19), 8706-8715.

6. Pickett, N. L.; O'Brien, P., Syntheses of semiconductor nanoparticles using single-molecular precursors. *Chem. Rec.* **2001,** *1* (6), 467-79.

7. Thurston, J. H.; Ely, T. O.; Trahan, D.; Whitmire, K. H., Nanostructured Bimetallic Oxide Ion-Conducting Ceramics from Single-Source Molecular Precursors. *Chem. Mater.* **2003,** *15* (23), 4407-4416.

8. Awang, N.; Nordin, N. A.; Rashid, N.; Kamaludin, N. F., Synthesis and characterisation of phenanthroline adducts of Pb(II) complexes of bisN-alkyl-N-ethyldithiocarbamates. *Orient. J. Chem.* **2015,** *31* (1), 333-339.

9. Oluwalana, A. E.; Ajibade, P. A., Effect of temperature and capping agents on structural and optical properties of tin sulphide nanocrystals. *J. Nanotechnol.* **2019,** *2019*, 8235816.

10. Paca, A. M.; Ajibade, P. A., Effect of temperature on structural and optical properties of iron sulfide nanocrystals prepared from tris(N-methylbenzyldithiocarbamato) iron(III) complex. *Inorg. Nano-Met. Chem.* **2020**, 1-10.

11. Chintso T, A. P., Synthesis and structural studies of hexadecyamine capped lead sulfide nanoparticles from dithiocarbamates single source precursors. *Mater. Lett.* **2015,** *141*, 1-6.

12. Mamiyev, Z.; Balayeva, N., Preparation and optical studies of PbS nanoparticles. *Opt. Mater.* **2015,** *46*, 522-525.

13. Mbese, J. Z.; Ajibade, P. A., Synthesis, spectroscopic, structural and optical studies of Ru_2S_3 nanoparticles prepared from single-source molecular precursors. *J. Mol. Struct.* **2017,** *1143*, 274-281.

14. Oluwafemi, O. S.; Mohan, S.; Olubomehin, O.; Osibote, O. A.; Songca, S. P., Size tunable synthesis of HDA and TOPO capped ZnSe nanoparticles via a facile aqueous/thermolysis hybrid solution route. *J. Mater. Sci. Mater. Electron.* **2016,** *27* (4), 3880-3887.

15. Ajibade, P. A.; Oluwalana, A. E.; Sikakane, B. M.; Singh, M., Structural, photocatalytic and anticancer studies of hexadecylamine capped ZnS nanoparticles. *Chem. Phys. Lett.* **2020,** *755*, 137813.

16. Shkir, M.; Khan, M. T.; Ashraf, I. M.; AlFaify, S.; El-Toni, A. M.; Aldalbahi, A.; Ghaithan, H.; Khan, A., Rapid microwave-assisted synthesis of Ag-doped PbS nanoparticles for optoelectronic applications. *Ceram. Int.* **2019,** *45* (17), 21975-21985.

17. Mbese, J. Z.; Meyer, E. L.; Agoro, M. A., Electrocatalytic properties of PbS nanocrystals structured from (bis(N-1,4-phenyl-N-(4-morpholine)dithiocarbamato Pb(II) complexes) as photosensitizer for quantum-dots-sensitized solar cells. *Mater. Lett.* **2020,** *271*, 127770.

18. Thangwane, C. S.; Xaba, T.; Moloto, M. J., Influence of Temperature and Capping Molecules on the Synthesis of Cubic Structured Lead Sulfide Nanoparticles from Substituted Benzimidazole Dithiocarbamate Complex. *Asian J. Chem.* **2017,** *29*, 2711-2716.

19. Oluwalana, A. E.; Ajibade, P. A., Structural, optical and photocatalytic studies of hexadecylamine-capped lead sulfide nanoparticles. *Int. J. Ind. Chem.* **2020,** *11* (4), 249-260.

20. Nejo, A. O.; Nejo, A. A.; Pullabhotla, R. V. S. R.; Revaprasadu, N., Facile synthesis of organically capped PbS nanoparticles. *J. Alloys Compd.* **2012,** *537*, 19-23.

21. Ajibade, P. A.; Oluwalana, A. E., Structural, optical, photocatalytic and electrochemical studies of PbS nanoparticles. *J. Nano Res.* **2020,** *61*, 18-31.

22. Nyamen, L. D.; Rajasekhar Pullabhotla, V. S. R.; Nejo, A. A.; Ndifon, P. T.; Warner, J. H.; Revaprasadu, N., Synthesis of anisotropic PbS nanoparticles using heterocyclic dithiocarbamate complexes. *Dalton Trans.* **2012,** *41* (27), 8297-8302.

23. Ma, J., Preparation and Characterization of ZrO_2 Nanoparticles Capped by Trioctylphosphine Oxide (TOPO). *J. Wuhan Univ. Technol. Mater. Sci. Ed.* **2011,** *26*, 611-614.

24. Onwudiwe, D. C.; Hrubaru, M.; Ebenso, E. E., Synthesis, structural and optical properties of TOPO and HDA capped cadmium sulphide nanocrystals, and the effect of capping ligand concentration. *J. Nanomater.* **2015,** *2015*, 143632.

25. Chen, S.; Zhang, X.; Zhang, Q.; Tan, W., Trioctylphosphine as both solvent and stabilizer to synthesize CdS nanorods. *Nanoscale Res. Lett.* **2009,** *4* (10), 1159.

26. Ahmad Daud, N.; Chieng, B. W.; Ibrahim, N. A.; Talib, Z. A.; Muhamad, E. N.; Abidin, Z. Z., Functionalizing graphene oxide with alkylamine by gamma-ray irradiation method. *Nanomaterials* **2017,** *7* (6), 135.

27. Sharma, L. K.; Kar, M.; Choubey, R. K.; Mukherjee, S., Low field magnetic interactions in the transition metals doped CuS quantum dots. *Chem. Phys. Lett.* **2021,** *780*, 138902.

28. Wei, S.; Guo, C.; Wang, L.; Xu, J.; Dong, H., Bacterial synthesis of PbS nanocrystallites in one-step with l-cysteine serving as both sulfur source and capping ligand. *Sci. Rep.* **2021,** *11* (1), 1216.

29. Koktysh, D. S.; McBride, J. R.; Rosenthal, S. J., Synthesis of SnS nanocrystals by the solvothermal decomposition of a single source precursor. *Nanoscale Res. Lett.* **2007,** *2* (3), 144.

30. Mohan Rao, M.; Mandapati, J.; sudarshan reddy, R., Time-selective hydrothermal synthesis of SnS nanorods and nanoparticles by thiourea hydrolysis. *Chem. Lett.* **2004,** *33*, 1044-1045.

31. Ain, Q.; Khurshid, S.; Gul, Z.; Khatoon, J.; Raza, M.; Hamid, I.; Khan, I.; Aslam, F., Anionic azo dyes removal from water using amine-functionalized cobalt–iron oxide nanoparticles: a comparative time-dependent study and structural optimization towards the removal mechanism. *RSC Adv.* **2020,** *10*, 1021-1041.

32. Rana, C.; Saha, S., Growth and study of tin sulfide nanocrystals by precipitation technique using triethylamine. *Mater. Today: Proc.* **2019,** *11*, 667-672.

33. Reza Judy Azar, A., An easy-to-work precursor and low-temperature method for synthesis of ultrafine and high purity SnS and PbS semiconductor nanoparticles. *Inorg. Chem. Commun.* **2021,** *131*, 108767.

34. Zhang, F.; Zhang, Y.; Zhang, G.; Yang, Z.; Dionysiou, D. D.; Zhu, A., Exceptional synergistic enhancement of the photocatalytic activity of SnS_2 by coupling with polyaniline and N-doped reduced graphene oxide. *Appl. Catal. B.* **2018,** *236*, 53-63.

CHAPTER FIVE

PHOTOCATALYTIC STUDIES OF PbS AND SnS NANOPARTICLES

5.1 Introduction

The concentration of hazardous organic substances in storm and wastewater effluent is the main hurdle to general acceptance of water treatment technology[1]. Furthermore, the diversity, toxicity, and persistence of hazardous organic contaminants can have a significant effect on ecological sustainability and danger to human health through contaminated water supply[2, 3]. As a result, achieving effective removal of persistent organic pollutants from wastewater effluents to reduce the danger of pollution concerns from such harmful chemicals while still allowing reuse has become a difficulty. As a result, significant work has gone into finding a purification technology that can effectively remove these bio-recalcitrant organic pollutants. They are found in low quantity in secondary wastewater effluents, rivers, and lakes due to inadequate removal during water treatment. These pollutants pose substantial health issue despite their low concentrations due to their exceptionally high endocrine disrupting ability and genotoxicity[4].

Recent studies showed that advanced oxidation processes (AOPs) which focuses on the uses of photocatalysts are beneficial, and that this technology facilitates the complete mineralization of organic compounds into harmless CO_2 and H_2O under atmospheric conditions[5-7]. Furthermore, AOPs produce hydroxyl radicals, which are the primary oxidizing agents that can eliminate even non-biodegradable organic molecules from the wastewaters[8, 9]. Photodegradation of organic pollutants has sparked a great deal of interest in recent research due to the obvious advantages it has over conventional methods[10-12]. It is also seen as a green and sustainable solution for a better future of the environment, as it primarily involves

oxidative decomposition and wastewater purification[13-15]. Numerous photocatalytic systems, such as metal chalcogenides, have developed as effective photocatalysts for photodegradation of organic dyes in the recent couple of decades[16]. This chapter contains the photocatalytic degradation studies of methylene blue, rhodamine B, phenol, and brilliant green dyes by the PbS and SnS nanoparticles and the evaluation of the effect of irradiation time, pH and recyclability of the as-prepared PbS and SnS nanoparticles.

5.2 Experimental

5.2.1 Effect of irradiation time for PbS nanoparticles

PbS nanoparticles were utilized as photocatalysts to degrade methylene blue dye. The experiment was carried out in a continuous swirling OSRAM VIALOX 70 W incandescent mercury lamp. To achieve the adsorption-desorption equilibrium, 5 mg of PbS NPs were introduced to 4 mL of dye solution (10 mg L^{-1}) and sonicated for 30 minutes before stirring in the dark for 60 minutes. The solutions irradiated with UV light and a sample was taken at regular intervals and the absorbance was measured using a UV-Vis spectrophotometer to evaluate the degradation of methylene blue. The equation below was used to determine photocatalytic degradation percentage.

$$D = \frac{C_0 - C_t}{C_t} \times 100\% \qquad (1)$$

where D is the degradation efficiency, C_0 is the absorbance at t=0 of the dye solution, and C_t is the final absorbance.

The kinetics were determined from the pseudo-first order, of the Langmuir-Hinshelwood model as shown in Eq (2).

$$\ln(C_t/C_0) = -kt \qquad (2)$$

where C_0 is the concentration of the dye solution at t=0 and Ct is the concentration after photodegradation time t, and k is the pseudo-first-order rate constant. To establish the rate of the reaction from the slope of the straight lines, a graph of $\ln(C_t/C_0)$ against time was plotted.

5.2.2 Effect of pH on photocatalysis of PbS nanoparticles

10 mg powdered dye was dissolved in 1000 mL distilled water to make a 10 mg/L methylene blue solution. The pH of the solution was measured with a pH meter, where 0.1 M HCl or 0.1 M NaOH was introduced dropwise into the dye until the desired pH was reached. Each vial was filled with 5 milligram of PbS nanoparticles and 4 mL of acidic/basic dye solution. In order to reach adsorption-desorption equilibrium, the solutions were sonicated for 30 minutes and then swirled in the dark for 60 minutes. The dye solutions were subjected to UV irradiation and samples were collected at regular intervals and the photodegradation of the dye was determined by UV-Vis spectrophotometer.

5.2.3 Recyclability

The photocatalyst was recycled 4 times to evaluate its reusability. To do this, the photocatalyst was filtered and rinsed with distilled water after each run and then dried in a 100 °C oven for 3 h.

5.3 Photocatalytic degradation of methylene blue dye by PbS1, PbS2 and PbS3 nanoparticles

5.3.1 Effect of irradiation time on methylene blue degradation by the PbS nanoparticles

Under UV light irradiation for 30, 60, 90, 120, 150, and 180 minutes, the photocatalytic degradation efficiencies of PbS nanoparticles were investigated for the removal of methylene blue dye (MB). The change in methylene blue dye absorption maxima peak at 664 was used to determine the dye degradation. Figure 5.1 showed that the absorption maxima of methylene blue decreases as irradiation time is increased. At 180 minutes, dye degradation efficiencies for PbS**1**, PbS**2**, and PbS**3** are 72.55%, 75.86%, and 47.37%, respectively. The size, degree of crystallinity, and bandgap of the three PbS nanoparticles all differ significantly. PbS**2** has higher photocatalytic activity than PbS**1** and PbS**3**, which could be attributed to their smaller particle sizes. The smaller the size of the nanoparticles, the larger the surface area, which translates to more accessible surface-active sites[17]. The particle size, shape, and high rate of electron-hole pair recombination in PbS**3** could be the reason for its poor degradation efficiency. Previous studies have demonstrated that the surface area of a catalyst influences its photodegradation efficiency[6, 18], particles with bigger particles sizes have a high rate of electron-hole recombination due to the huge number of free charges present, resulting in a decrease in photocatalytic efficiency.

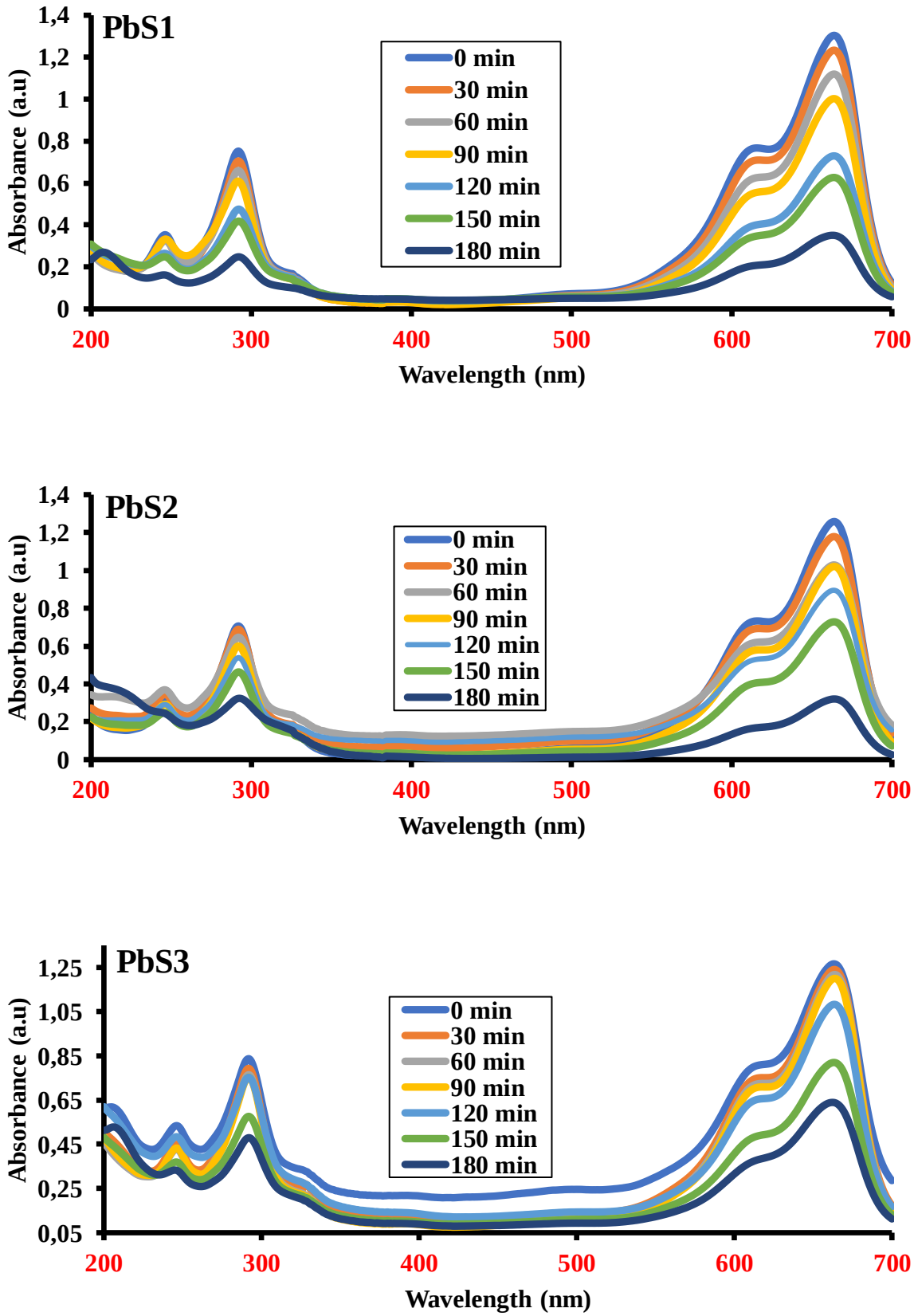

Figure 5.1: Absorption spectra for methylene blue degradation by PbS nanoparticles

5.3.2 Kinetics of photocatalytic degradation of methylene blue by PbS1, PbS2 and PbS3 nanoparticles

When the data was fitted to various kinetic models and the coefficients (R^2) were compared, it was observed that the degradation kinetics followed pseudo-first order, of the Langmuir-Hinshelwood model[19]. To establish the rate of the reaction from the slope of the linear plot, a graph of $\ln(C_t/C_0)$ against time was plotted, as shown in Fig. 5.2(b). The calculated rate constant for the nanoparticles are 0.0073 min^{-1} for PbS**1**, 0.0082 min^{-1} for PbS**2**, and 0.0040 min^{-1} for PbS**3**. The study revealed that PbS**2** has the fastest reaction rate than PbS**1** and PbS**3**. According to the pseudo-first order equation, photodecomposition of methylene blue dye is more reliant on the interactions on the surface of the PbS nanoparticles; thus, a large surface area provides high photocatalytic activity due to the greater contact area with the methylene blue dye solution.

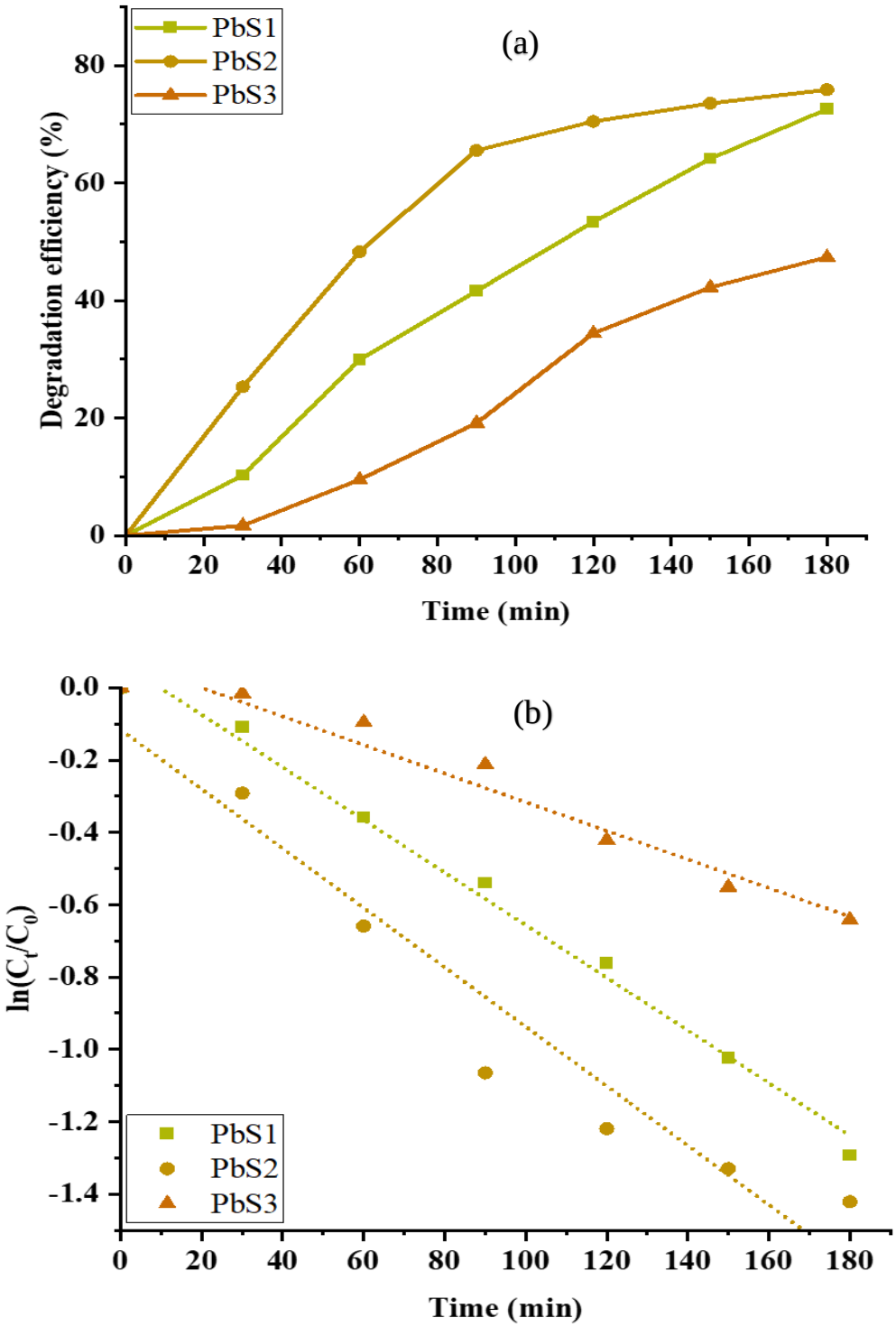

Figure. 5.2 (a) Degradation efficiency curve of methylene blue (b) photocatalytic degradation kinetics.

5.3.3 Effect of pH on photocatalytic degradation of methylene blue by PbS1, PbS2 and PbS3 nanoparticles

The influence of pH on degradation efficiency was studied in acidic pH 4, neutral pH 6.5, and alkaline pH 10 conditions, with the results shown in Figure 5.3 In acidic dye solution, the photocatalytic degradation efficiency of PbS**1** is 30.63%, PbS**2** is 48.88% and PbS**3** is 17.69%. The low photocatalytic degradation efficiencies could be attributed to the concentration of protons, which hinder methylene blue degradation. On the other hand, due to the high hydroxyl concentration in solution, which leads to the generation of hydroxyl radical as an efficient oxidizer of organic pollutants[20-22]. In alkaline medium degradation efficiencies are 85.29% for PbS**1**, 81.62% for PbS**2**, and 74.92% for PbS**3**.

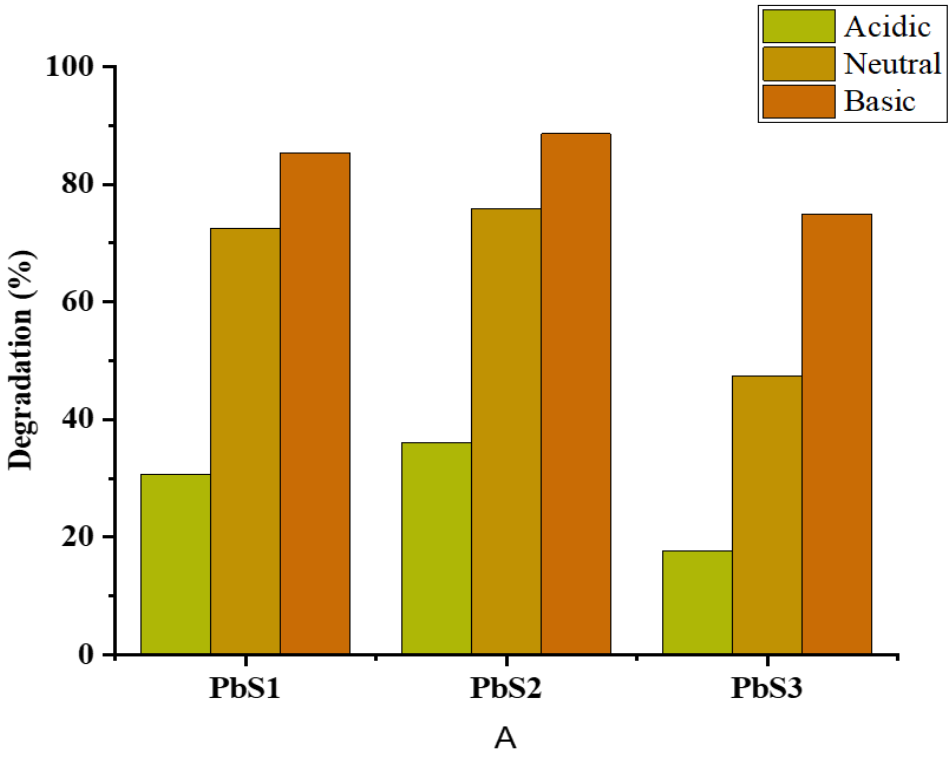

Figure 5.3: Effect of pH on methylene blue photocatalytic decomposition by PbS**1**, PbS**2** and PbS**3** nanoparticles

5.3.4 Recyclability of PbS nanoparticles

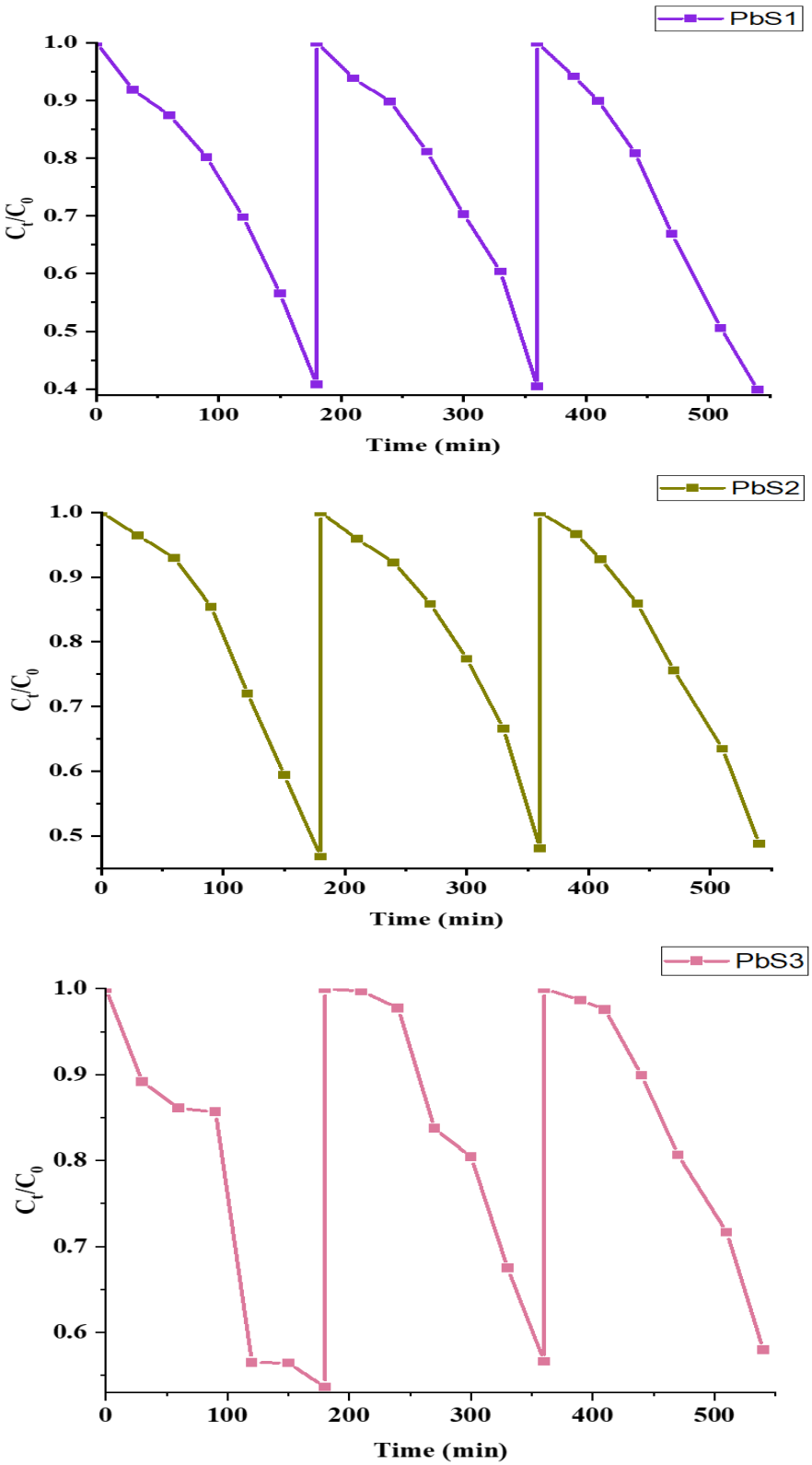

Figure 5.4: Recyclability studies of methylene blue degradation by PbS**1**, PbS**2** and PbS**3** nanoparticles

To examine the stability of the PbS nanoparticles, they were all subjected to multiple methylene blue dye degradation experiments. The recyclability results are shown in Fig. 5.4, and the data reveals that PbS**1** and PbS**2** nanoparticles may be efficiently reused three times with no substantial decrease in activity during three cycles. The loss of the photocatalyst during the separation process could explain the minor drop in degradation percentage as the number of cycles increase. PbS**3** is the least active and stable of the three PbS nanoparticles, with significant changes in degradation percentages found throughout all cycles.

5.4 Photocatalytic degradation of rhodamine B by PbS4 and PbS5 nanoparticles

5.4.1 Effect of irradiation time rhodamine B by the PbS nanoparticles

In the photocatalytic study of HDA, ODA, and TOPO capped PbS**4** and PbS**5** nanoparticles, the rhodamine B dye was used as an organic contaminant. Figure 5.5 illustrates the absorption of rhodamine B over time. The absorption spectra revealed that the absorption maxima of rhodamine B at 553 nm decreased with time. The photodegradation efficiency was determined using equation (1). The findings indicate that after 360 min, only about 46% of the dye was decomposed. The photodegradation efficiency by the PbS nanoparticles followed the order ODA-PbS**5** > TOPO-PbS**4** > TOPO-PbS**5** > HDA-PbS**5** > HDA-PbS**4** > ODA-PbS**4**. Previous studies have indicated that pure PbS nanoparticles have a low degradation efficiency due to poor separation efficiency, resulting in electron-hole pair recombination[23, 24], which is consistent with the results obtained in this study. The enhanced performance of ODA-PbS**5** nanoparticles may be ascribed to effective absorbance of rhodamine B due to surface atoms with unsatisfied valences[25]. These results are comparable to recent study of oleic acid-PbS and octadecylamine-PbS nanoparticles prepared from bis(phenylpiperazine dithiocarbamato)lead(II)[26].

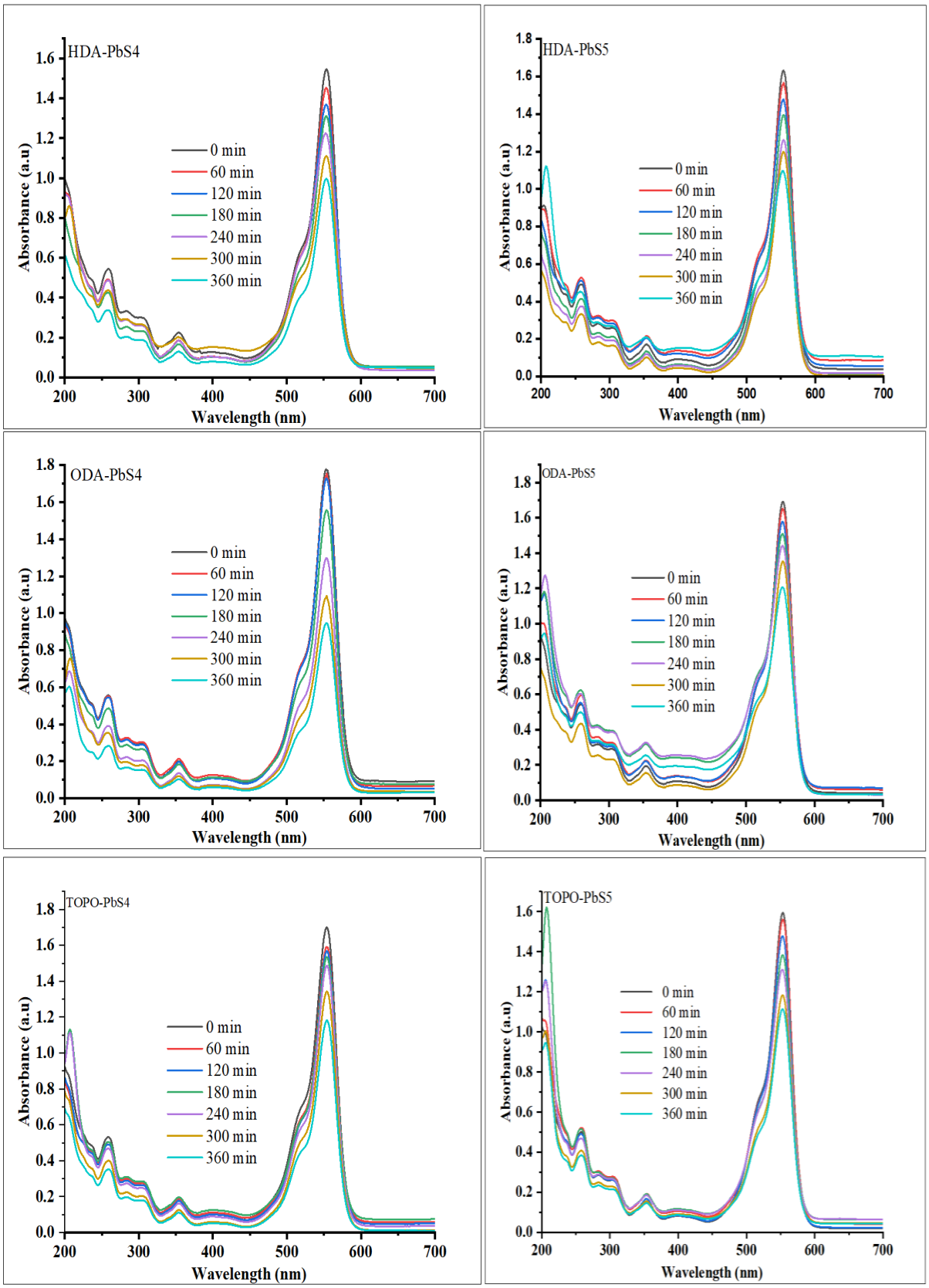

Figure 5.5: Rhodamine B degradation absorption spectra using PbS**4** and PbS**5** nanoparticles as photocatalysts.

5.4.2 Kinetics of photocatalytic degradation of rhodamine B by PbS4 and PbS5 nanoparticles

Figure 5.6 (b) shows the $\ln(C_0/C_t)$ plot where the slope of the curve is equivalent to the rate constant (*k*), indicating a linear correlation with irradiation time. ODA-PbS**4** has the highest rate constant of 0.0015 min^{-1} indicating higher photocatalytic activity[27], which correlates with the degradation efficiency curve in Figure 5.6 (a).

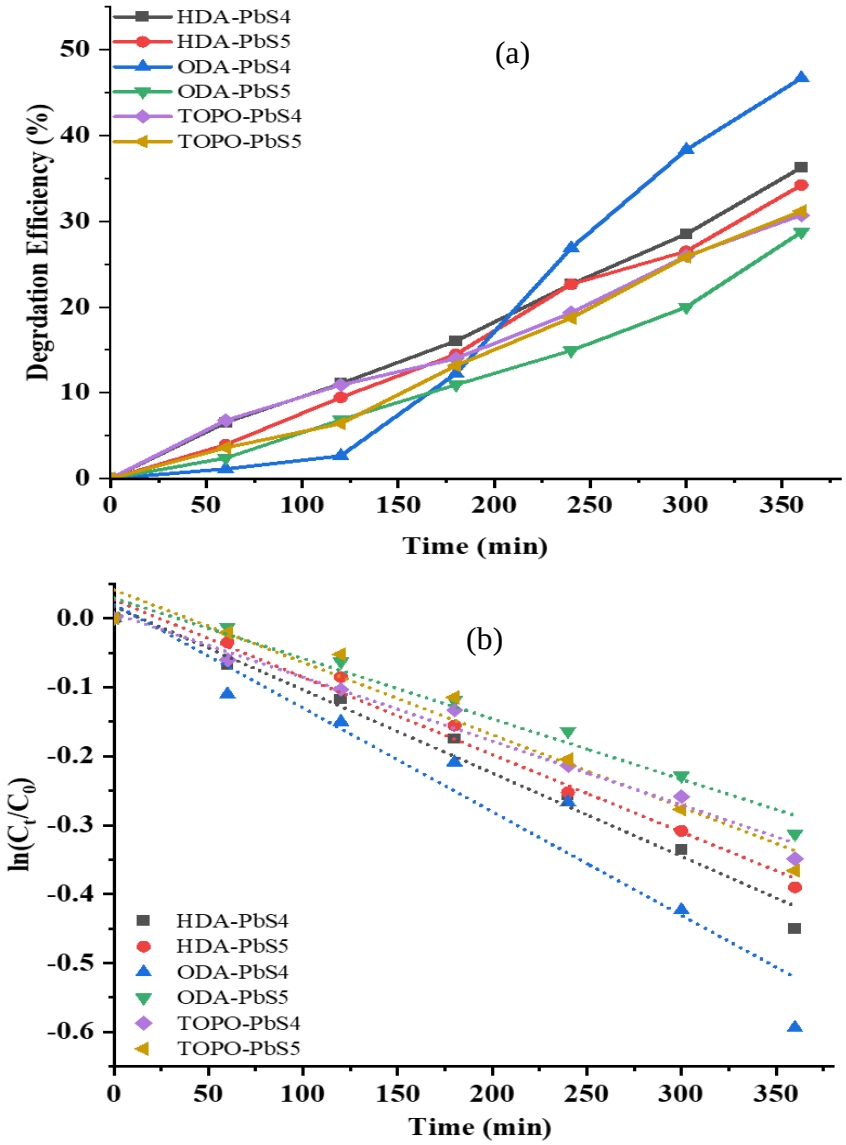

Figure 5.6: (a) Effect of time on Rhodamine B degradation (b) kinetic plot of rhodamine B using HDA-PbS, ODA-PbS and TOPO-PbS as photocatalysts.

Table 5.1 shows the percentage degradation efficiencies, rate constants, and correlation coefficients (R^2) calculated from the graphs in Figure 5.6. The high correlation coefficients (>0.90) indicate that the photodegradation of rhodamine B follows the pseudo-first-order kinetics[28]. Despite having somewhat comparable degradation efficiencies, the photocatalysts exhibit distinct rates of rhodamine B photodegradation.

Table 5.1: Percentage degradation of rhodamine B, rate constants and correlation coefficients using PbS4 and PbS5 nanoparticles

Compound	**Degradation (%)**	**Rate constant (min^{-1})**	**R^2**
HDA-PbS**4**	36.28	0.00121	0.98249
HDA-PbS**5**	34.22	0.00112	0.98516
ODA-PbS**4**	46.71	0.0015	0.93964
ODA-PbS**5**	28.75	8.75×10^{-4}	0.97162
TOPO-PbS**4**	30.71	9.25×10^{-4}	0.9826
TOPO-PbS**5**	31.17	0.00105	0.95905

5.4.3 Effect of pH on photocatalytic degradation of rhodamine B by PbS4 and PbS5 nanoparticles

Figure 5.7 illustrates the influence of the pH of the solution on the photocatalytic efficiency of the PbS nanoparticles. Measurements were carried out in acidic pH 4, neutral pH 6.5, and basic pH 10 conditions at a fixed concentration. Variation of the solution pH affects the number of available adsorption sites on the catalyst[29]. The charge of the contaminants and the catalyst, as

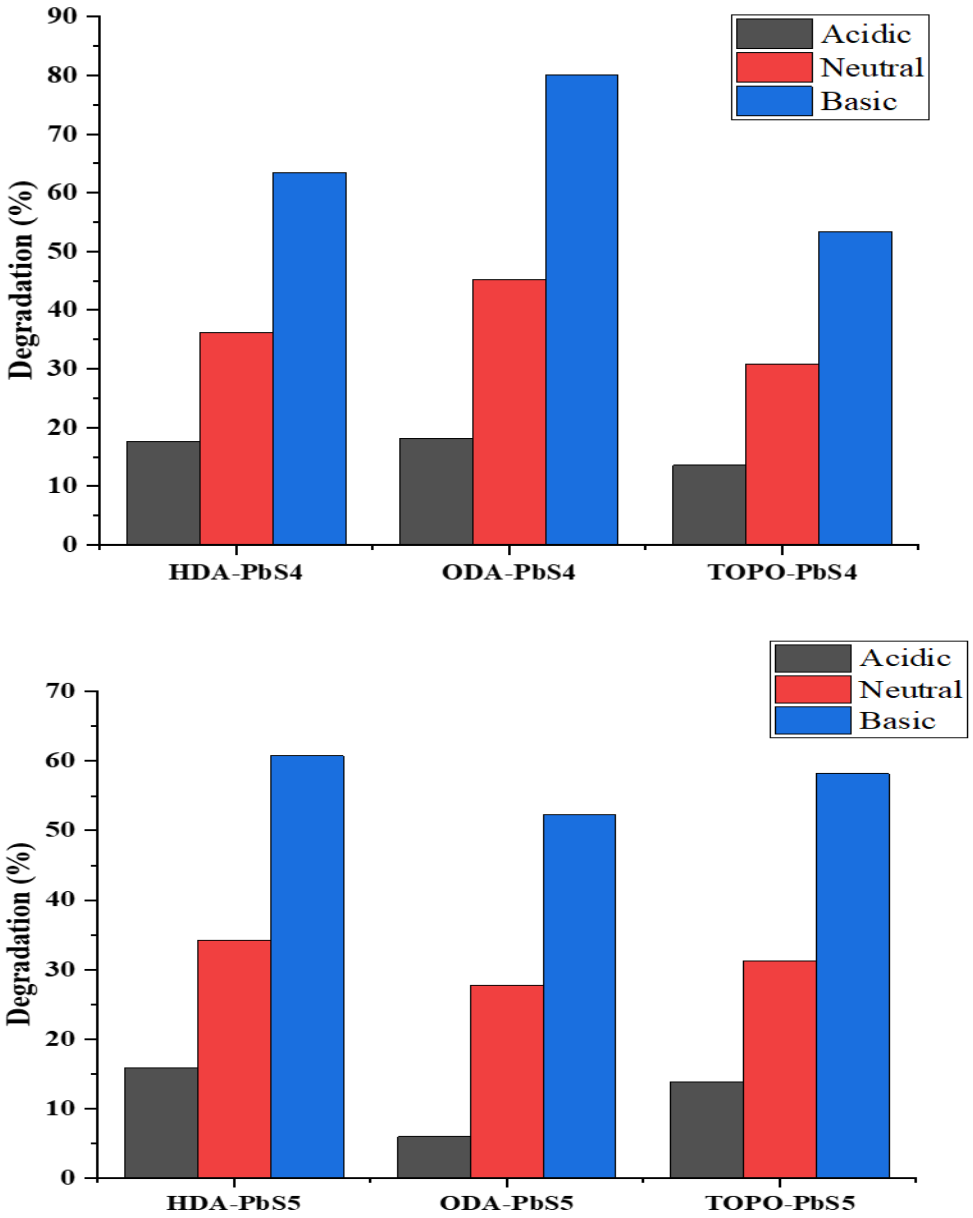

Figure 5.7: Effect of pH on rhodamine B photocatalytic degradation by HDA, ODA and TOPO capped PbS**4** and PbS**5** nanoparticles

well as the rate of adsorption on the catalyst active sites, can also be affected by the pH of the medium. It is apparent that as the pH increases, the efficiency of rhodamine B degradation increases. In acidic medium, the dye exists in the cationic form (RhB^+)[30]. Repulsive forces between RhB and the photocatalysts may develop as a result, which decreases the

photodegradation rate. As pH increases, RhB^+ deprotonates and generate the zwitter ion. In addition, basic medium may promote the production of hydroxyl radicals, which causes breakdown through oxidation process by the hydroxyl radical. All these factors promote the photodegradation of rhodamine B by the as-prepared PbS nanophotocatalysts.

5.4.4 Reusability of PbS4 and PbS5 nanoparticles

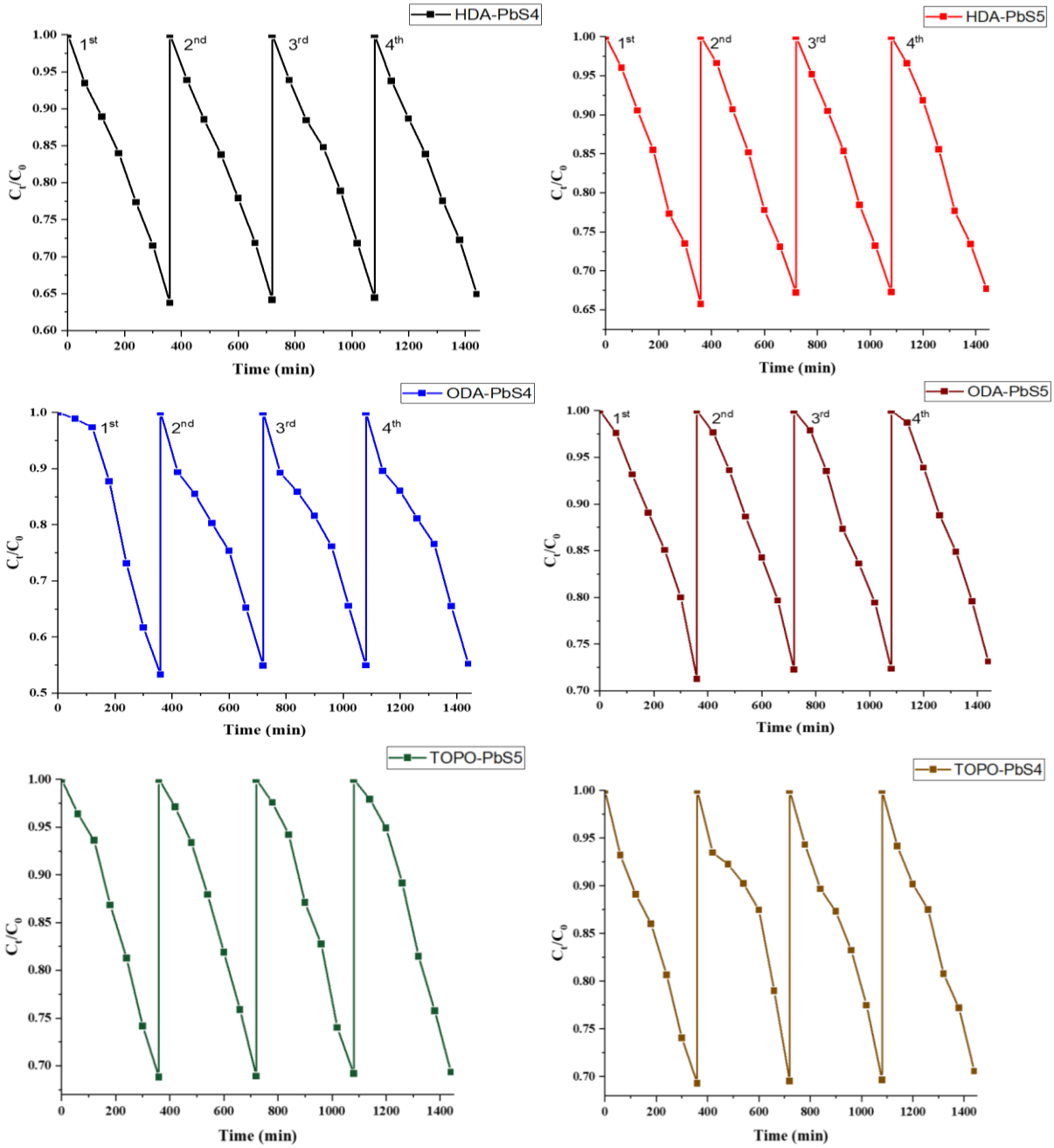

Figure 5.8: The reusability of HDA, ODA and TOPO capped PbS**4** and PbS**5** photocatalysts

To investigate the photostability of as-prepared PbS photocatalysts, their photocatalytic activities were further evaluated by recycling them in the repeated rhodamine B dye degradation experiments. As shown in Figure 5.8, 35.08%, 44.78%, 29.44%, 32.31%, 26.86%, and 30.66% of rhodamine B dye has been degraded after 360 minutes by HDA-PbS**4**, ODA-PbS**4**, TOPO-PbS**4**, HDA-PbS**5**, ODA-PbS**5**, and TOPO-PbS**5**, respectively on the fourth cycle. This marks a difference of 0.51-1.93% from the first cycle. The slight decrease in photocatalytic activity of the PbS nanoparticles due to the reduced number of active sites on the surface of the photocatalysts[31].

5.5 Photocatalytic degradation phenol by PbS4 and PbS5 nanoparticles

5.5.1 Effect of irradiation time on phenol degradation by the PbS nanoparticles

Irrespective of the type of photocatalyst used, there is an increase in the amount of phenol degraded over time as shown in Figure 5.9. ODA-PbS**4** showed the highest photocatalytic compared the others with a degradation efficiency of 32.84%. The poor photodegradation efficiencies observed in all the PbS nanoparticles could be attributed to the stability of the phenol molecule and the morphology of the nanoparticles. The photocatalytic degradation efficiency of ODA-PbS**4** may be attributed to the minimized recombination of electron-hole pair as evidenced by the lower photoluminescence signal obtained for the compound in comparison to the others[20].

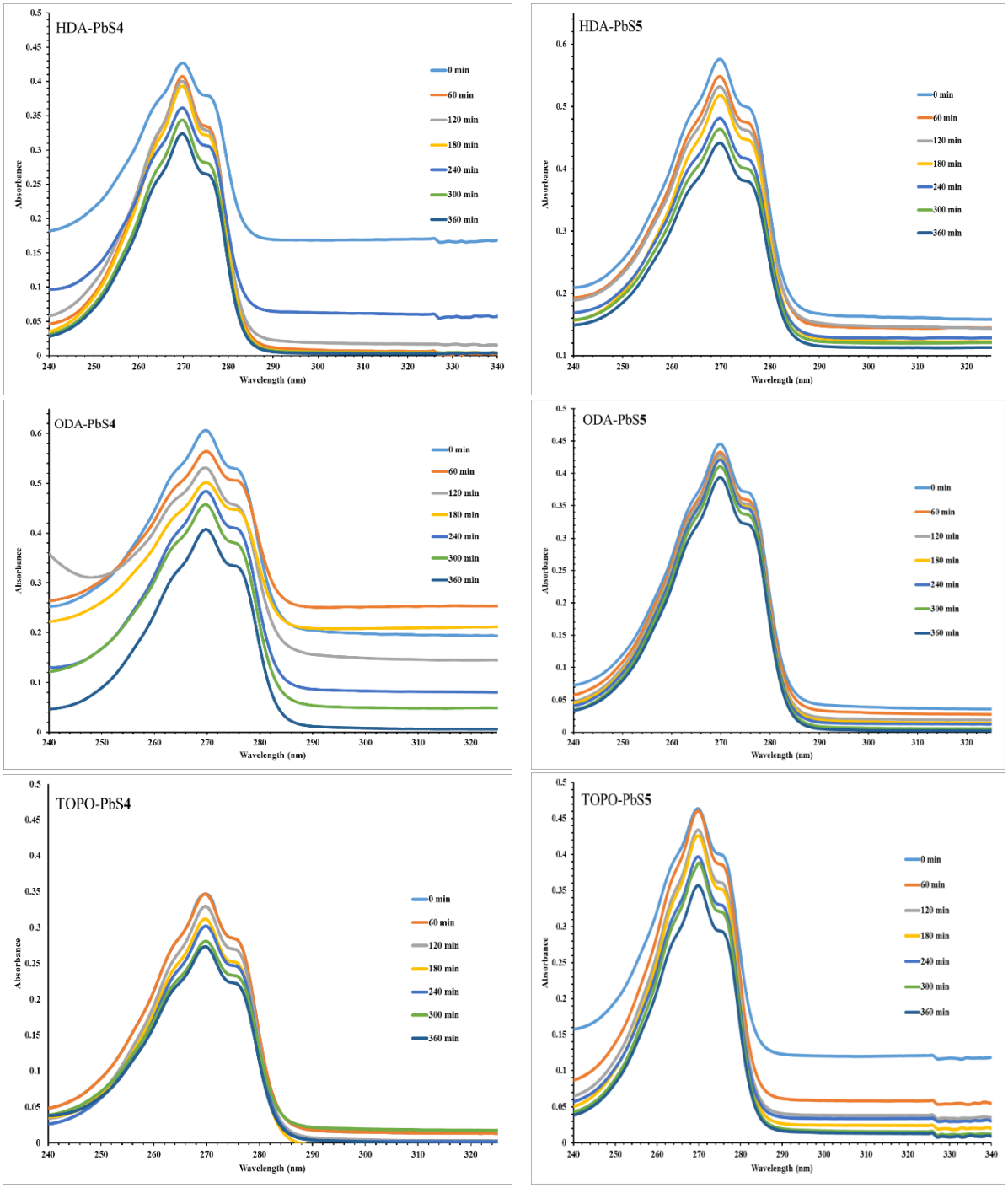

Figure 5.9: Absorption spectra of photodegradation of phenol by HDA, ODA and TOPO capped PbS**4** and PbS**5** nanoparticles

5.5.2 Kinetics of photocatalytic degradation of phenol by PbS4 and PbS5 nanoparticles

The photodegradation of phenol was found to obey a first-order reaction rate law with a good correlation value (R^2) close to 1 (Table 5.2). The degradation rate constant, *k*, was computed using the first-order plot (Eq. 2), and the reaction rates were found to be in the range of 2.9×10^{-4} to 1.02×10^{-3} min^{-1}. The rate of reaction in the case of ODA-PbS**4** is 3.5 times greater than that of ODA-PbS**5**.

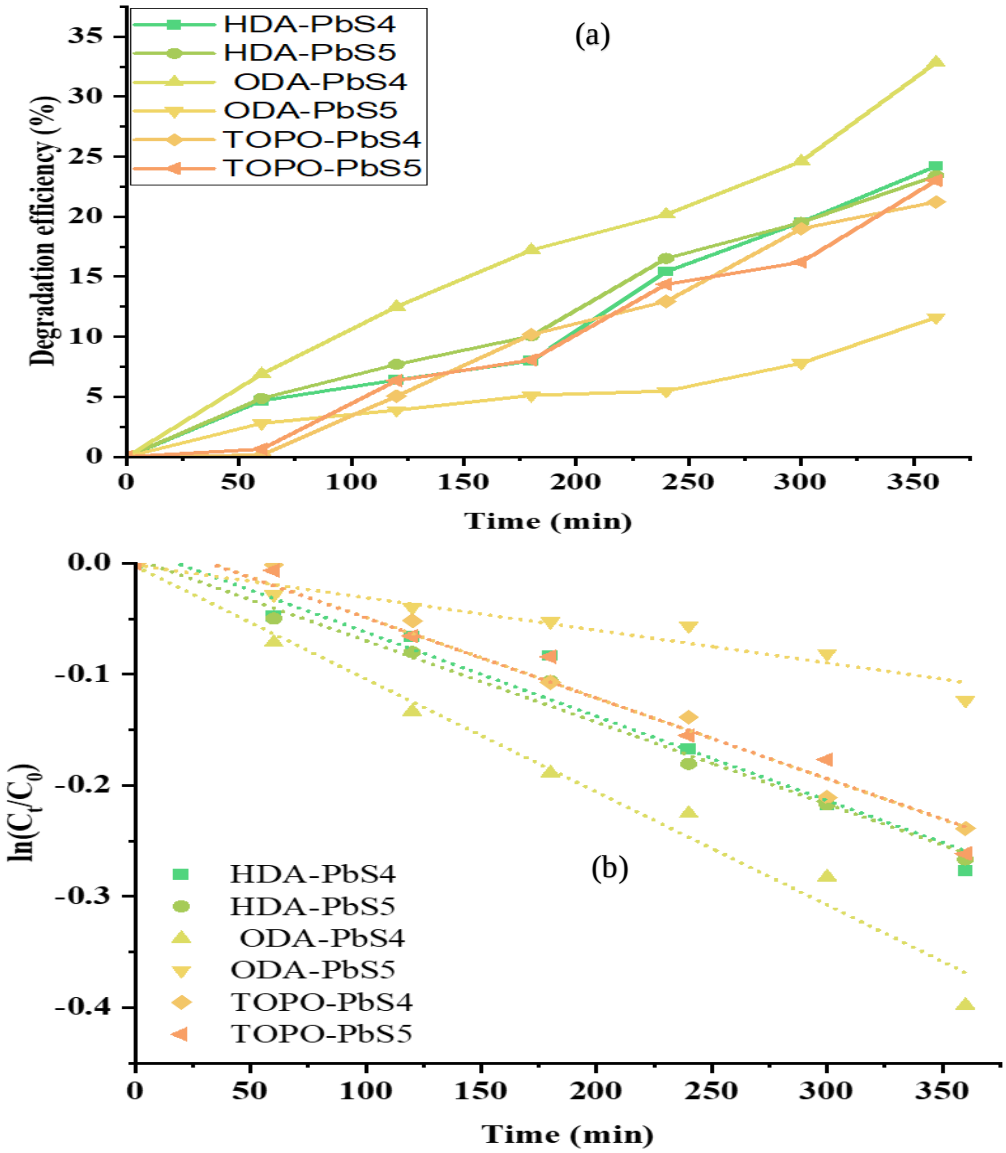

Figure 5.10: Phenol degradation efficiency curve (a) and kinetic plot (b) of phenol using HDA, ODA and TOPO capped PbS**4** and PbS**5** nanoparticles.

Table 5.2: Percentage photodegradation of phenol, rate constants and correlation coefficient using PbS**4** and PbS**5** nanoparticles

Compound	**Degradation (%)**	**Rate constant (min^{-1})**	**R^2**
HDA-PbS**4**	24.21	$7.51x10^{-4}$	0.95097
HDA-PbS**5**	23.41	$7.35x10^{-4}$	0.98419
ODA-PbS**4**	32.84	$1.02x10^{-3}$	0.97622
ODA-PbS**5**	11.61	$2.93x10^{-4}$	0.91296
TOPO-PbS**4**	21.24	$7.27x10^{-4}$	0.96805
TOPO-PbS**5**	23.02	$7.23x10^{-4}$	0.95286

5.5.3 Effect of pH on phenol photodegradation by PbS4 and PbS5 nanoparticles

The solution pH has a significant impact on adsorption and absorption because of its effect on the surface characteristics of the adsorbent[32]. The pH of the media used for the experiment was set at pH 4, pH 6.5 and pH 10 to investigate the effect of pH on the photocatalytic degradation of phenol. Adsorption investigations for all nanoparticles were carried out at various initial pH values of the phenolic aqueous medium, revealing that the photocatalysts favourably adsorb the phenol in alkaline medium over neutral media (Fig. 5.11). The phenoxy radical is generated at pH levels greater than phenol's pKa, resulting in the rapid production of hydroquinone as a key intermediary species. The produced phenoxy radical has also been shown to polymerize yielding dimeric compounds[33, 34]. Nonetheless, the created $HO^{\bullet}$ radicals have a substantially stronger oxidizing potential than the generated intermediate product, resulting in enhanced phenol degradation.

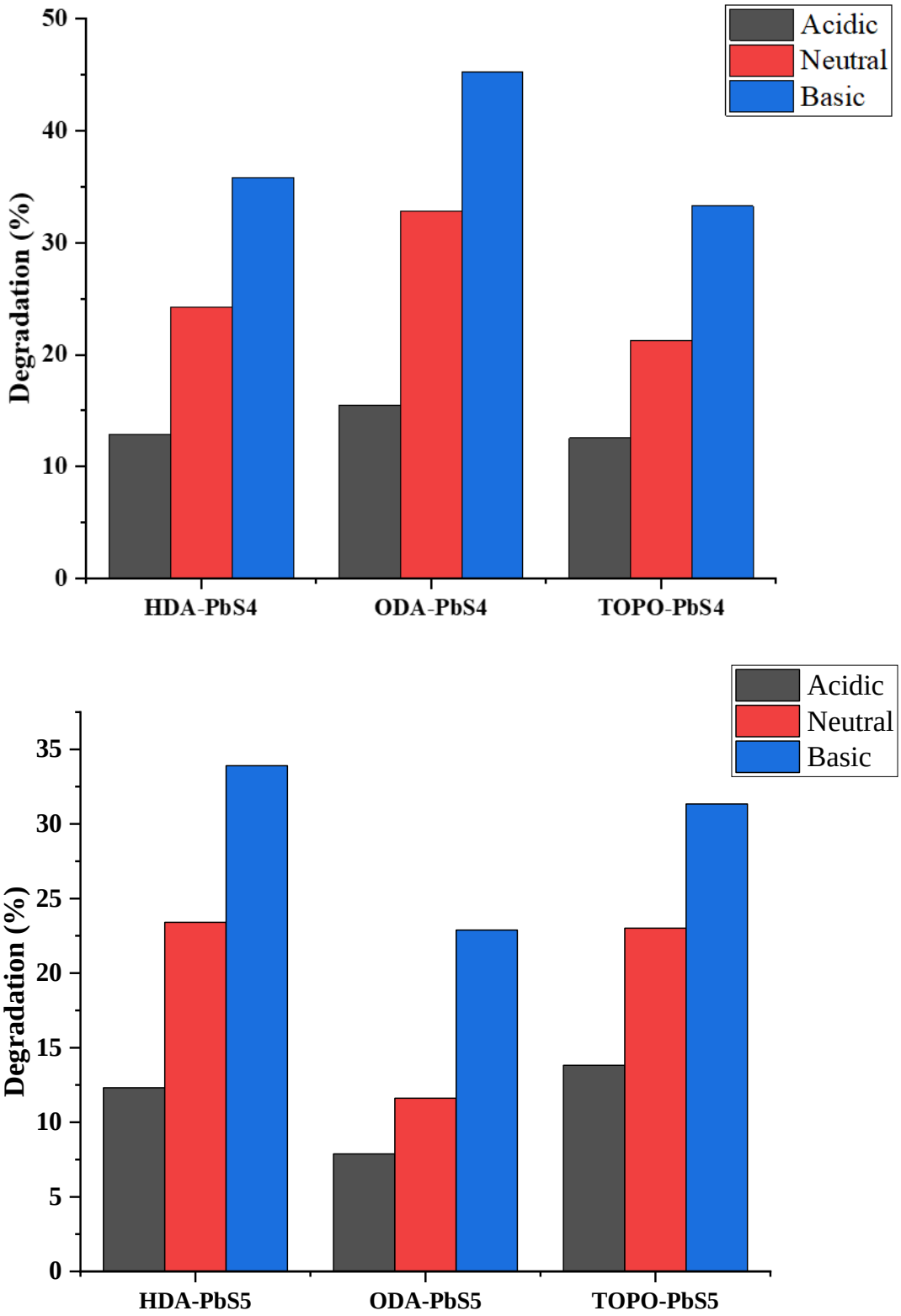

Figure 5.11**:** Effect of pH on photocatalytic degradation of phenol by HDA, ODA and TOPO capped PbS**4** and PbS**5** nanoparticles

5.6 Photocatalytic degradation of brilliant green dye by SnS nanoparticles

5.6.1 Effect of irradiation time

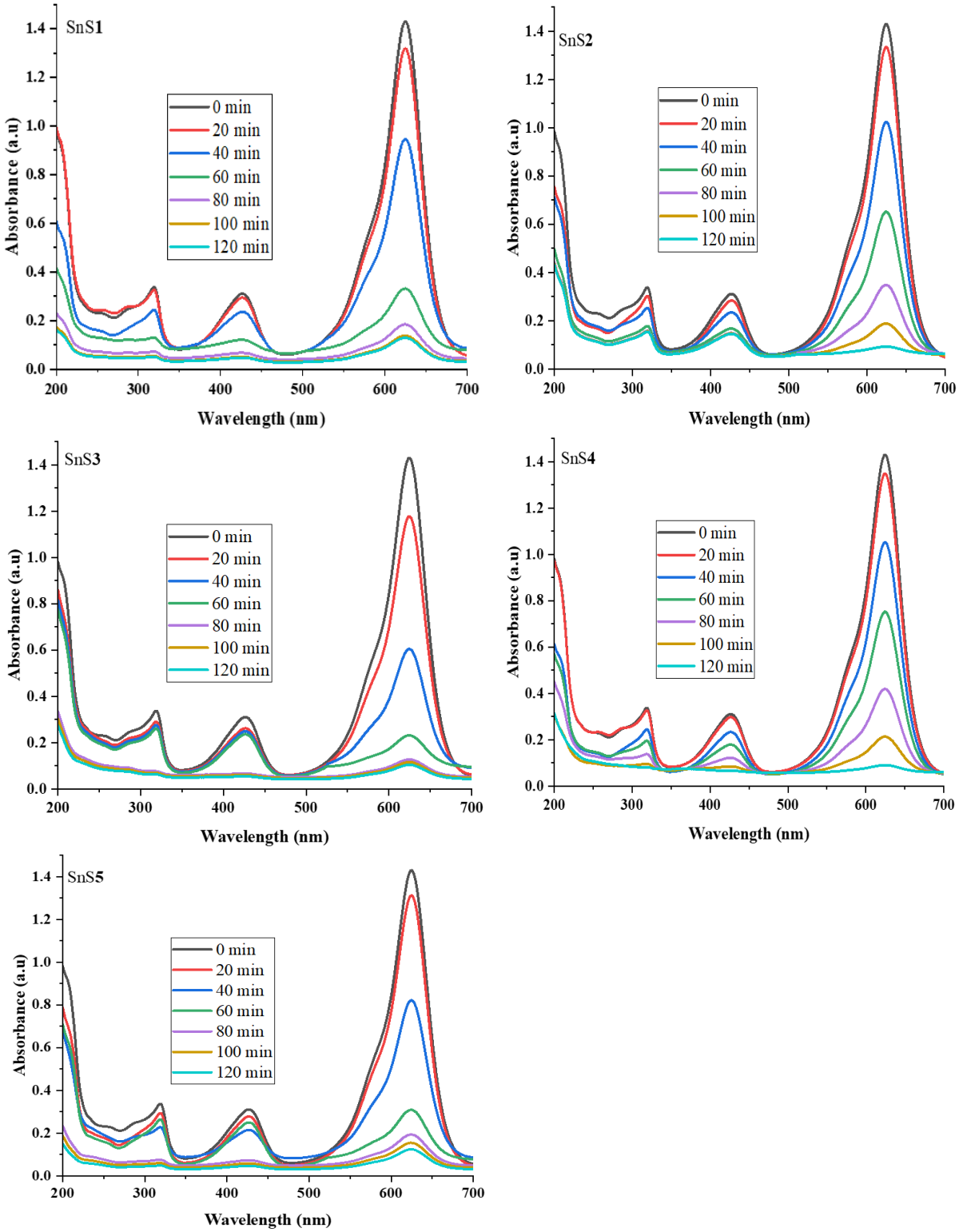

Figure 5.12: Brilliant green photocatalytic degradation absorption spectra using SnS nanoparticles as photocatalysts.

The photocatalytic degradation of the as-prepared SnS nanoparticles were investigated using brilliant green dye. The absorption spectra in Figure 5.12 show that the concentration of brilliant green decreased as the irradiation time increased, the characteristic absorption peak was lowered by more than 90% after 120 minutes. This could be due to the high surface area, which allows for more trapping sites on the surface of the nanoparticles, lowering the conduction band and increasing the transport of photogenerated electrons to the trapping site[35]. SnS**4** nanoparticles shows the highest photodegradation efficiency of 93%. The difference in the particle size and shape of the SnS nanoparticles could be responsible for the different photodegradation efficiencies observed in the study. SnS nanoparticles have been used in the photocatalytic degradation of rhodamine B and showed complete degradation after 90 min[36], while SnS nanofibres degraded 92.55% of rhodamine B after 200 min under ultraviolet irradiation[37]. Degradation efficiency of 93.14% was obtained against methylene blue by oleylamine-SnS nanoparticles prepared from tin(II) diallyl dithiocarbamate[38]. The highest photocatalytic efficiency of brilliant green obtained in this study is similar to that of SnS nanoparticles prepared from a different single precursor.

5.6.2 Langmuir-Hinshelwood kinetic model for the photocatalytic degradation of brilliant green dye by SnS nanoparticles

The Langmuir-Hinshelwood kinetic model was used to analyse the rate of photocatalytic degradation of brilliant green with relation to irradiation time in the presence of SnS nanoparticles as photocatalyst. Figure 5.13(a) shows the ratio of concentration relating to irradiation duration, which shows a decline with time. As shown in the Figure, SnS**3** and SnS**5** are observed to be almost constant from 80 min to 120 min and the same is observed

for SnS1 at 100 min to 120 min. The natural logarithm of C_t/C_0 vs irradiation duration was plotted which revealed a linear association (Figure 5.13(b)), and the calculated rate constants are 0.02364 min^{-1} for SnS**1**, 0.02360 min^{-1} for SnS**2**, 0.02305 min^{-1} for SnS**4**, and 0.02430 min^{-1} for SnS**3** and SnS**5**. These are consistent with the photodegradation efficiency curve shown in Figure 5.13(c).

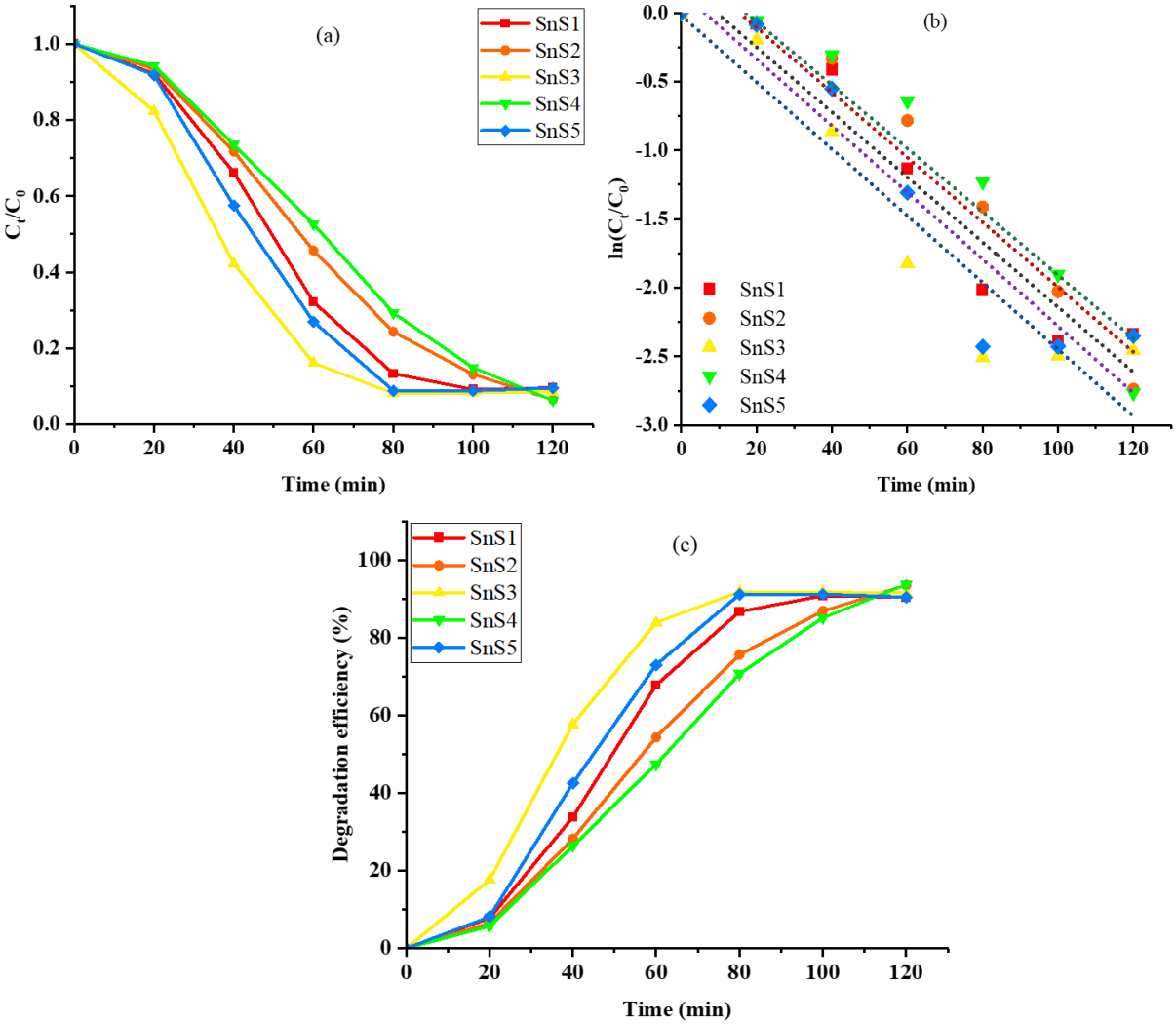

Figure 5.13: Effect of time on photocatalytic degradation of brilliant green by SnS nanoparticles (a), photocatalytic degradation kinetics (b) and degradation efficiency curve (c).

5.6.3 Effect of pH on photocatalytic degradation of brilliant green by SnS nanoparticles

The pH of the dye solution has a significant impact on adsorption capacity because it alters the stability, colour intensity, and amount of dye molecule decomposed[39]. The results show that the photodegradation of the brilliant green dye increase with increasing pH, as seen in Fig. 5.14. However, only an increase of 1.63-4.70% is observed between the neutral and basic conditions. This may be the result of brilliant green structural instability at higher pH[40]. The difference in photocatalytic degradation percentage as a function of pH can also be understood by considering pKa of brilliant green. When the pH of the medium is lower than the pKa of brilliant green, surplus H^+ ions compete for accessible adsorption sites of nanoparticles with bulky brilliant green molecules. Therefore, the adsorption sites are saturated with H^+ ions rather than brilliant green molecules, causing a drop in the amount of brilliant green absorbed. The rivalry for H^+ ions adsorption disappears when the pH rises from acidic to neutral, as the concentration of H^+ ions decreases. At neutral pH, practically all adsorbent surface are free for the adsorption of brilliant green molecules. A reduction in adsorption may occur at pH levels greater than 6.5 due to increasing OH ion concentrations, which can hinder brilliant green molecule adsorption[39].

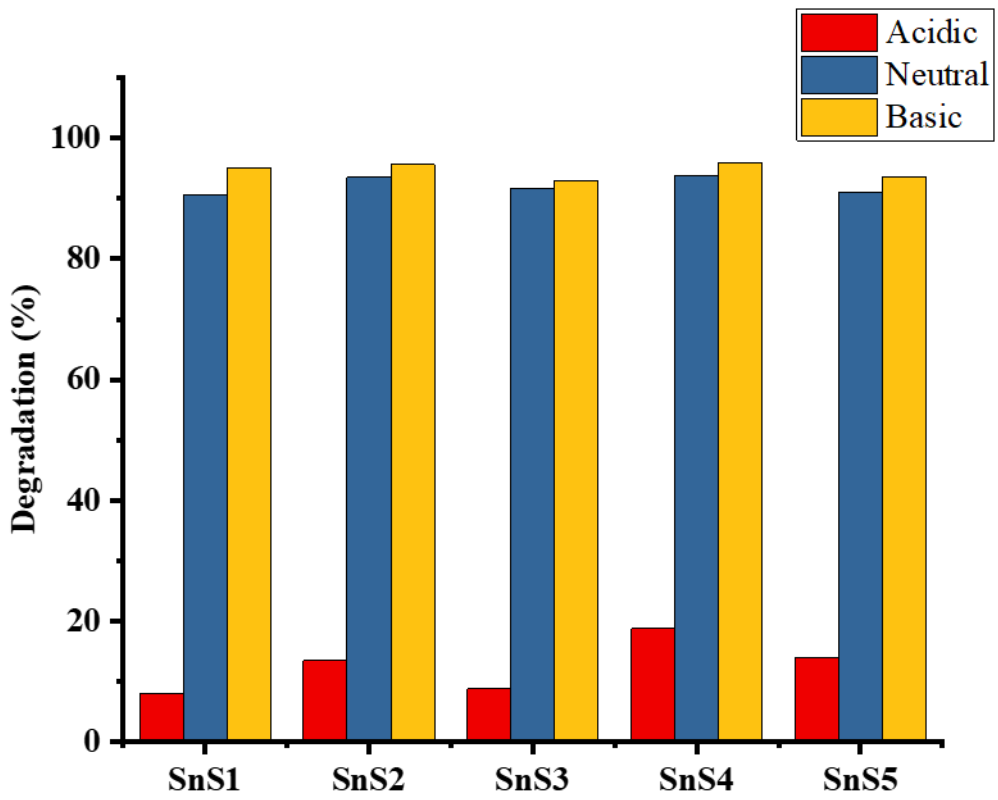

Figure 5.14: Effect of pH on brilliant green photocatalytic degradation by SnS

5.6.4 Recyclability of SnS nanoparticles

The reusability and stability of photocatalysts make them very appealing for practical applications. As a result, photocatalytic degradation of brilliant green was carried out for five cycles at neutral pH under UV irradiation. The reusability of SnS nanophotocatalysts is depicted in Figure 5.15. The results show that after five consecutive photodegradation cycles, the photocatalytic activity of the SnS nanoparticles decreases by 0.83 – 2.97%. This demonstrates that the SnS photocatalysts are stable for five cycles, indicating that it has a high potential for use in practical water treatment.

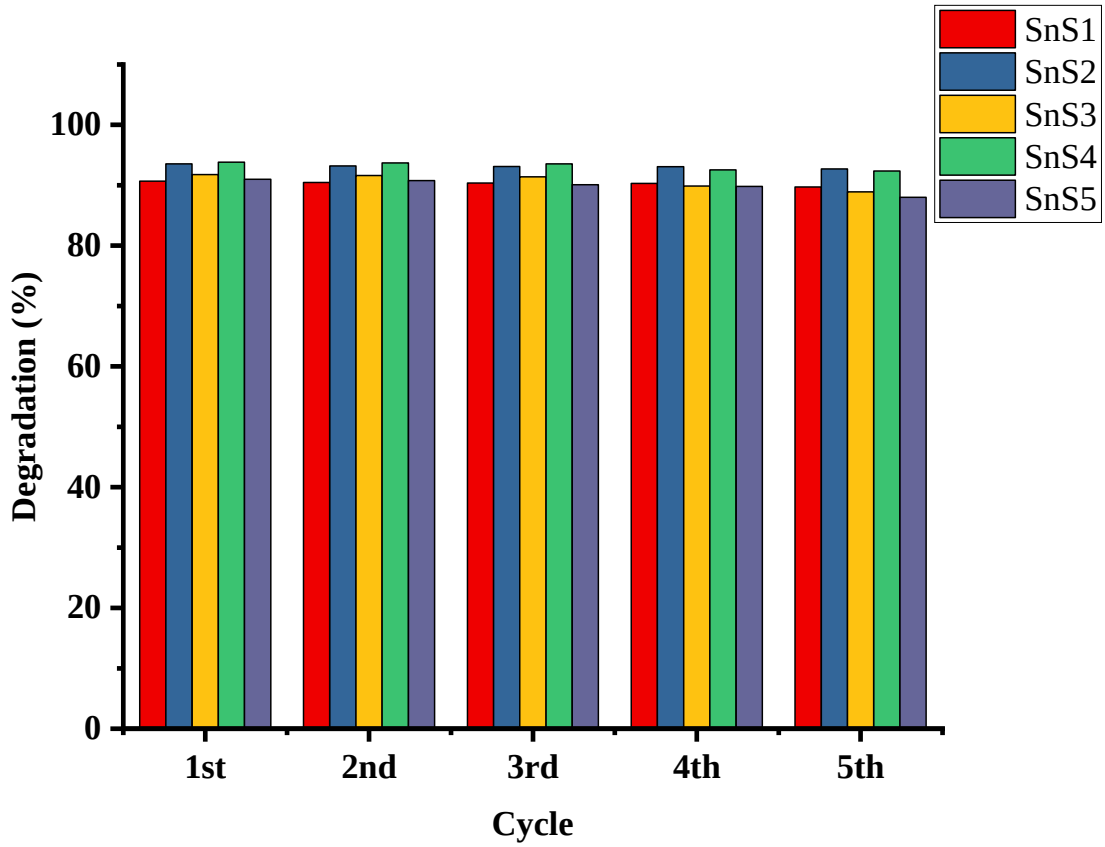

Figure 5.15: The recyclability of SnS nanophotocatalysts

References

1. Mahmoodi, N. M.; Arami, M.; Limaee, N. Y.; Gharanjig, K., Photocatalytic degradation of agricultural N-heterocyclic organic pollutants using immobilized nanoparticles of titania. *J. Hazard. Mater.* **2007,** *145* (1), 65-71.

2. van Leeuwen, J.; Awad, J.; Myers, B.; Pezzaniti, D., Introduction to urban stormwater: A global perspective. In *Urban Stormwater and Flood Management: Enhancing the Liveability of Cities*, Jegatheesan, V.; Goonetilleke, A.; van Leeuwen, J.; Kandasamy, J.; Warner, D.; Myers, B.; Bhuiyan, M.; Spence, K.; Parker, G., Eds. Springer International Publishing: Cham, **2019**; pp 1-28.

3. Eriksson, E.; Baun, A.; Mikkelsen, P. S.; Ledin, A., Risk assessment of xenobiotics in stormwater discharged to Harrestrup Å, Denmark. *Desalination* **2007,** *215* (1), 187-197.

4. Arques, A.; Amat, A. M.; García-Ripoll, A.; Vicente, R., Detoxification and/or increase of the biodegradability of aqueous solutions of dimethoate by means of solar photocatalysis. *J. Hazard. Mater.* **2007,** *146* (3), 447-452.

5. Vinu, R.; Akki, S. U.; Madras, G., Investigation of dye functional group on the photocatalytic degradation of dyes by nano-TiO_2. *J. Hazard. Mater.* **2010,** *176* (1), 765-773.

6. Pouretedal, H. R.; Norozi, A.; Keshavarz, M. H.; Semnani, A., Nanoparticles of zinc sulfide doped with manganese, nickel and copper as nanophotocatalyst in the degradation of organic dyes. *J. Hazard. Mater.* **2009,** *162* (2), 674-681.

7. Vu, T. T.; del Río, L.; Valdés-Solís, T.; Marbán, G., Stainless steel wire mesh-supported ZnO for the catalytic photodegradation of methylene blue under ultraviolet irradiation. *J. Hazard. Mater.* **2013,** *246-247*, 126-134.

8. Ju, Y.; Qiao, J.; Peng, X.; Xu, Z.; Fang, J.; Yang, S.; Sun, C., Photodegradation of malachite green using UV–vis light from two microwave-powered electrodeless discharge lamps (MPEDL-2): Further investigation on products, dominant routes and mechanism. *Chem. Eng. J.* **2013,** *221*, 353-362.

9. Shang, L.; Li, B.; Dong, W.; Chen, B.; Li, C.; Tang, W.; Wang, G.; Wu, J.; Ying, Y., Heteronanostructure of Ag particle on titanate nanowire membrane with enhanced photocatalytic properties and bactericidal activities. *J. Hazard. Mater.* **2010,** *178* (1), 1109-1114.

10. Oh, H.-J.; Lee, J.-H.; Kim, Y.-J.; Suh, S.-J.; Lee, J.-H.; Chi, C.-S., Synthesis of effective titania nanotubes for wastewater purification. *Appl. Catal. B.* **2008,** *84* (1), 142-147.

11. Tryk, D. A.; Fujishima, A.; Honda, K., Recent topics in photoelectrochemistry: achievements and future prospects. *Electrochim. Acta* **2000,** *45* (15), 2363-2376.

12. Kubacka, A.; Fernández-García, M.; Colón, G., Advanced Nanoarchitectures for Solar Photocatalytic Applications. *Chem. Rev.* **2012,** *112* (3), 1555-1614.

13. Tang, J.; Zou, Z.; Ye, J., Efficient photocatalytic decomposition of organic contaminants over $CaBi_2O_4$ under visible-light irradiation. *Angew. Chem.* **2004,** *116* (34), 4563-4566.

14. Sakthivel, S.; Kisch, H., Daylight photocatalysis by carbon-modified titanium dioxide. *Angew. Chem.* **2003,** *42* (40), 4908-4911.

15. Asahi, R.; Morikawa, T.; Ohwaki, T.; Aoki, K.; Taga, Y., Visible-light photocatalysis in nitrogen-doped titanium oxides. In *J science*, 2001; Vol. 293, pp 269-271.

16. Shamraiz, U.; Hussain, R. A.; Badshah, A.; Raza, B.; Saba, S., Functional metal sulfides and selenides for the removal of hazardous dyes from Water. *J. Photochem. Photobiol., B* **2016,** *159*, 33-41.

17. Mohamed, R. M.; McKinney, D. L.; Sigmund, W. M., Enhanced nanocatalysts. *Mater. Sci. Eng.* **2012,** *73* (1), 1-13.

18. Samanta, D.; Basnet, P.; Inakhunbi Chanu, T.; Chatterjee, S., Biomolecule assisted morphology-controllable synthesis of Zinc Sulphide nanomaterials for efficient photocatalytic activity under solar irradiation. *J. Alloys Compd.* **2020,** *844*, 155810.

19. Azmina, M.; Nor, R. M.; Rafaie, H.; Razak, N.; Sani, S.; Osman, Z., Enhanced photocatalytic activity of ZnO nanoparticles grown on porous silica microparticles. *Appl. Nanosci.* **2017,** *7* (8), 885-892.

20. Raja, V. R.; Rosaline, D. R.; Suganthi, A.; Rajarajan, M., Facile fabrication of PbS/MoS_2 nanocomposite photocatalyst with efficient photocatalytic activity under visible light. *Solid State Sci.* **2017,** *67*, 99-108.

21. Suroshe, J. S.; Mlowe, S.; Garje, S. S.; Revaprasadu, N., Preparation of iron sulfide nanomaterials from iron(II) thiosemicarbazone complexes and their application in photodegradation of methylene blue. *J. Inorg. Organomet. Polym. Mater.* **2018,** *28* (3), 603-611.

22. Uma, K.; Munusamy, K.; Munirathinam, E.; Yang, T. C. K.; Lin, J.-H.; Kannaiyan, D., Active synthesis of graphene nanosheet-embedded PbS octahedral nanocubes for prompt sonocatalytic degradation. *J. Inorg. Organomet. Polym. Mater.* **2020,** *30* (9), 3797-3807.

23. Suganya, M.; Balu, A. R.; Balamurugan, S.; Srivind, J.; Narasimman, V.; Manjula, N.; Rajashree, C.; Nagarethinam, V. S., Photoconductive, photocatalytic and antifungal properties of PbS:Mo nanoparticles synthesized via precipitation method. *Surf. Inter.* **2018,** *13*, 148-156.

24. Alarawi, A.; Ramalingam, V.; He, J.-H., Recent advances in emerging single atom confined two-dimensional materials for water splitting applications. *Mater. Today Energy* **2019,** *11*, 1-23.

25. Ain, N. u.; Zia ur, R.; Aamir, A.; Khan, Y.; Rehman, M.-u.; Lin, D.-J., Catalytic and photocatalytic efficacy of hexagonal CuS nanoplates derived from copper(II) dithiocarbamate. *Mater. Chem. Phys.* **2020,** *242*, 122408.

26. Ajibade, P. A.; Oluwalana, A. E., Structural, optical, photocatalytic and electrochemical studies of PbS nanoparticles. *J. Nano Res.* **2020,** *61*, 18-31.

27. Oluwalana, A. E.; Ajibade, P. A., Structural, optical and photocatalytic studies of hexadecylamine-capped lead sulfide nanoparticles. *Int. J. Ind. Chem.* **2020,** *11* (4), 249-260.

28. Solomane, N.; Ajibade, P. A., Synthesis and crystal structure of bis(thiomorpholinyldithiocarbamato)Cu(II) complex and its use as precursor for CuS nanoparticles photocatalyst for the degradation of organic dyes. *J. Sulfur Chem.* **2021,** *42* (2), 167-179.

29. Antoniou, M.; Dionysiou, D., Application of immobilized titanium dioxide photocatalysts for the degradation of creatinine and phenol, model organic contaminants found in NASA's spacecrafts wastewater streams. *Catal. Today* **2007,** *124*, 215-223.

30. Narayanan, H.; G, A.; E.P, Y.; Suguna, Y., Sunlight induced removal of rhodamine B from water through semiconductor photocatalysis: Effects of adsorption, reaction conditions and additives. *Res. J. Mater. Sci.* **2013,** *1*, 9-17.

31. Liu, S.; Han, L.; Liu, H., Synthesis, characterization and photocatalytic performance of PbS/Ni2P flowers. *Appl. Surf. Sci.* **2016,** *387*, 393-398.

32. Gnanaprakasam, A.; Sivakumar, V. M.; Thirumarimurugan, M., Influencing Parameters in the Photocatalytic Degradation of Organic Effluent via Nanometal Oxide Catalyst: A Review. *Indian J. Mater. Sci.* **2015,** *2015*, 601827.

33. Belhadj Tahar, N.; Savall, A., Electrochemical removal of phenol in alkaline solution. Contribution of the anodic polymerization on different electrode materials. *Electrochim. Acta* **2009,** *54* (21), 4809-4816.

34. Li, X.-y.; Cui, Y.-h.; Feng, Y.-j.; Xie, Z.-m.; Gu, J.-D., Reaction pathways and mechanisms of the electrochemical degradation of phenol on different electrodes. *Water Res.* **2005,** *39* (10), 1972-1981.

35. Chiu, Y.-H.; Chang, T.-F. M.; Chen, C.-Y.; Sone, M.; Hsu, Y.-J., Mechanistic Insights into Photodegradation of Organic Dyes Using Heterostructure Photocatalysts. *Catalysts* **2019,** *9* (5).

36. Chowdhury, A. P.; Shambharkar, B. H.; Ghugal, S. G.; Umare, S. S.; Shende, A. G., Ethylene glycol mediated synthesis of SnS quantum dots and their application towards degradation of eosin yellow and brilliant green dyes under solar irradiation. *RSC Adv.* **2016,** *6* (110), 108290-108297.

37. Cheng, L.; Li, D.; Dong, X.; Ma, Q.; Yu, W.; Wang, X.; Yu, H.; Wang, J.; Liu, G., Synthesis, Characterization and Photocatalytic Performance of SnS Nanofibers and SnSe Nanofibers Derived from the Electrospinning-made SnO_2 Nanofibers. *Mater. Res.* **2017,** *2017*, 1748-1755.

38. Oluwalana, A. E.; Ajibade, P. A., Tin sulfide nanoparticles as photocatalysts for the degradation of organic dyes. *J. Sulfur Chem.* **2021**, 1-22.

39. Chieng, H. I.; Priyantha, N.; Lim, L. B. L., Effective adsorption of toxic brilliant green from aqueous solution using peat of Brunei Darussalam: isotherms, thermodynamics, kinetics and regeneration studies. *RSC Adv.* **2015,** *5* (44), 34603-34615.

40. Mahmood, K.; Amara, U.; Siddique, S.; Usman, M.; Peng, Q.; Khalid, M.; Hussain, A.; Ajmal, M.; Ahmad, A.; Sumrra, S. H.; Liu, Z.-P.; Khan, W. S.; Ashiq, M. N., Green synthesis of Ag@CdO nanocomposite and their application towards brilliant green dye degradation from wastewater. *J. Nanostruct. Chem.* **2021**.

CHAPTER SIX

CONCLUSION AND RECOMMENDATION FOR FURTHER STUDIES

6.1 Conclusions

The aim of this study was to prepare PbS and SnS nanoparticles from Pb(II) and Sn(II) dithiocarbamate single source precursors, study their optical and structural properties and evaluate the potentials as photocatalysts for degradation of organic dyes. Five dithiocarbamate ligands were prepared from morpholine, thiomorpholine, N-(2-hydroxyethyl)aniline, 4-methylpiperidine, 4-benzylpiperidine. The absorption spectra of the dithiocarbamate ligands showed $\pi \rightarrow \pi^*$ transitions that are attributable to the N-C=S and S-C=S groups as well as $n \rightarrow \pi^*$ of the sulfur atoms. ^{1}H and ^{13}C NMR were used to characterize the ligands. The relevant peaks confirming the number of protons for each ligand were observed on the ^{1}H NMR spectra and the carbon resonance at about 200 ppm confirming the presences of the C—S in the ligands was observed on the carbon-13 spectra. Two peaks ascribed to C-S and C=S were observed in the FTIR spectra of ligands. The characterization methods used confirmed the successful synthesis of dithiocarbamate ligands.

Five lead(II) and five tin(II) dithiocarbamate complexes were synthesized from the ligands. The synthesis of the complexes from the ligands was verified by the appearance of MLCT peaks on the UV-Vis spectra for all complexes. Two structures of two lead(II) complexes were also confirmed by X-ray crystallography, namely bis(4-methylpiperidine-1-carbothioato)-lead(II)and bis(4-benzylpiperidine-1-carbothioato)-lead(II) and they crystallized in monoclinic C2/c and monoclinic C2/n space groups, respectively. The structures of the compounds revealed monomeric lead(II) complexes with lead(II) ions bonding to two dithiocarbamato

anions forming a distorted tetrahedral shape. The FTIR spectra revealed all of the significant functional groups anticipated from dithiocarbamate molecules, including C-S, C=S, and N-CS vibrations. The FTIR analysis also demonstrated that the dithiocarbamate ligands are bidentately coordinated to the Pb and Sn ions.

Five SnS nanoparticles were prepared from bis(morpholinyldithiocarbamato)Sn(II), bis(thiomorpholinyldithiocarbamato)Sn(II), bis(N-(2-hydroxyethyl)phenyldithiocarbamato)Sn(II), bis(4-methylpiperidinedithiocarbamato)Sn(II) and bis(4-benzylpiperidinedithiocarbamato)Sn(II). The complexes were all thermolyzed at 180 ℃ to study the influence of precursor on the optical properties and morphology of the SnS nanoparticles produced. Powder-XRD was used to study structural properties of the SnS nanoparticles and they were all indexed to orthorhombic SnS phase, this suggests that the precursor had no effect on the phase of the nanoparticles. The optical studies show SnS**1**, SnS**2**, SnS**3**, SnS**4** and SnS**5** with band gap energies of 3.85 eV, 3.97 eV, 3.42 eV, 3.82 eV and 3.60 eV, respectively. All the nanoparticles were quantum confined and SnS nanoparticles made from bulky precursors have a narrower energy bandgap than those prepared from small sized precursors. SEM images showed nanoparticles surface morphology varying from smooth, irregular, rough and asphalt crush-like. This suggests that the precursor has an effect on the morphology of the SnS nanoparticles.

Three Pb(II) dithiocarbamate complexes, namely bis(morpholinyldithiocarbamato)Pb(II), bis(thiomorpholinyldithiocarbamato)Pb(II) and bis(N-(2-hydroxyethyl)phenyldithiocarbamato)Pb(II), were thermolyzed at 180℃ and used to study the

effects of precursor on size, shape and optical properties of the PbS nanoparticles. HRTEM images show agglomerated semi-spherical particles with the size range of 16.55–35.16 nm for PbS**1**, 13.86–36.04 nm for PbS**2** and 25.43–36.06 nm for PbS**3**. The SEM micrographs revealed flaky, spherical to rough surface morphologies for the as-prepared PbS nanoparticles. The precursor has an effect on the sizes of the PbS nanoparticles obtained but not on the shape. The p-XRD patterns for all the PbS nanoparticles are indexed to face-centered cubic phase of PbS. This suggests that precursor had no effect on the phase of the nanoparticles. The optical studies show PbS**1**, PbS**2** and PbS**3** with energy band gap of 2.96 eV, 3.59 eV, and 3.83 eV, respectively. The nanoparticles are quantum confined and the precursor has an effect on optical properties of the PbS nanoparticles. It is observed that the band gap of the PbS nanoparticles increases with an increase in the molecular weight of the precursor.

Two lead(II) dithiocarbamate complexes, (bis(4-methylpiperidinedithiocarbamato)Pb(II) and bis(4-benzylpiperidinedithiocarbamato)Pb(II)) were also thermolyzed at 180℃ and used to study the effect of three different capping agents, hexadecylamine (HDA), octadecylamine (ODA) and (trioctylphosphine oxide (TOPO), on size, shape and optical properties of the PbS nanoparticles. The HRTEM images of HDA and ODA capped PbS nanoparticles show agglomerated cubic shape with average particle size of 58.88 nm for HDA-PbS**4**, 66.52 nm for HDA-PbS**5**, 47.29 nm for ODA-PbS**4** and 67.51 nm for ODA-PbS**5**. TOPO capped nanoparticles show closely packed agglomerates with mean size of 61.32 nm for PbS**4** and 58.21 nm for PbS**5**. SEM images revealed irregular, densely packed flakes, smooth, closely packed spherical and rough surface morphologies. The structural studies show that the shape of the PbS nanoparticles is dependent on the capping agent and not on the precursor, while the particle size is dependent on the precursor used. The p-XRD patterns of the all as-prepared PbS

nanoparticles are indexed to the face-centered cubic phase of PbS. The capping agents have no effect on the phase of the PbS nanoparticles. The optical studies show the highest bandgap energy of 4.50 eV was obtained for ODA-PbS**4**, while the lowest bandgap energy of 3.43 eV was obtained for TOPO-PbS**4** and the band gap energies of HDA-PbS**4**, HDA-PbS**5**, ODA-PbS**5** and TOPO-PbS**5** are 3.57 eV, 3.98 eV, 3.47 eV and 3.50 eV, respectively. The optical studies suggest quantum confinement and the energy band gaps of the nanoparticles are all different with no apparent trend. Therefore it can be concluded that the Pb(II) and Sn(II) dithiocarbamate complexes used in this study are effective single-source precursors for the fabrication of PbS and SnS nanoparticles.

The PbS**1**, PbS**2** and PbS**3** nanoparticles were used as photocatalysts for the degradation of methylene blue dye under UV irradiation for 180 min. The photodegradation of methylene blue dye by the PbS nanoparticles show degradation efficiency of 72.55 %, 75.86 % and 47.37 % for PbS**1**, PbS**2** and PbS**3**, respectively. There is correlation between the degradation efficiencies observed and morphological properties of the PbS nanoparticles. The degradation of methylene blue follow pseudo-first order kinetics of the Langmuir-Hinshelwood model with the rate constants of 0.0073 min^{-1} for PbS**1**, 0.0082 min^{-1} for PbS**2**, and 0.0040 min^{-1} for PbS**3**. An increase in degradation efficiency is observed as the pH of the medium increases. Low degradation percentage of 30.63% (PbS**1**), 48.88% (PbS**2**) and 17.69% (PbS**3**) is observed in acidic medium of pH (4) and high degradation efficiency of 85.29% (PbS**1**), 81.62% (PbS**2**) and 74.92% (PbS**3**) is observed in alkaline medium of pH (10). The recyclability study revealed that PbS**1** and PbS**2** nanoparticles have good photostability and can be recycled for three times, whereas PbS**3** is the least active and has low photostability.

The photocatalytic properties of PbS**4** and PbS**5** nanoparticles was studied by degradation of rhodamine B dye under UV-irradiation for 360 min. The photocatalytic studies show the lowest degradation efficiency of 28.75 %was obtained for ODA-PbS**5**, while the highest degradation efficiency of 46.71% was obtained for ODA-PbS**4** and the degradation efficiencies of HDA-PbS**4**, HDA-PbS**5**, TOPO-PbS**4** and TOPO-PbS**5** are 36.28%, 34.22%, 30.71% and 31.17%, respectively. The degradation efficiencies observed relate to the structural properties of the as-synthesize PbS nanoparticles. The photocatalytic degradation of rhodamine B follows the pseudo-first-order kinetics with ODA-PbS**4** having the fastest rate of 0.0015 min^{-1}. Degradation of rhodamine B is favourably influenced by an increase in the pH of the dye solution. The dye degradation is enhanced with increasing the pH. Highest degradation percentage of 79.99% is observed at pH (10) for ODA-PbS**4** and the lowest degradation efficiency of 5.95% is observed at pH (4) for ODA-PbS**5**. The recycling studies show a slight decrease of 0.51-1.93% in degradation efficiency of the PbS nanoparticles over four cycles with TOPO-PbS**5** being the most photostable.

Photocatalytic degradation of phenol by the PbS**4** and PbS**5** nanoparticles was evaluated under UV irradiation. The degradation efficiencies of phenol by the as-synthesized PbS nanoparticles after 360 min are 24.21% (HDA-PbS**4**), 23.41% (HDA-PbS**5**), 32.84% (ODA-PbS**4**), 11.61% (ODA-PbS**5**), 21.24% (TOPO-PbS**4**) and 23.02% (TOPO-PbS**5**). The degradation of phenol by PbS nanoparticles follow pseudo-first order kinetics of the Langmuir-Hinshelwood model. Among six PbS nanoparticles ODA-PbS**4** exhibited faster degradation rat $1.02x10^{-3}$ min^{-1}. The photocatalysts degrade phenol dye better in basic medium than in acidic medium. The results reveal that the photocatalytic degradation efficiencies of phenol are influenced by the morphological properties of the PbS nanoparticles and reactive oxidative species.

The photocatalytic properties of SnS nanoparticles was studied by degradation of brilliant green dye under UV-irradiation, evaluating the effect of irradiation time, pH and recyclability. The concentration of dye is observed to decrease as irradiation time increases. The photodegradation efficiencies of all SnS nanoparticles are above 90% after 120 min, with the highest being 93% for SnS**4**. The photocatalytic degradation of brilliant green by the as-prepared SnS nanoparticles follows the pseudo-first order kinetics with slightly different rate constants of 0.02364 min^{-1} for SnS**1**, 0.02360 min^{-1} for SnS**2**, 0.02305 min^{-1} for SnS**4**, and 0.02430 min^{-1} for SnS**3** and SnS**5**. The brilliant green degradation is enhanced with increasing the pH and the maximum degradation of 95.88% is observed at pH (10). The SnS nanoparticles are recyclable for five times. The results show that the SnS nanoparticles have good photocatalytic activity and recyclability, and the photodegradation of brilliant green is influenced by irradiation time and solution pH.

6.2 Future recommendations

The lead sulfide nanoparticles were not very active on the photodegradation of phenol and rhodamine B dyes which may the due to the agglomeration observed. Therefore, it is recommended that other reaction parameters such as reaction temperature and duration are explored so as to produce smaller sized nanoparticles with narrow distribution which may enhance their activity towards the degradation of these organic compounds. It is also necessary to study the effects of different capping agents on the morphologies and optical properties of the tin sulfide nanoparticles and further explore their potentials as nanophotocatalysts and investigate the effect of dye concentration and the amounts of catalyst used.

Appendix List

7. Appendix

7.1 Appendix A: Mass spectra of dithiocarbamate ligands and their Pb(II) and Sn(II) complexes

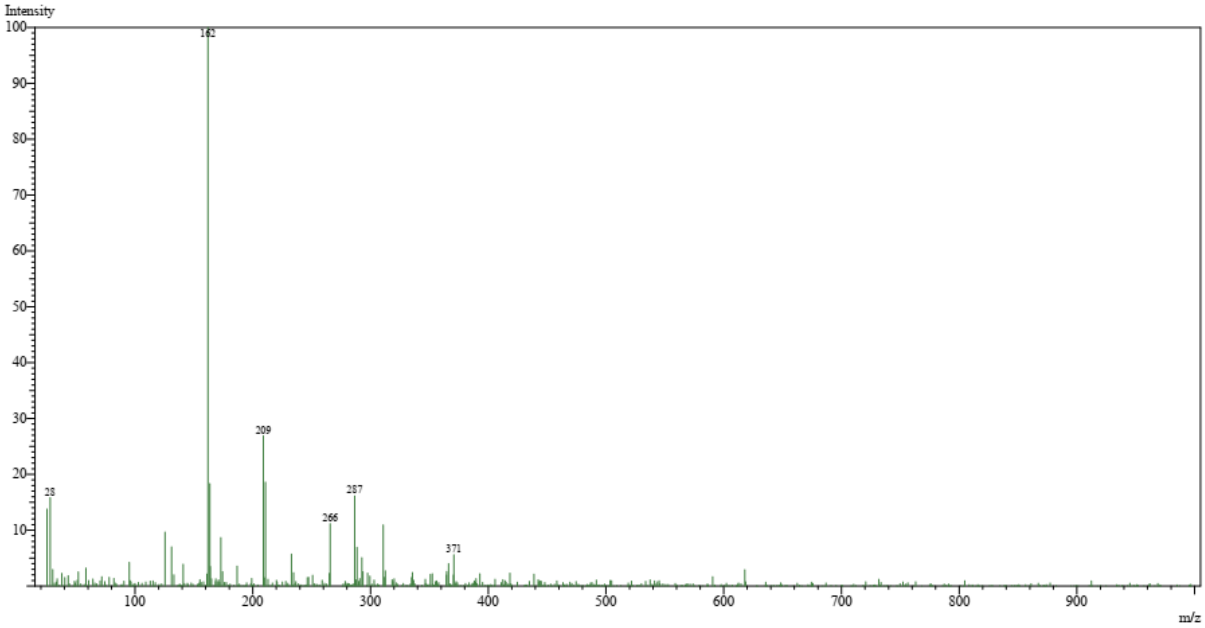

Appendix A1: Mass spectrum of morpholine dithiocarbamate ligand (L^1)

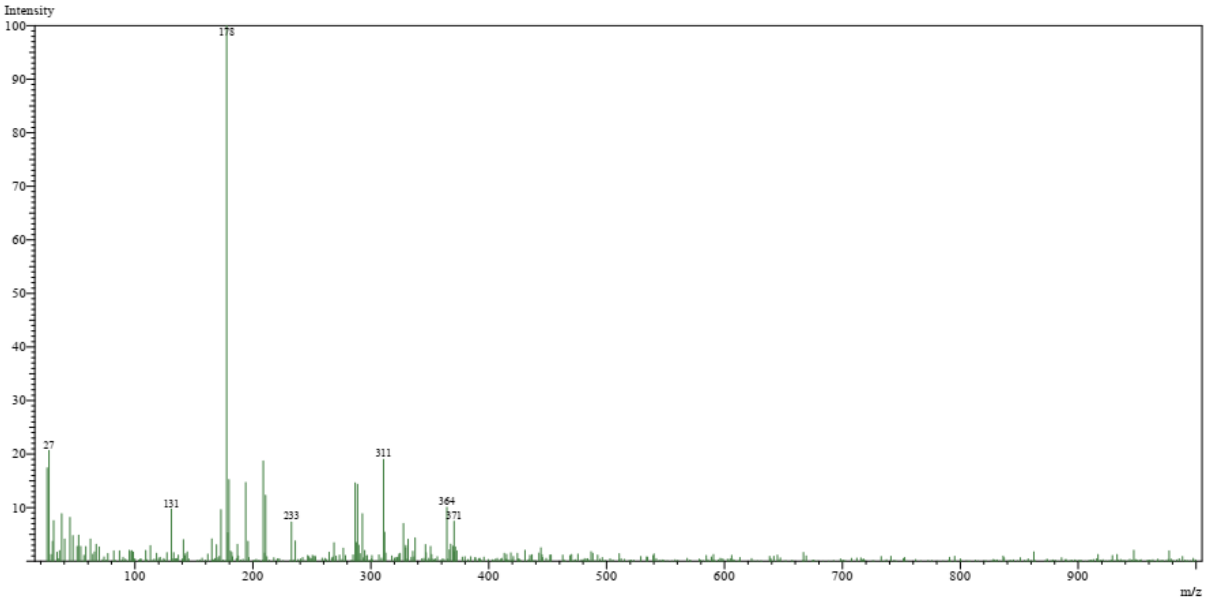

Appendix A2: Mass spectrum of thiomorpholine dithiocarbamate ligand (L^2)

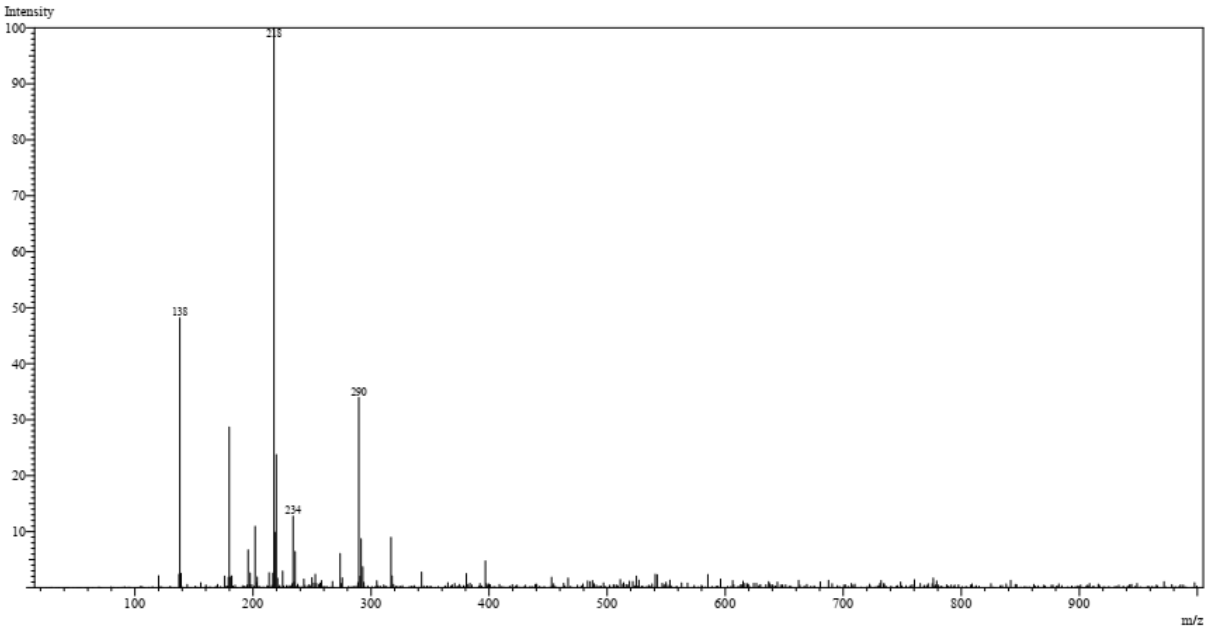

Appendix A3: Mass spectrum of N-(2-hydroxyethyl)phenyl dithiocarbamate ligand (L^3)

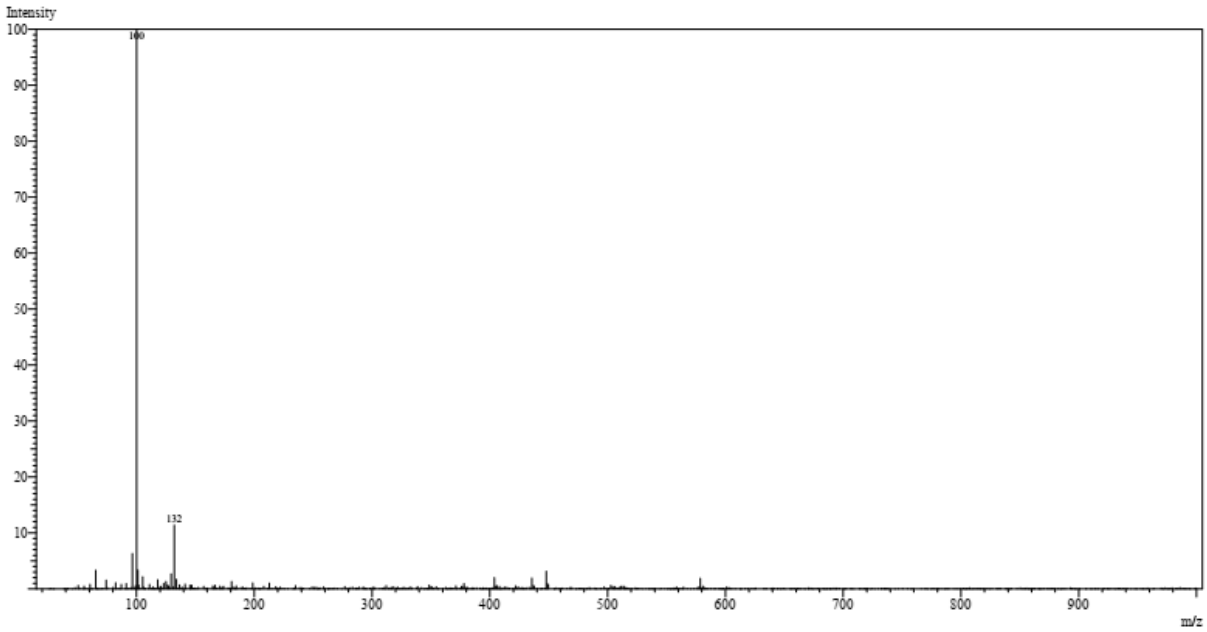

Appendix A4: Mass spectrum of 4-methylpiperidine dithiocarbamate ligand (L^4)

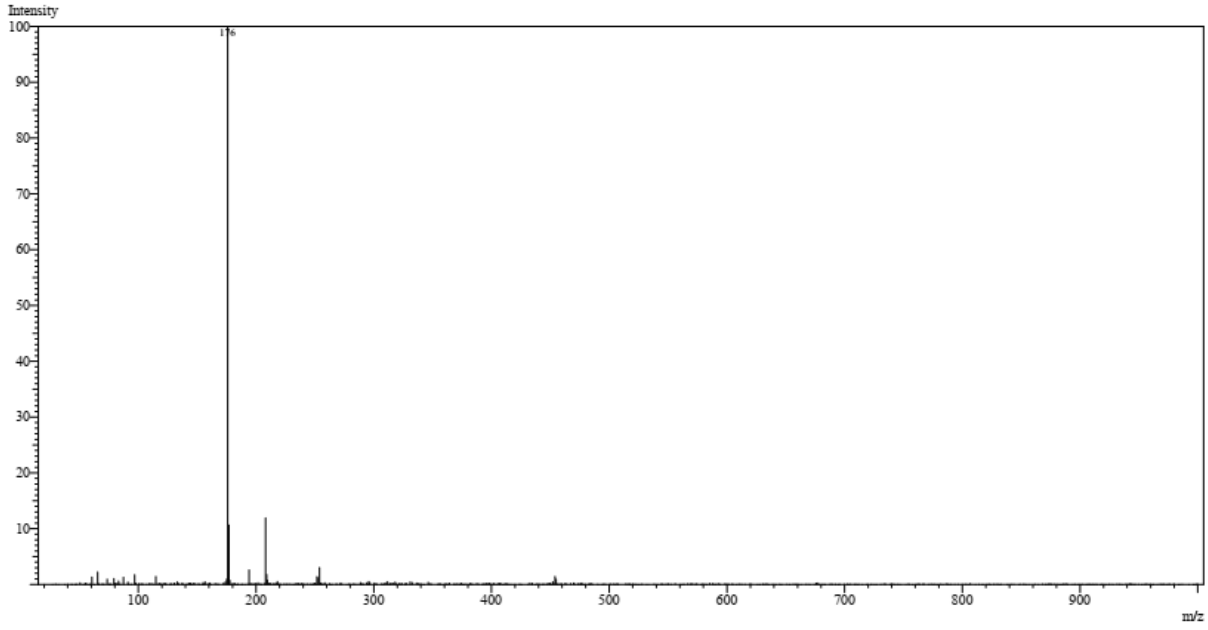

Appendix A5: Mass spectrum of 4-benzylpiperidine dithiocarbamate (L^5)

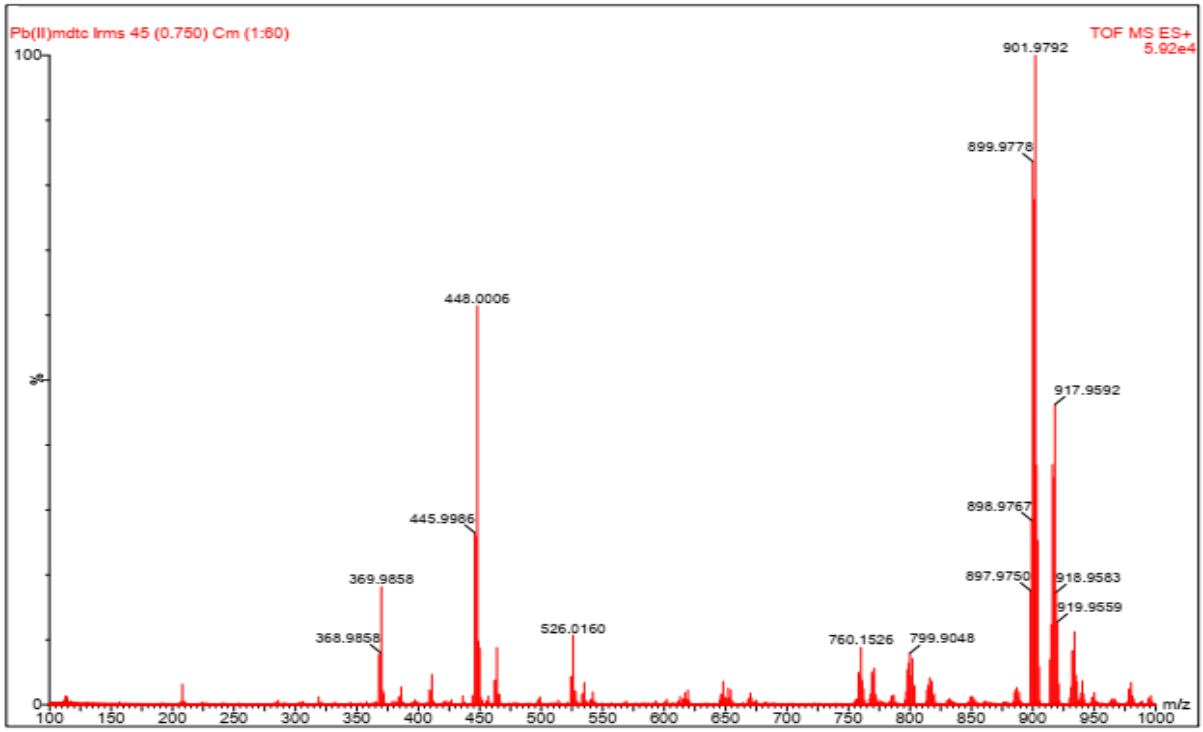

Appendix A6: Mass spectrum of bis(morpholinedithiocarbamate)Pb(II)

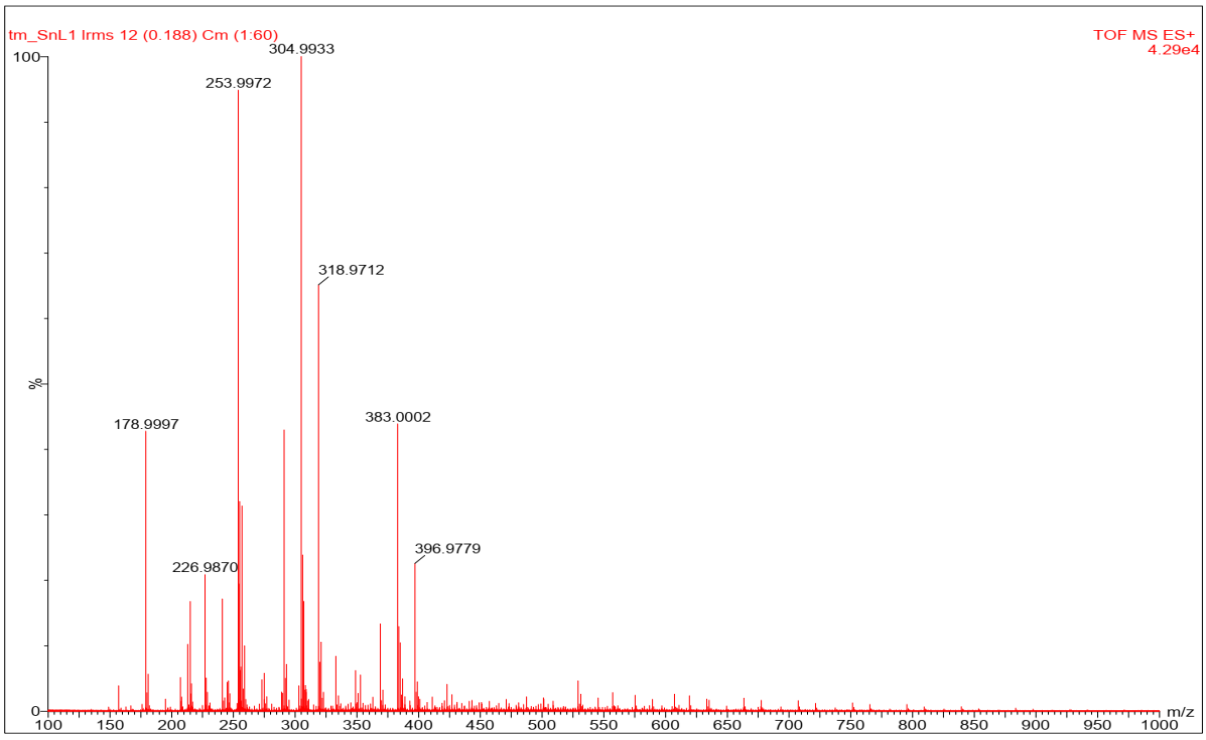

Appendix A7: Mass spectrum of bis(morpholinedithiocarbamate)Sn(II)

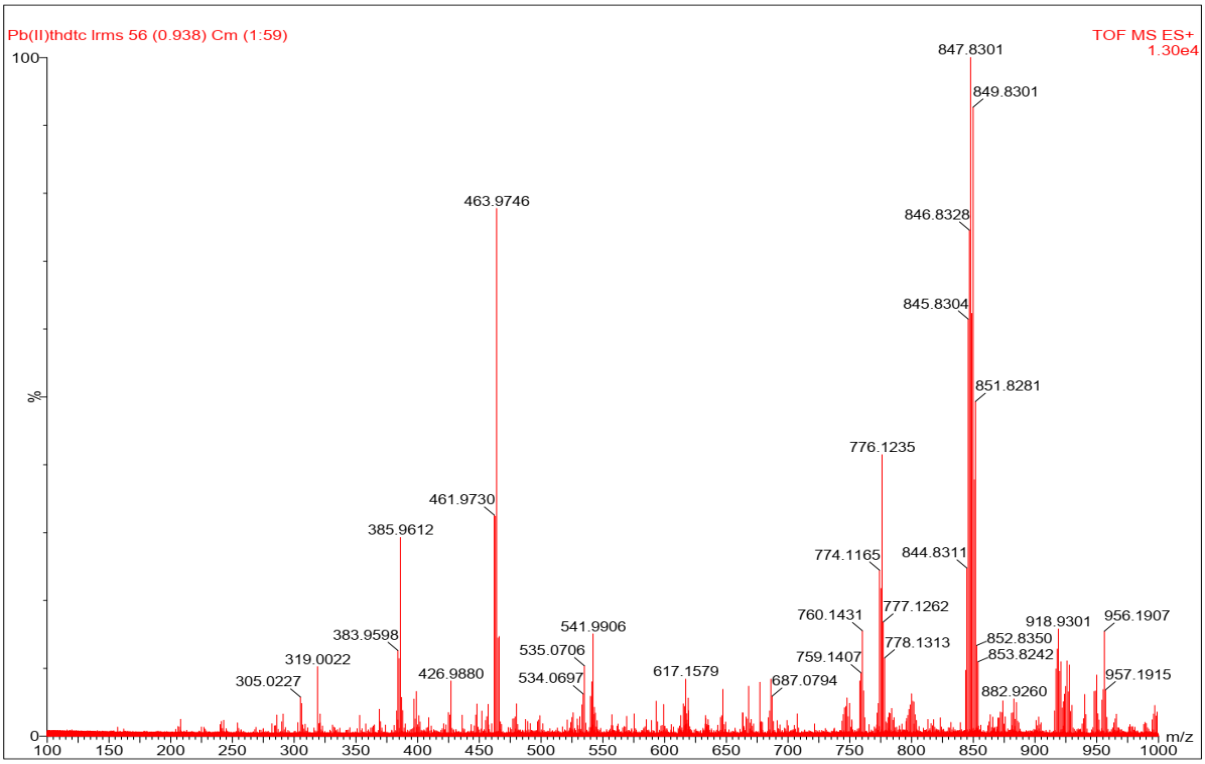

Appendix A8: Mass spectrum of bis(thiomorpholinedithiocarbamate)Pb(II)

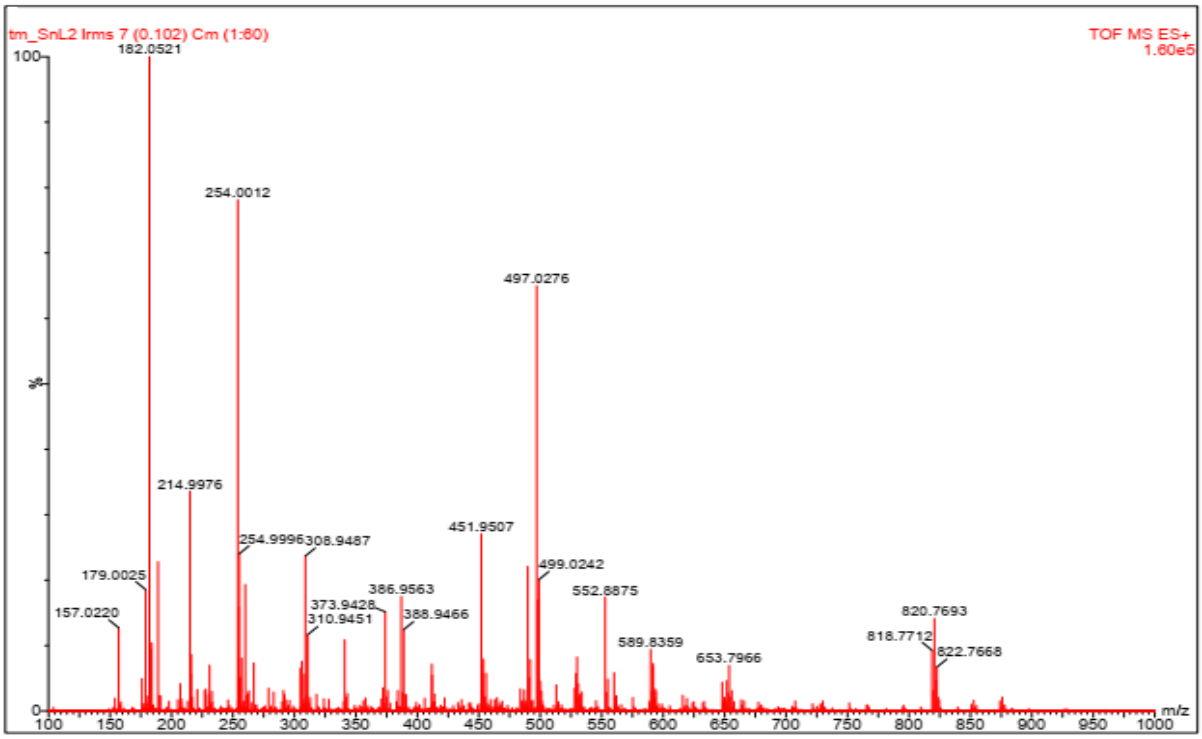

Appendix A9: Mass spectrum of bis(thiomorpholinedithiocarbamate)Sn(II)

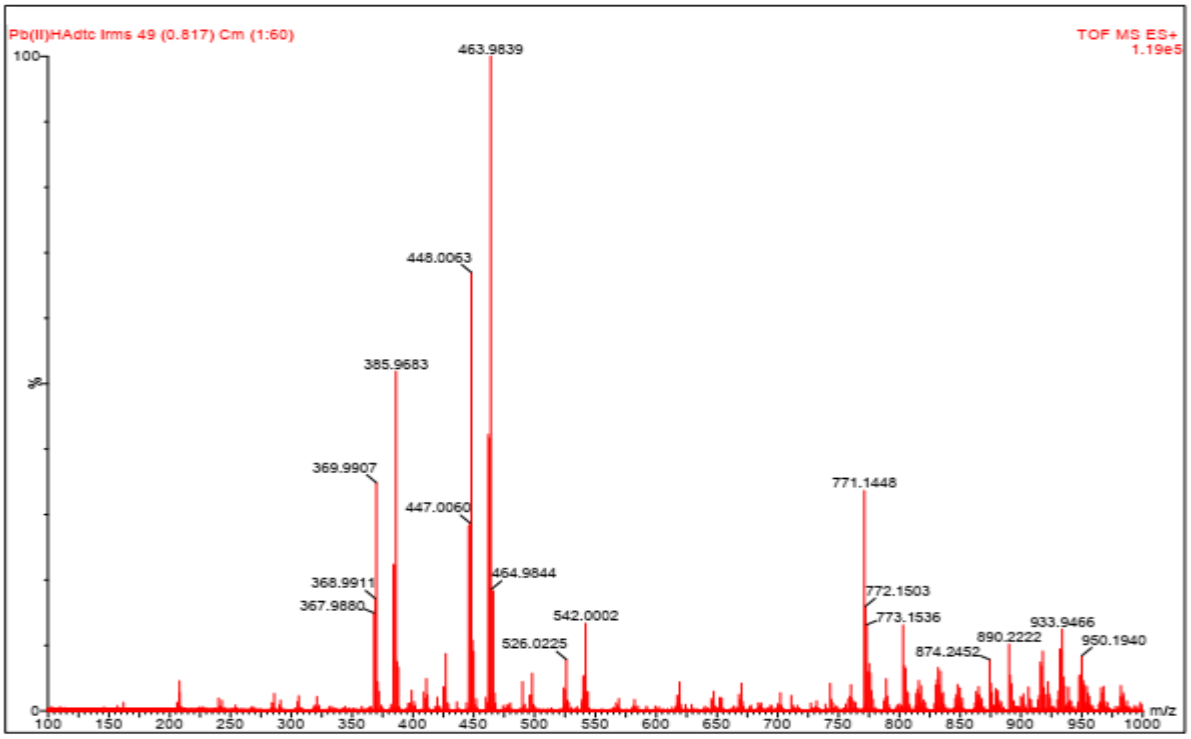

Appendix: A10: Mass spectrum of bis(N-(2-hydroxyethyl)phenyl)Pb(II)

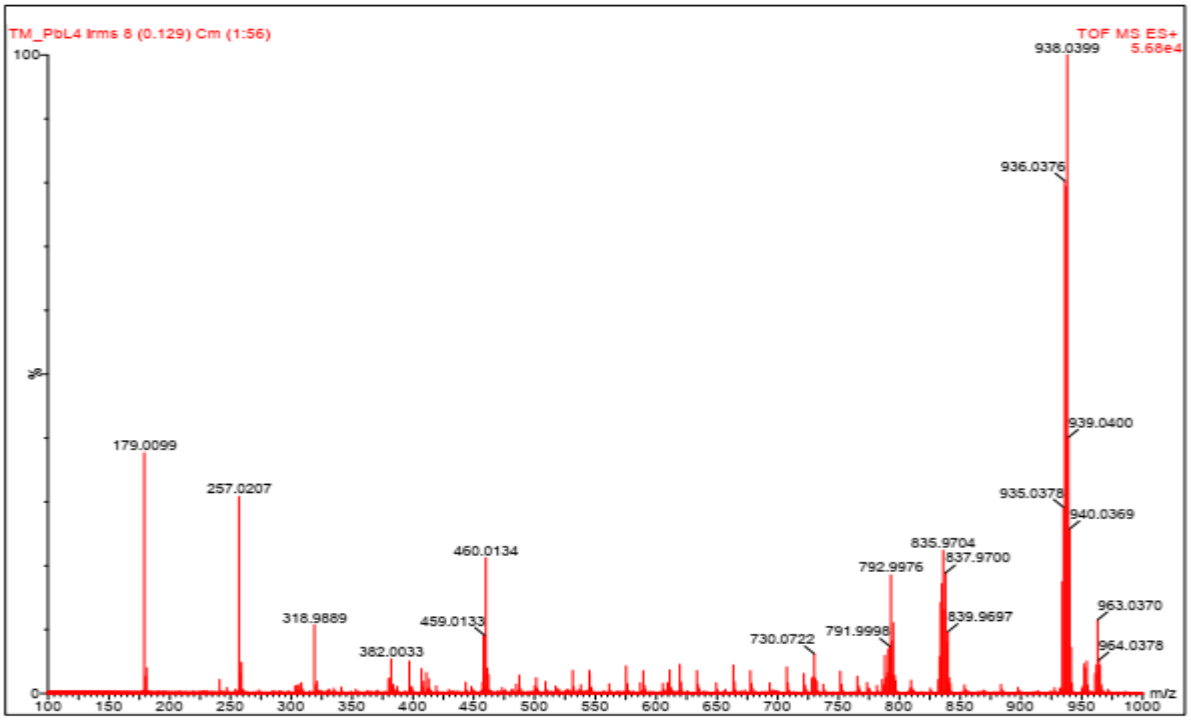

Appendix A11: Mass spectrum of bis(4-methylpiperidine-1-carbothioato)Pb(II)

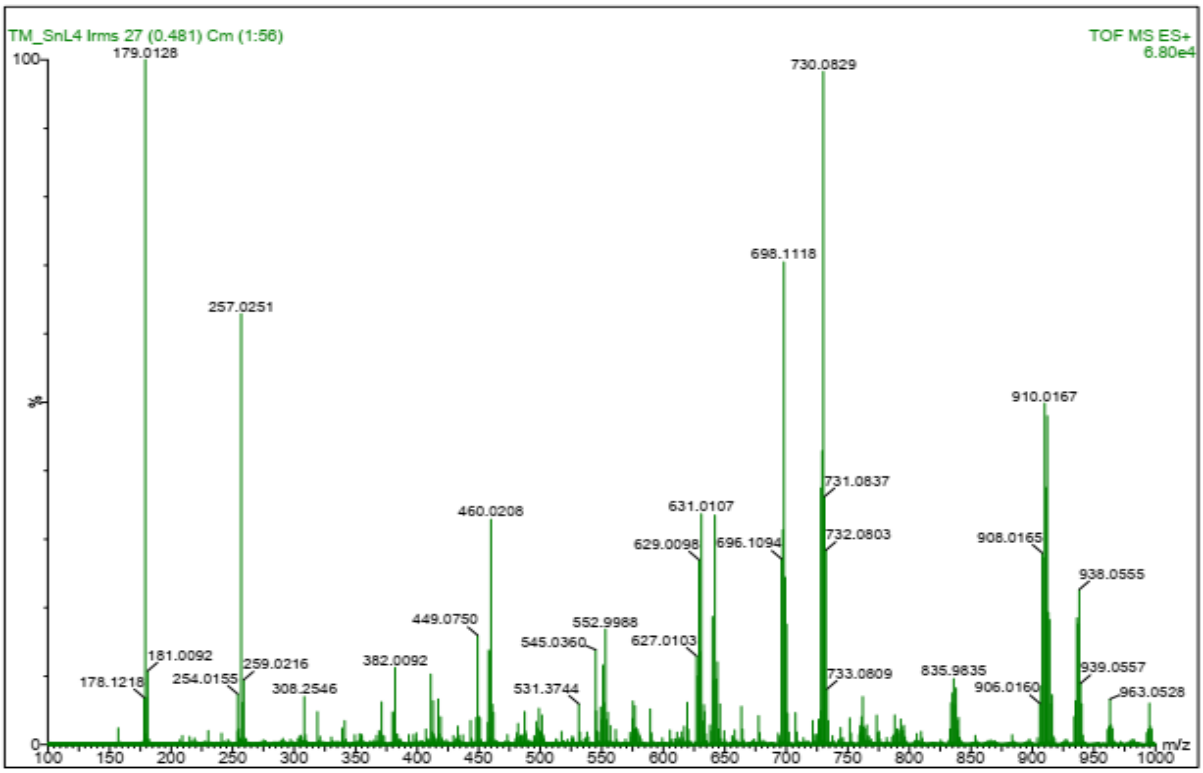

Appendix A12: Mass spectrum of bis(4-methylpiperidine-1-carbothioato)Sn(II)

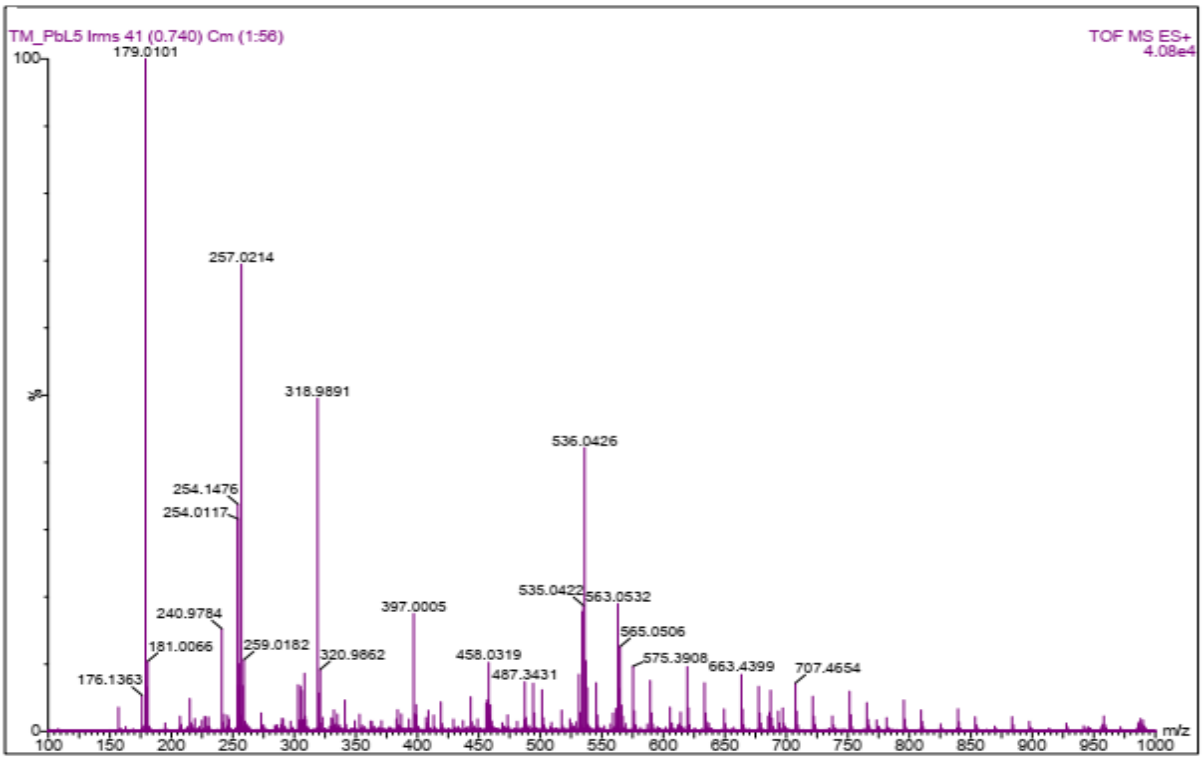

Appendix A13: Mass spectrum of bis(4-benzylpiperidine-1-carbothioato)Pb(II)

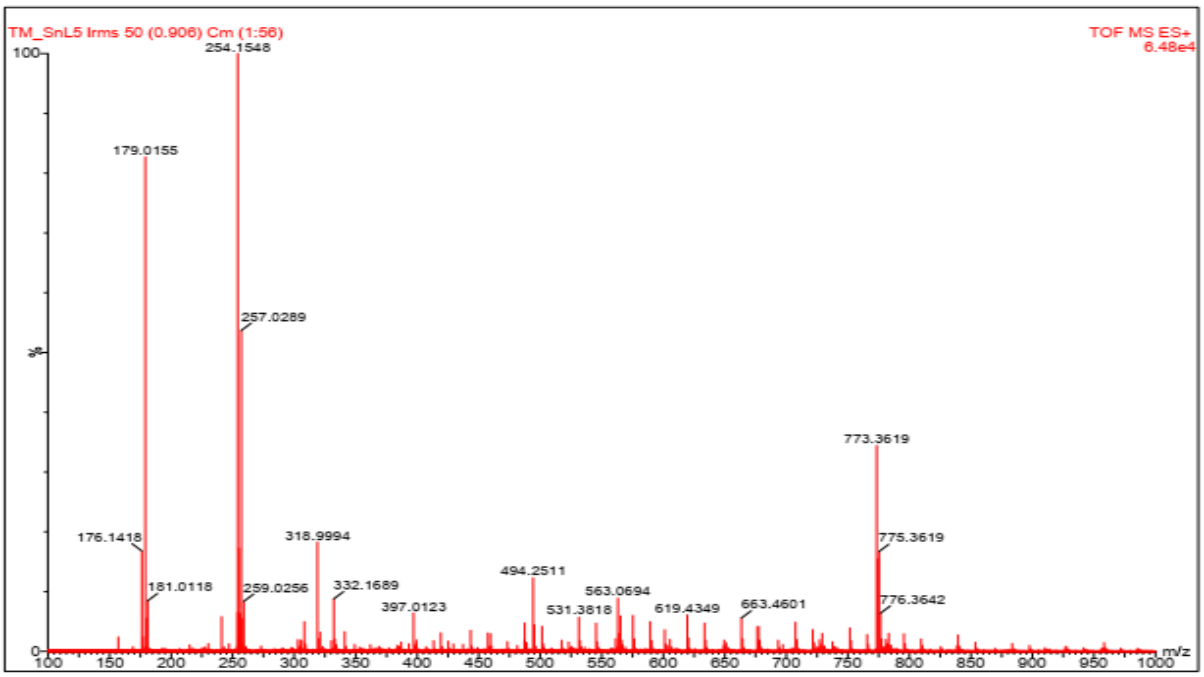

Appendix A14: Mass spectrum of bis(4-benzylpiperidine-1-carbothioato)Sn(II)

7.2 Appendix B: Particle size distributions of PbS4 and PbS5

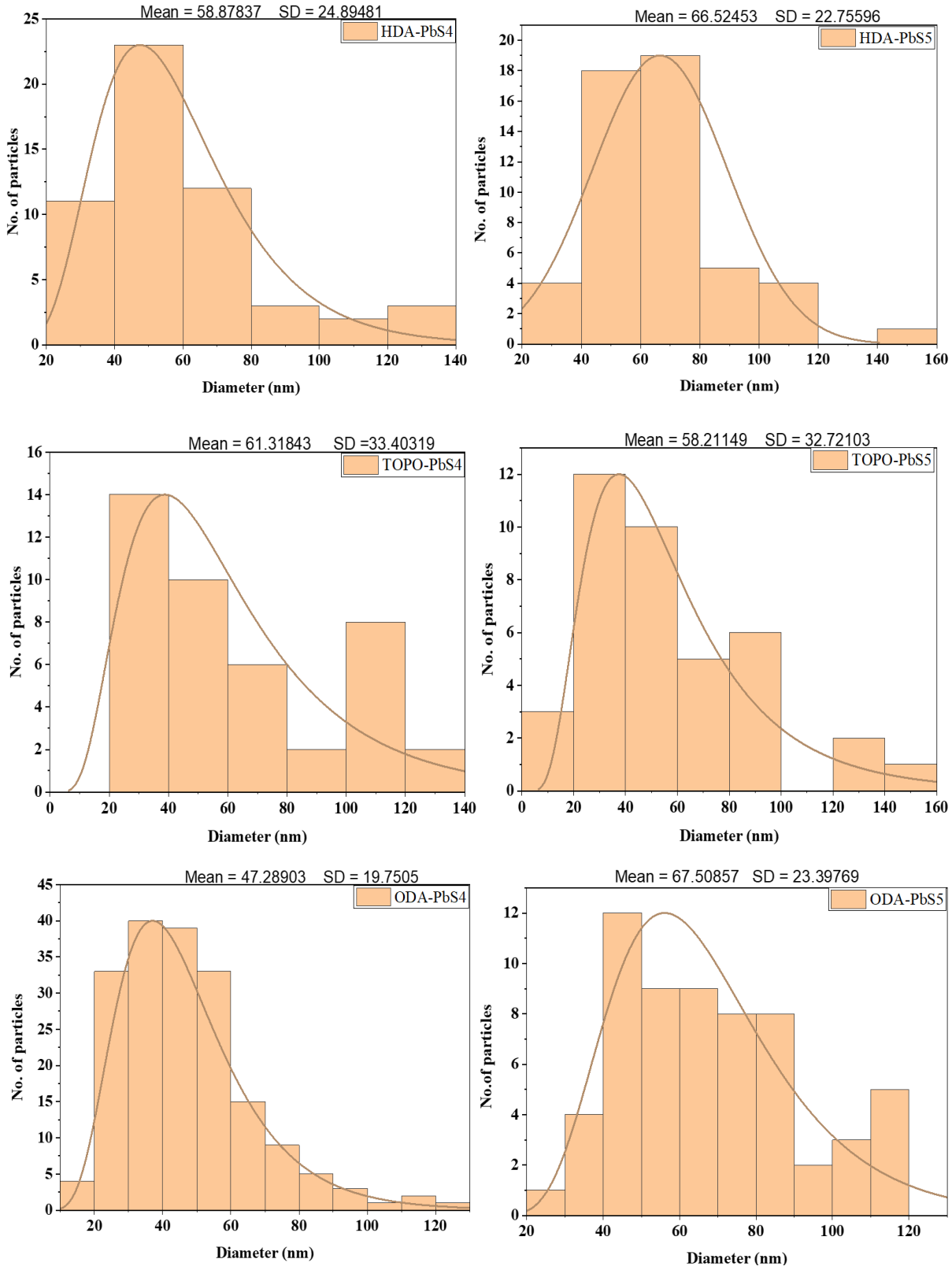

Appendix B1: Particle size distributions of HDA, ODA, and TOPO capped PbS**4** and PbS**5** nanoparticles

7.3 Appendix C: EDX spectra of PbS4 nanoparticles

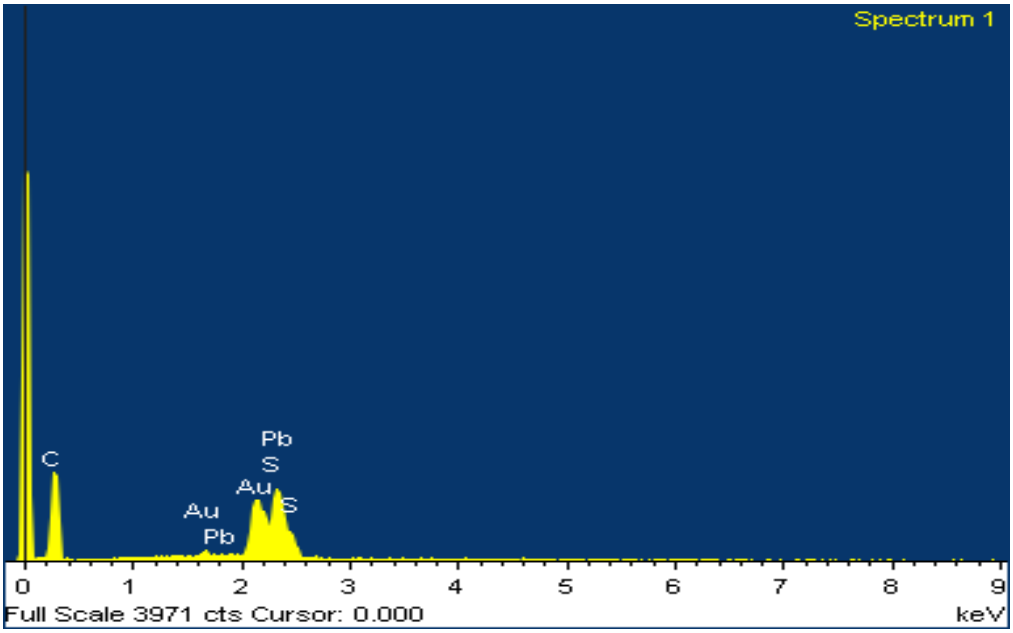

Appendix C1: EDX spectrum of HDA capped PbS**4** nanoparticles

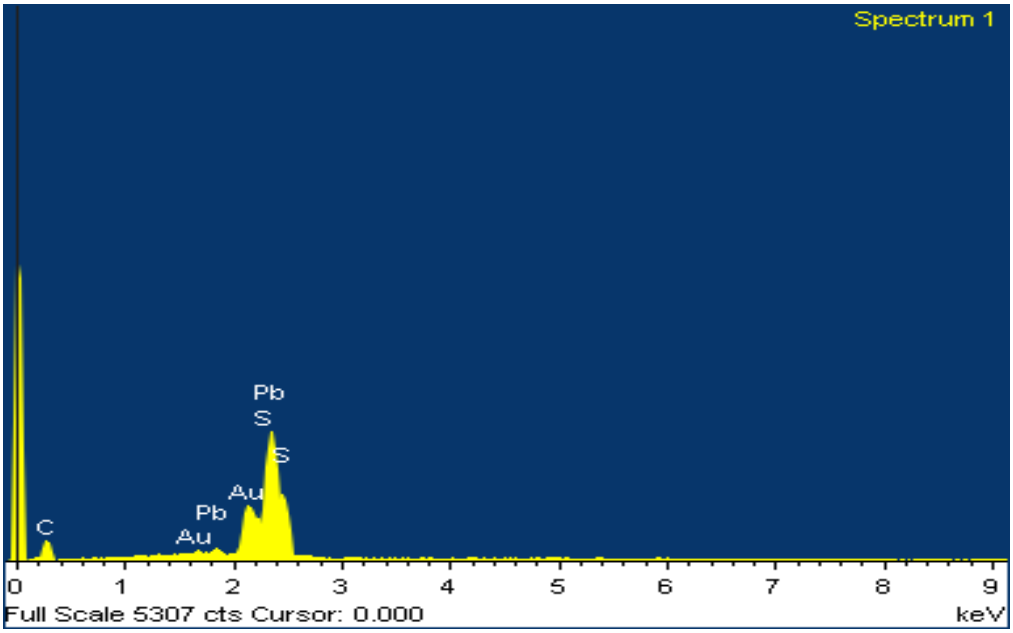

Appendix C2: EDX spectrum of ODA capped PbS**4** nanoparticles

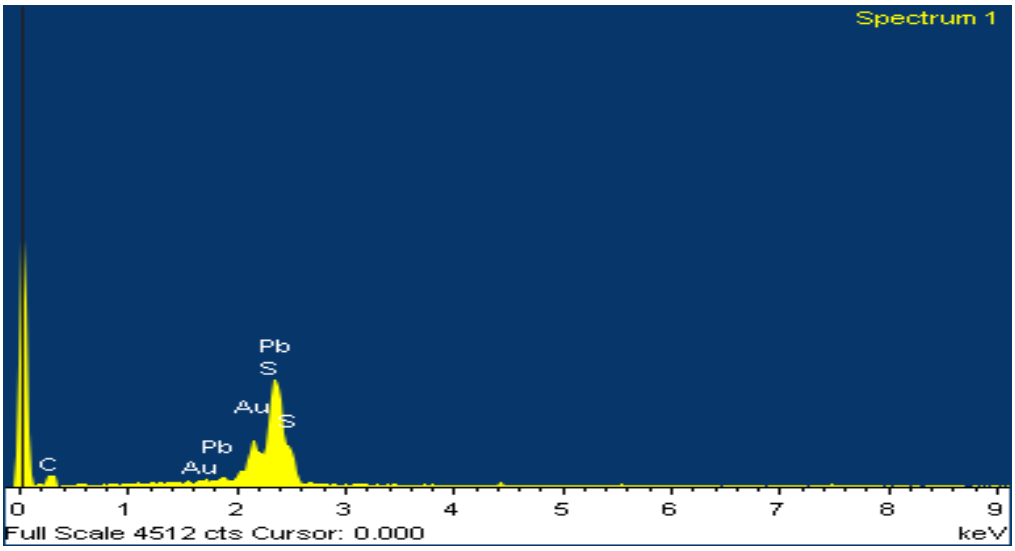
Spectrum 1
Pb
S
Au
S
Pb
Au
C
0
1
2
3
4
5
6
7
8
9
Full Scale 4512 cts Cursor: 0.000
keV

Appendix C3: EDX spectrum of TOPO capped PbS**4** nanoparticles

7.4 Appendix D: EDX spectra of PbS5 nanoparticles

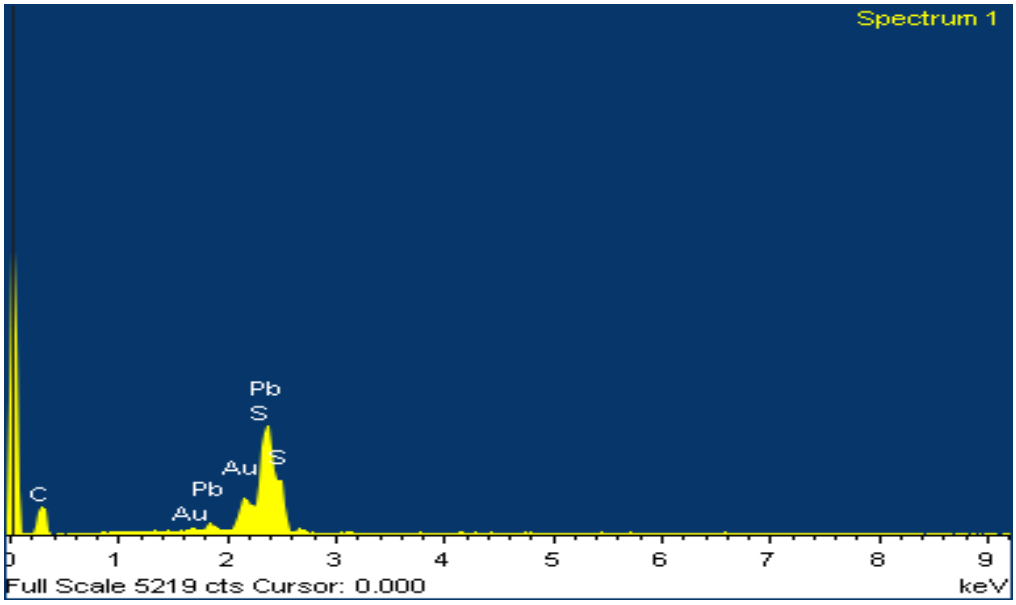

Appendix D1: EDX spectrum of HDA capped PbS**5** nanoparticles

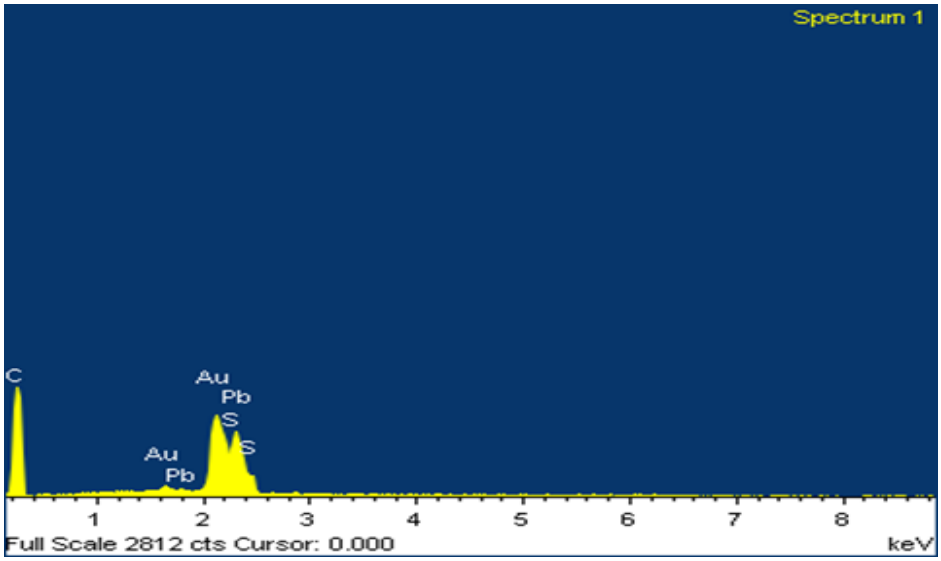

Appendix D2: EDX spectrum of ODA capped PbS**5** nanoparticles

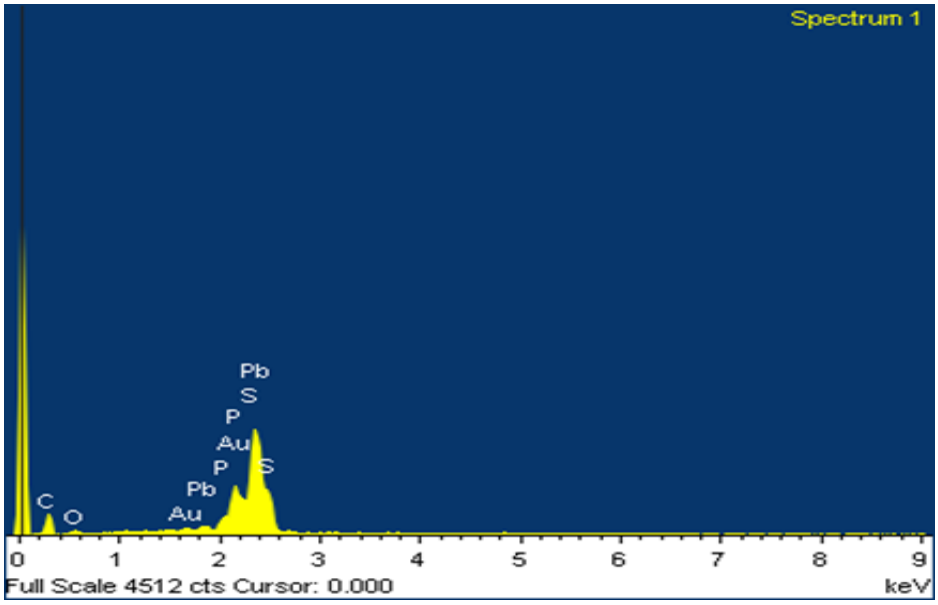

Appendix D3: EDX spectrum of TOPO capped PbS**5** nanoparticles

7.5 Appendix E: EDX spectra of SnS nanoparticles

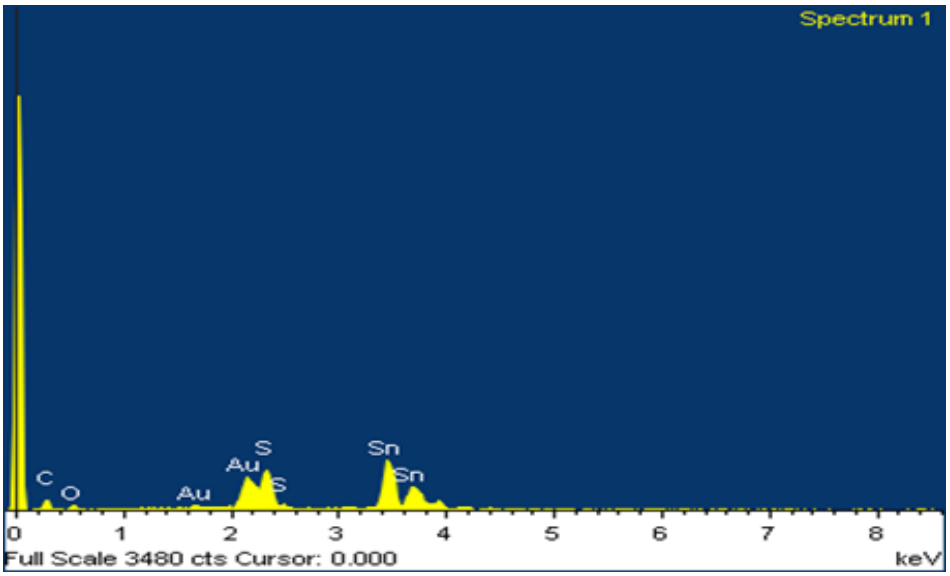

Appendix E1: EDX spectrum of SnS**1** nanoparticles

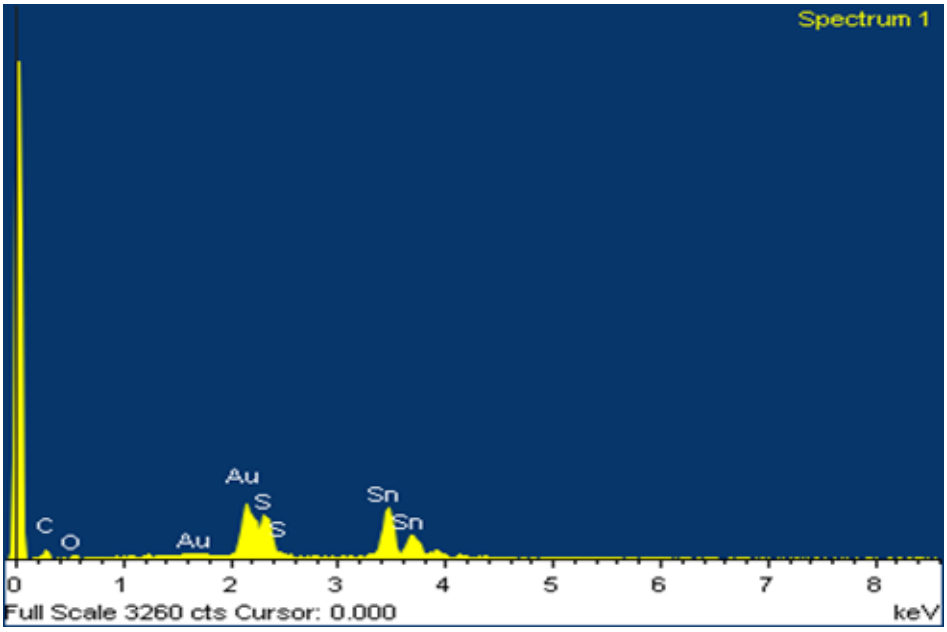

Appendix E2: EDX spectrum of SnS**2** nanoparticles

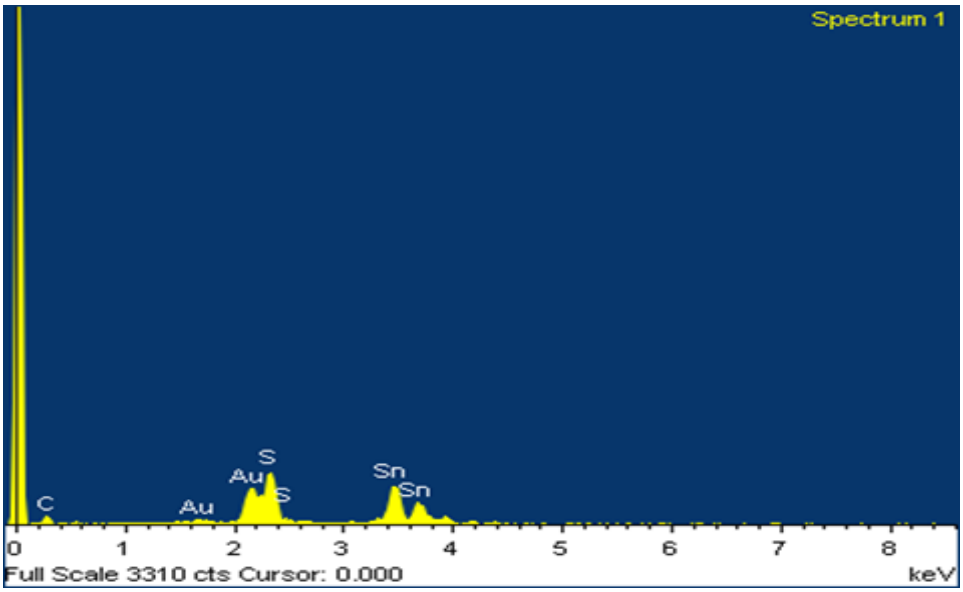

Appendix E3: EDX spectrum of SnS**3** nanoparticles

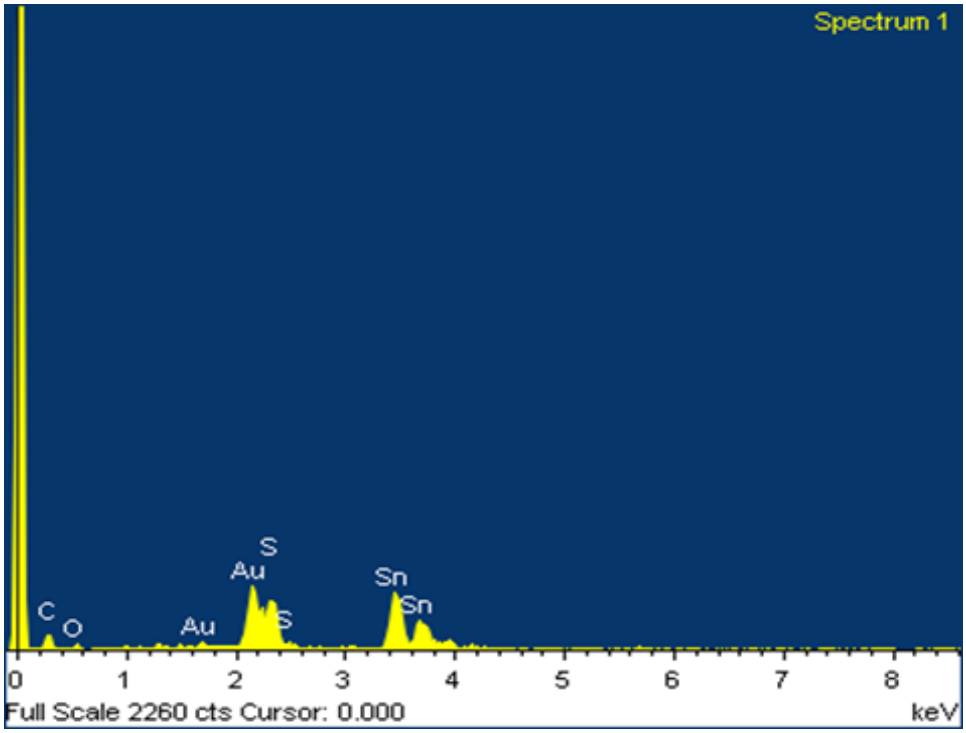

Appendix E4: EDX spectrum of SnS**4** nanoparticles

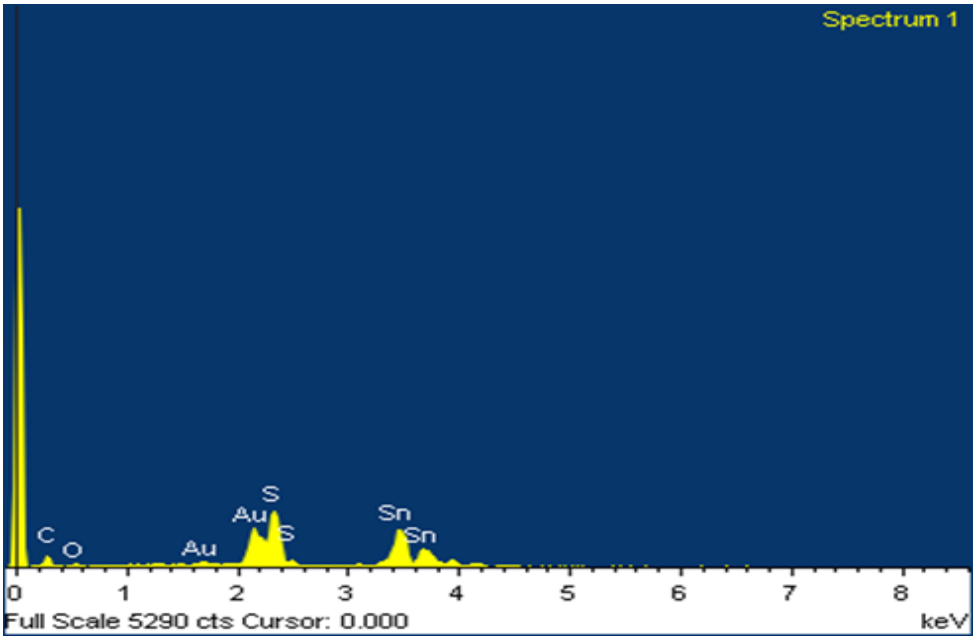

Appendix E5: EDX spectrum of SnS**5** nanoparticles